Università degli Studi di Ferrara

Dipartimento di Ingegneria

Dottorato di Ricerca in Scienze dell'Ingegneria – Ciclo XXVI

Coordinatore: Chiar.mo Prof. Ing. Stefano Trillo

SHAPE MEMORY ALLOYS AND POLYMERS: EXPERIMENTAL 1D MECHANICAL CHARACTERIZATION AND APPLICATIONS

Settore Scientifico Disciplinare ICAR/08

Anni 2011/2013

Dottorando: Ing. Andrea Chiozzi

Tutore: Chiar.mo Prof. Ing. Antonio Tralli

Cotutore: Dott. Ing. Raffaella Rizzoni

SUMMARY

Recent advances in materials engineering have given rise to a new class of materials known as active materials. These materials when used appropriately can aid in development of smart structural systems. Smart structural systems are adaptive in nature and can be utilized in applications that are subject to time varying loads such as aircraft wings, structures exposed to earthquakes, electrical interconnections, biomedical applications, and many more. Materials such as piezoelectric crystals, electro-rheological fluids, shape memory alloys (SMAs) and shape memory polymers (SMPs) constitute some of the active materials that have the innate ability to response to a load by either changing phase (e.g., liquid to solid), and recovering deformation. Active materials when combined with conventional materials (passive materials) such as polymers, stainless steel, and aluminum, can result in the development of smart structural systems (SSS). SMAs and SMPs have a unique ability to recover extensive amounts of deformation (up to 8% strain for SMAs and up to 300% strain for SMPs). This Dissertation focuses on a subclass of active materials, namely shape-memory materials; in particular the focus is on the experimental assessment of two one dimensional constitutive models for NiTiNOL, the most commonly used commercially available SMA with application to the development of a new seismic protection device for masonry historical constructions which has been conceived and constructed at the University of Ferrara and on the mechanical characterization of a brand new shape memory polyurethane named DESMOPAN, patented by Bayer Material Science. Experimental tests on NiTiNOL were conducted in the laboratories of the University of Ferrara, the shape memory alloy device has been tested in the laboratories of the University of Florence and experimental tests on DESMOPAN were conducted in the laboratories of the RWTH Aachen University. The interest on these materials is driven by their potential applications in the developing of new anti-seismic dissipation devices for masonry historical buildings.

The present dissertation is subdivided into four chapters.

First chapter contains a general discussion on smart materials, with a particular focus on shape memory alloys and shape memory polymers. Of both classes of materials an introduction on their mechanical behavior has been outlined and a broad review of their potential applications both in civil engineering and in other fields (such as the biomedical one) has been presented.

Second chapter deals with the first theme on which the PhD activity was focused on: a comparative assessment of two 1D constitutive models for shape memory alloys wires based on an experimental campaign carried at the University of Ferrara in which two NiTiNOL wires of different composition

suitable for seismic applications were tested. The models are representative of two broad classes of constitutive models for shape memory alloys. The goal was to determine which kind of model was best suited to predict experimental observation on real specimens.

Third chapter describes the experimental activity of design, construction and testing of a new seismic dissipater based on the superelastic properties of NiTiNOL wires. The device was subject to 1D traction tests at the University of Ferrara and to quasi-static tests when applied on scale models of masonry buildings at the University of Florence. Finally some numerical simulation was carried on in order to replicate the results obtained during the testing of the device.

Finally, fourth chapter describes the experimental activity that was conducted at the RWTH Aachen University on the mechanical characterization of a new type of shape memory polymer, namely DESMOPAN, produced by Bayer Material Science. 1 dimensional thermo-mechanical tests where carried on polymer bone-shaped specimens in order to assess their thermo-mechanical behavior to set the basis for future research on shape memory polymers constitutive modeling.

Summary

1. INTRODUCTION TO SMART MATERIALS

1.1 General discussion

Shape memory materials (SMMs) are featured by the ability to recover their original shape from a significant and seemingly plastic deformation when a particular stimulus is applied (Otsuka and Wayman 1998). This is known as the shape memory effect (SME). Superelasticity (in alloys) or visco-elasticity (in polymers) are also commonly observed under certain conditions. The SME can be utilized in many fields, from aerospace engineering (e.g., in deployable structures and morphing wings) to medical devices (e.g., in stents and filters) (Otsuka and Wayman 1998), (Funakubo 1987), , (Lipscomb and Nokes, The Applications of Shape Memory Alloysin Medicine 1996), (Duerig 1990). This paragraph aims to introduce and summarize the most recent advances in SMMs. The focus is twofold. One is on the new features found in traditional SMMs, namely shape memory alloys (SMAs) and shape memory polymers (SMPs), which are the object of this Dissertation, and the other is on a newly emerging type of SMM, namely shape memory hybrid (SMH). The latter enables non-experts to design the SMMs with tailored properties/features for a particular application.

Despite the fact that the SME had been found in an AuCd alloy as early as 1932, the attraction of this phenomenon was not so apparent until 1971, when significant recoverable strain was observed in a NiTi alloy at the Naval Ordinance Laboratories, USA (Funakubo 1987). Today a wide range of SMAs have been developed in solid, film and even foam shapes. Among them, only three alloy systems, namely NiTi-based, Cu-based (CuAlNi and CuZnAl) and Fe-based, are presently more of a commercial importance. A systematic comparison of NiTi, CuAlNi and CuZnAl SMAs, in terms of various performance indexes, which are of engineering application interest, has been done (W. Wang 2002). NiTi should be the first choice since it has high performance (Otsuka and Ren 2005) and good biocompatibility. The latter is crucial in biomedical applications, for instance stents and guide wires in minimally invasive surgery (Pelton, A. 1997). Cu-based SMAs have the advantages of low material cost and good workability in processing, and some of them even have the rubber-like behavior after aging in a martensite state (Ren and Otsuka 1997). The SME in Fe-based SMAs is traditionally known to be relatively much weaker and Fe-based SMAs were most likely used only as a fastener/clamp for one-time actuation largely due to the extremely low cost (Funakubo 1987), (Pelton, A. 1997). However, Tanaka et al. (Y. Tanaka 2010) recently reported a ferrous polycrystalline SMA showing huge superelasticity (13%) and high tensile strength (over 1 GPa).

All these SMAs are thermo-responsive i.e., the stimulus required to trigger the shape recovery is heat. In recent years, good progress has been made in developing ferromagnetic SMAs, which are magneto-responsive (Karaca and et al. 2009). However, thermo-responsive SMA has matured more from the real engineering application point of view and many commercial applications have, so far, been realized (Otsuka and Wayman 1998), (Funakubo 1987), (Duerig 1990).

In addition to the SME, some of the SMAs also have the temperature memory effect (TME), so that the highest temperature(s) in the previous heating process(es) within the transition range can be recorded and precisely revealed in the next heating process (Sun and Huang 2010). Partially different martensite after a thermal programming processis believed to be the underlying mechanism for the TME. Based on the same principle, a piece of SMA strip can be thermo-mechanically programmed to bend forward and then backward upon heating. This is a kind of phenomenon, known as the multi-SME (Xie, Tunable polymer multi-shape memory effect 2010), in which a piece of SMM recovers its original shape in a step-by-step manner through one or a few intermediate shapes. The multi-SME can be utilized to work virtually as a machine, but the fascinating point here is that the material is the machine (Battacharya and James 2005).

Let's now introduce shape memory polymers. From the engineering aspect, tailoring the material properties of polymers is much easier than compared with that of metals/alloys (Xie and Rousseau 2009), (Yakacki 2008). In addition, the cost (both material cost and processing cost) of polymers is traditionally much lower. A variety of SMPs have been invented and well-documented in the literature, while presently new ones keep on emerging every week, if not every day (Mather, Luo and Rousseau 2009), (Liu, Qin and Mather 2007). In addition to the above-mentioned advantages, SMPs are much lighter, have much higher (an order higher at least) recoverable strain than SMAs, and can be triggered for shape recovery by various stimuli and even multiple stimuli simultaneously (Yang and Huang 2006), (Huang and Yang 2010). Light (UV and infrared light) and chemical (moisture, solvent and pH change), in addition to heat, are two such types of stimuli (Leng and Haibao 2009), (Lendlein and Jiang, Light-induced shape-memory polymers 2005). Furthermore, many SMPs are naturally biocompatible and even biodegradable (Lendlein and Langer 2002). Consequently, we have more degrees-of-freedom in manipulating SMPs to meet the needs of a particular application. The thermoplastic polyurethane SMP originally invented by Dr. S. Hayashi at Nagoya R&D Center of Mitsubishi Heavy Industry, Japan has been successfully marketed for over 15 years (Hayashi 1990). The same SMP has been developed into open-cell foams for space

missions and biomedical applications based on the concept of cold hibernated elastic memory (CHEM) proposed by Dr. W. Sokolowski at Jet Propulsion Laboratory, USA (Sokolowski and Metcalfe 2007), (Sokolowski and Tan 2007). Currently, biomedical application emerges as a promising area for SMPs (Small and Singhal 2010), while surface patterning (for altering various surface related properties, such as reflection, surface tension etc.) is another area (Fu and Grimes 2009). Fig. 3 is a zoom-in view of a patterned surface atop an SMP, which is produced by a laser beam after one single exposure through a microlens. As compared with patterning atop SMAs (e.g. (Wu and Huang 2009)), this is more cost-effective and convenient, in particular for different shaped/sized patterns. In indentation-polishing-heating (IPH) produced patterns , while the ones atop SMAs are normally reversible between two shapes during thermal cycling, the ones atop SMPs are fixed and permanent. A further step is to integrate micro/nano sized wrinkles with such surface patterns for dramatically improved performance, such as self-cleaning (Patankar 2004), cell adhesion (Bernard and Guedeau-Boudeville 2000), water splitting and light extraction, etc.

The underlying mechanism for the SME in SMPs is the dual-segment/domain system (one is always hard/elastic, while the other can be soft/ductile or stiff depending on whether a right stimulus is presented). The former is called the elastic segment, and the latter is the transition segment. Take the thermo-responsive SMP as an example. The mechanism for the SME is illustrated in the following chapters. As we will see, the SMP is normally much softer at high temperature than that at low temperature. This mechanism is different from the reversible martensitic transformation, which is well-known and highly predicable (Bhattacharya and Conti 2004), between the high temperature austenite phase (which is hard and stiff) and low temperature martensite phase (which is soft and flexible) in SMAs. As SMPs have a much higher recoverable strain and normally a wider shape recovery temperature range, it is possible to have more than one intermediate shape in the multi-SME through a proper programming procedure as recently demonstrated by (Xie 2010). We have proved that during constrained recovery (i.e., heating with the temporary shape of SMP fixed), the maximum reaction force/stress should appear at the temperature that the SMP is deformed (which should be within the transition temperature range according to (Xie 2010)). This feature reveals the TME in SMPs. The underlying mechanism behind this feature is the step-by-step release of the elastic energy stored in the elastic segment during programming, which is different from that of SMAs. Alternatively, the multi-SME in SMPs can be achieved by means of setting different shape recovery conditions, e.g., different stimuli or multiple transitions within different temperature ranges and even a gradient transition temperature. As such, programmed recovery in a well controllable fashion can be realized. SMP composites have remarkably widened the potential

applications of SMPs (Gunes and Jana 2008). In addition to using various types of fillers (including various types of clay, SiC nano particles, etc.) to reinforce SMPs, heating of thermo-responsive SMPs can also be realized by joule heating (by means of filling with various kinds of conductive inclusions), induction heating (by means of energy dissipation through hysteresis upon applying an alternating magnetic/electrical field, etc.), and even radiation. As opposed to SMAs, SMPs normally soften in the presence of the right stimulus, therefore most SMPs are not suitable for cyclic actuation and cannot be trained to have the so-called two-way SME (which is the ability to repeatedly switch between two shapes, depending on whether the stimulus is applied). On the other hand, the shape recovery of SMPs can be accompanied with color change, excellent transparency, reversible adhesion/peeling and even for self-healing. Similar to SMAs, the SME has been demonstrated in submicron sized SMP. While it is difficult to fabricate high quality porous SMAs till now, it is always easy to produce SMP foams by many conventional polymer foaming techniques.

1.2 Martensite and Shape-Memory Effect

1.2.1 Introduction

Shape memory refers to the ability of certain materials to "remember" a shape, even after extensive deformations. Once deformed at low temperatures (martensitic phase), these materials will stay deformed until heated, upon which they will spontaneously return to their original, pre-deformation shape. This phenomenon is called shape memory effect (SME). The basis for SME is that materials can easily transform to and from Martensite. Even the elementary engineering aspects of SME cannot be understood without first familiarizing oneself with some basic principles of Martensite and its formation.

1.2.2 A microscopic perspective of Martensite

Solid state transformations are usually of two types: diffusional and displacive. *Diffusional transformations* are those in which the new phase can only be formed by moving atoms randomly over relatively long distances. This requires long range diffusion as the new phase that is formed is of a different chemical composition than the matrix from which it is formed. Since this type of a transformation requires atomic migration, the diffusional transformation is dependent upon both

time and temperature. *Displacive transformations*, on the other hand, do not require, large atomic migration; in this case the atoms are cooperatively rearranged into a new, more stable crystal structure. This rearranging is done without changing the chemical nature of the matrix. Since no atomic migration is involved, these displacive transformations progress in a time independent fashion, with the motion of the surface between the two phases being limited by only the speed of sound. These transformations are also referred to as *athermal* transformations. Martensitic transformations are of the displacive type, and are formed upon cooling from a higher temperature phase called the parent phase, or Austenite. It is important to note that a precise definition for Martensite has never been agreed upon. The terms "Martensite" and "Austenite" were used to refer to phases of steel. However a more generalized definition for Martensite is based on the product of the phase transformation rather than a particular material is now more widely accepted.

Martensitic transformations are first order transformations. This means that heat is liberated when Martensite is formed. There is a hysteresis associated with the transformation and there is a temperature range over which Martensite and Austenite coexist. Therefore it is possible to state that Martensite is formed upon cooling with the volume fraction of Martensite increasing as the temperature is reduced. It is important to note that the volume fraction is independent of time and is dependent solely on temperature.

In a crystallographic context, the phase transformation from Austenite to Martensite is thought of to occur in two parts: the *Bain strain* and the *lattice invariant shear*. These mechanisms in a crystallographic sense are quite complex. However, it is possible to explain them adequately in a quite simple fashion using a two-dimensional approach. The Bain strain, also referred to as lattice deformation, consists of all atomic movements that are needed to form the new structure (i.e., phase) from the old. Figure 1 illustrates the austenitic structure schematically in diagram (a), and the progression of the transformation to a fully martensitic structure is schematically illustrated by (b) through (d). It is important to note that as the interface progresses through each atomic layer, each atom is required to move by only a very small amount (Figure 1c). The end result of all these coordinated movements is the new martensitic structure. The movements that are required to produce the new structure are called Bain strain. In real materials, Bain strain generally consists of several atomic shuffles in addition to the movement illustrated in Figure 1.

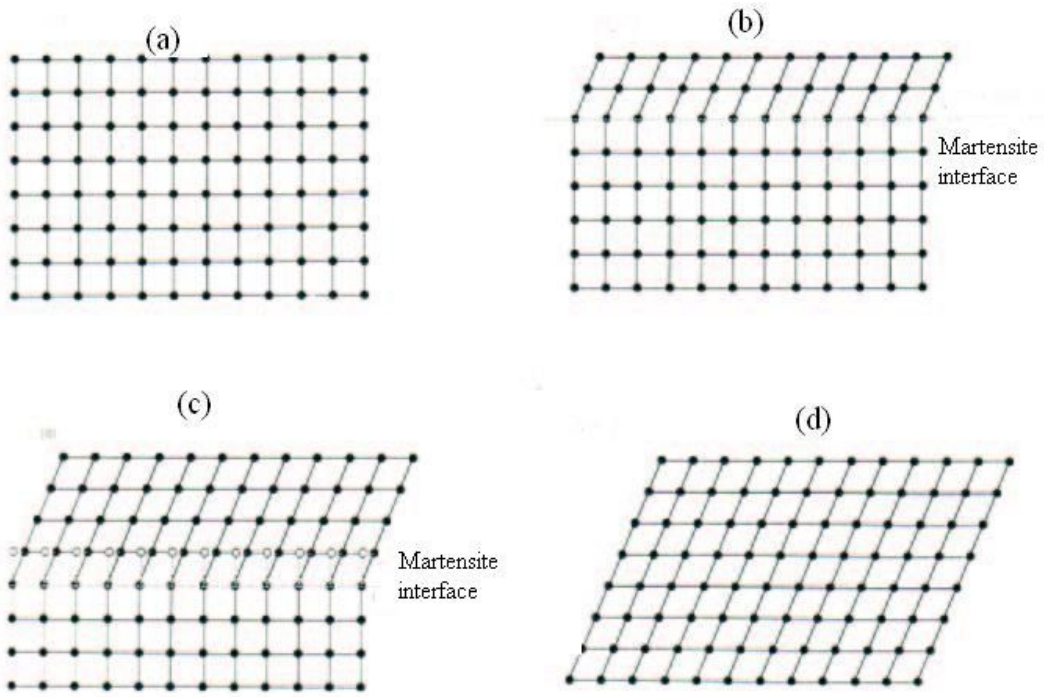

Figure 1 Transformation from Austenite to Martensite in two-dimensions: (a) being completely austenitic and (d) being completely martensitic. In (b) and (c) the interface advances, each layer of atoms being displaced only by a small distance.

The second part of a martensitic transformation is referred to as the *lattice invariant shear*. It is an accommodation step: the martensitic structure produced by the Bain strain is of a different shape, and often volume, than the surrounding Austenite (Figure 1(a-d)). Martensite in steel however involves both a volume change and a shape change, whereas shape memory alloys like NiTiNOL undergo only a shape change. Either the overall shape of the new phase, or the surrounding Austenite must be altered to accommodate the new structure. There are two mechanisms by which this is possible: slip (Figure 2a) and twinning (Figure 2b). In both cases, each individual cell, or parallelogram, has the new martensitic structure, but the overall shape is that of the original Austenite. Slip is a permanent process and is a common accommodation mechanism in many Martensites. Twinning is unable to accommodate volume changes, but can accommodate shape changes in a reversible way. For shape memory to occur to any significant extent, it is required that the accommodation be fully reversible or, stated alternately, that twinning be the dominant accommodation process. In Figure 2, only two directions or variants of shear are required to restore the original, overall shape of the matrix; in three-dimensions the situation can be complicated: Cu-Zn-Al Martensites for example, require four Martensite variants for full, three-dimensional accommodation, and Ni-Ti Martensites require three.

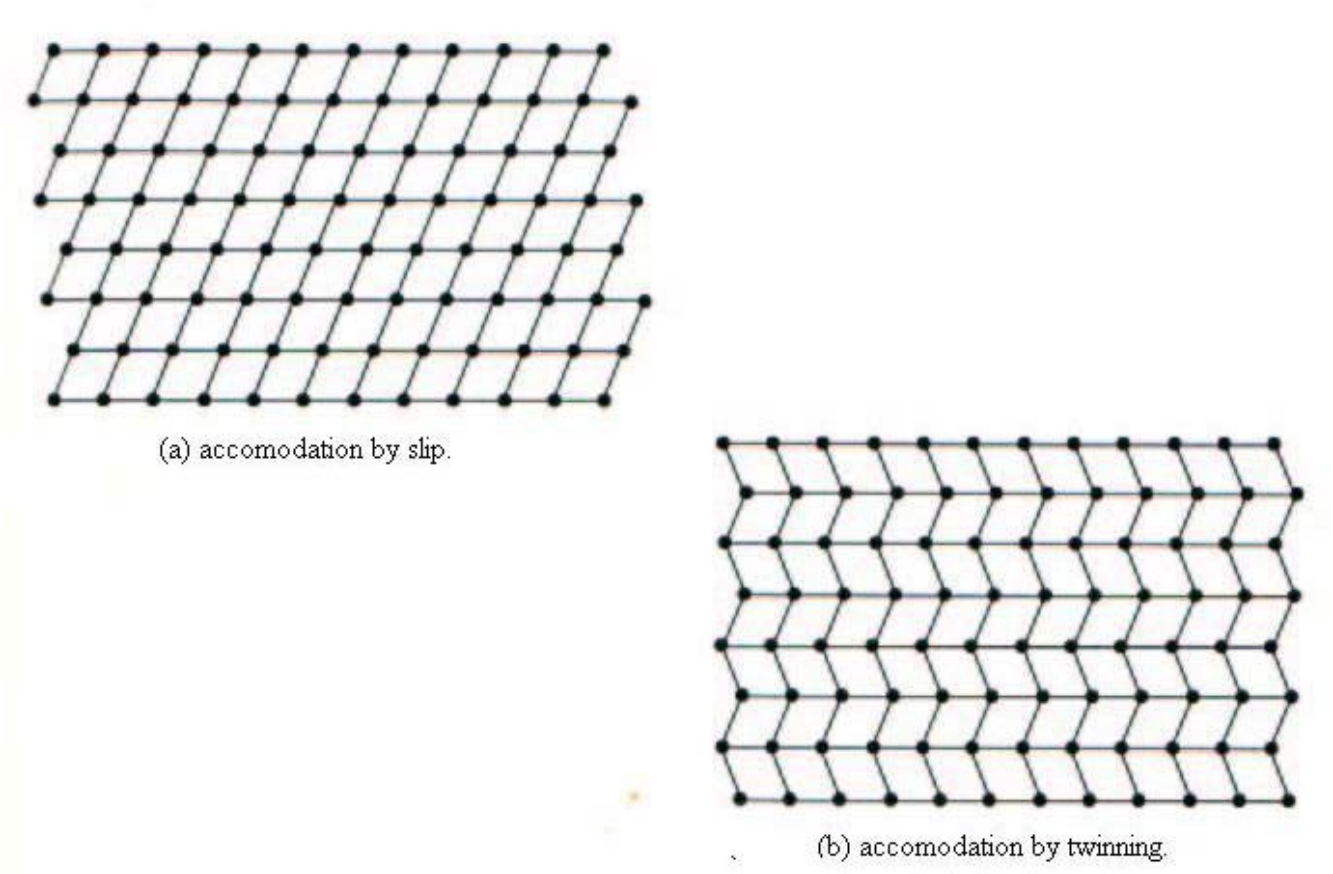

Figure 2 Two mechanisms of accomodating the shape change due to the atomic shear of a martensitic transformation (a) accommodation by slip, (b) accommodation by twinning

The twinning process of accommodation plays a key role in the shape memory effect and should be reviewed in more detail. As can be seen in Fig. Figure 3, the twin boundary is a mirror plane: when positioned on the boundary, the view in one direction is a mirror image of the other. Atoms situated on that boundary see the same number and type of bonds in both directions. Some key properties of twin boundaries are that they are of a very low energy and they are quite mobile; thus the relative stability of a martensitic phase is not strongly affected by the number or location of these boundaries. By comparing edges of the structures shown in Figure 2(a) and Figure 2(b), one can see that slip accommodation requires that atomic bonds be broken, while all bonds remain intact in the twinned structure. If a stress is applied to the structure shown in Figure 2(b), the twin boundaries will easily move, producing a shape that better accommodates the applied stress. The result of moving a twin boundary is to convert one orientation or twin variant into another. That variant will be chosen which is most favorably oriented to the applied stress. In the ideal case, a single variant of Martensite can be produced by straining a sufficient amount. This process of condensation of many twin variants into a single favored variant is called detwinning. In the foregoing discussion,

only the twins within individual martensitic plates have been considered. However crystallographic analysis
has shown that the boundaries between martensitic plates also behave as twin boundaries – i.e., the individual plates of Martensite themselves are twins with respect to adjoining plates. Therefore the term twin boundaries refers to the boundaries between Martensite plates as well as the boundaries within plates.

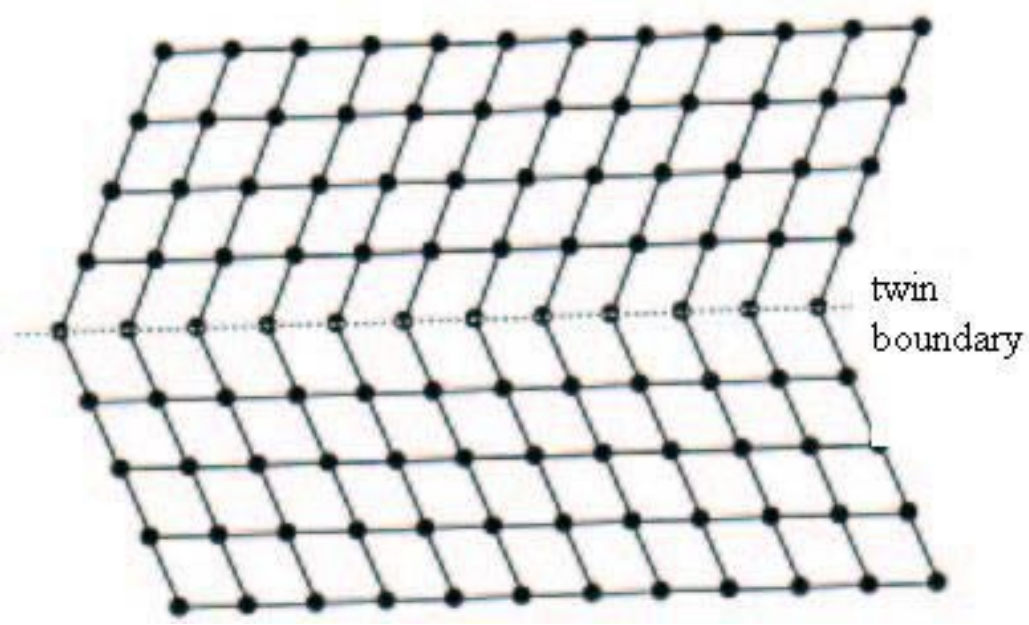

Figure 3 Schematic view of a twin boundary

In Figures 1 through 4, the atom types have not been identified. In an alloy, however, there exist several species of atoms. It is therefore important to identify the lattice site locations of these atoms. In steel, for example, these atoms are disordered, meaning that different elements are randomly distributed on the lattice sites. In NiTiNOL, however, the atoms are ordered, meaning that the Ni and Ti atoms are found on very specific sites (Figure 4). During the course of a martensitic transformation, the Martensite takes on the same ordering as the Austenite. This is referred to as inherited ordering. Shape memory alloys are generally based on a BCC symmetry, some with the BCC structure, more often with the B2 structure, and some with an even more complex ordering called DO_3, still based on the BCC symmetry.

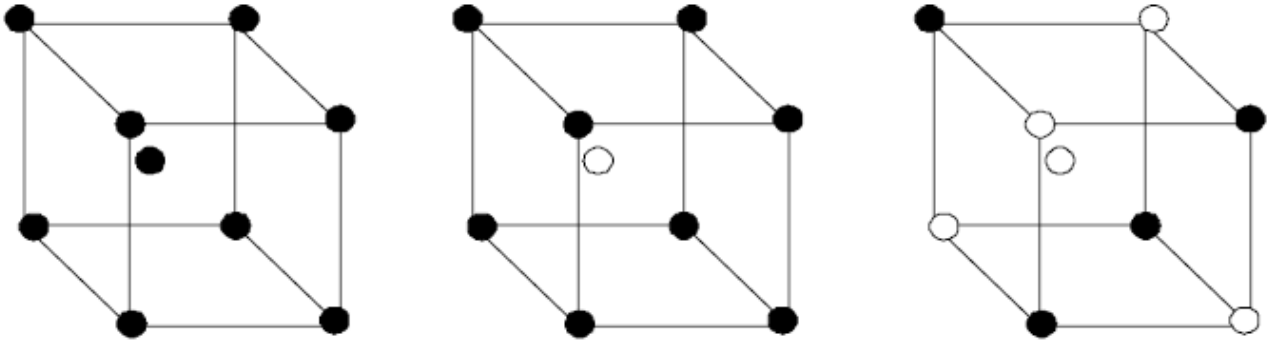

Figure 4 Ordered and disordered structures commonly found in shape memory alloys: (a) disordered BCC structure, where different atom types are randomly distributed, (b) B2 structure, found mostly in NiTiNOL, where different atom types are found in specific locations, (c) higher order phase than (b) called DO_3 state, found for example in Cu-Al-Ni alloys.

Martensite normally appears as plates, resting on complex crystallographic planes known as habit planes. In many shape memory alloys, the Martensite plates are easily viewed through an optical microscope (Figure 5).

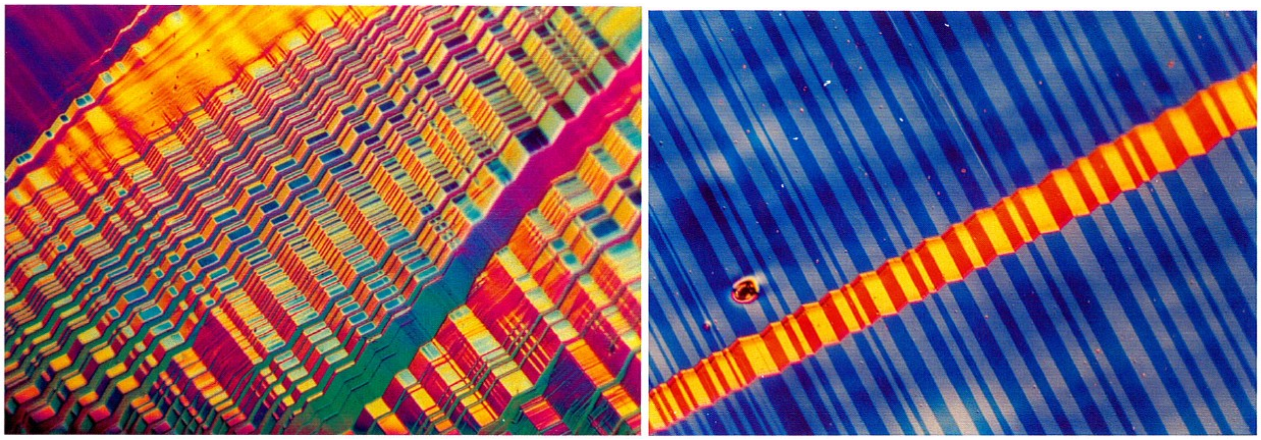

Figure 5 Examples of martensitic microstructures

1.2.3 A macroscopic perspective of Martensite

The physical properties of Austenite and Martensite are different. Therefore as the phase transformation progresses and the transformation point is passed, a variety of property changes occur. Any of these property changes can be used to follow the progression of the phase transformation. There are four significant temperatures that characterize the transformation from Martensite to Austenite and vice versa. Four temperatures indicated by M_s, M_f, A_s, and A_f (Figure 6) refer to temperatures at which the transformation to Martensite starts and finishes, and the temperatures at which the reversion to Austenite starts and finishes, respectively. There is a

hysteresis associated with this phase transformation (martensitic transformation). Stated alternatively, the transformation temperatures differ upon heating and cooling during the martensitic transformation. The magnitude of the hysteresis varies from one alloy system to another, and has typical values ranging from 20ºC to 40ºC. Microscopically, hysteresis can be attributed to friction associated with the movement of twin-related Martensite boundaries.

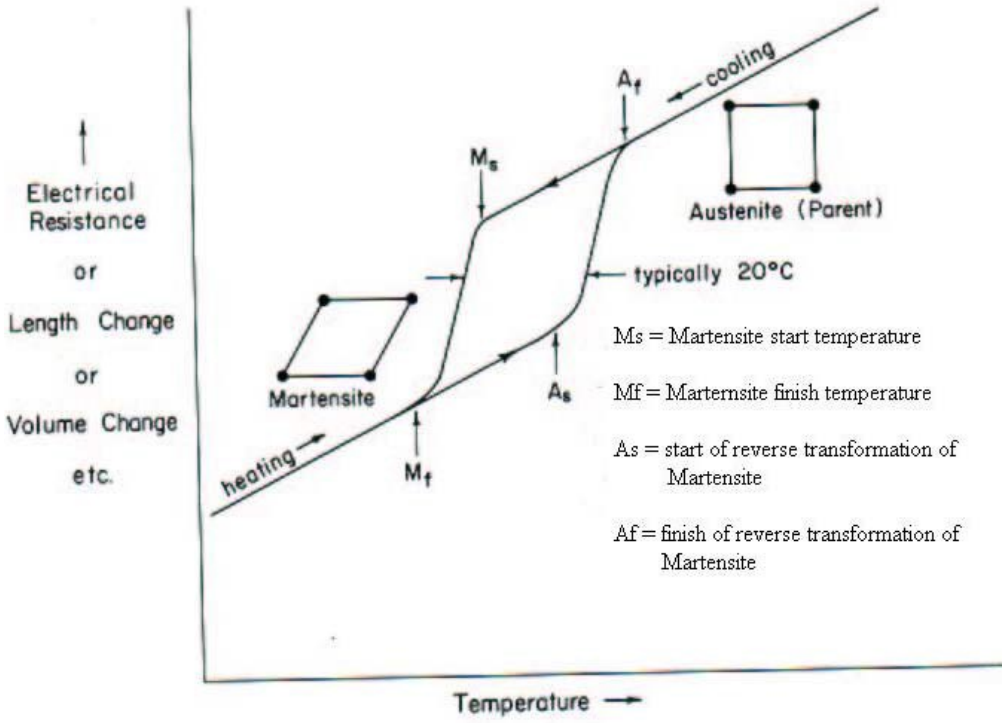

Figure 6 Hypothetical plot of property change versus temperature for a martensitic transformation occurring in SMA

One of the many mechanical properties that change during the phase transformation is the yield strength. The martensitic structure deforms by moving twin boundaries. These twin boundaries are quite mobile. Martensite therefore has low yield strength. Austenite, on the other hand, deforms by dislocation generation and movement. Only a certain amount of Martensite can deform based on this twin movement process and once this limit is exceeded, the material will again deform elastically and eventually yield the second time by an irreversible process (movement of dislocations). The resulting unusual tensile behavior is indicated in Figure 7. In Figure 7, the plateau refers to the thermal hysteresis, which means that both Martensite and Austenite are controlled by the frictional stress of the twin boundaries. It is the yield strength ratio between the Martensite and Austenite that controls the ratio of resistances to reversible and irreversible deformations (twin movement to slip). In shape memory alloys, it is important to have this ratio as high as possible in

order to recover the most amount of the deformation. Typical values of these ratios are 0.1 to 0.2 (Duerig 1990).

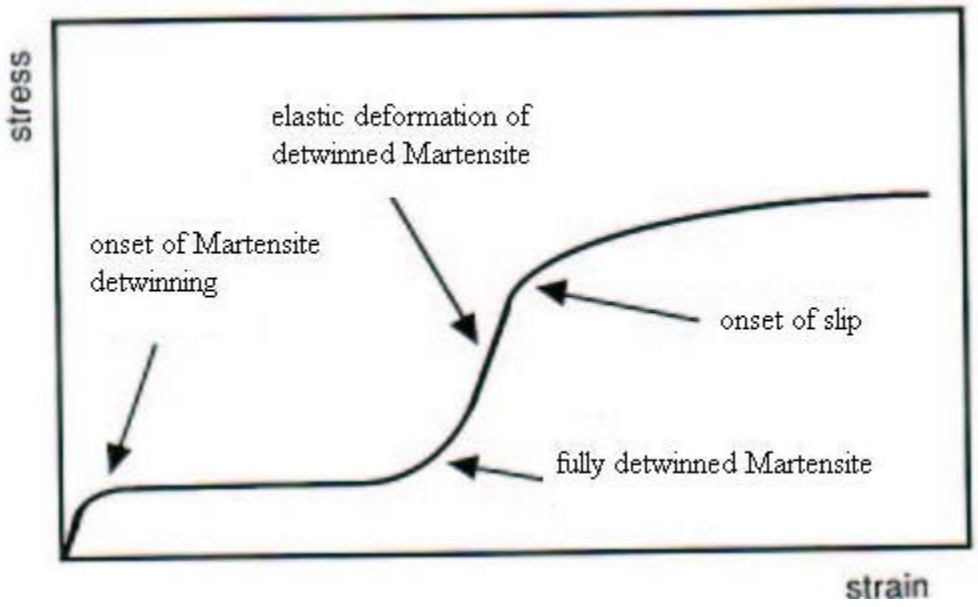

Figure 7 Typical stress-strain curve for a twinned martensite material

1.2.4 The origin of Shape Memory Effect

Martensite is generally of a lower symmetry phase than Austenite. Therefore there are several ways by which Martensite can be formed out of Austenite. However there is only one route by which the Martensite formed will revert back to Austenite. Shape memory effect can be explained in a very simple manner by a 2D geometrical concept depicted in Figure 8 (Duerig, 1990). Upon cooling from Austenite Figure 8(a), the self-accommodating variants of Martensite Figure 8(b) are formed. During the application of stress (deformation), the twin boundaries migrate and therefore result in a biased distribution of Martensite variants Figure 8(c). It is however important to note that no matter what the distribution of Martensite is, there is only one possible austenitic structure that these variants can revert back to. Therefore the martensitic variants must return back to the original undeformed shape after reverting back to Austenite. Therefore the shape accommodation due to a twin boundary movement can only be supported by a low symmetrical martensitic structure, and when the more symmetric Austenite structure is returned, the twinning deformation must also disappear.

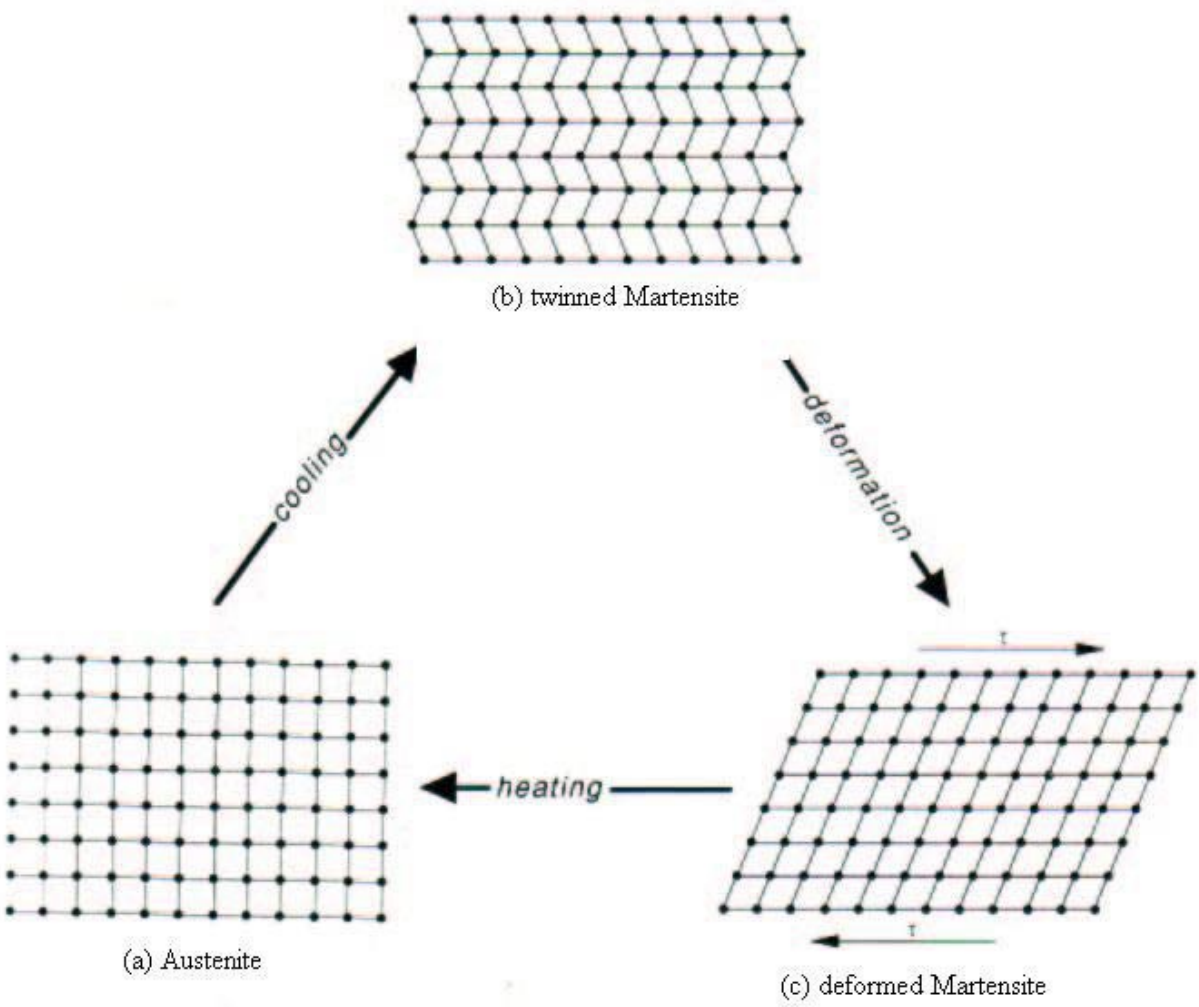

Figure 8 Shape memory shown microscopically: Austenite (a) is cooled to form twinned Martensite (b) without undergoing a shape change, then is deformed by moving twin boundaries (c). Heating either state (b) or (c) will return the originally austenitic structure and shape.

Once the shape has recovered at A_f there is no change in shape when the specimen is cooled to below M_f and the shape memory can be reactivated only by deforming the martensitic specimen again. In other words, the shape memory effect is a onetime only occurrence and therefore it is frequently referred to as the one-way shape memory effect. Typical recoverable strains for most SMAs are about 7%, while some of them can recover strains up to 10%. Among the many alloys that exhibit SME, only the Cu-Zn-Al, Cu-Zn-Ni, and Ti-Ni alloys are presently of commercial importance.

1.2.5 Stress-induced Martensite and Superelasticity

So far shape memory effect has been considered to be both thermal and mechanical. The Martensite is initially formed during cooling and is then deformed below the M_f temperature, and then heated to above the A_f temperature to cause the shape to recover. This means that shape memory is caused by heating. There is also another type of shape memory that is dependent upon temperature, which is referred to as *superelasticity*. It is a known fact that the formation of Martensite is a thermoelastic process, which means that a decrease in temperature between M_s and M_f results in a slight growth of existing martensitic plates and the nucleation of new ones. However when the temperature is incrementally raised the newly nucleated plates disappear and those which grew slightly on incremental cooling correspondingly shrink back a little. Stated alternately, there is equivalence between temperature and stress: a decrease in temperature is equivalent to an increase in stress, and these both stabilize Martensite. The Martensite is also crystallographically reversible, which means that the reversion of a given plate upon heating is just the reverse of the formation process, i.e., the plates undergo a backward shear as it disappears. Normally, on cooling, the Martensite forms under M_s if a stress is applied and the so-formed Martensite is called as stress-induced Martensite (SIM). The driving force for the transformation is, in this case, mechanical rather than thermal. Above M_s the stress required to produce SIM increases with increasing temperature, as shown in Figure 9.

The variation in stress required to produce SIM increases linearly with temperature above M_s,. Figure 10 shows that the extrapolated stress drops to zero at the temperature M_s. The linear variation of stress to induce Martensite as a function of temperature obeys the Clausius-Clayperon equation, and is written as

$$\frac{dP}{dT} = \frac{\Delta H}{T\Delta V} \tag{1.1}$$

where P is the pressure, T is the temperature, and ΔH is the transformation latent heat and ΔV is the volume change of the phase transformation. Equation 1.1 has been traditionally used by chemists (Duerig, 1990), but metallurgists, on the other hand, use the Clausius-Clayperon in the following form:

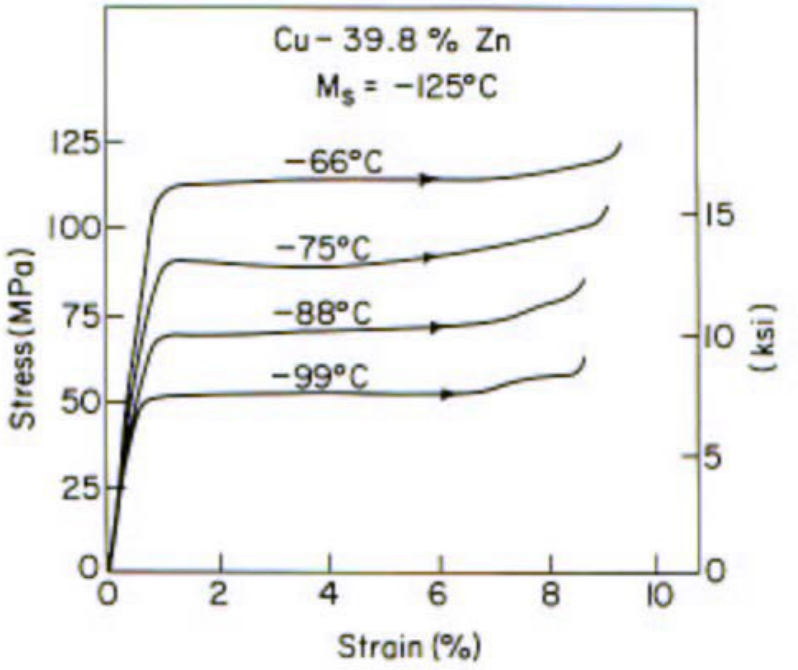

Figure 9 Stress-strain curves for Cu-Zn single crystal loaded in tension above Ms

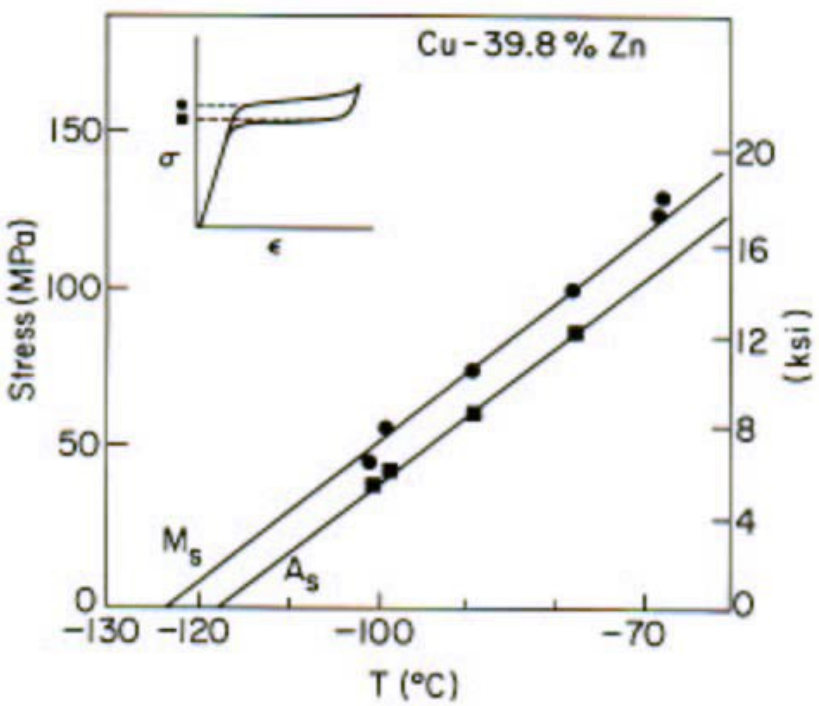

Figure 10 Stress plateau as a function of temperature

$$\frac{d\sigma}{dM_s} = -\frac{\Delta H}{T\varepsilon_0} \tag{1.2}$$

where ΔH and T have the same interpretation as for Equation 2.1, and σ, M_s, and ε_0 are the applied stress, the shifted M_s temperature and the transformational strain resolved along the direction of the applied stress. The difficulty to stress induce Martensite continues to increase with temperature until M_d, above which the critical stress required to induce Martensite is greater than the stress required to move the dislocations. Therefore the temperature range for SIM is from M_s to M_d. For a number of SMA systems, the agreement in the temperature dependence of the stress to form SIM according to the Clausius-Clayperon equation is quite striking. The equation works equally well for the non-isothermal case, i.e., the case where temperature was held constant while the stress needed to form Martensite was measured.

Superelasticity occurs when a material is deformed above A_s, but still below M_d. In this range, Martensite can be made stable with the application of stress, but becomes unstable upon removal of stress. Figure 11 shows a superelastic stress-strain curve for a Cu-39.8%Zn SMA. The upper plateau corresponds to the formation of Martensite under stress whereas the lower plateau represents SIM when the load is released (Duerig, 1990). Note that 9% strain is fully recovered during unloading, and can be viewed as a mechanical shape memory effect. When the SIM is formed for a single crystal Cu-Zn shape memory alloy only a single variant is formed during the application of stress. This results in an elongation (or shape change) which is fully recovered upon release of the applied stress. This situation is unlike the case of thermal Martensite, there is no overall net shape change accompanying the formation of various variants of Martensite.

1.2.6 Mathematical background for martensitic transformation

Experimental evidence from optical, SEM (Scanning Electron Microscope), and TEM (Transmission Electron Microscope) observations indicate that during a MT, a line and surface is converted to another line and surface. This conversion can be represented mathematically by a matrix operator. The parent (Austenite) and martensitic phases are of different microstructures. A coordinate transformation must be performed to mathematically explain the MT. Linear algebra is used to perform such a transformation. During a coordinate transformation, the mathematical operator will itself undergo a transformation.

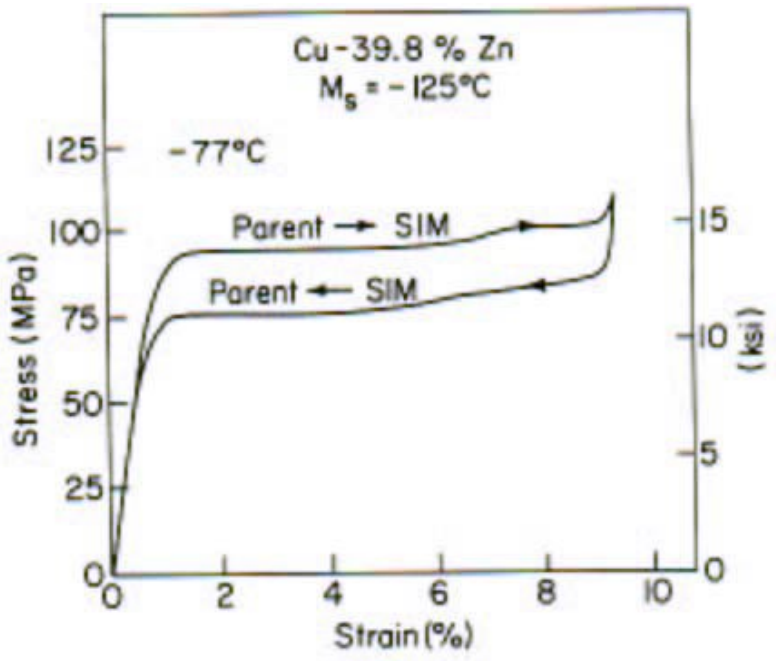

Figure 11 Stress-strain curve for a Cu-Zn shape memory alloy, loaded above the As temperature and then unloaded, shows superelastic behavior.

Application of a coordinate transformation to a vector results in the transformation of the mathematical operator based on a similarity transformation. Wayman and Duerig (1990) have discussed the mathematics of the similarity transformation.

A martensitic crystal is formed from the parent phase through a diffusionless transformation. This type of a transformation is well explained for the FCC to BCT (Base Centered Tetragonal) transformation in steels, Figure 12. Generally a FCC twin has a BCT lattice with an axial ratio of 1.414. Martensite in general has a ratio close to one. This is possible when the *Z* axis is contracted and *X* and *Y* axes are elongated, according to the mechanism first proposed by Bain. Even though the mechanism differs for different type of SMA systems. A Martensite can always be created from a parent phase by a combination of elongation, contraction and shear along certain directions (Otsuka, 1998). Since MT is a diffusionless transformation, there exists a one-to-one relation between the parent and the martensitic phase.

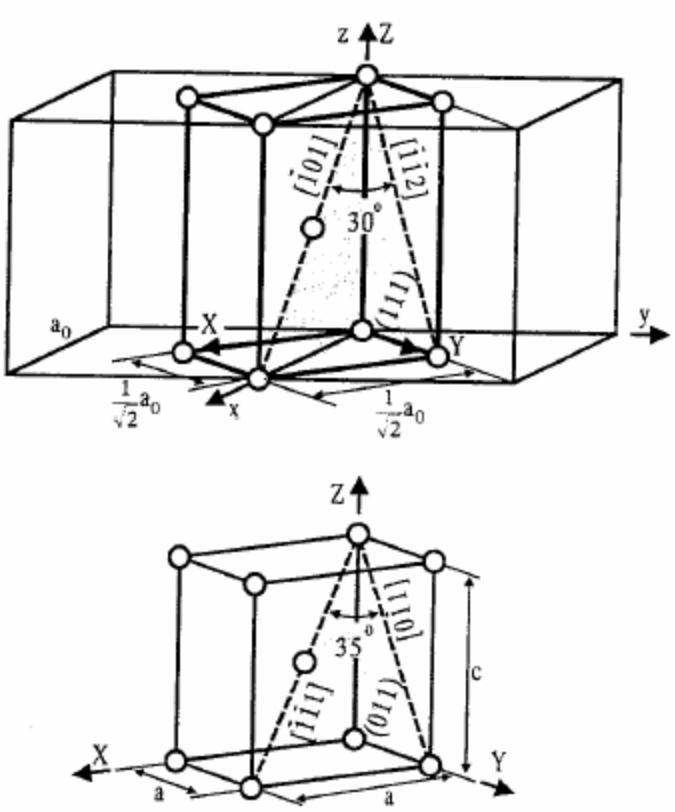

Figure 12 Mechanism of FCC-BCT (or BCC) transformation Bain strain. XYZ represent the crystal axes in the parent FCC lattice, while XYZ represent the axes in the BCT Martensite.

1.2.7 Phenomenological theory of the martensitic transformation

The crystallographic characteristics of the martensitic transformation are well understood by the phenomenological crystallographic theory. The theory requires that the MT consists of the following components

1) a lattice deformation B, as a result of the formation of Martensite from the parent phase,
2) lattice invariant shear P_2 (as a result of twinning, slip, or faulting),
3) a lattice rotation R.

Theory requires that the shape memory strain produced by the MT consists of a lattice invariant strain and is homogeneous macroscopically. It consists of a shear strain parallel to the habit plane and an expansion or contraction normal to the habit plane. The shape memory strain can also be represented as follows (Wayman and Duerig, 1990).

The crystallographic theory has been so far successfully applied to Au-Cd, Fe-Pt, Fe-Ni-C and Fe-Al-C alloys with a good correlation between experimental and theoretical results. The theory when applied to other SMA systems, does not provide overall agreement between experiment and theory.

1.2.8 Thermodynamic aspects of the martensitic transformation

The MT can be explained based on a thermodynamic analysis, as it is driven either by stress or temperature. There is heat interaction between the SMA specimen and the surroundings and specific temperatures characterize the phase transition. Even though these temperatures can be determined by the DSC (Differential Scanning Calorimetry) methods, a thermodynamic analysis will provide an insight into characteristics unique to SME like hysteresis, superelasticity, one-way effect, rubberelasticity, and two-way effect.

A gas can be liquefied by the application of a suitable pressure. Similarly, a phase transition from the parent phase to Martensite can be induced by the application of a stress. A thermodynamic analysis explains thermal and mechanical effects on the SME. Thermodynamics is a good tool to perform calculations on the thermal implications of the stress induced phase transition. It also explains the reversibility of the phase transition in certain SMAs and highlights energy contributions that control the hysteresis phenomenon.

Gibbs theory of thermodynamic stability is used to describe the phase transition under the consideration that the alloy system is in equilibrium. Based on the above consideration it is evident that Gibbs theory is not suitable for systems not in equilibrium, for which fluctuations are amplified to generate new structures. An MT can be considered to be a succession of several equilibrium states and Gibbs approach based on free energy can be used. The thermodynamic analysis is based on work and methodology presented in the work on SMAs by Trochu (1996).

The MT is a solid state transformation and a thermodynamic analysis, based on internal variables such as the latent heat of the phase transformation, enthalpy, and entropy for a single crystal of SMA, is presented in this Section. Derivation of the classical Clausius-Clayperon equation that relates stress and temperature is also presented. The analysis is conducted for a single crystal of SMA, because this facilitates the investigation of the SMA specimen as a thermodynamic system with only one component.

1.2.8.1 Thermally induced phase transformation

In this particular case, the martensitic phase transformation is thermally induced. The SMA crystal has energy interactions with its surroundings in the form of heat and work and this can result in an increase, or decrease, in the internal energy. The change in internal energy undergoing a heat transfer with its surroundings, or doing useful work, can be written in thermodynamic terms as follows:

$$dE = dQ + dW \tag{1.3}$$

where E is the internal energy, dQ is the heat exchange between the SMA crystal and its surroundings, and dW is the work accomplished as a result of dQ. Assuming the phase transformation as a reversible heat transfer situation and using the second law of thermodynamics the following relation is obvious and valid:

$$dQ = TdS \tag{1.4}$$

where T is the temperature and dS is the change in entropy of the SMA crystal. According to thermodynamic convention, work done by a system is positive and energy transfer into the system is also positive. Keeping this in consideration and also from the assumption that that work done by the crystal is a hydrostatic work, an expression for the work done can be written as

$$dW = -pdV \tag{1.5}$$

where p is the pressure and dV is the change in volume.

From Eqs. (1.4) and (1.5),

$$dE = TdS - pdV \tag{1.6}$$

All properties that are used in the thermodynamic analysis are extensive and refer to per unit mass basis of the SMA crystal. As E, S, and V are difficult to control during experimentation, additional thermodynamic potentials in the form of enthalpy H and the Gibbs free energy G have to be introduced. They can be defined in terms of E, S, T and V as follows (Trochu, 1996):

$$H = E + pV \tag{1.7}$$

and

$$G = H - TS \tag{1.8}$$

Differentiating Eqs (1.7) and (1.8), and rearranging the results for *dE* and *dG* we have

$$dH = TdS + Vdp \tag{1.9}$$

$$dG = Vdp - SdT \tag{1.10}$$

The entropy S and the pressure p are natural variables that appear in the expression for the increment of enthalpy dH. At constant pressure, dH corresponds to the amount of heat transferred between the crystal and the surroundings. The temperature T and pressure p constitute natural variables in the expression for dG. These natural variables are easier to control during experimental procedures and hence are very useful in thermodynamic analyses of the phase transformation. Thermodynamic equilibrium is achieved when $dG = 0$. If the temperature T is altered at constant pressure, then a plot of the Gibbs free energy as a function of temperature T can be constructed and can be represented schematically, in Figure 13.

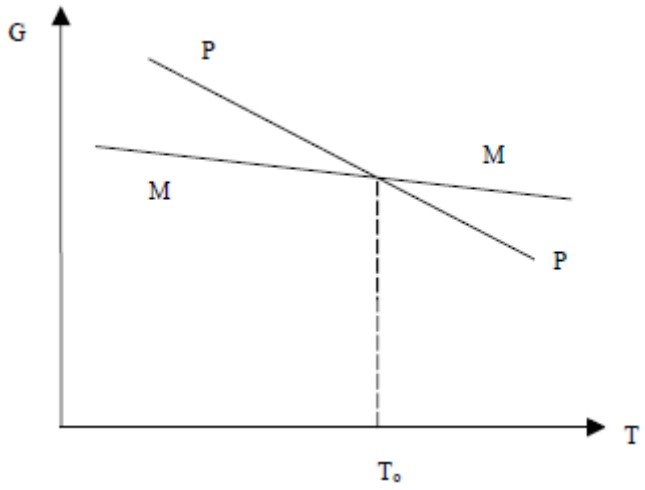

Figure 13. Evolution of free energies for the parent and martensitic phases at constant stress

The slope of $G_P(T, p)$ represents the entropy of the parent phase and is a function of temperature. For small intervals of the temperature T, G_P can be considered to be a constant and the following relation between the enthalpy, temperature T, and entropy S can be written

$$G^P = H^P - TS^P \tag{1.11}$$

Similarly, an expression for the martensitic phase can also be written and is of the form:

$$G^M = H^M - TS^M \tag{1.12}$$

From Figure 13 it can be noted that at a particular temperature $T=T_0$, phase transition from the parent phase to Martensite as well as the reverse transformation are possible without any hindrance. Also, at $T<T_0$, Martensite is stable and at temperatures $T>T_0$ Austenite is stable. Hence T_0 is also called as the transition temperature and can be determined from the Gibbs free energies of the two phases. The expression for the transition temperature can be written as

$$T_0 = \frac{\Delta H}{\Delta S} = \frac{H^P - H^M}{S^P - S^M}. \tag{1.13}$$

In this particular analysis if the interaction between the two phases is to be taken into account, then an additional variable is to be considered. This variable, f_M , is the fraction of Martensite that has been transformed into Austenite. The entropy, S , in such a situation is given by the expression (Trochu, 1996)

$$S = (1-f)S^P + fS^M \tag{1.14}$$

On multiplying Eq. 1.14 by Eq. 1.13 and differentiating the result with respect to S, we obtain:

$$T_0 dS = T_0 (S^M - S^P) df = dQ \tag{1.15}$$

Where dQ is the latent heat of the phase transformation and experimentally can be determined by the use of a DSC.

1.2.8.2 Stress induced phase transformations at constant temperature

When a stress is applied to a single crystal of SMA in the parent phase, it gives rise to a response that can be written mathematically as follows:

$$dW = V_0 \sigma_{ij} d\varepsilon_{ij} \tag{1.16}$$

where V_0 is the volume of the SMA crystal, dW is the mechanical work done as a result of the applied stress σ_{ij} , and ε_{ij} is the incremental macroscopic strain. The change in internal energy for such a system can be written as

$$dE = TdS + V_0 \sigma_{ij} \varepsilon_{ij}, \tag{1.17}$$

and also an expression for the change in enthalpy dH can be written as

$$dH = TdS + V_0 \sigma_{ij} d\varepsilon_{ij} \tag{1.18}$$

Equations 1.17 and 1.18 can be simplified for the one-dimensional case and rewritten as

$$dE = TdS + V_0 \sigma d\varepsilon \tag{1.19}$$

$$dH = TdS + V_0 \sigma d\varepsilon \tag{1.20}$$

respectively.

The pressure p is atmospheric and hence a constant and also the volume change is negligible for the martensitic transformation. Similarly, an expression for dG can be written in the form

$$dG = -SdT + V_0 \sigma d\varepsilon \tag{1.21}$$

Deformation is more difficult to control than stress and, therefore, it is necessary to introduce a generalized form of the Gibbs free energy G^* into Eq. 2.21, which becomes

$$G^* = G - V_0 \sigma d\varepsilon \tag{1.22}$$

Differentiating Eq. 1.22 with respect to G we obtain

$$dG^* = dG - V_0 \sigma d\varepsilon - V_0 d\sigma\varepsilon \tag{1.23}$$

Substituting Eq. 1.21 into Eq. 1.23 and rearranging we get

$$dG^* = -SdT - V_0 \varepsilon d\sigma \tag{1.24}$$

At constant temperature T and stress σ, thermodynamic equilibrium is characterized by $dG^* = 0$. For a single crystal SMA specimen subjected to a uniaxial stress, the expressions for the Gibbs free energy for the parent and the martensitic phases can be written as

$$\begin{aligned} (\mathrm{G}^*)^P &= H^P - S^P T - V_0 \varepsilon^P \sigma, \\ (\mathrm{G}^*)^M &= H^M - S^M T - V_0 \varepsilon^M \sigma \end{aligned} \tag{1.25}$$

The stress and temperature imposed on the SMA are assumed to be the same for both of the phases, with the thermodynamic potential being different as a result of the phase transformation. An expression for a finite change in the Gibbs free energy can be then written as

$$\Delta G^* = \Delta H^* - T\Delta S - V_0 \sigma \Delta \varepsilon. \tag{1.26}$$

During phase transformation $\Delta G^* = 0$ is reached and the latent heat of phase transformation $Q(\sigma)$ can be defined as follows:

$$Q(\sigma) = TdS = \Delta H - V_0 \sigma d\varepsilon. \tag{1.27}$$

Rearranging terms in Eq. 1.27 the classical relation between stress and temperature as a result of the phase transformation can be written as follows:

$$\frac{d\sigma}{dT} = \frac{\Delta S}{V_0 \Delta \varepsilon}. \tag{1.28}$$

Equation 1.28 is also called as the Clausius-Clayperon equation and is of vital importance in thermomechanical analysis. Equation 1.28 relates stress and temperature during a phase transformation. In Eq. 1.28, ΔS and $\Delta \varepsilon$ are characteristic parameters for a given SMA. The Clausius-Clayperon equation shows a linear dependence between stress and temperature when ΔS is independent of temperature. When the stress reaches a critical value given by $\sigma_0(T)$, a volume change equal to $V_0 d\varepsilon$ occurs. An interaction between the parent and the martensitic phases was not taken into account in the previous analysis. That is, the parent and the martensitic phases are not independent. The transformation is discontinuous, is produced in a step by step with each individual step taking less time than the total time for the transformation to occur. Let f_M be the molar fraction of Martensite crystal during transformation. The variation of the internal energy of the transformed fraction increment df_M can be written as

$$\Delta E df_M = T\Delta S df_M + V_0 \sigma d\varepsilon df_M. \tag{1.29}$$

The crystal gains elastic energy and interfacial energy at the interface between the two phases during the parent to the MT. These energies can be restored during the reverse transformation. The portion of heat loss due to the internal friction cannot be recovered and taking into considerations all these different energies, the change in internal energy can be written as follows:

$$dE = TdS - TdS_i - dE_{el} + V_0 \sigma d\varepsilon, \tag{1.30}$$

where dE_{el} is the reversible part of the interfacial and elastic deformation energies, TdS_i is the irreversible heat loss, $V_0\sigma d\,\varepsilon$ is always positive as it represents dissipated energy, and

$$dG^* = -SdT - V_0\sigma d\varepsilon - dE_{el} - TdS_i,$$
$$dG^* = dG_c + dG_R + dW_i, \tag{1.31}$$

where dG_c is the increment of absorbed or dissipated energy during the chemical reaction, dG_R is the reversible energy of non-chemical nature associated with the transformation, and dW_i is the energy dissipated that represents irreversible energy loss.

1.2.9 Overview of applications of shape memory alloys

1.2.9.1 SMA applications in the biomedical field

1.2.9.1.1 SMA applications in the orthodontic field

The first application of NiTi in the biomedical field dates back to 1975 when Dr. Andreasen from Iowa University made the first implantation of an orthodontic device exploiting the pseudoelastic property of the alloy (Andreasen e Hilleman 1971). NiTi wires, which are in austenitic phase at the temperature of the buccal cavity, have been successfully used for years in fixed orthodontic treatment with multibrackets (Torrisi 1999), Figure 14.

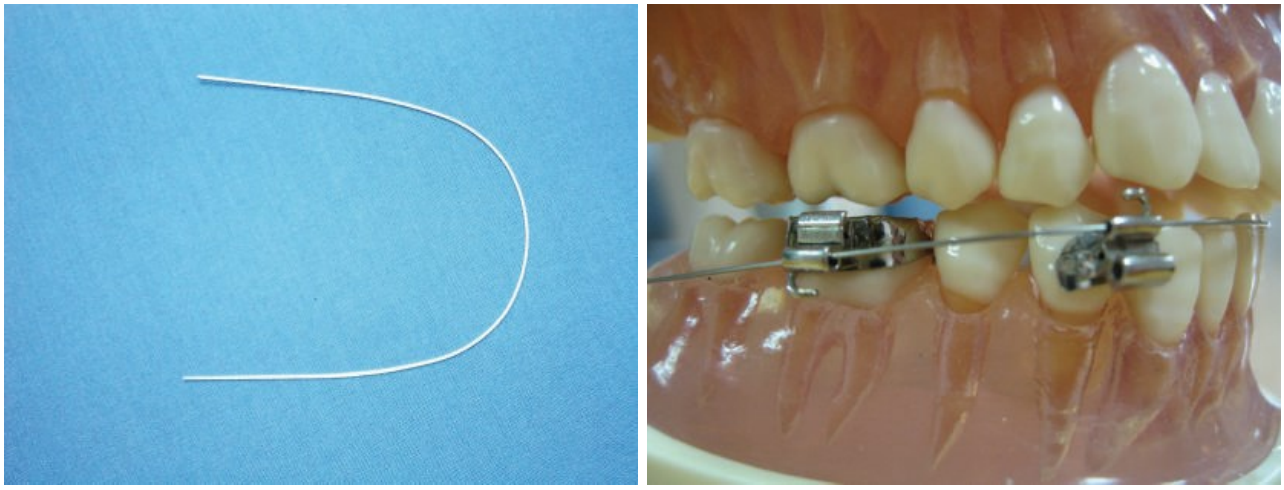

Figure 14 SMA orthodontic wires.

In particular, pseudoelasticity is exploited for generating constant force, after positioning of the wire into the brackets, for wide dental movements. During the insertion phase, the physician deforms the wire thereby inducing a transformation phase from austenite to single-variant martensite; once positioned, the material tries to go back to austenite phase (stable at the buccal cavity temperature) and hence tries to recover the original shape following the descendent path of the force-displacement curve in austenitic phase, which is characterized by a wide plateau. The shape memory effect, and in particular the "constraint recovery" effect, is exploited for producing wires that are in martensitic phase during the positioning into the buccal cavity: deformed during the insertion into brackets, they try to recover the original undeformed shape whenever the patient ingests hot food or drinks. Because the recovery is prevented, the wires exert light forces on the teeth for the entire period in which the temperature is above the normal values (Airoldi, Riva e Vanelli 1995). SMA wires are also inserted into steel palatal arches Figure 15 (a); a palatal arch is mounted on superior molars and applies rotating, expanding and torquing forces. The presence of parts made by SMA exploiting pseudoelasticity allows the device to apply lighter (with respect to the forces generated by an arch completely in steel) and constant forces. Pseudoelastic behavior is also exploited for producing orthodontic distractors (Idelsohn, Pena e Lacroix 2004) Figure 15 (b), which are used for solving the problem of teeth overcrowding in the mandible district: after a mandibular symphyseal distraction osteogenesis, the device is applied in order to produce an expansion of the mandible. Also in this case the use of SMA assures tensile forces nearer to the physiological values and constant in time.

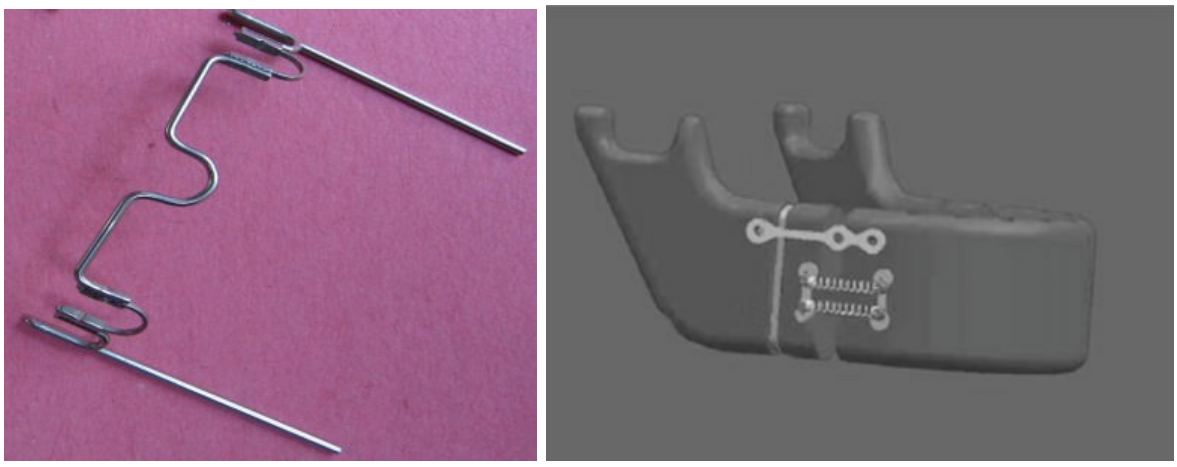

Figure 15 (a) Palatal arch. (b) Orthodontic distracters.

Figure16 Endodontic file.

These forces create stress conditions that improve the tissue growth and hence teeth movement into the correct position. In the endodontic field (the dentistry branch that studies the problems related with the tooth pulp and the tissues surrounding the root of a tooth), the medical treatment foresees the use of rotating devices (files) working inside the root canal to perform a perfect cleaning and shaping: the decontaminated canal is then filled with an inert filling. The files must have good flexibility and a cutting blade. The first devices were from steel and used manually. At the end of the 80's, a great improvement in the technique was given by the introduction of NiTi: the pseudoelastic behavior assured a high flexibility, recovery of deformation (without production of plastic strain), and limitation of the applied force, thus allowing the use of NiTi files Figure16 with a rotating motor (Sattapan, Palamara e Messer 1993).

1.2.9.1.2 SMA applications in the orthopedic field

The stress generated by SMA, when the shape recovery is constrained during heating from Mf to Af, is exploited for fracture treatment by using orthopedic staples (Dai, et al. 1993) or plates. The device Figure 17, characterized by a temperature Af lower than that of the body, is deformed in the martensitic phase ($T \leq Mf \leq Af$) and hence inserted into the body where the fracture is present. The body temperature induces the shape memory effect; because of the constrained recovery, the plates induce a constant stress, consequently joining the two fractured pieces.

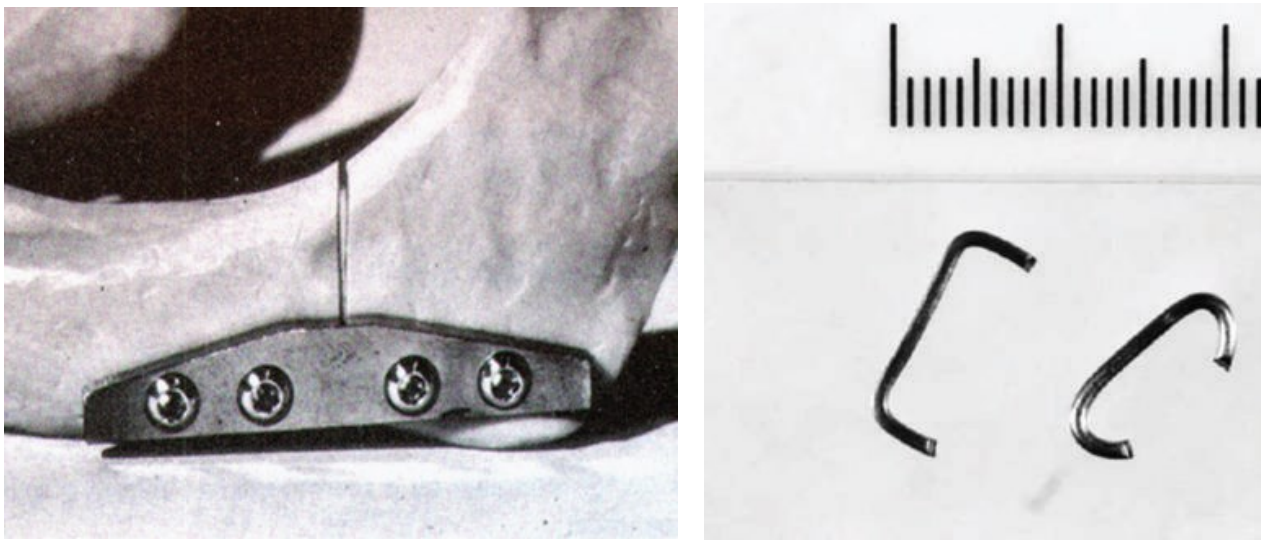

Figure 17 (a) NiTi plate for mandible fracture; (b) staple before and after distraction.

In Figure 18 (a), an application for the treatment of mandible fracture is reported (Laster e MAcBean 2001). NiTi rods are also inserted in devices for correcting scoliosis (Schmerling, Wilkor e Sanders 1976); in this case, the constrained recovery is used for modifying vertebrae relative position. It has also been proposed (Duerig 1990) to exploit the shape memory effect for designing a spinal vertebrae spacer with a rounded shape to be used on behalf of the damaged intervertebral disc.

Figure 18 (a) staple for fixing a frontozygomatic fracture [27]; (b) spinal vertebrae spacer.

By exploiting the material's high deformability in martensitic phase, it is possible to modify the device shape for facilitating the insertion between the vertebrae where, being that the temperature is

higher than Af, the device recovers to its original shape Figure 18 (b). Recently, intraspinal implants exploiting pseudoelasticity have been studied for stabilizing spinous processes in the case of vertebral discs (Contro, et al. 2005).

In orthopedics treatments, the SMA properties are also exploited during the physiotherapy of partially atrophied muscles (Machado e Savi 2003). Gloves for promoting the movements of hands were developed by positioning SMA wires in correspondence of the fingers. In this application the two-way shape memory effect is exploited; heating or cooling, the wires contract or stretch and accordingly the hand is closed or opened.

Another recent application of SMA in the orthopedic field refers to SMA foams. Porous NiTi, characterized by low density, high surface area, high permeability, high strength (important to prevent deformation or fracture), relatively low stiffness (useful to minimize stress shielding effects), high toughness (essential to avoid brittle failure), and by a shape-recovery behavior (facilitating implant insertion and ensuring good mechanical stability within the host tissue), is particularly interesting for osteointegration processes.

1.2.9.1.3 SMA applications in the vascular field

Besides the orthodontic field, the SMA devices are broadly applied in the vascular one. In particular, the introduction of the shape memory alloys boosted the development of mini-invasive techniques where the pathology is treated by the percutaneous insertion of the device rather than surgical intervention. The first vascular SMA application was the venous “Simon filter”, Figure 19 (a), used to prevent emboli in patients unable to tolerate anticoagulants. It can be inserted thanks to the shape memory effect (Lipscomb e Nokes 1996).

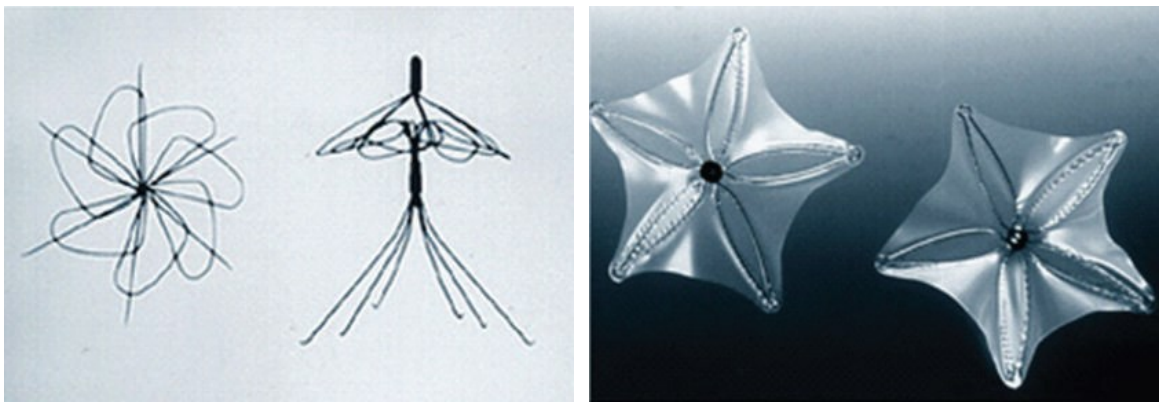

Figure 19 (a) Venous filter: Simon filter; (b) device to close ventricular septal defects.

The device is produced in the open conFiguretion with a NiTi alloy having Af equal to the body temperature, which depicts it in the martensitic phase at ambient temperature. Thus, during the crimping of the device on the catheter, a residual deformation is present as-consequence of themartensitic transformation from multivariant to single-variant phase, which allows the device to be closed and easily placed in the catheter. A saline solution flows in the catheter to keep the temperature low during its insertion into the body. When the catheter is in position, the filter is released, the saline solution is stopped and the body heat induces the martensite-austenite transformation with recovery of the device's original shape. The filter is now able to block the possible clots of the blood stream. In literature, it is possible to find a variety of different filters (Asch 2002) which use the pseudoelastic effect; similarly in this situation, the open conFiguretion at ambient temperature is already in a stable austenitic phase; the crimped device, as soon as it is released in the body, recovers to its original open conFiguretion.

Other common devices are those used to close ventricular septal defects (Thanopoulos, et al. 1998), which are characterized by the presence of an atrial hole in the surface between the two low pressure chambers of the heart. The surgical method includes an invasive and hazardous approach via a thoracotomy and manual suture of the hole. The alternative of using a mini-invasive approach is appealing. The device is made of SMA wires and of an impermeable polyurethane membrane Figure 19 (b). The insertion procedure consists of three steps: (i) positioning of the catheter with the crimped device through the superior vena cava, (ii) positioning of the catheter tip in the left atrium and release of half of the device, and (iii) completion of procedure via release of the remaining part of the device in the right atrium. According to the device typology, both shape memory and pseudoelastic effects are utilized.

NiTi alloys are also used in numerous applications of the self-expandable vascular stents. Stents are metallic "nets" (built by means of laser cutting stainless steel, Cr-Co, or NiTi alloy tubes) which open a stenotic vessel (obstructed by atherosclerotic deposits), therefore allowing restoration of the blood stream to peripheral tissues (Tragy, et al. 2003). For the stainless steel and Cr-Co alloy stents, the stenting procedure consists of: (i) crimping the stent in the terminal part of a catheter which has an inflatable balloon, (ii) insertion of the catheter through a surgical incision in a vessel and positioning of the catheter through the vessel in the stenotic region, (iii) inflation of the balloon with expansion of the stent which pushes against the arterial vessel and (iv) deflation of the balloon and removal of the catheter. Following elastic recoil, the stent remains in an open conFiguretion (plastic deformation) and counteracts the natural vessel contraction, which would tend to reocclude the vessel. For the NiTi stent, the stenting procedure consists of: (i) crimping the stent into the catheter

in the austenitic phase (Af is lower than body temperature) by means of a protective sheath, (ii) insertion of the catheter as stated above and (iii) removal of the sheath and expansion of the stent which tries to recover its original shape thereby enlarging the stenotic vessel. During this phase, the inverse transformation from martensite to austenite occurs, which is due to the martensitic instability at a temperature higher than Af . The advantage of the self-expandable stent with respect to the stainless steel one is that it does not need balloon expansion which possess the risks of further damage of the vascular tissue due to its inflation, it does not require an overexpansion to account for the elastic recoil, and, when positioned, it exerts on the artery a constant force (due to the plateau) unless the artery does not try to occlude the device. The disadvantage, in case of calcified plaques, is that the stent is not able to bring the vessel lumen to the original healthy dimensions.

Self-expandable stents are used to treat atherosclerotic lesions in the coronary arteries, the carotid arteries, and in the peripheral arteries, such as the iliac and femoral arteries Figure 20. The pseudoelasticity property is very important in the peripheral stent which is subjected to possible squeezing manoeuvres such as muscle contractions.

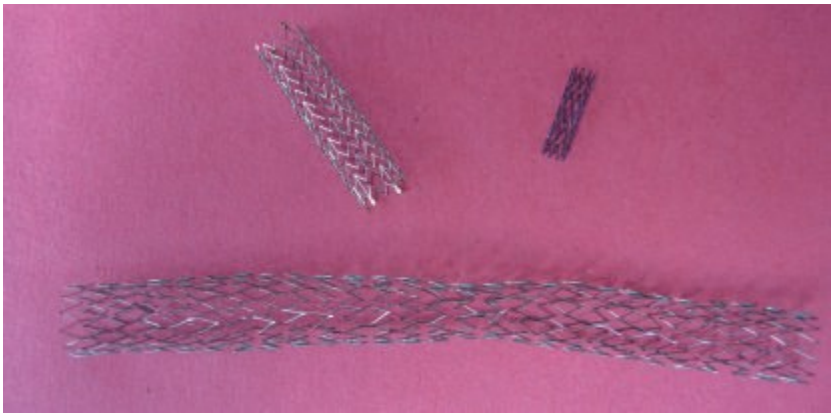

Figure 20 Example of SMA stents: (top right) coronary stent, (top left) carotid stent, (bottom left) femoral stent.

Another successful application of the NiTi alloys is the use of the stent-graft for the treatment of abdominal aortic aneurisms (AAA) (Carpenter, et al. 2000). An aneurism is a permanent dilatation of a portion of an arterial vessel because of vessel wall alterations. For the treatment of this pathology, in the last years, in conjunction with classical surgical techniques, endovascular techniques, with the percutaneous insertion of stent-graft, gained popularity. This means that the stent-graft is easily crimpable on a catheter, sufficiently flexible during the insertion phase, and able to recover its original shape anchoring to the aorta once it has been positioned correctly. All of these

features are present in the pseudoelastic behaviour of the NiTi alloys. This is an explanation of the numerous different prostheses present on the market (Cattaneo 2006), Figure 21.

A recent and very promising field of SMA application is related to the stenotic and regurgitant cardiac valves (Coats e Bonhoeffer 2007). The common adopted strategy to overcome this pathology consists of surgical valve replacement with a mechanical or biological valvular prosthesis. A thoracotomy is present in this substitution eliciting possible surgical complications. The use of mini-invasive techniques allows the surgeon to reduce, in a significant way, the risks of the procedure. For this reason, there are different companies which are developing percutaneous devices to treat mitral, pulmonary, and aortic valvular diseases.

Figure 21 Example of stent-graft in NiTi alloys.

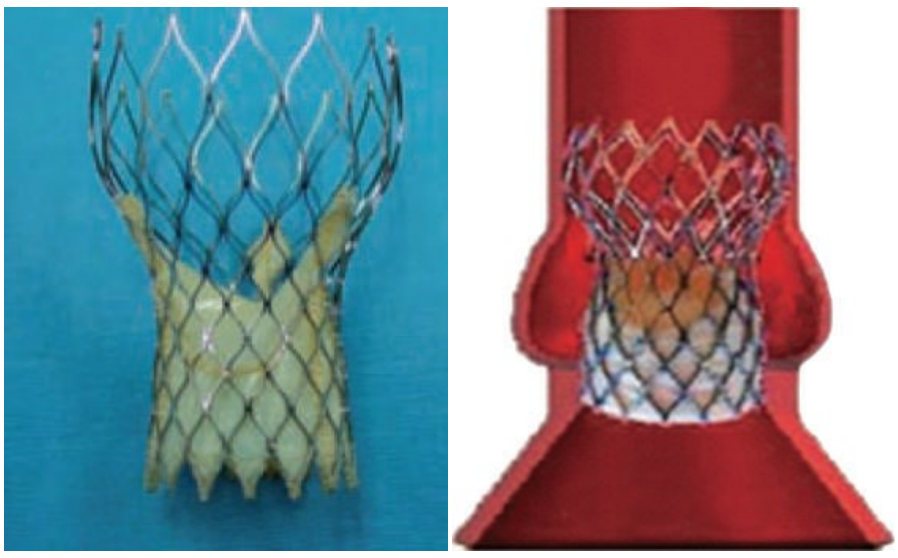

Figure 22 CoreValve aortic valve http://www.medtronic.com/corevalve/ous/index.html

For the aortic position, for example, CoreValve developed a device Figure 22 (a) which consists of a biological prosthesis made with bovine pericardium mounted and sutured on a self-expandable stent. The insertion procedure consists of positioning the device with a specifically designed catheter without the need for removal of the native valve. The self-expandable stent shows a diamond-like cell design with struts at different lengths and thicknesses to optimize the expansion to a nonregular shape Figure 22 (b).

In the last years, the ever more extended use of NiTi in cardiovascular applications has pointed out the problem of its fatigue behaviour (Pelton, Kusnezov e Carman 2008). In particular, for the treatment of peripheral arterial diseases with self-expandable stents, there is a growing concern about observations of fractures during follow-up procedures. Fractures are mainly detected in superficial femoral artery and this is probably related to the combination of pulsatile forces, due to systolic/diastolic pressure cycles, and nonpulsatile forces (torsion, compression, extension, and flexion), due to leg movements, which characterize the stent solicitations. The study of NiTi fatigue life is a current and very complex problem: the nonlinear nature of the pseudoelastic behaviour entails that conventional fatigue life theory is difficult to apply; the strong influence of the production treatments on the material characteristics requires fatigue specimens having the same dimensions and production treatments of the device under study; design, material, and surface conditions together play an important role for the definition of NiTi alloy stent fatigue and durability. For all these reasons, great efforts are currently directed to a more rigorous understanding of NiTi fatigue behavior and to the design ofNiTi medical devices that aremore fatigue resistant.

1.2.9.2 SMAs applications in the civil engineering field

1.2.9.2.1 Research on the damping properties of SMAs

Using SMAs for passive structure control relies on the SMA's damping capacity, which represents its ability to dissipate vibration energy of structures subject to dynamic loading. As reviewed in the last section, the damping capacity comes from two mechanisms: martensite variations reorientation which exhibit the SME and stress-induced martensitic transformation of the austenite phase which exhibit the superelasticity. The energy dissipation of the widely-used Nitinol superelastic SMA wires was investigated (Dolce e Cardone, Mechanical behaviour of shape memory alloys for seismic application 1. Martensite and Austenite NiTi bars subjected to torsion 2001), (Piedboeuf e

Gauvin 1998). Dolce and Cardone (Dolce e Cardone 2001) investigated the superelastic Nitinol wires subjected to tension loading. They observed the dependence of the damping capacity on temperature, loading frequency and the number of loading cycles. It is found that the mechanical behavior of the wires is stable within a useful range for seismic application. Also, they suggested that the austenite wires should be pretensioned for larger effectiveness of energy dissipation. Piedboeuf and Gauvin, (Piedboeuf e Gauvin 1998), reported that the influence of ambient temperature on the damping capacity of the superelastic Nitinol wires can be negligible. Gandhi and Wolons (Granghi e Wolons 1999) proposed using a complex modulus approach to characterize the damping capacity of superelastic SMA wires for convenient integration with structure dynamics. A superelastic SMA wire demonstrates the damping capacity not only under tension loading, but also under cyclic bending. In 2000, Song et al. presented his effort to predict the energy dissipation in SMA wire under pure bending loading. His numerical results showed that the energy dissipated by the superelastic SMA wire is highly sensitive to its diameter; in detail, the thicker the SMA wire, the more energy was dissipated. Recently, as large cross-section-area SMAs become available, studies on the properties of SMA bars or rods have attracted more attentions (Dolce e Cardone, Mechanical behaviour of shape memory alloys for seismic application 1. Martensite and Austenite NiTi bars subjected to torsion 2001). As discovered by Liu et al. (Liu, Xie e J.V. 1999), the damping capacity of a martensite Nitinol bar under tension–compression cycles increases with increasing strain amplitude, but decreases with loading cycles and then reaches a stable minimum value. Dolce and Cardone (Dolce e Cardone, Mechanical behaviour of shape memory alloys for seismic application 1. Martensite and Austenite NiTi bars subjected to torsion 2001) compared the martensite damping and austenite damping of Nitinol bars subjected to torsion. They found that the damping capacity of the martensite Nitinol bar is quite a bit larger than that of the austenite Nitinol bar, although the prior cannot remain at its highest value as the residual strain accumulates. They also noticed that the martensite bar's mechanical behavior is independent of loading frequency and that of the austenite bar slightly depends on the frequency. This implies that both martensite and austenite Nitinol bars can work in a wide frequency range and have a good potential for seismic protection. An overview of the damping capacity of martensite SMAs is presented in (Humbeeck 2003).

1.2.9.2.2 Classification of applications of SMAs in civil structure control

The vibration suppression of civil structures to external dynamic loading can be pursued by using active control, semiactive control, and passive control. In the active control mode, an external power source controls actuators to apply forces to the object structures. For a passive control system, no external power source is required and the impact forces are developed in response to the motion of the structures. The semi-active control devices use considerably less energy to adjust the structural properties than the active control devices.

Based on this classification methodology, the current applications of SMAs on structure control can be classified into three categories: passive structural control, active frequency tuning (semi-active) and active damage control.

1.2.9.2.3 SMAs for passive structural control

1.2.9.2.3.1 Classification of SMAs for passive structural control

The passive structural control using SMAs takes advantage of the SMA's damping property to reduce the response and consequent plastic deformation of the structures subjected to severe loadings. SMAs can be effectively used for this purpose via two mechanisms: ground isolation system and energy dissipation system (Saadat, et al. 2002). In a ground isolation system, SMA-made isolators, which are installed between a super-structure and the ground to assemble an uncoupled system, filter the seismic energy transferred from the ground motion to the superstructure so that the damage of the super-structure is attenuated. On the other hand, via the energy dissipation mechanism, martensite or austenite SMA elements integrated into structures absorb vibration energy based on the hysteretic stress–strain relationship.

Although the two mechanisms are based on the damping capacity of SMAs, they are different in arrangement and function. An SMA isolator provides variable stiffness to the structure according to the excitation levels, in addition to energy dissipation and restoration after unloading. Therefore, superelastic SMAs are appropriate for isolators. On the other hand, an SMA energy dissipation element mainly aims to mitigate the dynamic response of structures by dissipating energy. Both martensite and superelastic SMAs have been studied for this case.

In general, for SMA devices for passive vibration control, martensite SMAs have a larger damping capacity; however, it requires external heat to cause a phase transformation to restore its original shape. On the other hand, superelastic SMAs have a smaller damping capacity, but they have a strong re-centering force to restore the structure's initial position and there will be little residual strain of the superelastic SMAs.

1.2.9.2.3.2 SMA isolation devices

The reported SMA isolation systems include SMA bars for highway bridges (Wilde, Gardoni e Fujino 2000), SMA wire re-centering devices for civil buildings (Dolce, Cardone e Marnetto 2001), SMA spring isolation system (Kahn e Lagoudas 2002) and SMA tendon isolation system for a multi-degree-of-freedom (MDOF) shear frame structure (Corbi 2003).

Wilde et al. (Wilde, Gardoni e Fujino 2000) investigated a base isolation system with superelastic SMA bars for elevated highway bridges. The SMA bar isolation system is illustrated in Figure 23.

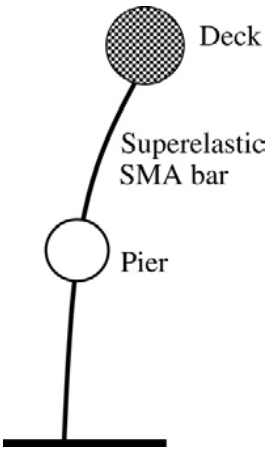

Figure 23 Schematic of the SMA isolation device for elevated highway bridges.

Comparative simulations of the SMA isolation system and a conventional isolation system were conducted with three excitation levels. The results revealed that the SMA isolation system provided variable responses to excitation as well as a notable damping. For small excitation level, the SMA isolation system firmly links the pier and the deck, while the relative motion emerges in the case of the conventional system. For a medium excitation level, the SMA bar undergoes a stress-induced martensitic transformation so that the soft stiffness allows a relative displacement comparable to

that of the conventional isolation system. At severe loading, the SMA bar enters an elastic range of martensite and the maximum displacement is one fifth as much as that of the conventional isolation system. The comparison shows that the damage energy of the bridge with the SMA isolation system is smaller than with the conventional system.

Dolce et al. (Dolce, Cardone e Marnetto 2001) developed and tested the full-scale Nitinolwire-based isolation system within the MANSIDE (Memory Alloys for New Seismic Isolation and Energy Dissipation Devices) project to study the feasibility of Nitinol wire for vibration isolation.

The operation principle is schematically shown in Figure 24.

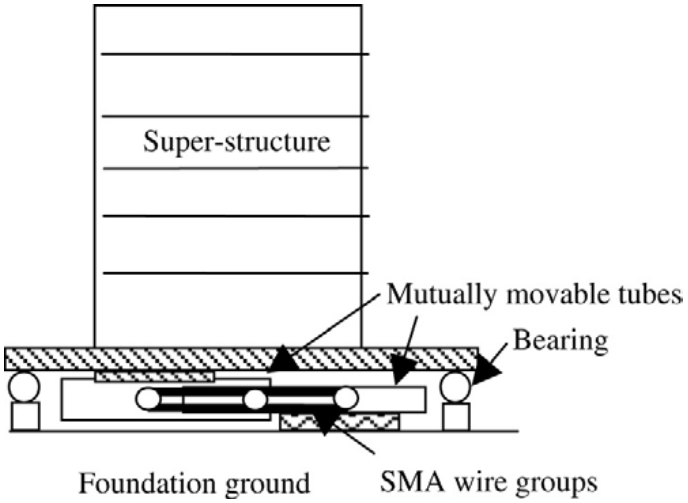

Figure 24 Schematic of the SMA isolation system for buildings.

A superelastic SMA wire is so wound around three stubs which are connected to the tubes that, when there is reciprocal movement between the super-structure and the foundation, the wire is elongated and the vibration magnitude is damped by the wire. The isolation system is able to carry out up to 600 kN maximum force and to reach up to 180 mm displacement. Cyclic loading tests show that the isolation system shows a variable stiffness with the loading intensity, and a high effectiveness in filtering energy transmission. They tested the isolation system to control the free vibration of a real base-isolated building with 140 mm initial displacement. The test fully confirms the applicability of an SMA wire recentering isolation system on passive structural control.

Khan and Lagoudas (Kahn e Lagoudas 2002) analytically studied using SMA springs to isolate a single-degree-of-freedom (SDOF) system from a ground excitation simulated by a shake table. It

was shown that the vibration isolation depended on the relative displacement of SMA springs, because small displacements did not trigger the stress-induced martensitic transformation. Moreover, the SMA springs achieved the best isolation effect only when the system vibrated at a frequency near its resonance frequency and under higher loading levels. Figure 25 shows the experimental setup for the SMA spring isolation system developed by Mayes et al. (Mayers, Lagoudas e Henderson 2001), on which the experiments were conducted by the same research group. It was shown that the significant impact of SMA springs on the dynamic response of the vibration system lied on two aspects: greatly altering the system's resonance frequency and resonance amplitude. Corbi (Corbi 2003) proposed using the SMA tendon associated low level part of a multi-story shear frame (shown in Figure 26) to isolate the ground excitation. The numerical simulation showed that the SMA tendon isolation device decisively improves the dynamic response capacity of the structures either in terms of response reduction or re-centering capacity.

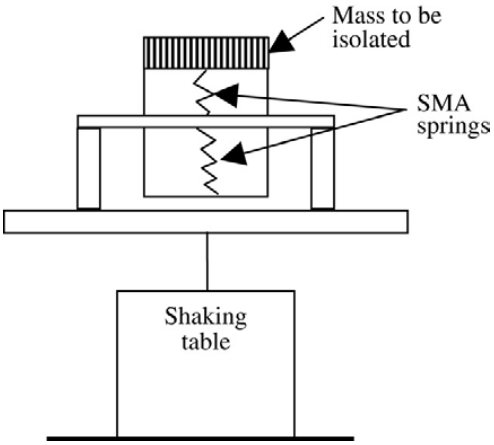

Figure 25 Schematic of the SMA spring isolation device.

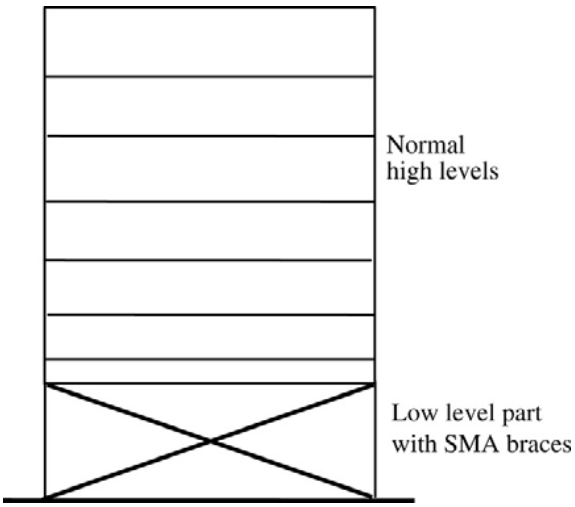

Figure 26 Schematic of the SMA tendon isolation system for a MDOF structure

It should be emphasized that for isolation devices only superelastic SMA has been studied due to its zero residual strain after unloading. However, to improve the damping effect of the superelastic SMA isolation devices, martensite SMA elements can be introduced to help dissipate more energy. The re-centering device by Dolce et al. (Dolce, Cardone e Marnetto 2001) is a good example of combining the superelastic and martensitic SMAs.

1.2.9.2.3.3 SMA isolation devices

The SMA energy dissipation devices have been seen in the forms of braces for framed structures [see e.g. (Clark, et al. 1995), (Han, et al. 2003), (Dolce, Cardone e Marnetto 2001)], dampers for cable-stayed bridges (Li, Liu e Ou 2004) or simply supported bridges (DesRoches e Delemont 2002), connection elements for columns (Tamai, et al. 2003) and retrofitting devices for historic buildings (Indirli, Demo application of shape memory alloy devices: the rehabilitation of S. Georgio Church Bell Tower 2001), (Croci, Bonci e Viskovic 2000). Experiments or simulations or both have been carried out to explore the potentials of the SMA-based energy dissipation devices in passive structure control. That research focused on three aspects: modeling for dynamic response of the structures with SMA devices, experimentally verifying the feasibility of the SMA devices and optimizing the SMA devices' design in terms of vibration suppression using experimental and numerical methods.

A. SMA braces for frame structures

The SMA wire braces are installed diagonally in the frame structures. As the frame structures deform under excitation, SMA braces dissipate energy through stress-induced martensite transformation (in the superelastic SMA case) or martensite reorientation (in the martensite SMA case). Clark et al. (Clark, et al. 1995) conducted a study on a six-story two-bay by two-bay steel frame which was installed with the Nitinol wire energy dissipation devices (shown in Figure 27).

210 loops of Nitinol wire were wrapped around two cylindrical support posts to assemble the braces. Several different scale prototypes of the devices were designed, implemented and tested. They showed that the proposed devices have characteristics of great versatility, simplicity of functioning mechanism, self-centering capability, high stiffness for small displacements and good energy dissipation capability.

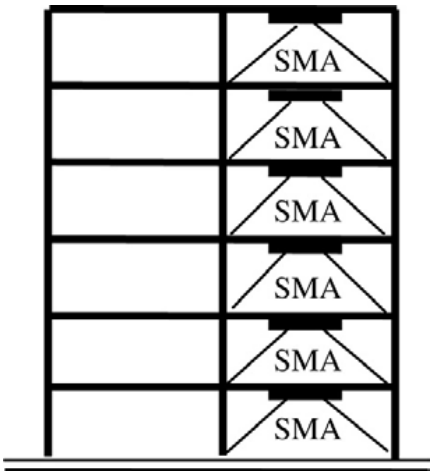

Figure 27 Schematic of the setup of the SMA brace reinforced frame structure

In the work by Han et al. (Han, et al. 2003), eight damper devices made of the SMA wires and steel wires were diagonally installed in a two-story steel frame structure, as shown in Figure 28. Both experimental analysis and numerical verification were conducted to demonstrate the effectiveness of the SMA dampers on vibration reduction.

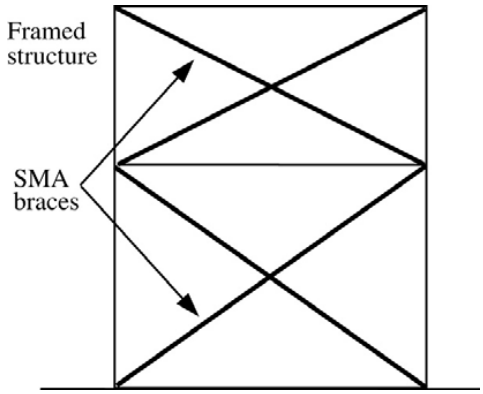

Figure 28 Schematic of the SMA braces for a two-story steel frame

Experimental comparisons of the frame responses with and without dampers showed that the vibration of the controlled frame decayed very much faster than that of the uncontrolled frame. The simulation has demonstrated that the largest displacement of the controlled frame is only 15% of that of the uncontrolled case.

B. SMA damping elements for bridges

Both superelastic and martensite SMAs can be used as damper elements for bridges. Li et al. (Li, Liu e Ou 2004) theoretically studied the vibration mitigation of a combined cable–SMA damper system which can be used on a stay-cable bridge (shown in Figure 29).

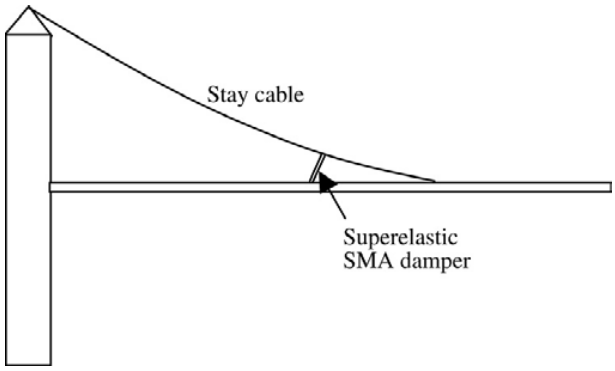

Figure 29 Schematic of the SMA damper for a stay-cable bridge

The dynamic responses of the SMA damped cable were simulated as it vibrated at its first mode or at its first few modes respectively. They stated that the proposed superelastic SMA damper can suppress the cable's vibration in both cases. As shown in Figure 30, DesRoches and Delemont (DesRoches e Delemont 2002) reported their testing on a full-scale superelastic SMA bar used for seismic retrofit of simply support bridges and their simulation analysis on a multi-span simply supported bridge with the SMA restrainer.

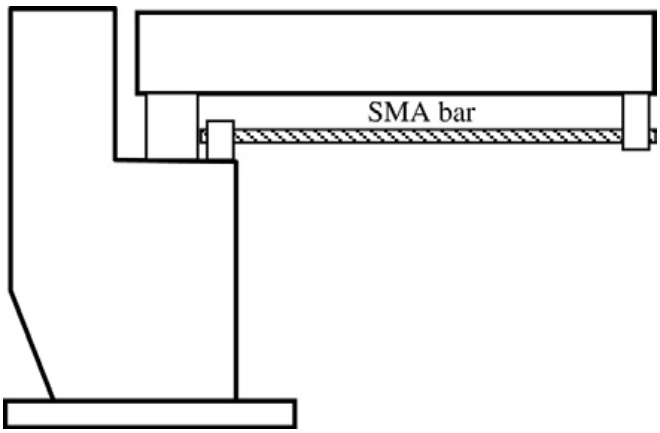

Figure 30 Schematic of the setup of SMA restrainer for a simple-supported bridge.

The results have shown that the SMA restrainer more effectively reduced relative hinge displacement at the abutment and it provided a large elastic deformation range in comparison with conventional steel restrainer cables. In addition, the SMA restrainer extremely limits the response of bridge decks to nearfield ground motion.

C. SMA connectors

Connectors or connections in various structures are prone to damage during an earthquake event. SMA connectors have been designed to provide damping and tolerate relatively large deformations. Tamai and Kitagawa (Tamai, et al. 2003) proposed an exposed-type column base with SMA anchorage for seismic resistance. The SMA anchorages are made of the Nitinol SMA rods in 20–30 mm diameter and steel bars, as shown in Figure 31. The results obtained from the pulsating tension loading tests and numerical simulation of the SMA rods, have shown that the SMA wires were very effective in dissipating energy and reducing the building's vibration under severe seismic ground motion. It was observed that, contrary to the accumulated residual strain of ordinary anchorages, the SMA anchorages can recover their original shape after cyclic loadings and therefore their resisting performance remains the same to prevent plastic deformation and damage in the structural columns. Leon et al. (Leon, et al. 2001) used martensite SMA tendons as the primary load transferring elements in steel beam–column connections (shown in Figure 32). Based on loading tests of the two full-scale SMA enhanced connections, they concluded that the connection exhibited stable and repeatable hysteresis for rotations up to 4% and the SMA tendon was able to sustain up to 5% strain without permanent damage.

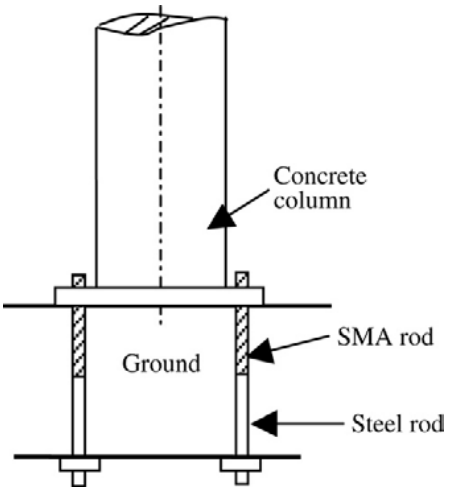

Figure 31 Schematic of SMA bar anchorage for a column

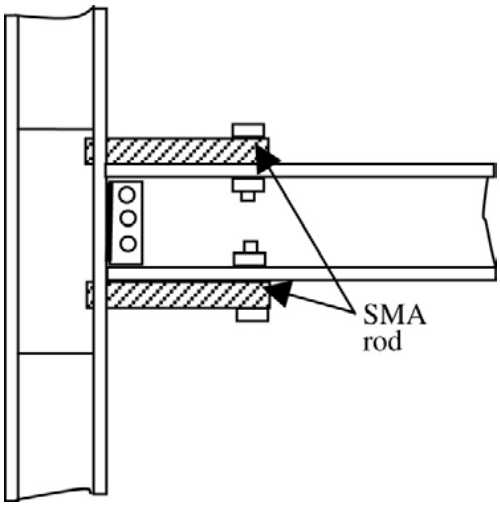

Figure 32 Schematic of SMA connector for steel structures

D. Structural reinforcement for earthquake retrofit

SMAs have also been used to retrofit existing or damaged structures. As seen in Fig. 15, superelastic SMA tie bars were used by Indirli et al. (Indirli, Demo application of shape memory alloy devices: the rehabilitation of S. Georgio Church Bell Tower 2001) to rehabilitate the S. Giorgio Church Bell-Tower, which was seriously damaged by the earthquake of Oct. 15th 1996. The SMA tie bars, which run through the height of the tower and are anchored at its foundation, reinforce the structure and increase its modal frequencies. This historical tower was declared intact after an similar earthquake in 2000 (Indirli 2001).

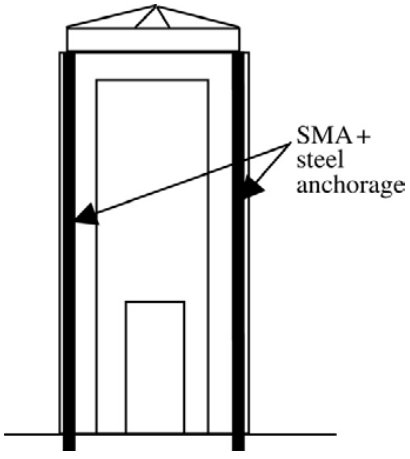

Figure 33 Schematic of retrofit of a bell tower using SMA anchorage

More in general, in the field of the retrofitting techniques for hystorical masonry buildings, the development of innovative SMA-based techniques, devoted to seismic protection of masonry structures, began in Italy within the EU funded ISTECH Project, coordinated by FIP Industriale and ENEA as a partner (ISTECH, 1996). The reference (Indirli and Castellano 2008) contains every information regarding the main properties of these SMA anti-seismic devices, testing results, and structural conFiguretions selected for applications. In particular, the multi-plateau device (based on the superelastic effect of multiple sets of shape memory alloy wires) has the capacity to work at increasing force levels, being also less sensitive to the masonry tensile strength (Figure 34, Figure 35).

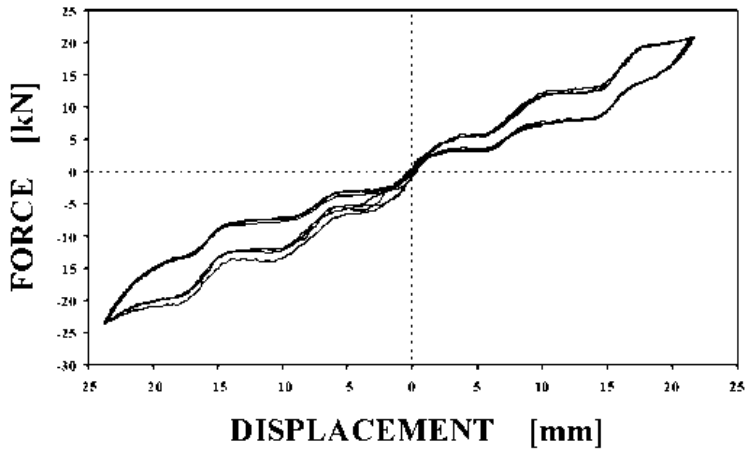

Figure 34 FIP Multiplateau SMA device force-displacement response

Figure 35 FIP Multiplateau SMA devices.

ISTECH led to significant exploitations, in particular the reinforcement measures for the Upper Basilica of St. Francis in Assisi (Figure 36, Figure 37, Figure 38), hit by the 1996 Marche-Umbria (Italy) earthquake. At the end of the project, FIP Industriale patented the SMA device (EU Patent, 2000).

Figure 36 St. Francis Basilica in Assisi: earthquake damage in the transept tympana.

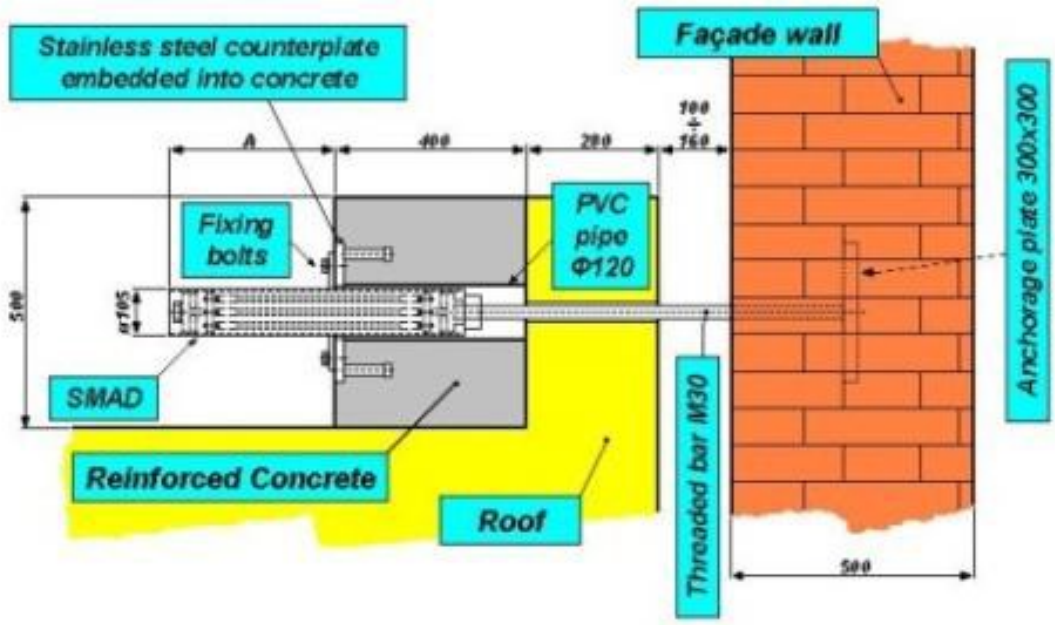

Figure 37 Scheme of the reinforcement intervention with SMA devices in series with conventional steel ties.

Figure 38 Picture of the entire SMA devices row at the end of the work.

1.3 Shape memory polymers

1.3.1 Introduction to SMP's

The focus of this paragraph is on thermo-responsive shape-memory polymers. The shape-memory effect is not related to a specific material property of single polymers; it rather results from a combination of the polymer structure and the polymer morphology together with the applied processing and programming technology (Landlein e Kelch, Shape-Memory Polymers 2002). Shape-memory behavior can be observed for several polymers that may differ significantly in their chemical composition. However, only a few shape-memory polymers are described in the literature. The process of programming and recovery of a shape is shown schematically in Figure 39.

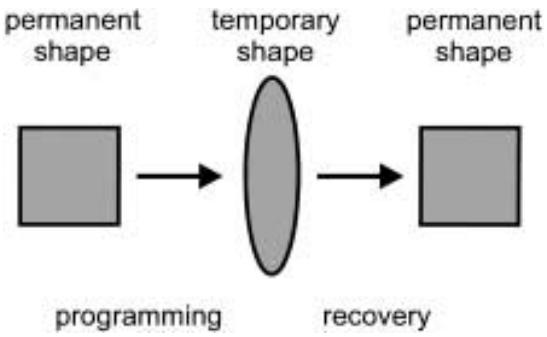

Figure 39 Schematic representation of the thermally induced one-way shape-memory effect. The permanent shape is transferred to the temporary shape by the programming process. Heating the sample to a temperature above the switching transition Ttrans results in the recovery of the permanent shape.

First, the polymer is conventionally processed to receive its permanent shape. Afterwards, the polymer is deformed and the intended temporary shape is fixed. This process is called programming. The programming process either consists of heating up the sample, deforming, and cooling the sample, or drawing the sample at a low temperature (so called "cold drawing"). The permanent shape is now stored while the sample shows the temporary shape. Heating up the shape-memory polymer above a transition temperature T_{trans} induces the shape-memory effect. As a consequence, the recovery of the stored, permanent shape can be observed. Cooling down the polymer below the transition temperature leads to solidification of the material, however, no recovery of the temporary shape can be observed. The effect described is named as a one-way shape-memory effect. By further programming, including mechanical deformation, the work piece can be brought into a temporary shape again. This new temporary shape does not necessarily match

the first temporary shape. In Figure 40 a picture sequence demonstrates impressively the performance of shape-memory polymers.

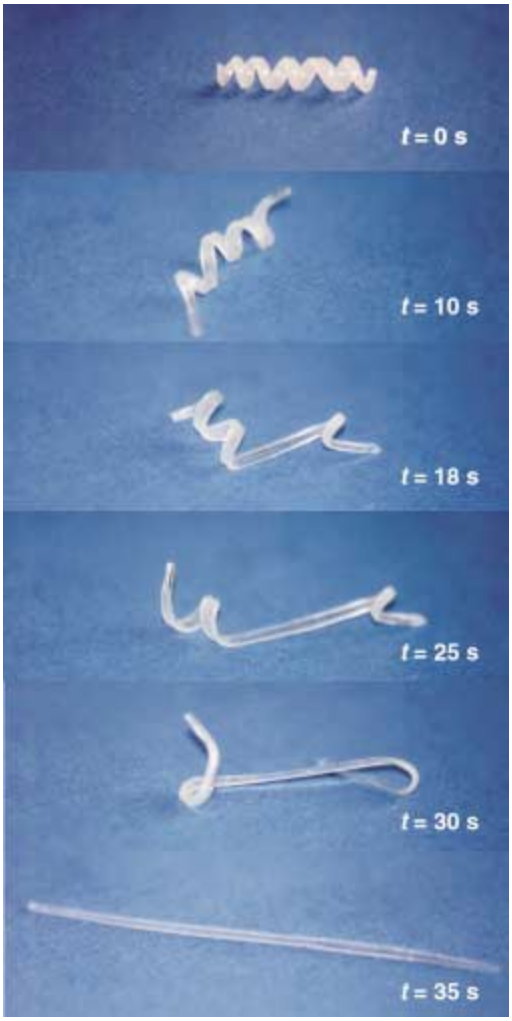

Figure 40 Transition from the temporary shape (spiral) to the permanent shape (rod) for a shape-memory network that has been synthesized from polydimethacrylate. The switching temperature of this polymer is 46°C. The recovery process takes 35 s after heating to 70C.

The permanent shape of the polymers formed from 1 and 2 is that of a rod, which has been deformed to a spiral (temporary shape) during the programming process. Under the influence of hot air having a temperature of 70 °C the permanent shape is recovered as soon as the switching temperature T_{trans} is reached. The permanent shape is recovered with a precision of more than 99% with appropriately optimized programming conditions. This precision makes these materials suitable for highly demanding applications (Landlein, Schmidt e Langer, AB-Polymer networks based on oligio(e-caprolactone) segments showing shape memory properties 2001). Since the 1960s, polyethylene that is covalently cross-linked by means of ionizing radiation has found broad

application as heat-shrinking film or tubing, especially for the insulation of electric wires or as protection against corrosion of pipe lines (Charlesby 1960), (Machi 1996). These materials are marketed under the catchphrase “heat-shrinkable materials”. The mechanism of the heat-shrinking process is in analogy with the thermally induced shape-memory effect. Here, the permanent shape is also fixed by covalent cross-links and the switching process is controlled by the melting temperature of the polyethylene crystallites. More and more reports about linear, phase-segregated multiblock copolymers, mostly polyurethanes, can be found in the literature under the name of the generic term .shape-memory polymers. These elastic materials show at least two separated phases. The phase showing the highest thermal transition T_{perm} acts as the physical cross-link and is responsible for the permanent shape. Above this temperature the polymer melts and can be processed by conventional processing techniques such as extrusion or injection molding. A second phase serves as a molecular switch and enables the fixation of the temporary shape. The transition temperature for the fixation of the switching segments can either be a glass transition (T_g) or a melting temperature (T_m). After forming the material above the switching temperature, but below T_{perm}, the temporary shape can be fixed by cooling the polymer below the switching temperature. Heating up the material above T_{trans} again cleaves the physical cross-links in the switching phase. As a result of its entropy elasticity the material is forced back to its permanent shape. Polyurethanes with shape-memory properties have found application as, for example, components in auto chokes. In this application it is not the shape-memory effect that is used, but the property of the polymer to soften upon being heated up above the switching temperature. A substantially new development in connection with the design of shape-memory polymers are polymer systems. These are families of polymers in which macroscopic properties (for example, mechanical properties or T_{trans}) can be controlled by a specific variation of molecular parameters. This makes it possible to tailor the specific combination of the properties of the shape-memory polymers that are required for specific applications just by a slight variation of the chemical composition. The shape-memory material presented in Figure 40 belongs to a family of multiphase polymer networks that are biocompatible and biodegradable. Such materials are highly interesting for applications in the field of minimally invasive surgery.

1.3.2 Thermally Induced Shape-Memory Effect in Polymers

Before the molecular mechanism of the thermally induced shape-memory effect is explained in detail, the basic principles of entropy elasticity are discussed. A structured overview of

thermoplasts and polymer networks that show shape-memory properties will be concluded by a summary of current research work in the field of shape memory polymers.

1.3.2.1 Thermodynamic Aspects Significant for the Shape Memory Effect of Polymers

1.3.2.1.1 Chain Conformation of Linear, Amorphous Polymers

In the amorphous state, polymer chains take up a completely random distribution in the matrix, without the restriction that is given by the order of crystallites in semicrystalline polymers. All possible conformations of a polymer chain have the same inner energy. If W expresses the probability of a conformation, a strongly coiled conformation, which is the state of maximum entropy, represents the most probable state for an amorphous linear polymer chain according to the Boltzmann equation:

$$S = k \ln W \tag{1.32}$$

where S is entropy and k is the Boltzmann constant.

1.3.2.1.2 Transition from the Glassy State to the Rubber-Elastic State

In the glassy state all movements of the polymer segments are frozen. The transition to the rubber-elastic state occurs upon increasing the thermal activation, which means that the rotation around the segment bonds becomes increasingly unimpeded. This situation enables the chains to take up one of the possible, energetically equivalent conformations without disentangling significantly. The majority of the macromolecules will form compact random coils because this conformation is entropically favored and, as a result, much more probable than a stretched conformation.

In this elastic state a polymer with sufficient molecular weight (M_n>20 000) stretches in the direction of an applied external force. If the tensile stress is only applied for a short time interval, the entanglement of the polymer chains with their direct neighbors will prevent a large movement of the chain. Consequently, the sample recovers its original length when the external stress is released. In this way, the sample shows a kind of memory for the nonstretched state. This recovery is sometimes called “memory effect”, and is based on the sample’s tendency to return to its original, most randomly coiled state that represents the most probable state. However, if the external tensile stress is applied for a longer time period, a relaxation process will take place which

results in a plastic, irreversible deformation of the sample because of slipping and disentangling of the polymer chains from each other. The tendency of the polymer chains to disentangle and to slip off each other into new positions enables the segments to undergo a relaxation process and to form entropically more favorable random coils.

In a similar way, an increasing rise in temperature above the glass transition temperature favors a higher segment mobility and a decrease in the mechanical stress in the elastic material being stretched by an external force.

1.3.2.1.3 Entropy Elasticity

The described slipping or flow of the polymer chains under stress can be stopped almost completely by cross-linking the chains. The cross-linkage points act as anchors or "permanent entanglements" and prevent the chains from slipping from each other. The cross-links can either be chemical and/or physical. Those materials are called elastomers.

Chemically cross-linked polymers form insoluble materials which swell in good solvents. Their shape is fixed during the cross-linking and cannot be changed afterwards.

Thermoplastic elastomers contain physical netpoints. A requisite for the formation of the netpoints is the existence of a certain morphology of a phase-separated material, as found for block copolymers containing thermodynamically immiscible components. The highest thermal transition T_{perm} is related to the hard-segment-forming phase. If this thermal transition is not exceeded, these domains will stabilize the permanent shape by acting as physical netpoints in the material. Thermoplastic elastomers are very soluble in suitable solvents and can be processed from the melt.

Besides the netpoints, networks contain flexible components in the form of amorphous chain segments. If the glass transition temperature of these segments is below the working temperature, the networks will be elastic. They show entropy elasticity and can be stretched with a loss of entropy. The distance between netpoints increase during stretching and they become oriented. As soon as the external force is released, the material returns to its original shape and gains back the entropy lost before. As a result, the polymer network is able to maintain the mechanical stress in equilibrium.

Elastomers exhibit some extraordinary properties: they warm up when they are stretched; the elastic modulus increases upon heating; the coefficient of thermal expansion for a stretched

elastomer is negative above the glass transition temperature; below the Tg value the sample behaves like a glass and contracts if it is further cooled down Figure 41. While the coefficient of thermal expansion is negative for a stretched sample, it is positive for an unloaded sample.

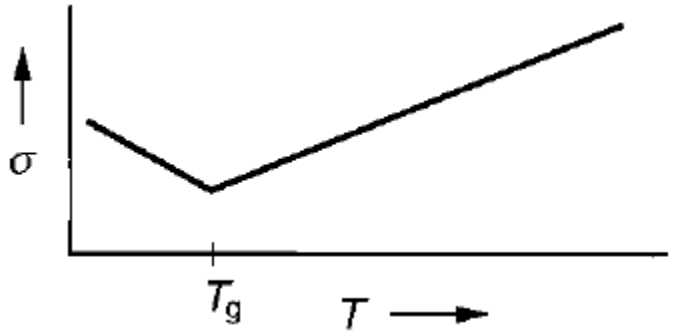

Figure 41 Plot of the stress σ in an elastomer which is stretched and then kept under constant strain over a temperature range above and below the T_g value.

The inner energy of an ideal elastomer will not change if it is stretched. For this reason, the Helmholtz equation for the free energy U is reduced according to (1.33). From the stress - strain behavior of a polymer network with a low degree of cross-linking and netpoints that

$$U = -T\Delta S \tag{1.33}$$

are sufficiently far away from each other, the change in free energy for the stretching of a standard volume is given by (1.34). N is the number of chain segments between the netpoints and λ_x, λ_y, and λ_z represent the elongation ratios in three dimensions ($\lambda = l/l_0$), where l represents the length of the segments between the netpoints in the stretched state, and l_0 represents the length of the segments in the unloaded state.

$$U = \frac{1}{2} NkT(\lambda_x^2 + \lambda_y^2 + \lambda_z^2 - 3) \tag{1.34}$$

1.3.2.2 Molecular Mechanism of the Shape-Memory Effect of Polymers

An elastomer will exhibit a shape-memory functionality if the material can be stabilized in the deformed state in a temperature range that is relevant for the particular application. This can be reached by using the network chains as a kind of molecular switch. For this purpose the flexibility of the segments should be a function of the temperature. One possibility for a switch function is a thermal transition (T_{trans}) of the network chains in the temperature range of interest for the particular application. At temperatures above T_{trans} the chain segments are flexible, whereas the

flexibility of the chains below this thermal transition is at least partly limited. In the case of a transition from the rubber-elastic or viscous state to the glassy state, the flexibility of the entire segment is limited. If the thermal transition chosen for the fixation of the temporary shape is a melting point, strain-induced crystallization of the switching segment can be initiated by cooling the material which has been stretched above the T_{trans} value. The crystallization achieved is always incomplete, which means that a certain amount of the chains remains amorphous.

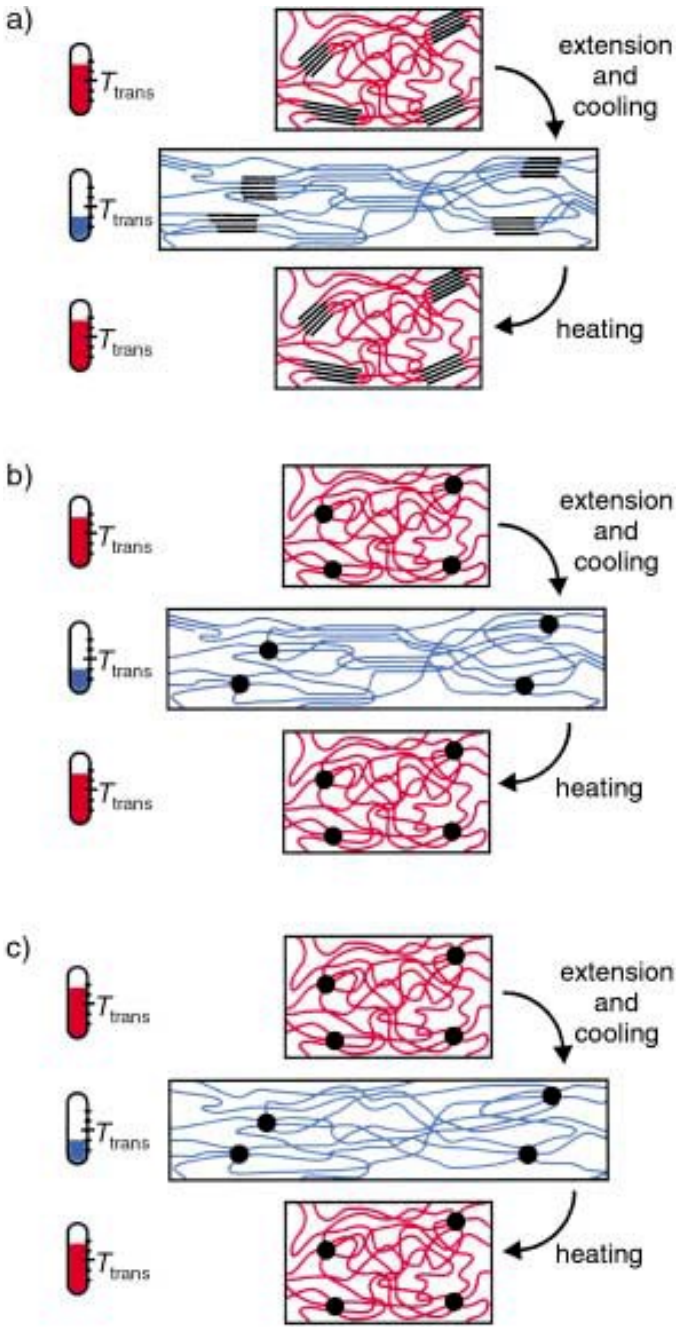

Figure 42 Schematic representation of the molecular mechanism of the thermally induced shape-memory effect for a) a multiblock copolymer with T_{trans} = Tm, b) a covalently cross-linked polymer with T_{trans} = Tm, and c) a polymer network with T_{trans} = T_g . If the increase in temperature is higher than T_{trans} of the switching segments, these segments are flexible (shown in red) and the polymer can be deformed elastically. The temporary shape is fixed by cooling down below T_{trans} (shown in blue). If the polymer is heated up again, the permanent shape is recovered.

The crystallites formed prevent the segments from immediately reforming the coil-like structure and from spontaneously recovering the permanent shape that is defined by the netpoints. The permanent shape of shape-memory networks is stabilized by covalent netpoints, whereas the permanent shape of shape-memory thermoplasts is fixed by the phase with the highest thermal transition at T_{perm}.

The molecular mechanism of programming the temporary form and recovering the permanent shape is demonstrated schematically in Figure 42 for a linear multiblock copolymer, as an example of a thermoplastic shape-memory polymer, as well as for two covalently cross-linked polymer networks.

The "memory effect" mentioned formerly is not a shape-memory effect. This expression describes the property of an elastomer one would not expect for an amorphous polymer chain. The "memory effect" represents a problem in the processing of non-vulcanized natural rubber. In the case of a quick deformation of the amorphous material by a sudden subsequent decrease or removal (or reduction) of the external force, the polymer re-forms its original shape. Such polymers will also exhibit a shape-memory effect if a suitable programming technique is applied. In this case, temporary entanglements of the polymer chains which act as physical netpoints can be used for the fixation of the permanent shape. This thermal transition can be used as a switching transition if the glass transition of the amorphous material is in the temperature range that is relevant for a specific application.

1.3.2.3 Macroscopic Shape-Memory Effect and Thermomechanical Characterization

The shape-memory effect can be quantified by cyclic, thermomechanical investigations. The measurements are performed by means of a tensile tester equipped with a thermochamber. In this experiment, different test protocols are applied that differ, for example, in the programming procedure (cold drawing at $T<T_{trans}$ or temporarily heating up of the test piece to $T>T_{trans}$) or in the control options (stress or strain controlled). A single cycle includes programming the test piece and recovering its permanent shape. A typical test protocol is as follows: first, the test piece is heated up to a temperature T_{high} above the switching temperature T_{trans} and is stretched to the maximum strain ε_m. In the case of thermoplasts it is important not to exceed the highest thermal transition T_{perm} which would cause the polymer sample to melt. The sample is cooled down below the transition temperature T_{trans} under a constant strain ε_m to a temperature T_{low}, thus fixing the

temporary shape. Retracting the clamps of the tensile tester to the original distance of 0% strain causes the sample to bend. After heating the sample up to $T_{high}>T_{trans}$, it contracts and the permanent shape is recovered. The cycle then begins again.

The result of such a measurement is usually presented in a ε-σ curve (Figure 43 a; σ = tensile stress). This is the reason for this test protocol being called a "two-dimensional measurement". Figure 43 represents schematic curves. Different effects can result in changes to the curve, particularly when the stretched sample is cooled down (position 2 in Figure 43 a). Among others, the following effects play a role in these changes: differences in the expansion coefficient of the stretched sample at temperatures above and below T_{trans} as a result of entropy elasticity (see Figure 41), as well as volume changes arising from crystallization in the case of T_{trans} being a melting point.

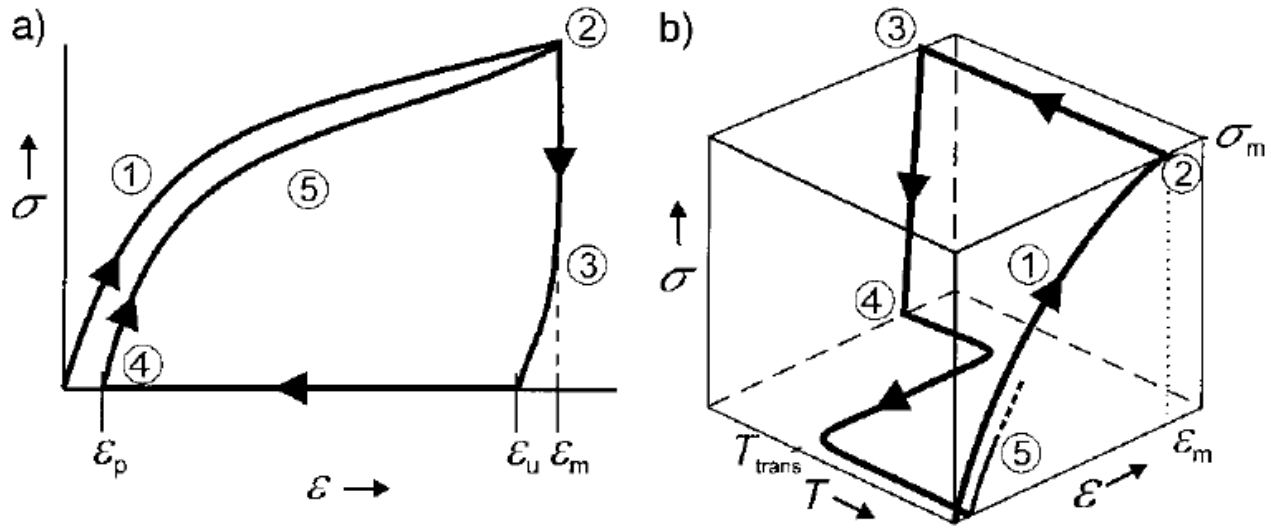

Figure 43 Schematic representation of the results of the cyclic thermomechanical investigations for two different tests: a) ε-σ diagram: 1 – stretching to ε_m at T_{high}; 2 – cooling to T_{low} while ε_m is kept constant; 3 – clamp distance is driven back to original distance; 4 – at ε = 0% heating up to T_{high} ; 5 – start of the second cycle. b) ε-T-σ diagram: 1 – stretching to ε_m at T_{high} ; 2 – cooling down to T_{low} with cooling rate k_{cool} = dT/dt while ε_m is kept constant; 3 – clamp distance is reduced until the stress-free state σ = 0 MPa is reached; 4 – heating up to T_{high} with a heating rate k_{heat} = dT/dt at σ = 0 MPa; 5 – start of the second cycle.

In addition to the elastic modulus $E(T_{high})$ at T_{high} , which can be determined from the initial slope in the measurement range 1 (Figure 43 a), the elastic modulus of the stretched sample at T_{low} can also be determined from the slope of the curve at 3 (Figure 43 a). The important quantities to be determined for describing the shape-memory properties of the material at a strain ε_m are the strain

recovery rate R_r and the strain fixity rate R_f. Both can be determined according to equations (1.35), (1.36), and (1.37) from cyclic, thermomechanical measurements.

The strain recovery rate R_r quantifies the ability of the material to memorize its permanent shape and is a measure of how far a strain that was applied in the course of the programming $\varepsilon_m - \varepsilon_p(N-1)$ is recovered in the following shape-memory transition. For this purpose the strain that occurs upon programming in the N^{th} cycle $\varepsilon_m - \varepsilon_p(N)$ is compared to the change in strain that occurs with the shape memory effect $\varepsilon_m - \varepsilon_p(N)$:

$$R_r(N) = \frac{\varepsilon_m - \varepsilon_p(N)}{\varepsilon_m - \varepsilon_p(N-1)} \tag{1.35}$$

$\varepsilon_m - \varepsilon_p(N-1)$ and $\varepsilon_m - \varepsilon_p(N)$ represent the strain of the sample in two successively passed cycles in the stress-free state before yield stress is applied. The total strain recovery rate $R_{r,tot}$ is defined as the strain recovery after N passed cycles based on the original shape of the sample [Eq. (5)].

$$R_{r,tot}(N) = \frac{\varepsilon_m - \varepsilon_p(N)}{\varepsilon_m} \tag{1.36}$$

The strain fixity rate R_f describes the ability of the switching segment to fix the mechanical deformation which has been applied during the programming process. It describes how exactly the sample can be fixed in the stretched shape after a deformation to ε_m. The resulting temporary shape always differs from the shape achieved by deformation. The strain fixity rate R_f is given by the ratio of the strain in the stress-free state after the retraction of the tensile stress in the Nth cycle $\varepsilon_u(N)$ and the maximum strain ε_m:

$$R_f(N) = \frac{\varepsilon_u(N)}{\varepsilon_m} \tag{1.37}$$

As indicated in Figure 43, the first few cycles can differ from each other. The curves become more similar with an increasing number of cycles. The process of deformation and recovery of the permanent shape becomes highly reproducible. The changes in the first few cycles are attributed to the history of the sample, thus, processing and storage play an important role. During the first cycles a reorganization of the polymer on the molecular scale takes place which involves deformation in a certain direction. Single polymer chains arrange in a more favorable way in regard to the direction of deformation. Covalent bonds may be broken during this process.

An important variable that cannot be determined by a two-dimensional measurement is T_{trans}. In this respect, the three-dimensional test record is interesting, and is shown schematically in Figure 43 b. In contrast to the two-dimensional measurement, the sample is cooled down in a controlled way at a strain of ε_m and a constant tensile stress ε_m. The change in strain in this region is influenced by the temperature dependence of the coefficient of thermal expansion of the stretched polymer and volume effects based on the thermal transition at T_{trans} (for example, a crystallization process). Having reached T_{low}, the strain is driven back until a stress-free state is reached. The sample is then heated up to T_{high} in a controlled way. In the course of this experiment the tensile stress is kept constant at 0 MPa, which means that the clamps follow the movement of the test piece. The mechanical movement occurring in the course of the shape-memory effect is recorded as a function of the temperature. Both the temperature interval as well as T_{trans} in which the shape-memory effect takes place can be determined from the interpretation of the ε-T plane of the σ-T-ε diagram.

1.3.3 Application of Shape-Memory Polymers

Since shape-memory effects in polymeric materials were first discovered, many applications have been developed for these unique materials that allow triggered responses. Besides traditional applications such as heat shrinkable tapes and tubes made with radiation-cross-linked polyethylene, these materials have also been used for information storage that can allow thermally reversible recording, (Ookubo 1995), temperature sensors, (Adachi, et al. 1990), and actuators, (Seward e Krulevitch 2002). However, our literature search found that recent applications are mainly focused on medical areas, such as biodegradable sutures (Landlein e Langer 2002), actuators (Sharp, et al. 2006), catheters, and smart stents (Figure 44 and Figure 48), (Gall, et al. 2005). Smart stents match mechanical properties of artery which is very complex thanks to its adjustable shape. Moreover, SMP foams for treating aneurysms (chemically blown, open cell foam, Figure 45) and SMP baskets for catching large emboli (micro injection molded, Figure 46) have been developed. Another kind of SMP device in the field are SMP intravenous syringe cannulae (Figure 47): when injection is performed the needle keeps its rigid state. Once under the skin it becomes flexible, resulting in greater comfort.

Figure 44 SMP stent, dip coated and laser machined.

Figure 45 SMP foam for treating aneurysms.

Figure 46 Basket for catching large emboli (micro-injection molded).

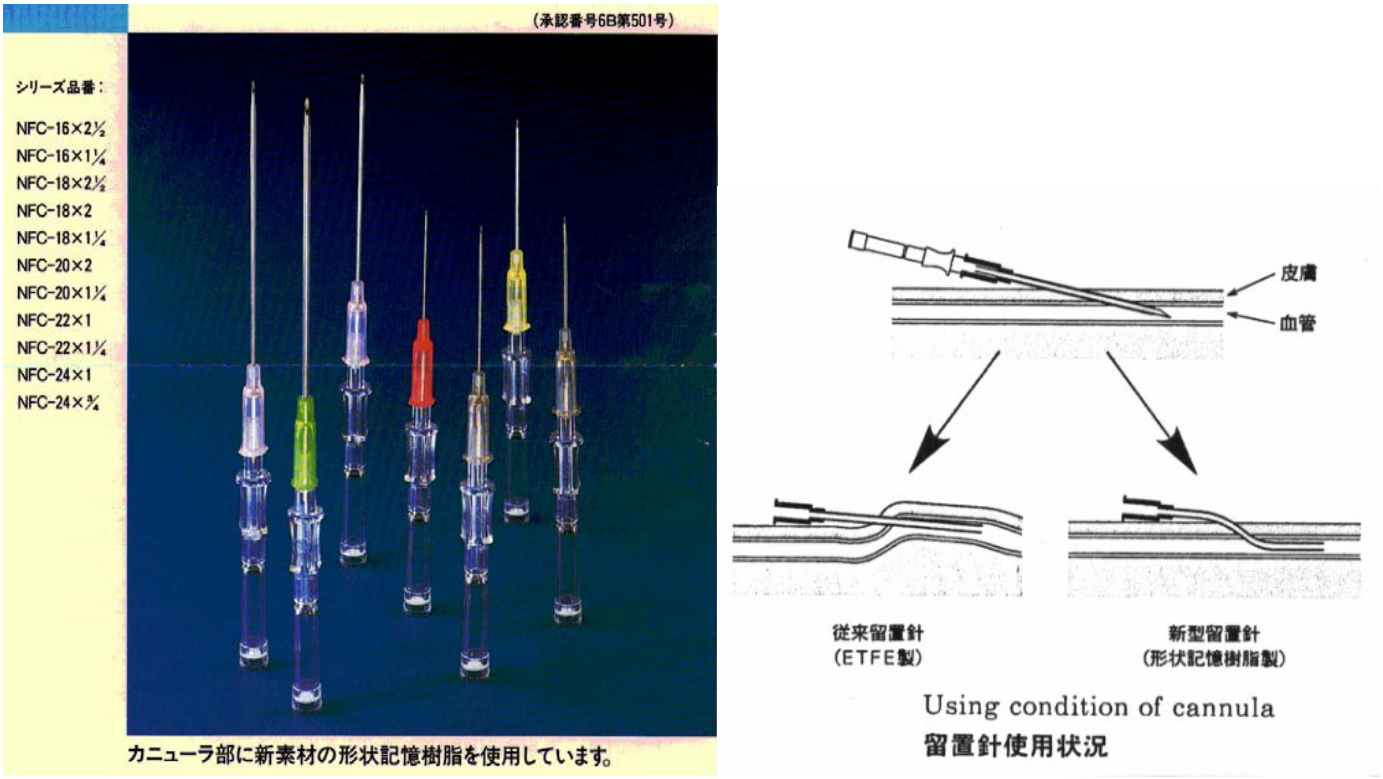

Figure 47 Intravenous syringe cannula, copyright 2007 Diaplex Co.

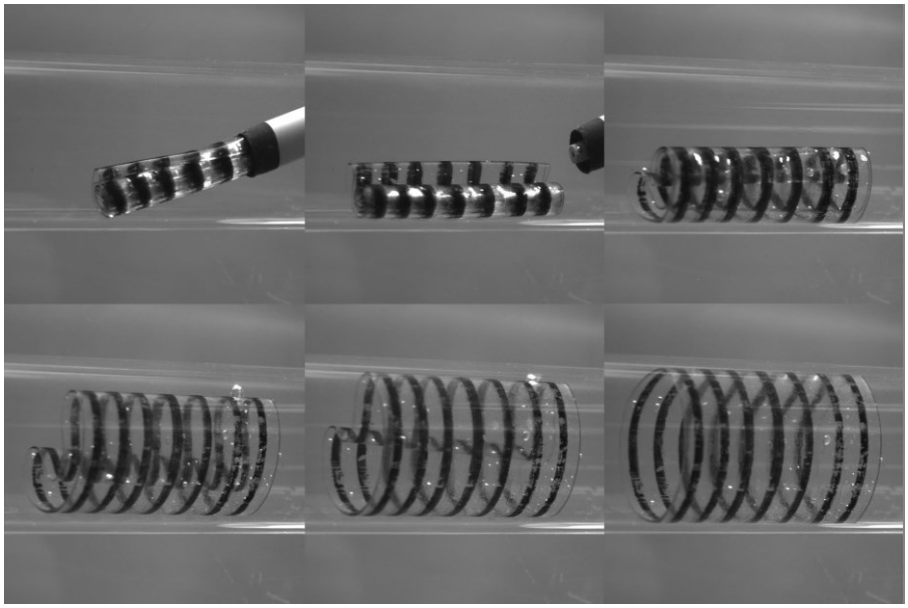

Figure 48 Deployment of a SMP stent from a catheter.

Orthodontic applications (Mather, Liu e Burstone 2005), of class I and class II SMPs have been elaborated, focusing on devices that simplify ligation and other time-intensive orthodontic procedures (Figure 49). The medical applications of shape-memory polymers are of great interest

due to a combination of biocompatibility with their wide range of tunable stiffness ($0.01 < E < 3$ GPa), tailorable transition temperatures with sharp transition zones, fast actuation, large shape deformation and complete recovery, and elastic properties of the materials.

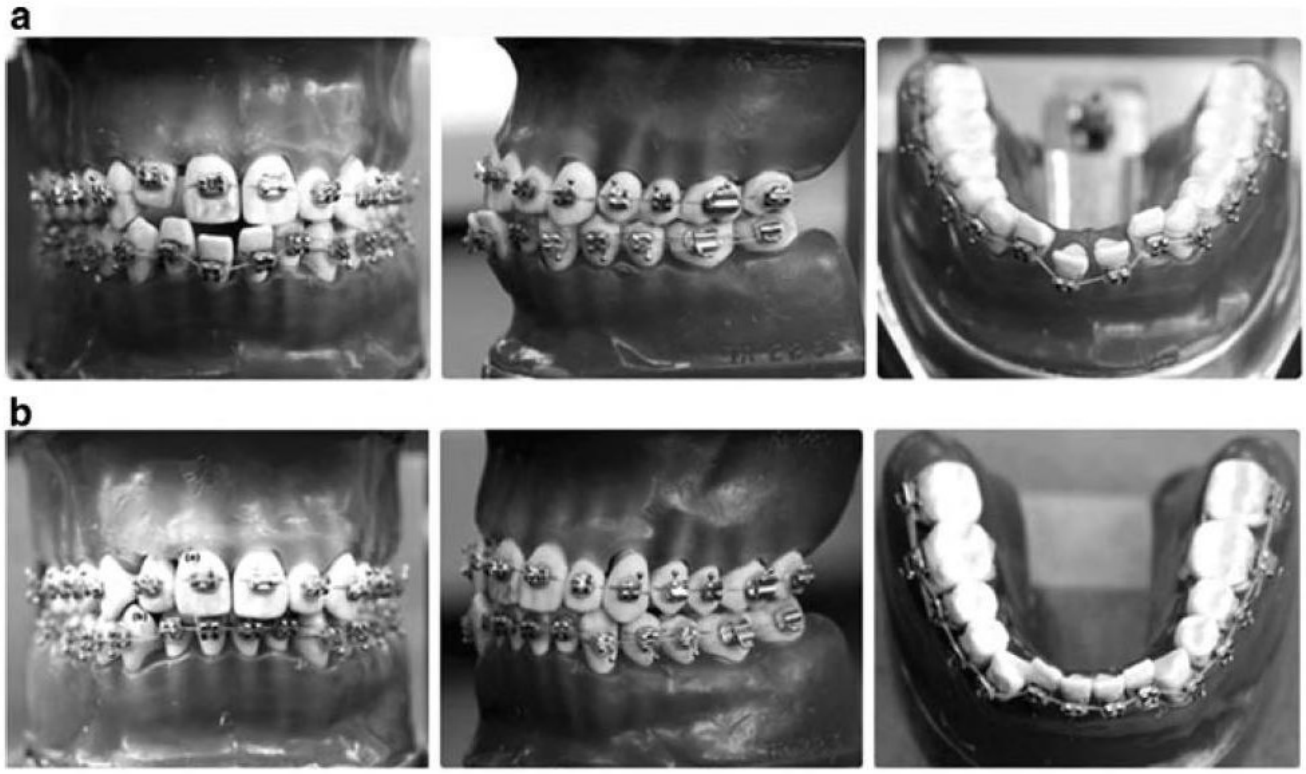

Figure 49 An SMP arch-wire was stretched to 50% strain and installed in a dental mode misaligned teeth (a). After heating above T_{trans} to 50°C, the teeth were corrected within 1h (b).

A. Lendlein and R. Langer fabricated a self-tightenable biodegradable suture from a biodegradable shape-memory thermoplastic monofilament fiber (Landlein e Langer 2002). This fiber was extruded through a 1 mm rod die, prestretched above the critical temperature, and fixed to a stretched temporary shape by cooling below its critical temperature. When used, the suture can be loosely connected and then heated above critical temperature to trigger the shape recovery and tighten the suture. A series of snapshots were presented in their paper, showing that at 40 °C, only 20 s were required to completely tighten this suture (Figure 50(a)).

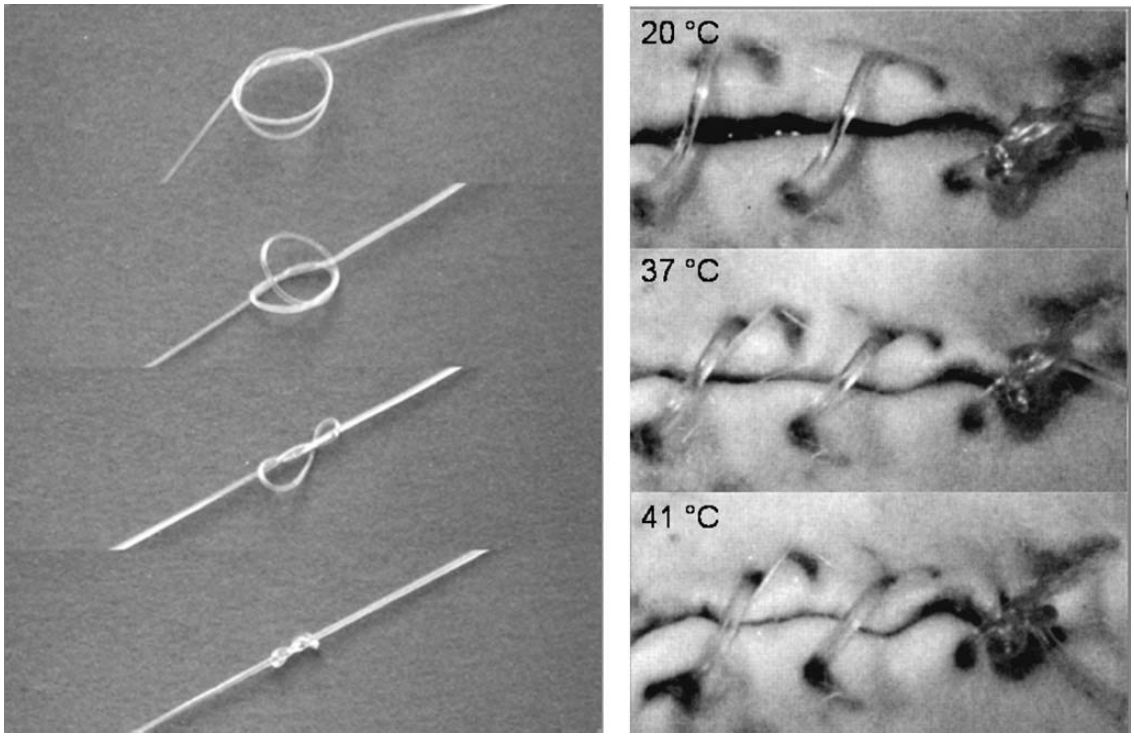

Figure 50 (a) A smart surgical suture self-tightening at elevated temperatures (left). A thermoplastic shape-memory polymer fiber was programmed by stretching to about 200% at a high temperature and fixing the temporary shape by cooling. After forming a loose knot, both ends of the suture were fixed. The photo series shows, from top to bottom, how the knot tightened in 20 s when heated to 40°C. (b) Degradable shape-memory suture for wound closure (right). The photo series from the animal experiment shows (top to bottom) the shrinkage of the fiber while the temperature increases from 20 to 41 °C.

An additional set of experiments was performed to test the feasibility of this concept by extruding some monofilaments out of this material, sterilizing them, stretching under sterile conditions at controlled stress, and subsequent thermal quenching to fix the temporary shape. Such programmed sutures were then loosely stitched through incised rat belly tissue and the abdominal muscle. When heated to 41 °C, shape recovery was triggered and the suture tightened by itself (Figure 50(b)). The authors claim that when stretched to 200%, an impressive force of 1.6 N could be generated upon shape recovery. Another example of a biomedical application is a microactuator made from an injection-molded shape-memory thermoset polyurethane that was used to remove blood vessel clots. The permanent shape of the SMP microactuator was a cone-shape coil, which could be elongated to a straight wire and fixed before surgery. The wire was then delivered distally to an occlusion through a catheter, where triggering the shape recovery using optical heating restored the original coil shape. After thermal triggering, both the microactuator and the thrombus could be removed from the vessel, restoring the blood flow. Further work on new materials and experimental models have appeared recently.

2 A COMPARATIVE ASSESSMENT OF TWO CONSTITUTIVE MODELS FOR SUPERELASTIC SHAPE-MEMORY ALLOY WIRES

The main objective of this chapter is to assess a computational tool which is suitable to be used in the structural analysis of structures retrofitted with SMA seismic protection devices, on the basis of the experimental results obtained during an experimental campaign on commercial NiTiNOL wires.

2.1 Introduction: state-of-the-art of the modelling approaches of SMA behavior

From 1980 up to now, constitutive modeling of shape memory alloys has been an active research subject. The resulting models can be in general classified into three major categories:

Macroscopic phenomenological models (macro-models): Macroscopic phenomenological models are built on phenomenological thermodynamics and/or directly curve fitting experimental data. Many are based on the common phase diagram of SMA transformation where the transition regions of martensite to parent phase or parent phase to martensite transformation are determined experimentally and plotted in stress-temperature space. Researchers typically use the martensite volume fraction as an internal variable and different mathematical functions to describe a smooth transition. These kinds of models are generally more suitable for engineering applications due to their simplicity and fast computations, but they can only describe the global mechanical response while all the microscopic details are ignored; because the phase diagram is built on experimental data, the models are also quite accurate. Based on continuum thermodynamics with internal variables, several three-dimensional macroscopic phenomenological models have been proposed, in the literature, with success.

Microscopic thermodynamics models (micro models): Micro-models focus on the description of micro-scale features, such as nucleation, interface motion, twin growth, etc. (Abeyaratne e Knowles 1990), (Ball e James 1987). They are extremely helpful to understand the fundamental phenomena, but are often difficult to apply for engineering applications. They do not take into account phase volume fractions as a-priori internal variables, but as a consequence of interface movements. More details can be found, e.g., in (Falk, Model free-energy, mechanics and thermodynamics of shape memory alloys 1980), (Falk 1983) and (Ball e James 1987).

Micro-mechanics based macroscopic models (micro-macro models): The essence of the micro-mechanics-based models is in the modeling of a single grain and further averaging the results over a representative volume element (RVE) to obtain a polycrystalline response of the SMA. Such models have been presented in the literature by different researchers. As an example, (Patoor, Eberhard e Berveiller, Micromechanical modelling of superelasticity in shape memory alloys 1996) have modeled the behavior of a polycrystalline SMA by utilizing the model for single crystals and using the self-consistent averaging method to account for the interactions between the grains. A micro-mechanical model for SMAs which is able to capture different effects of SMA behavior such as superelasticity and shape memory effect has been presented by Sun and Hwang (Sun e Hwang 1993). In other words, this group of models uses thermodynamics laws to describe the transformation and utilizes micro-mechanics to estimate the interaction energy due to the transformation in the material, which is a key factor in the transformation mechanism. Appropriate formulation of this interaction energy is very important and requires knowledge of the micro-structural evolution. Several assumptions at the micro-structure level is made to approximate the interaction energy (Fischer e Tanaka 1992), (Gao, Huang e Brinson, A multivariant micromechanical model for SMAs 2000); (Huang e Brinson, A multivariant model for single crystal shape memory alloy behavior 1998); (Huang, Gao e Brinson 2000); (Lexcellent, Goo, et al. 1996); Patoor et al., (Patoor, Eberhardt e Berveiller 1994); (Sun e Hwang 1993). These models appear to have good predictive capabilities and moreover, in some cases they are also able to successfully reproduce reorientation and detwinning of martensite variants (Gao e Brinson 2002); (Huang e Brinson 1998); (Marketz e Fischer 1996); (Thamburaja, Constitutive equations for martensitic reorientation and detwinning in shape-memory alloys 2005). However, they employ a large number of internal variables which makes computations time intensive, resulting in a difficult application for engineering purposes. One can summarize the advantages and disadvantages of the different approaches by the following general remarks. First, the models developed with the macroscopic approach are generally easy to use and allow quick computations but they are less predictive. Concerning the micro-macro approach, it is much more predictive, but a large number of internal variables is introduced. That is the reason why micro-mechanical models still remain difficult to be used in structural engineering applications. The micro-level approach is more suitable for the development of fundamental studies than for the quantitative description of macroscopic behaviors.

2.1.1 Literature review: SMA phenomenological models

2.1.1.1 Models without internal variables

In such models the material behavior is described by strain, stress, temperature, and entropy without the introduction of quantities representing phase mixture.

Polynomial potential models

In this approach, constitutive information are provided by a polynomial free energy function whose partial derivatives provide constitutive equations for strain (or stress) and entropy. In 1980, Falk proposed a Landau-Devonshire like free energy function based on the analogy between SMA uniaxial stress-strain curves and the electric field-magnetization curves of ferromagnetic materials. In his work, Non-monotone stress-strain curves were obtained, and the unstable negative slope part was interpreted as the occurrence of the phase transition. The actual pattern followed during the transformation was assumed to proceed at constant stress. The particular form of the Landau-Devonshire free energy accounts for the temperature dependence of the isothermal stress-strain behavior. We can address (Falk 1980); (Falk 1983); (Falk e Konopka 1990) as models in this group. The main advantage of these models is their simple form, but they are not able to model complicated behavior of the material as well as they do not describe accurately the evolutive nature of the processes.

Hysteresis models

Hysteresis models seek to reproduce experimentally observed curves that involve high nonlinearity and complex looping. They have been widely used in several fields, in particular for magnetic materials. In this approach, constitutive equations are proposed directly on the basis of their mathematical properties, often without explicit focus on their link with the underlying physical phenomena of interest. Two main algorithm classes have received special attention in the context of SMA phase transformation. The first one is based on tracking sub-domain conversion/reversion and lead to integral based algorithms. The most common of these is known as the Preisach algorithm and it has been used to describe uniaxial isothermal pseudo-elastic stress-strain SMA response (Huo 1989); (Ortin 1992). The second algorithm class involves differential equations with

separate forms for driving input increase and driving input decrease. Differential equations of Duhem-Madelung form have been used to model SMA phase fraction evolution during the thermally induced transformation (Ivshin e Pence, A constitutive model for hysteretic phase transition behavior 1994); (Likhacev e Koval 1992).

2.1.1.2 Models with internal variables

The key feature of this approach is to introduce appropriate internal variables describing the material internal structure. Internal variables, along with a set of mechanical and thermal control variables, define a collection of state variables. A general thermodynamical consistent approach then allows to derive evolution equations for the internal variables. Mechanical control variables can be either strain or stress, while thermal control variables can be either temperature or entropy. The internal variables typically include one or more phase fractions and/or macroscopic transformation strains. The first application of such an approach to SMAs seems to be due to (Tanaka e Nagaki, A thermomechanical description of materials with internal variables in the process of phase transitions 1982), where internal variables are employed to describe the development of the underlying phase mixture. The models based on internal variables can furthermore be categorized into two groups:

Models with assumed phase transformation kinetics

Models with assumed phase transformation kinetics consider the involved martensitic volumetric fraction as internal variable, which is expressed as function of current values of stress and temperature. Several authors propose different functions to describe the volumetric fraction evolution. The model firstly developed by Tanaka and coworkers (R. Lin, et al. 1994); (K. Tanaka 1986); (K. Tanaka 1990); (Tanaka e Iwasaki 1985); (Tanaka e Nagaki 1982); (Tanaka, Nishimura, et al., Phenomenological analysis on sbloops and cyclic behavior in shape memory alloys under mechanical and/or thermal loads 1995); was originally conceived to describe three-dimensional problems involving SMAs. Nevertheless, its implementation was naturally restricted to the one-dimensional context. The authors considered exponential functions to describe phase transformations. Since an exponential function was adopted, there should be an extra consideration for the phase transformation final bounds. (Boyd e Lagoudas 1994) rewrote Tanaka's original model, for a three-dimensional theory, while the relations used to describe phase transformation

evolution remained the same as in Tanaka's model. (Liang e Rogers 1990) presented an alternative evolution law for the volumetric fraction based on cosine functions. The authors also developed a three-dimensional model, in which they suggest that phase transformations are driven by the associated distortion energy. (Brinson 1993) offered an alternative approach to the phase transformation kinetics, in which, besides considering cosine functions, the martensite fraction was split into two distinct quantities, the temperature-induced martensite and the stress-induced martensite. The author also considered different elastic moduli for austenite and martensite.

Models with internal variable(s) evolution equation(s)

These models are developed within a more rigorous thermodynamical continuum approach. The theory is then composed of physical laws, i.e. the constitutive equations that characterize the features typical of each material, and material behavior requirements that ensure thermo-dynamical process restrictions. Constitutive information are specified by two kinds of relations:

1. state equations for the entities conjugate to control variables. These can be formulated directly or obtained as partial derivatives of a suitable free energy function after enforcing the Clausius-Duhem inequality for every process. If heat conduction is to be included, then a constitutive equation relating temperature gradient and heat u_x (usually the Fourier equation) is also required;

2. kinetic equations for the internal variables. In view of phase transformation hysteresis, these equations generally depend on the material past history.

Standard practice in most internal variable models is to specify this dependence through equations relating the rates of the internal variables to the current state and its time derivatives. The internal state then follows from the solution of differential equations in time. Although, sometimes employing formalisms are quite different, several models fitting into this basic framework have been proposed to describe SMA behavior. While most of the efforts are limited to modeling one-dimensional behavior of the material, in the last decade, motivated by extensive engineering applications as well as available multiaxial experimental data, considerable attention has been devoted into developing threedimensional constitutive models. Nowadays, there are varieties of 3D phenomenological models trying to properly capture different aspects of SMA behaviors. Compared with the extensive efforts in constitutive modeling, there are not considerable publications in the corresponding numerical implementation. This fact is partially due to unavailability of proper constitutive models suitable for the corresponding numerical implementation. High nonlinear behavior of material and complicated structure of models -

compared to plasticity - are other obstacles in numerical implementation. It is generally accepted in the literature that in order to reach a computational tool for design and analysis of SMA devices and structures, 3D phenomenological constitutive models in the framework of continuum thermodynamics with internal variables should be developed.

2.1.1.2.1 Phenomenological models based on continuum thermodynamics with internal variables between 1980-1995

After the discovery of Nitinol in 1963 and first commercial application as F-14 coupling in 1971, it seems that the first book on shape memory alloys appeared in 1975 by Perkins which presented some metallurgical aspects of SMAs (Perkins 1975). As we mentioned in previous sections, most of the works in the beginning of 1980 is devoted to micro-modeling or simple phenomenological ones. In a series of papers, Muller and his colleagues developed a systematic thermodynamic theory of pseudo-elasticity and presented a plausible one-dimensional theory which is very useful in understanding the physics of most phenomena in the material (Hu e Müller 1993); (I. Müller, Pseudoelasticity in shape memory alloys - an extreme case of thermoelasticity 1986); (I. Müller 1989); (Müller e Wilamanski 1980); (Müller e Xu 1991). (Tanaka e Nagaki 1982) were evidently the first researchers who discussed martensitic transformations within the context of continuum thermodynamics with internal variables. The phase transformation is basically governed by the minimization of the free energy. The energy equation and Clausius-Duhem inequality were used to describe the hysteresis associated with the phase transformation (P. Lin, et al. 1994); (K. Tanaka 1986); (Tanaka e Iwasaki 1985); (Tanaka, Nishimura, et al. 1995). In 1987, another book on shape memory alloys appeared (Funakubo 1987). In the setting of 3-D media, (Bondaryev e Wayman 1988) proposed a phenomenological model inspired by the classical plasticity theory. Motivated by the work of (K. Tanaka 1986), (Liang e Rogers 1990) proposed a model with cosine kinetics for martensite volume fraction. In 1990, there were several motivations toward SMA applications, e.g. various medical applications were introduced. Moreover, the first comprehensive book on engineering applications of SMAs appeared in 1990 (Duerig et al., 1990). Inspired from several SMA medical and industrial applications, it seems that, after 1990, there was more motivation toward SMA three-dimensional macro-modeling (e.g., (Raniecki, Lescellent e Tanaka, Thermodynamic model of pseudoelastic behaviour of shape memory alloys 1992), (Grasser e Cozzarelli 1994), (Boyd e Lagoudas 1994), (Ivshin and Pence 1994) and (Raniecki e Lexcellent 1994)). However, one-dimensional modeling yet remained interesting due to the use of SMA wires

in smart composites and similar applications e.g., for actuators; we can refer to the work by Brinson in 1993 where she introduced the decomposition of the martensite volume fraction into stress-induced and temperature-induced parts. In 1995, two comprehensive experimental studies published which affected considerably the SMA modeling after on; the work by (Shaw e Kyriakides, Thermomechanical aspects of NiTi 1995) presented several aspects of thermo-mechanical behavior of NiTi wires and addressed questions concerning local versus average measures of strains, spurious measurements of residual strains and dependence of the heat transfer conditions on the stress-strain curves. The work by (Sittner, Hara e Tokuda, Experimental study on the thermoelastic martensitic transformation in shape memory alloy polycrystal induced by combined external forces 1995), for the first time, presented a comprehensive multiaxial study on Cu-Al-Zn-Mn SMAs.

2.1.1.2.2 Phenomenological models based on continuum thermodynamics with internal variables after 1995

Starting 1996, there was more motivation toward SMA three-dimensional modeling due to: it was generally accepted that continuum thermodynamics with internal variable is a proper tool for effective SMA 3-D macro-modeling, there was extensive multidimensional experimental data under proportional and non-proportional loadings and there was much interest in medical and industrial applications. However, due to simplicity in one-dimensional models and applications to smart composites (in a wire form), the one-dimensional modeling yet remained active, with focus on secondary effects, e.g., progressive accumulated strain in (wire) actuator applications, different material properties for austenite and martensite and so on. Therefore, it was expected that the future research to be directed toward proposing accurate 3D macro models and studying material behavior under multidimensional loading (e.g., phase transformation surface) and reporting more experimental data. From a different aspect, engineering applications yet needed a proper computational tool in design and simulation of SMA devices, specifically for biomedical applications. Accordingly, developing a 3D SMA model to consider many SMA complicated behaviors does not mean that it is an effective SMA model in engineering applications. To this end, besides research activities in SMA modeling, it was necessary to decide on which behaviors should be included in modeling according to engineering requirements as well as corresponding computational tool development. In the following, we focus on 3D macro-modeling, experimental studies and numerical implementations of SMA models. We remark that we only focus on the

works which present a new modeling approach or a new model, skipping the works focused just on secondary effects modeling. Following the work by (Raniecki e Lexcellent 1994), (Leclercq e Lexcellent 1996) presented a macroscopic description for the simulation of the global thermo-mechanical behavior of SMAs; two internal variables were taken into account, i.e., the volume fraction of self-accommodating (pure thermal effect) and oriented (stress-induced) product phases. (Lubliner e Auricchio, Generalized plasticity and shape memory alloys 1996) applied the generalized plasticity theory (Lubliner 1984) to SMAs and proposed a three-dimensional model. In 1997, based on a plasticity-like return mapping method, (Masud, Panahandeh e Auricchio 1997) presented a finite deformation finite element model for the pseudo-elastic response of shape memory alloys under stress loading-unloading conditions at constant temperature. Similarly, a plasticity-like finite element model for super-elastic SMA structures was proposed by (Trochu e Y.Y. 1997). (Sittner, Takakura, et al. 1996) presented several experimental data on thin wall tubes made of CuAlZnMn subjected to combined axial and torsional loads in low temperature martensite state (SME). With the aid of developing a computational tool to be used during the design of SMA-based devices, (Auricchio, Taylor e Lubliner 1997) and (Auricchio e Taylor 1997) proposed constitutive models in small and finite strain regimes, respectively, and implementing in the FEM, they solved several boundary value problems (BVP). (Souza, Mamiya e Zouain 1998) proposed a model which can describes the main features of polycrystalline shape memory materials in the setting of 3D media. It had been conceived within the framework of generalized standard materials (Maugin 1992), that internal variables were defined to describe the phase transformation processes. (Raniecki e Lexcellent 1992) generalized the thermodynamic theory of pseudo-elastic behavior of SMAs to account for the large differences between hysteresis loops in tension and compression. In 1998, Otsuka and Wayman published a book on shape memory materials, with focus on metallurgical aspects (Otsuka e Wayman 1998). (Qidwai e Lagoudas 2000) investigated various transformation functions and proposed a generalized type transformation function. (Auricchio 2001) presented a robust integration algorithm for a 3D finite-strain SMA model. Also, (Liew, et al. 2002) simulated multidimensional super-elastic behavior of shape memory alloys via nonlinear finite element method. (Thamburaja e Anand 2002) presented a model for super-elastic behavior in tension-torsion of an initially textured NiTi shape memory alloy. (Lexcellent, Vivet, et al. 2002) determined the initial surface of phase transformation under biaxial loading in some polycrystalline shape memory alloys both experimentally and numerically. (Auricchio e Petrini 2002) improved the model proposed by (Souza, Mamiya e Zouain 1998) and obtained a robust integration algorithm. In another work, (Auricchio e Petrini 2004a) included the asymmetric behavior and simulated several SMA-devices. Moreover, the same model was extended to capture thermo-

mechanical coupling effects in (Auricchio e Petrini 2004b). (Helm e Haupt 2003) have proposed a model to represent the multiaxial material behavior of shape memory alloys which is able to represent the main effects of shape memory alloys; i.e., the one-way shape memory effect, the two-way shape memory effect due to external loads, the pseudo-elastic and pseudo-plastic behavior as well as the transition range between pseudo-elasticity and pseudo-plasticity. (Bouvet, Calloch e Lexcellent 2004) have proposed a phenomenological model, taking into account the tension-compression asymmetry effect, the temperature effect, the return point memory effect and the influence of the loading path non-proportionality on the SMA mechanical behavior. (Terriault, Viens e Brailovski 2006) have proposed a non-isothermal finite element modeling of SMA actuators using the commercial software ANSYS. (Müller e Bruhns 2006) have proposed a thermodynamic finite strain model to describe the pseudo-elastic response of shape memory alloys. The model is based on a self-consistent Eulerian theory of finite deformations using the logarithmic rate. Based on a modified phase transformation diagram, (Popov e Lagoudas 2007) proposed a 3D constitutive model for polycrystalline shape memory alloys. (Thiebaud, et al. 2007) have presented an implementation of a phenomenological model based on the so-called RL model (Raniecki e Lexcellent 1998) in a finite element code called COMSOL. (Panico e Brinson 2007) have proposed a model that accounts for the effect of multiaxial stress states and non-proportional loading histories. The model is able to account for the evolution of both twinned and detwinned martensite. Moreover, this model accounts for the reorientation of the product phase according to loading direction. Within the framework of generalized standard materials with internal constraints, (Zaki e Moumni 2007) have used the martensite volume fraction and the martensite orientation strain tensor as internal variables to account for self-accommodation, orientation and reorientation of martensite, as well as super-elasticity and one-way shape memory. In another work, (Moumni, Zaki e Nguyen 2008) have simulated the pseudo-elastic response of SMAs as well as the one-way shape memory effect. In addition, they have compared the results with the experimental data reported in (Sittner, Hara e Tokuda 1995) and (Takuda, Takakura e Sittner 1999). Extending the small-strain model by (Helm e Haupt 2003), (Reese e Christ 2008) have recently suggested a finite strain phenomenological model and implemented into finite element formulation to simulate NiTi stents. After around 15 years of research in SMA modeling, Lagoudas published the first book on constitutive modeling of shape memory alloys (Lagoudas 2008).

2.1.2 Literature review: microscopic thermodynamic models with dynamic phase transition

2.1.2.1 Sharp interface models

One of the most cited works on modeling of SMAs is (Abeyaratne e Knowles 1993). They were one of the first to investigate explicitly the nucleation of a phase and its propagation in SMAs. They introduce the displacement gradient as a field and construct Helmholtz free energy function based on trilinear stress-strain relation at fixed temperature. The trilinear stress-strain function is integrated to obtain stress varying part of Helmholtz function. Since strain is used as an independent variable, the temperature dependence of strain is brought through specific identity of thermodynamics which is equivalent to the Clausius-Clapeyron relation. Nucleation criterion is expressed as a jump or discontinuity in the Gibbs free energy. This manifests as a generally non-zero traction or driving force across the interface. Driving traction equation is obtained using the stability criterion similar to C-D inequality. Explicit kinetic relation and nucleation criterion are developed. Kinetics developed here has form ś =V(f,θ), based on classical notion of thermally activated phase transitions. The velocity ś of the phase boundary is the macroscopic measure of the net rate at which the atoms change from the low-strain phase to the high-strain phase and is taken to be the difference betwen the average rates associated with the two atomic transitions. This kinetics takes the form of product of error functions and hyperbolic sine. This implies that the rate has monotonic increasing nature, unlike that obtained from cosine kinetics for the phase fraction. Exploiting the smallness of driving traction due to the quasistatic and reversible nature of the process, the kinetics is then linearized in temperature. The nucleation criterion is derived from Gibbs free energy and the sign of the latent heat is used to distinguish the forward and reverse transformation direction. They also discuss how the model parameters concerning nucleation can be derived from Ms and As. Finish of transformation depends upon the process. They investigate both SE and SME at constant stress. They also show the relationship between the phase boundary velocity and driving traction at various temperatures. (Abeyaratne e Knowles 1997) extended this approach to solve a BVP wherein a CuAlNi SMA single crystal is subjected to impact loading. This is posed as a Riemann problem, which consists of a conservation law together with a piecewise constant field having a single discontinuity. It may be noted that the Riemann problem is useful in investigating hyperbolic partial differential equations because properties like shocks and rarefaction waves appear as characteristics in the solution. It also yields an exact solution to complicated, non-linear equations like the Euler equation. They show the relationship between the impact velocity and the phase front velocity for different values of impact angles representing

different tangential and longitudinal velocities. (Abeyaratne e Kim 1997) generalized this approach to include effects due to cyclic loading. An additional internal variable is introduced to track the changes due to defects that get precipitated during cycling. These defects are shown to ease formation of transformation fronts. A time discrete Ginzburg-Landau formalism is used by (Wang e Khachaturyan 1997) to build 3-D stochastic kinetic field model of 'improper' martensitic transformations which explicitly takes into account the transformation induced elastic strain. The model is able to predict the major structural characteristics of martensite during the entire MT process including nucleation, growth and eventually formation of internally twinned plates. Numerical simulations are performed for a generic cubic-tetragonal martensitic transformation in a single crystal ZrO2 which is elastically isotropic and homogeneous. The simulation results are in good agreement with experimental observations. This work has led to the development of several models for the dynamics of MT in SMAs.

2.1.2.2 Diffuse interface models

Models with sharp interface have computational difficulties in tracking multiple moving interfaces. Hence as an alternative, diffuse interface theories are used to investigate the propagation characteristics. As the name suggests the sharp jump like interfaces are treated in a weaker set-up wherein the changes in properties are assumed to vary in a more continuous and diffuse manner across the phase boundaries. Hence, theories like phase field theory are used. (Vedantam 2006) proposes a diffuse interface theory for SMA based on the formalism proposed by (Fried e Gurtin 1994) using an order parameter field which has rapid, but continuous change across phase boundary. Evolution of this order parameter is specified through an equivalent Ginzburg-Landau equation. In addition to the strain energy, latent energy and exchange energy, the free energy includes gradient energy due to the phase jump. Gradient energy penalizes the presence of interfaces. An additional material parameter is introduced as constant of proportionality in the gradient energy term, which needs experimental evaluation. Exchange energy reflects the energetic preference for each phases. One of the key aspects of this approach is the notion of micro-force which can be treated as generalized force at the microscale with following characteristics.

1. Micro-force balance supplements the usual balance laws of linear and angular momentum
2. Micro-forces are distinct from classical Newtonian forces and perform work against changes in order parameters

3. Micro-force balance supplied with an appropriate constitutive equation provides an evolution equation for the order parameter.

For a 1-D SMA rod, momentum balance equation and micro-force balance are coupled and cast as a system of nonlinear partial differential equations which is solved using finite difference scheme. The model is able to capture the nucleation peak in the stress-strain response. Also, the model can capture effects due to the rate of elongation. However, simulation for tracking dynamics of phase transition is investigated giving relevant details. Shaw and coworkers ((Shaw 2002), (Iadicola e Shaw 2002) and (Chang, Shaw e Iadicola 2006)) have studied the effects of nucleation and propagation of transformation fronts. Both experiments and numerical investigations are performed. To capture the diffuse interface in polycrystalline SMA wires, a 1-D model with strain gradient as an additional state variable is developed. The model is especially aimed capturing the Lüder like transformation bands or propagation effects seen in SMAs. Helmholtz free energy is adopted since the experiments are in displacement (strain) control mode. The rate of evolution of the phase fractions has been independently assumed. A 1-D coupled BVP in terms of both thermal and momentum balance equations are formulated and solved to elicit the SMA response. They discuss several aspects that govern the response in terms isothermal and adiabatic effects that alters the nature of hardening. They also discuss the influence of nature of interaction energy on the stability. They state that the nucleation in the macroscale manifests due to loss of stability in the microstructure. Elaborate experiments on wires are used to show the thermal and strain gradients that exist due to transformation and the influence of loading rate on the number and nature of transformation fronts. The complexities observed regarding the nucleation and propagation of transformation fronts even at relatively low strain rates are discussed. As previously stated these models do not cater to several important aspects of MT in sufficient detail to make them flexible for application in wide range of scenarios.

2.1.3 The work of dos Santos and Cismasiu (2010)

(Dos Santos e Cismasiu 2011) analyzed two different constitutive models with respect to their adequateness to be used in numerical simulations for seismic applications. A simple, rate and temperature independent constitutive model proposed by (Fugazza 2003) and a more complex one coupling the mechanical and kinetic laws with a balance equation that considers the thermal effects on the material proposed by Tanaka (Tanaka, Kobayashi e Sato 1986) were taken into account and

their ability to efficiently predict the dynamic behaviour of structures including SMA elements subjected to dynamic loading has been investigated.

Numerical simulations of SDOF passive vibration control devices, comprising superelastic SMA components, were used to compare the efficiency of the two constitutive models. Three superelastic oscillators with one, two and three SMA restitutive elements were subjected to several harmonic loads, characterised by different strain rates and different ambient temperatures. The dynamical response of the devices was compared for the two constitutive models. The numerical model of a railway viaduct with superelastic passive vibration control devices was subjected to several artificially generated seismic actions. This more realistic application was used to test the influence of the constitutive model in the structural response for seismic analysis.

It was shown that the mechanical behaviour of SMAs changes significantly when passing from pseudo-static to dynamic conditions. However, for seismic applications, with frequencies in the range of 0.2 to 4 Hz, the cyclic behaviour of SMAs wires is mainly insensitive to strain rate. Hence, for these conditions, both numerical models produce similar results, once calibrated with dynamic experimental tests. As the simplicity of the strain rate and temperature independent constitutive model makes it more robust and more easy to implement from a computational point of view, this model was suggested as a very appealing option when simulating superelastic seismic passive control for Civil Engineering applications.

2.2 Motivation

In this chapter, following the steps shown in (Rizzoni, et al. 2013) and in (Chiozzi, et al. 2012), we review and compare a model proposed by Kim and Abeyaratne (Kim e Abeyaratne 1995) and a model proposed by Auricchio, Fugazza and Des Roches (Auricchio, Fugazza e DesRoches 2008). The first model belongs to the class of the phenomenological thermodynamic models with internal variable; the second belongs to the class of the sharp-interface microscopic thermodynamic model with dynamic phase transition. The focus is on investigating how the two models compare with experimental data obtained from testing superelastic NiTi wires used in the design of a prototypal anti-seismic device (Indirli e Castellano 2008). After model calibration and numerical implementation, numerical simulations based on the two models are compared with data obtained from uniaxial tensile tests performed at two different temperatures and various strain rates.

Unlike from what was shown in (Dos Santos e Cismasiu 2011) this study takes into account different class models, namely a phenomenological one and a sharp-interface one.

The Kim and Abeyaratne model (KA model) is a sharp interface model developed within the continuum thermo-mechanical theory of Abeyaratne and Knowles for phase transforming materials, (Abeyaratne e Knowles 2006), (Abeyaratne e Knowles 1991), (Abeyaratne e Knowles 1993). A two-well Helmoltz free-energy density is introduced, based on a trilinear stress-strain relation at fixed temperature, and an explicit kinetic relation and a nucleation criterion are assumed. In the present paper, the KA model was modified in order to take into account the different elastic moduli of the austenite and of the martensite phases. Moreover, following a remark in (Kim e Abeyaratne 1995), we introduce an isothermal model, which is based on the approximation that the temperature is spatially uniform over the body. As discussed in (Kim e Abeyaratne 1995), the isothermal KA model corresponds to a case where the heat conduction rate is much faster than the loading rate, a situation typical of small and moderately large strain rates.

The Auricchio, Fugazza and Des Roches model (AFD model) is a diffuse interface, phenomenological constitutive model based on the theory of irreversible thermodynamics with internal variables (Auricchio, Fugazza e DesRoches, Rate-dependent thermo-mechanical modelling of susuperelastic 2008). The martensitic fraction is introduced as single internal scalar variable, for which a rate-independent evolutionary equation in rate form is assumed.

The main goal of this study is to investigate how the models (the KA, isothermal KA and AFD models) compare with experimental data obtained for two different sets of commercial superelastic austenitic NiTi wires of the type used in seismic applications. A material characterization of the wires was carried out, employing quasistatic tensile tests at 25 °C and 50 °C and at various elongation rates, and based also on differential scanning calorimetry (DSC) tests, which are useful to investigate the transformation characteristics of the alloy. Section 3 is devoted to the description of the parameters identification for the three models. For the two sets of wires, the experiments at 25 °C and at the lowest strain rate are used to identify the material parameters shown in Table 3 for the constitutive models. After implementing the KA model, its isothermal approximation and the AFD model through standard numerical algorithms, in section 4 we compare their stress-strain responses with the other experimental data. The simulations are found to reproduce the behavior at moderate strain rates, with marginal differences. However, numerical results are not able to satisfactorily fit the experimental data for the largest strain rates highlighting the limit applicability of the numerical simulations in this case. Namely, the isothermal KA model and the AFD model do not apparently capture the behavior at large strain rates. The full non isothermal KA model shows

an increasing of the plateau stresses with increasing strain rate, providing an effective improvement over the isothermal models. However, also in this case, the results could be further improved, possibly by adopting kinetic functions more general than the linear one considered in the present study. Another possible improvement could be obtained by removing the assumption that all nucleations occur at the instant at which phase transformation is initiated and no more phase boundaries are nucleated after that instant.

Moreover, annihilation of interfaces, observed in experiments (Chang, Shaw e Iadicola 2006), cannot be reproduced.

Finally, note that the models cannot describe the martensite twinning-detwinning mechanism which is responsible for the shape memory effect at low temperatures, because they capture only the phase transformation from austenite to martensite and vice versa. This is however sufficient to model the superelastic behavior exhibited by the shape-memory wires studied in this paper and proposed for the prototypal presented in (Indirli e Castellano 2008). Investigation of the prediction capabilities of the two models in relation to tension and compression asymmetry, sub-loop deformation behavior, and stabilization and cyclic behavior are all beyond the scope of the present dissertation.

2.2 Kim and Abeyaratne model (1995)

Let $u(x,\ t)$, $\epsilon(x,\ t)\ =\ ux(x,\ t)$ and $\theta(x,\ t)$ be the displacement field, the strain field and the temperature field of a rod occupying the interval $0\ \leq x\ \leq L$ in the reference conFiguretion. We assume the following boundary and initial conditions:

$$u(0,t)=0,\ u(L,t)=\delta(t),\ u(x,0)=0,\ \theta(x,0)=\theta_0(t). \tag{1.38}$$

Let $u(x,\ t)$, $\epsilon(x,\ t)\ =\ ux(x,\ t)$ and $\theta(x,\ t)$ be the displacement field, the strain field and the temperature field of a rod occupying the interval $0\ \leq x\ \leq L$ in the reference conFiguretion. We assume the following boundary and initial conditions:

$$\rho\psi(\varepsilon,\theta)=\begin{cases}\dfrac{E_a}{2}\varepsilon^2-E_a\alpha\varepsilon(\theta-\theta_T)+\rho c\theta(1-\log(\theta/\theta_T)) & on\ P_1,\\ \dfrac{E_m}{2}(\varepsilon-\varepsilon_L)^2-E_m\alpha(\varepsilon-\varepsilon_L)(\theta-\theta_T) & \\ +\rho c\theta(1-\log(\theta-\theta_T))-\rho\lambda_T(1-\theta/\theta_T) & on\ P_3,\end{cases} \tag{1.39}$$

defined on the two regions P_1, P_3 of the (ϵ, θ)–plane shown in Figure 51. In Eqn (1.39), ρ is the density; E_a, E_m are the elastic moduli of the austenite and of the martensite phases, respectively; α is the coefficient of thermal expansion and c is the specific heat, both taken to be equal for the two phases; ϵ_L is the transformation strain; θ_T is the transformation temperature at zero stress; λ_T is the latent heat at the transformation temperature. The Helmholtz free-energy, assumed to be quadratic and concave on an intermediate region P_2, is not further specified on P_2, which corresponds to an unstable phase.

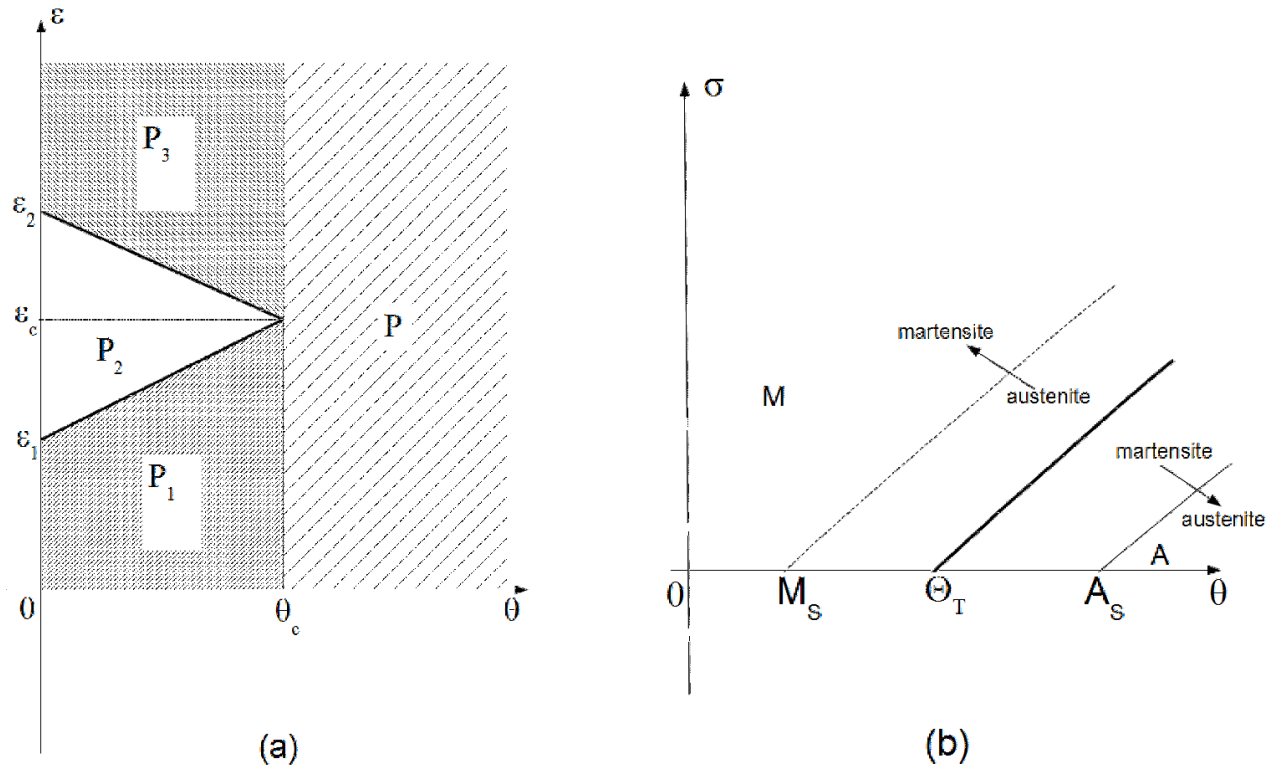

Figure 51 a) The temperature-strain plane; (b) the temperature-stress plane.

The stress-strain relation and the relation between specific entropy, strain and temperature that follow from Eqn (1.39) are

$$\sigma(\varepsilon,\theta) = \rho\psi(\varepsilon,\theta)_{,\varepsilon} = \begin{cases} E_a[\varepsilon - \alpha(\theta-\theta_T)] & on\, P_1, \\ E_m[(\varepsilon-\varepsilon_L) - \alpha(\theta-\theta_T)] & on\, P_3, \end{cases} \tag{1.40}$$

and

$$\eta(\varepsilon,\theta) = -\psi(\varepsilon,\theta)_{,\theta} = \begin{cases} E_a\alpha\varepsilon/\rho + c\log(\theta/\theta_T) & on\ \ P_1, \\ E_m\alpha(\varepsilon-\varepsilon_L)/\rho + c\log(\theta/\theta_T) - \lambda_T/\theta_T & on\ \ P_3, \end{cases} \tag{1.41}$$

respectively. In absence of body forces and wherever the fields are smooth, mechanical equilibrium and the first and second laws of thermodynamics require that

$$\sigma_{,x} = 0, \; -q_{,x} + \rho r = \rho\theta\eta_{,t}, \; q\theta_{,x} \le 0, \tag{1.42}$$

where $q(x, t)$ is the heat flux in the +x-direction and $r(x, t)$ is the heat supply rate to the rod per unit mass. If there is a discontinuity in the fields at $x = s(t)$ (displacement and temperature fields are assumed to remain continuous throughout the rod), one has the following jump conditions

$$\sigma = 0, \quad q = (f + \rho\theta \eta) \dot{s}. \tag{1.43}$$

where f is the driving force on the phase boundary at $x = s(t)$ defined by

$$f = \rho \psi - \sigma \varepsilon . \tag{1.44}$$

To describe the onset and evolution of the martensitic phase transformations, a nucleation criterion and kinetic law are explicitly specified in terms of the driving force on the phase boundary. Assume that the material on the left of the phase boundary is in the martensite phase and the material on the right is in the austenite phase. Then, in view of (1.39) and (1.40), the driving force is

$$f = \varepsilon_L \sigma - \frac{\rho\lambda_T}{\theta_T}(\theta - \theta_T) + \frac{\sigma^2}{2\bar{E}} - \frac{\bar{\alpha}}{2}(\theta - \theta_T)^2, \tag{1.45}$$

where

$$\bar{E} := \frac{E_m E_a}{E_a - E_m}, \; \bar{\alpha} := \alpha^2(\mathrm{E}_a - \mathrm{E}_m). \tag{1.46}$$

In view of (1.43), austenite grows if $f < 0$, while martensite grows if $f > 0$. In the temperature-stress plane, the curve $f = 0$, depicted in bold in Figure 51(b), separates the region A where $f < 0$, and thus austenite is the preferred phase, from the region M where $f > 0$, and thus martensite is the preferred phase.

The nucleation criterion assumed in (Kim e Abeyaratne 1995) states that nucleation occurs at a point if the local driving force exceeds a critical value. To express the critical values in terms of the transformation temperatures, let M_s denote the temperature at which martensite is nucleated in an austenitic rod cooled from above θ_T at zero stress. The critical value for nucleation in the A → M (direct) phase transformation is thus given by

$$f_{nuc}^{MA} := -\frac{\rho\lambda_T}{\theta_T}(M_s - \theta_T) - \frac{\bar{\alpha}}{2}(\mathrm{M}_s - \theta_T)^2. \tag{1.47}$$

Similarly, denoted as A_s the temperature at which austenite is nucleated in a martensitic rod heated from below θ_T, one defines the following critical value for nucleation in the M → A (inverse) phase transformation:

$$f_{nuc}^{AM} := -\frac{\rho\lambda_T}{\theta_T}(\mathrm{A}_s - \theta_T) - \frac{\bar{\alpha}}{2}(\mathrm{A}_s - \theta_T)^2. \tag{1.48}$$

Accordingly to the nucleation criterion, the rod undergoes the direct transformation if $f \geq f_{MA\ nuc}$ and the inverse transformation if $f \leq f_{AM\ nuc}$. Because f depends on the uniaxial stress σ and on the temperature θ, the same considerations can be restated in terms of σ and θ, by solving a quadratic algebraic equation. Thus, direct transformation occurs whenever σ reaches the critical value

$$\sigma_{nuc}^{AM} = \bar{E}\left(-\varepsilon_L + \sqrt{\varepsilon_L^2 + \frac{2(\theta - M_s)}{\bar{E}}\left[\frac{\rho\lambda_T}{\theta_T} + \frac{\bar{\alpha}}{2}(\theta + M_s - 2\theta_T)\right]}\right), \tag{1.49}$$

while, inverse transformation occurs whenever σ reaches the critical value

$$\sigma_{nuc}^{MA} = \bar{E}\left(-\varepsilon_L + \sqrt{\varepsilon_L^2 + \frac{2(\theta - A_s)}{\bar{E}}\left[\frac{\rho\lambda_T}{\theta_T} + \frac{\bar{\alpha}}{2}(\theta + A_s - 2\theta_T)\right]}\right), \tag{1.50}$$

In the temperature-stress plane, the relations (1.49), (1.50) determine two critical curves across which the direct and inverse phase transformations activate upon cooling and heating, respectively Figure 51(b). Note that one necessarily has $M_s \leq \theta_T \leq A_s$.

The evolution of the phase transformation is specified by a kinetic law relating the normal component of the interfacial velocity to the driving force acting on the interface:

$$\dot{} \qquad), \ V(f,\theta)f > 0. \tag{1.51}$$

Various phenomenological models have been proposed in the literature: linear, monotonic nonlinear , “lattice trapping” or maximally dissipative kinetic responses (Abeyaratne e Knowles 2006). For our calculations, we make the simple choice V (f, θ) = μf, where the mobility coefficient μ > 0 is a material constant.

Heat conduction is assumed to be governed by the simple law

$$q = -k\theta_{,x} \tag{1.52}$$

where the heat conductivity, $k > 0$, is assumed to be equal for both phases and constant on the domains P1, P3. The heat supply term r, accounting for the heat exchange through the lateral surface of the rod, and the thermal boundary conditions at the ends of the rod are given by Newton's law of cooling

$$r(x,t) = -\varsigma(\theta(x,t) - \theta_0(t)), \tag{1.53}$$

$$q(0,t) = -\xi(\theta(0,t) - \theta_0(t)), \tag{1.54}$$

$$q(L,t) = \xi(\theta(L,t) - \theta_0(t)). \tag{1.55}$$

Here $\zeta > 0$ and $\xi > 0$ are the heat conduction and the heat convection coefficients, respectively. With regard to thermal boundary conditions at the ends of the bar, we thus have:

$$k\theta_{,x}(0,t) = -\xi(\theta(0,\mathrm{t}) - \theta_o(\mathrm{t})), \tag{1.56}$$

$$k\theta_{,x}(L,t) = \xi(\theta(L,\mathrm{t}) - \theta_o(\mathrm{t})). \tag{1.57}$$

Under the assumption of vanishing thermal expansion and in view of (1.41), (1.52), (1.53), the energy equation (1.42) simplifies as

$$\frac{k}{\rho c}\theta_{,xx} = \theta_{,t} + \frac{\varsigma}{c}(\theta - \theta_0). \tag{1.58}$$

At each phase boundary, the jump condition (1.43) must hold, and, in view of (1.41), (1.52), it can be written as

$$\theta^+_{,x} - \theta^-_{,x} = \mp \dot{} \qquad \rho\lambda_T + \frac{\sigma^2}{2\bar{E}}\Big), \tag{1.59}$$

where the upper sign is taken if the phase boundary has martensite on its left and austenite on its right, the lower sign in the converse case.

Following the remark in (Kim e Abeyaratne 1995), if the heat conduction rate is much faster than the loading rate, one can approximate the response of the rod with an isothermal model obtained by enforcing the first law of thermodynamics for the entire rod. Integrating (1.42) along the entire rod we have:

$$q(0,t)-q(L,t)+\sum_{i=1}^{N} q_{\ i}+\int_0^L \rho r dx=\int_0^L \rho\theta\eta_{,t}dx, \tag{1.60}$$

where N is taken to denote the number of the phase boundaries located at $s = s_i(t) \in (0,L)$, $i = 1, 2, \ldots N$. Setting $\theta(t) := \theta(x, t)$ and using (1.39), (1.40), (1.41), (1.43), and (1.53)-(1.55), we obtain the following integral form of the energy equation:

$$\begin{aligned}&\left(1+\frac{\alpha^2\theta(t)}{\rho c}(E_a(1-\chi(t))+E_a\chi(t))\right)\dot{\ } \qquad \frac{\varsigma}{\rho cL}+\frac{\varsigma}{c}\Big)(\theta(t)-\theta_0(t))\\&+\frac{\alpha}{\rho c}\dot{\ } \qquad \frac{\dot{\ }}{\rho c}\ \omega_L+\rho\lambda_T+\frac{\sigma^2(t)}{2\bar{E}}+\bar{\alpha}(\theta^2(t)-\theta_T^2),\end{aligned} \tag{1.61}$$

where $\chi \in [0, 1]$ is the martensite volume fraction.

The system of equations (1.58), (1.59) (or the differential equation (1.61) which holds only in the isothermal approximation) has to be solved together with the differential equation arising from the kinetic relations (1.51)), with the following compatibility equation:

$$\frac{\delta(t)}{L}=\left(\left(\frac{1-\chi(t)}{E_a}+\frac{\chi(t)}{E_m}\right)\sigma(t)+\chi(t)\dot{\ } \qquad)-\theta_T)\right), \tag{1.62}$$

and with suitable initial conditions on σ and θ. In the isothermal theory, the following differential equation arises from the kinetic relations at the interfaces s_i :

$$\dot{\ } \qquad \dot{\ }\left(\varepsilon_L\sigma(t)-\frac{\rho\lambda_T}{\theta_T}(\theta(t)-\theta_T)+\frac{\sigma^2(t)}{2\bar{E}}-\frac{\bar{\alpha}}{2}(\theta(t)-\theta_T)^2\right). \tag{1.63}$$

To understand how the KA model works, consider a rod entirely in the austenitic phase with assigned elongation and external temperature histories, $\delta(t)$ and $\theta_0(t)$. Initially, the material of the rod remains in the austenitic phase and the equations governing the stress-response of the rod are equations (1.58), equation (1.62) with $s = 0$, the initial condition (1.38) and the boundary conditions (1.56), (1.57). For the theory with the isothermal approximation, the governing equations are (1.61), (1.62) written for $N = 0$, $\chi = 0$, and to be integrated with the boundary conditions (1.56), (1.57).

At some instant, say t_1, the nucleation criterion $\sigma = \sigma_{AM\ nuc}$ is satisfied and martensite begins to grow at some nucleation sites, which are determined through (1.49). Then, the governing equations correspond to a "moving boundary problem" similar to a classical Stefan problem but with two main differences: in the present problem the temperature of the moving interface in unknown and

instead the kinetic relation (1.51) has to be enforced; the stress, that is unknown, and the latent heat λ_T enter the energy jump condition (1.59).

In the isothermal theory, the nucleation criterion loses the ability to detect a nucleation region because the temperature field is now uniform over the rod. However, the macroscopic stress-strain response does not depend on the phase boundaries initial locations, which do not enter (1.61), (1.62) . In fact, the relevant initial conditions for (1.61), (1.62) are conditions on the temperature, the stress and the total martensite fraction χ

$$\theta(t_1)=\theta_0,\ \sigma(t_1)=\sigma_{nuc}^{AM},\ \chi(t_1)=0. \tag{1.64}$$

Thus, for $t > t_1$, the material is composed of martensite phase in a portion of the rod of total length χL and it is composed of austenite elsewhere. To calculate the evolution of the phase boundaries in the isothermal theory, one has to assume that one or more phase boundaries $s = s_i(t),\ i = 1, 2, \ldots N,$ emerge from some initial locations $s_{i0},\ i = 1, 2, \ldots N.$ After integrating (1.61), (1.62) with respect to the triplet (σ, θ, χ), the position of the phase boundaries $s_i(t)$ can be calculated by using the N kinetic equations:

$$\dot{s}_i = \frac{\mu}{L}\left(\varepsilon_L\sigma(t)-\frac{\rho\lambda_T}{\theta_T}(\theta(t)-\theta_T)+\frac{\sigma^2(t)}{2\bar{E}}-\frac{\bar{\alpha}}{2}(\theta(t)-\theta_T)^2\right), \tag{1.65}$$

for $i = 1, 2, \ldots N,$ together with the appropriate initial conditions $s_i(0) = s_{i0}.$ In (28), the plus (minus) sign applies if the material on the left of the phase boundary is in the martensite (austenite) pase.

In both cases, isothermal or non-isothermal, the phase transformation proceeds until $\chi = 1$ and the entire rod is composed of martensitic phase. A similar procedure would be used to calculate the onset and the evolution of the inverse transformation starting from a rod made entirely of martensite, whose evolution problem in the isothermal theory is initially governed by the equations (1.61), (1.62) written now for $N = 0,\ \chi = 1.$

We note that the number N of the phase boundaries and their initial locations can be chosen different for loading and unloading. In the experimental observations of Chang et. al., two nucleation fronts (only one for the smallest strain rate) originate under the tensile tester grips during loading (Chang, Shaw e Iadicola 2006). Moreover, Chang et. al observe that, if the strain rate is large enough, "self-heating can become severe enough to trigger nucleation events at internal points" and phase boundaries annihilation is observed . Up to eight transformation fronts are observed at the largest strain rate, with coalescence events of touching fronts. The number of

transformation fronts observed on unloading is greater than the number observed during loading, with a maximum number of twelve fronts observed.

Kim and Abeyaratne (S. Kim 1995) assume that all nucleations occur at the instant at which phase transformation is initiated and therefore no more phase boundaries are nucleated after that instant. This assumption seems to reproduce Chang's results only for small loading rate. To reproduce the experimental behavior inside the KA model, we assume that the number of interfaces depends on the strain rate, allowing also the possibility of a different number of interfaces for loading and unloading. However, this assumption appears not to be completely satisfactory probably because it does not take into account coalescence and annihilation of transformation fronts observed in experiments (Chang, Shaw e Iadicola 2006).

In the KA and isothermal KA models, the macroscopic stress-strain response (σ, δ/L) is clearly rate dependent due to the coupling between the purely mechanical problem described by the compatibility condition (1.62) and the thermal problem governed by the energy and the kinetic equation (1.51), (1.61).

2.3 Auricchio, Fugazza and DesRoches model (2008)

In the AFD model, the strain ϵ and the temperature θ are chosen as external variables and the martensitic volume fraction, $\chi \in [0,\ 1]$, is chosen as a scalar internal variable. All the variables, external and internal, are assumed to be uniform within the rod. Assuming a regime of small deformations, Auricchio et. al. adopted an additive strain decomposition into two parts, a thermo-elastic part ϵ_{th} and an inelastic part, ϵ_{in}, as follows:

$$\varepsilon = \varepsilon_{th} + \varepsilon_{in}. \tag{1.66}$$

The inelastic strain is assumed to be entirely associated with the transformation strain

$$\varepsilon_{in} = \varepsilon_L \chi \operatorname{sgn}(\sigma) \tag{1.67}$$

where ϵ_L is the maximum transformation strain and sgn is the sign function defined as

$$\operatorname{sgn}(x) := \begin{cases} -1 & if \quad x < 0 \\ 0 & if \quad x = 0 \\ 1 & if \quad x > 0 \end{cases} \tag{1.68}$$

The constitutive behavior is characterized by the following free-energy

$$\phi(\varepsilon,\theta,\chi)=[(u_a-\theta\eta_a)-\chi(\Delta u-\theta\Delta\eta)]+C[(\theta-\theta^*)-\theta\log(\theta/\theta^*)]$$
$$+\frac{1}{2}E(\chi)[\varepsilon-\varepsilon_L\chi\,\mathrm{sgn}(\sigma)]^2-(\theta-\theta^*)[\varepsilon-\varepsilon_L\chi\,\mathrm{sgn}(\sigma)]E(\chi)\alpha. \tag{1.69}$$

Here u_a and η_a are the internal energy and entropy of the austenite in a stress free-condition, respectively; Δu and $\Delta\eta$ are the internal energy and entropy differences between austenite and martensite, respectively; C is the heat capacity, α denotes the coefficient of thermal expansion, and both C and α are taken to be the same for the two phases; θ_* is the reference temperature; $E(\chi)$ is the overall equivalent elastic modulus defined as

$$E(\chi):=\frac{E_aE_m}{E_m+(E_a-E_m)\chi}. \tag{1.70}$$

In view of (1.69), the stress is given by the following equation:

$$\sigma=\frac{\partial\phi}{\partial\varepsilon}=E(\chi)[\varepsilon-\varepsilon_L\chi\,\mathrm{sgn}(\sigma)]-E(\chi)\alpha(\theta-\theta^*). \tag{1.71}$$

The heat equation is written so as to neglect the contribution given by the heat flux, which is assumed to be negligible for elements of small size cross sections:

$$C\dot{\theta}=\qquad\qquad)-\theta_0) \tag{1.72}$$

where b is the heat source and γ is the heat convection coefficient. The heat source b is taken to be the sum of two parts:

$$b=H+D \tag{1.73}$$

where H denotes the heat production associated to the thermo-mechanical coupling, and it is defined as:

$$H=\theta\frac{\partial^2\phi}{\partial\theta\partial\varepsilon}\dot{\varepsilon}\qquad\qquad\cdot \tag{1.74}$$

D is the heat dissipated in the mechanical process, defined as:

$$D=\sigma\dot{\qquad}\qquad\cdot\qquad\cdot \tag{1.75}$$

Due to the specific form of the free energy ϕ, relations (1.74) and (1.75) specialize as

$$H = \theta[-E(\chi)\alpha \quad \cdot \tag{1.76}$$

$$D = \Pi \cdot \tag{1.77}$$

where

$$\Pi = \Delta u - \theta \Delta \eta + \varepsilon_L |\sigma| \tag{1.78}$$

is the thermodynamic force conjugated to χ. We recall that the second law of thermodynamics requires D to be non-negative.

To complete the set of the constitutive assumptions, the evolution equations of the internal state variable χ has to be determined. Variations of the martensite fraction are assumed to occur in the direct ($A \rightarrow M$) and inverse ($M \rightarrow A$) transformation. For each process, an evolution or kinetic law is specified, linking $\dot{\chi}$ with the driving force defined as

$$F = |\sigma| - \theta \frac{\Delta \eta}{\varepsilon_L}. \tag{1.79}$$

Three types of kinetic laws are proposed for each conversion process, named linear, power and exponential kinetic laws. In the present study, we considered only the linear kinetic law, which, for the direct transformation, takes the form:

$$\dot{} \qquad \dot{} \frac{\dot{}}{F - R_f^{AM}} \quad . \tag{1.80}$$

The activation factor term H^{AM} is defined as:

$$H^{AM} = \begin{cases} 1 & \dot{} \qquad < F < R_f^{AM} \\ 0 & otherwise, \end{cases} \tag{1.81}$$

where

$$R_s^{AM} = \sigma_s^{AM} - \theta_R \frac{\Delta \eta}{\varepsilon_L}, \quad R_f^{AM} = \sigma_f^{AM} - \theta_R \frac{\Delta \eta}{\varepsilon_L}. \tag{1.82}$$

The terms $\sigma_{AM\,s}$ and $\sigma_{AM\,f}$ are the stress levels at which the $A \rightarrow M$ transformation starts and finishes at a temperature θ_R, respectively. A similar relation is assumed to hold for the reverse transformation $M \rightarrow A$:

$$
-\overline{R_f^{MA}} \quad . \tag{1.83}
$$

The activation factor term H_{MA} is now defined as:

$$
H^{MA} = \begin{cases} 1 & i \qquad {}^{4} < F < R_f^{MA} \\ 0 & otherwise, \end{cases} \tag{1.84}
$$

where

$$
R_s^{MA} = \sigma_s^{MA} - \theta_R \frac{\Delta\eta}{\varepsilon_L}, \quad R_f^{MA} = \sigma_f^{MA} - \theta_R \frac{\Delta\eta}{\varepsilon_L}. \tag{1.85}
$$

The terms $\sigma MA\ s$ and $\sigma MA\ f$ are the stress levels at which the $M \rightarrow A$ transformation starts and finishes at the temperature θ_R, respectively.

The model is rate dependent because the heat source term b in the heat equation (1.72) depends on the strain rate through (1.73) and (1.74), thus making the mechanical and thermal problems thoroughly coupled. An overview of the numerical scheme adopted to numerically solve the equations governing the equilibrium problem in the case of activated phase transformation is given in the next section.

2.4 Numerical schemes adopted

The numerical implementation of the two models employed an incremental procedure, whose algorithm gave out the stress and temperature values at each time step. For the isothermal KA model, the additional information of the interface locations along the rod was obtained. In the isothermal KA model, the problem is governed by the set of three ordinary differential equations (1.61), (1.62), (1.63) whose unknowns are stress, temperature and, in the case of activated phase transformation, the volume fraction of martensite. The system (1.61), (1.62), (1.63) was solved by using the inner built-in *Mathematica* function *NDSolve*. For the full non isothermal model, periodically distributed interfaces whose number increases with the strain rate were assumed; moreover, an implicit scheme was implemented with a variable time step, chosen such that the interfaces were always located on mesh points at the end of each step.

In the AFD model, the equations governing the problem in case of activated phase transformation are the constitutive law (1.71), the heat equation (1.72) and the kinetic equation (1.80). These equations are coupled, and a backward Euler integration scheme was adopted in order to follow the algorithmic scheme proposed in (Auricchio, Fugazza e DesRoches 2008). To solve the discretized governing (algebraic) equations of the implicit scheme, the standard built-in MATLAB function *fsolve()* was used, which is based on a classic Newton-Raphson iterative scheme, and a time step of 0.1 s was chosen.

2.5 Models calibration

2.5.1 Material characterization of superelastic wires

To identify the parameters of the two models, we analyzed and tested two different types of commercial superelastic NiTi wires, hereafter named wires 1 and 2. Both types of wires had a diameter of 1 mm and a slightly different content of Ni (see Table 1). The choice of these kind of wires was due to their ranges of transformation temperatures (collected in Table 2), which are optimal for the application described in (Indirli e Castellano 2008).

Element (wt.%)	Wire 1	Wire 2
Ni	54.8	55.1
Ti	(bal.)	(bal.)

Table 1 Chemical composition (wt.%) of wire 1 and wire 2

Specimen	$M_F[°C]$	$A_S[°C]$	$M_S[°C]$	$A_F[°C]$	$\Delta H_{M\to A}[Jg^{-1}]$	$\Delta H_{A\to M}[Jg^{-1}]$
1	-16	-10	14	18	2.49	2.61
2	-14	-4	20	24	3.00	4.14

Table 2 Transformation temperatures and latent heats per unit mass (Δ H) determined by DSC.

Differential scanning calorimetry (DSC) was employed in order to investigate the transformation characteristics of the wires. The DSC samples had a weight of 10 mg and a constant heating/cooling rate of 10 ./min was used. Figure 52 and Figure 53 show the DSC thermograms.

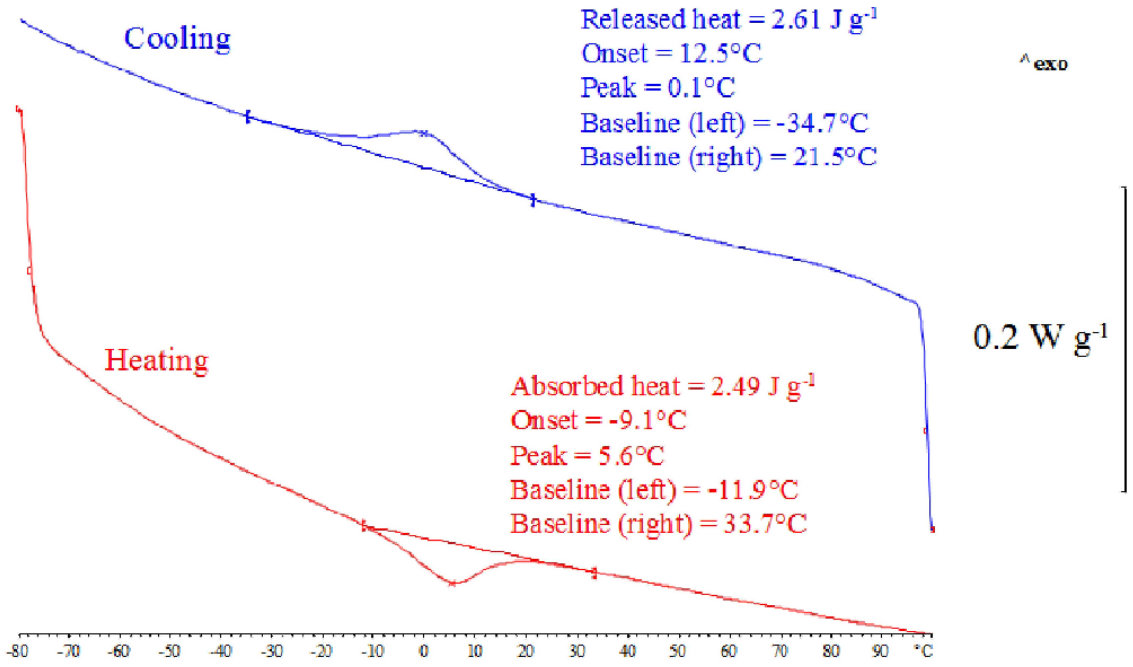

Figure 52 DSC heating (red line) and cooling (blue line) curves for wires 1.

The characteristic martensitic and austenitic starting and finishing temperatures, MS, MF , AS, and AF respectively, were determined by the intersection between the baseline of the DSC curves and the tangents to the peaks. Table 2 collects the transformation temperatures and the latent heats per unit mass of the two types of wires in the range of the phase changes on heating and cooling.

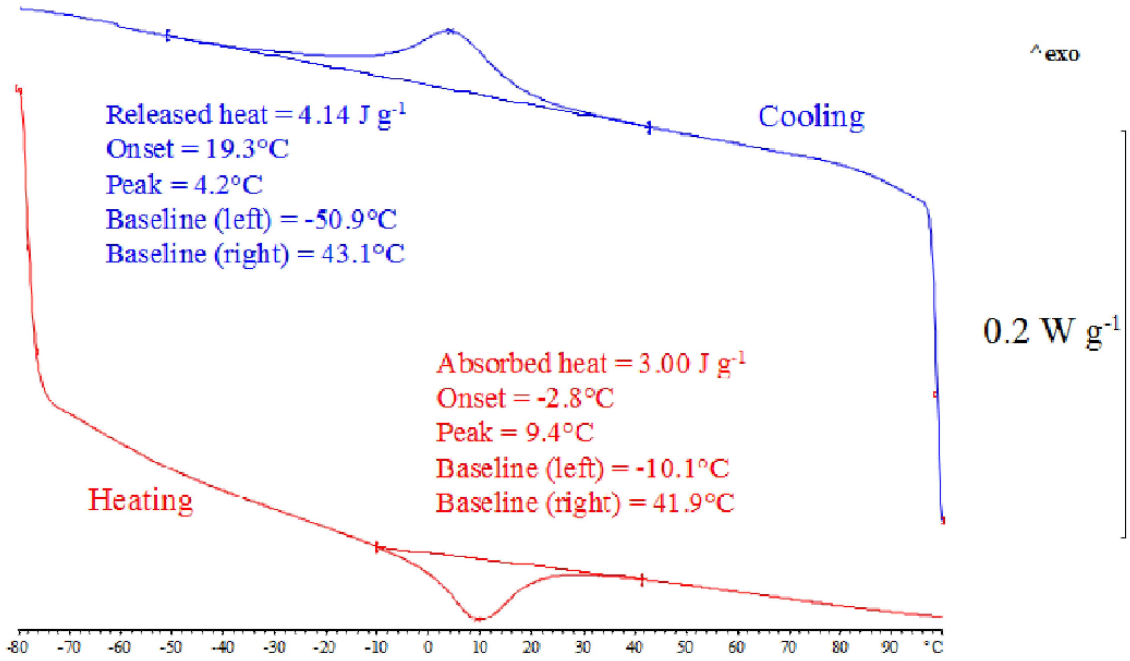

Figure 53 DSC heating (red line) and cooling (blue line) curves for wires 2.

To evaluate the mechanical properties of the material, uniaxial tensile tests were performed at the temperatures of 25°C and of 50°C on the two types of wires. An Instron 4467 testing machine with a 30 kN load cell and a convective air thermal bath (Criotest - Mazzali system) were used. All tests were performed under displacement controlled loading conditions. The test specimens had an overall length of L = 200 mm. The temperature was measured with a thermocouple placed close to the wire.

Figure 54 and Figure 55 compare the stress-strain curves obtained at the indicated temperatures for different loading rates (1 mm/s, 10 mm/s, 20 mm/s, 50 mm/s, 100 mm/s). They clearly illustrate the sensitivity of the SMA's stress-strain response to temperature and strain rate.

2.5.2 Parameters identification

The elastic moduli of the austenite and martensite phases, E_a and E_m, were estimated by linear interpolation of the first and the second ascending branches of the stress-strain diagram obtained at 25 °C for the smallest elongation rate (1 mm/min). The linear interpolation of the second ascending branch gives also the transformation strain ϵ_L (see Figure 56). The estimated values of these material parameters are collected in Table 3. For simplicity, the thermal expansion coefficient α was set equal

to zero for both models. The value assumed for density ρ is typical for NiTi (Chang, Shaw e Iadicola 2006). For the length of the wires we assumed the value L = 200 mm. The heat conductivity was assumed identical for martensite and austenite and equal to 15 W m−1 K−1.

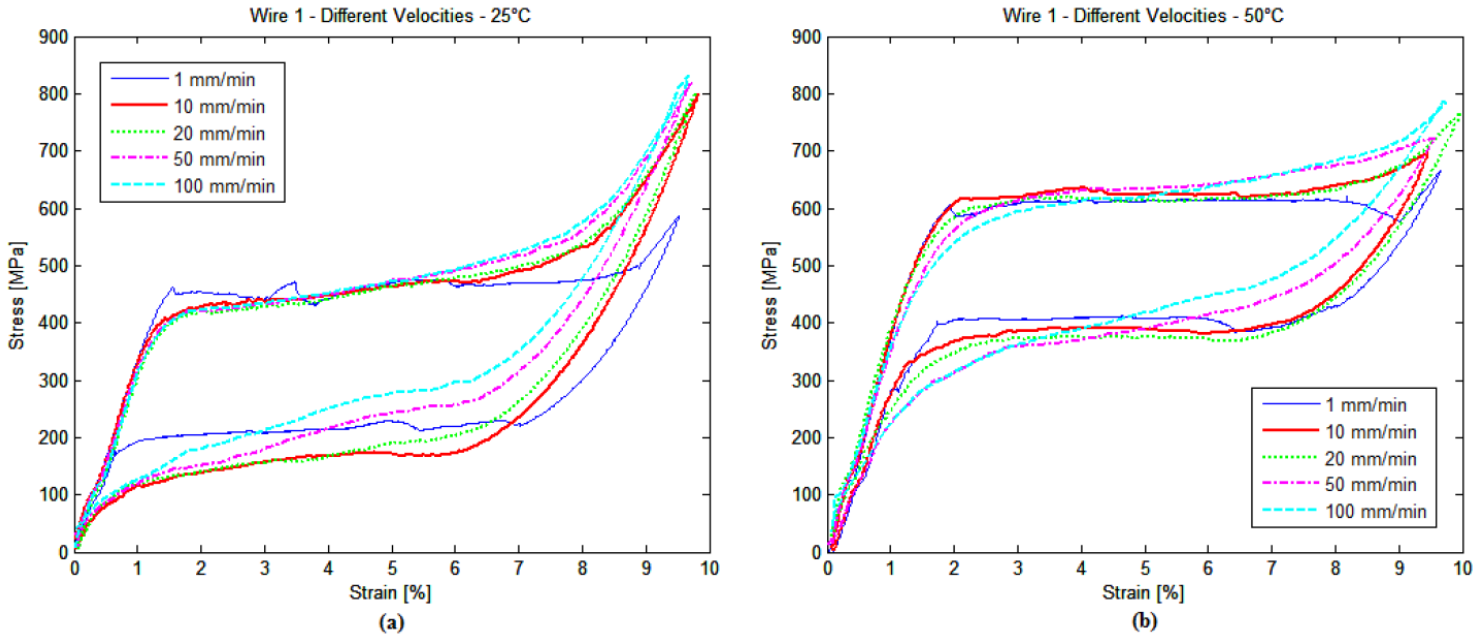

Figure 54 Stress-strain curves for wires 1 at 25 . (a) and at 50 .(b) for different elongation

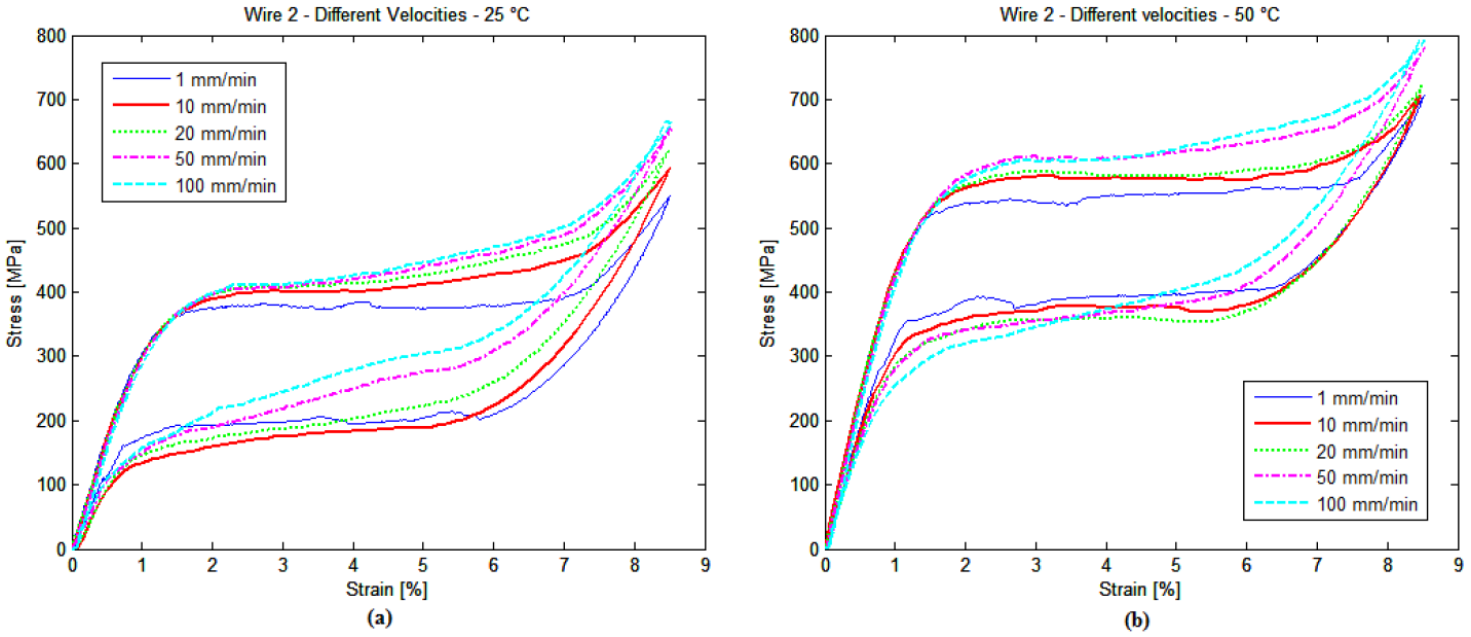

Figure 55 Stress-strain curves for wires 2 at 25 . (a) and at 50 .(b) for different elongation

	isothermal KA Model		AFD Model		
Constant	Wire 1	Wire 2	Wire 1	Wire 2	Units
E_a	32000	35000	32000	35000	MPa
E_m	22222	20000	22222	20000	MPa
ϵ_L	0.070	0.057	0.070	0.057	-
σ_s^{AM}	-	-	420	370	MPa
σ_f^{AM}	-	-	450	390	MPa
σ_s^{MA}	-	-	195	210	MPa
σ_f^{MA}	-	-	165	190	MPa
ρ	6450				kg m^{-3}
α	0				K^{-1}
M_s	236.1	256.6	-	-	K
A_s	261.2	274.2	-	-	K
θ_T	233.0	265.4	-	-	K
$\theta^\star$	-	-	298.15		K
θ_R	-	-	298.15		K
c	322		-	-	J kg^{-1} K^{-1}
λ_T	17410	18570	-	-	J kg^{-1}
ξ	0		-	-	W m^{-2} K^{-1}
ζ	15.5		-	-	W kg^{-1} K^{-1}
Δu	-	-	30		MPa
$\Delta\eta$	-	-	0.53	0.47	MPa K^{-1}
C	-	-	2.1		MPa K^{-1}
γ	-	-	0.1		MPa s^{-1} K^{-1}
k	15	-	-	-	W m^{-1} K^{-1}

Table 3 Parameters for the two models.

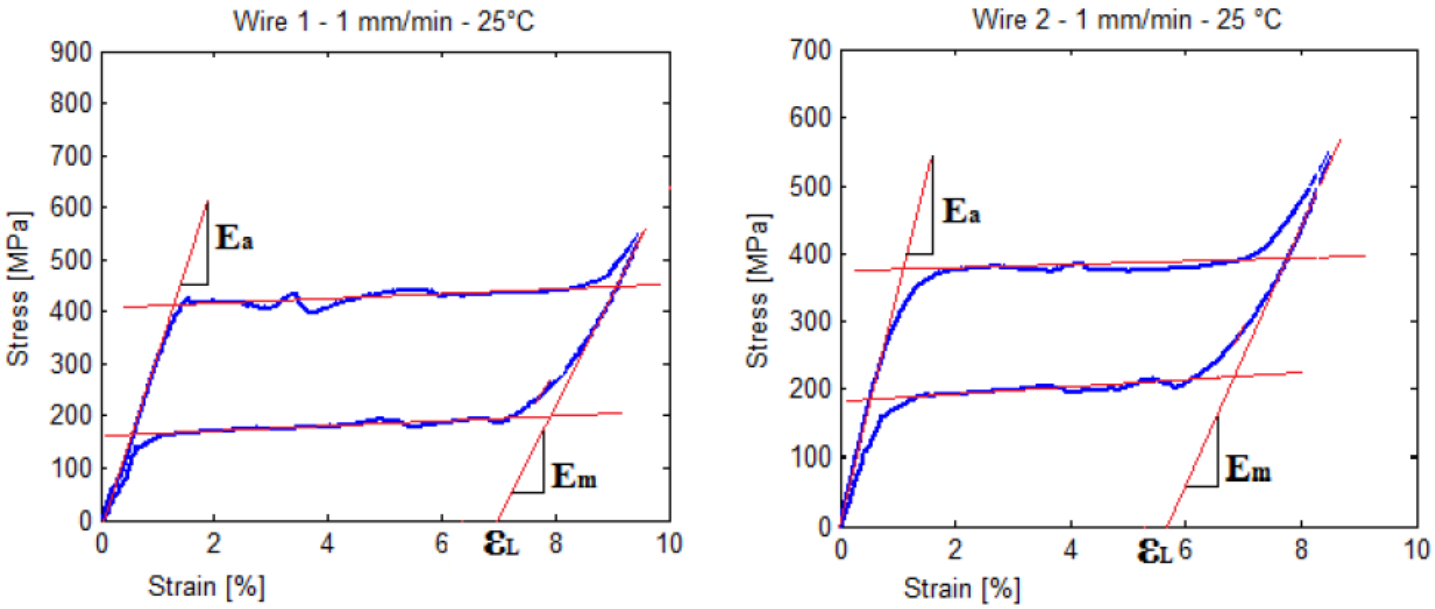

Figure 56 Determination of the elastic moduli of the phases and of the transformation strain.

2.5.3 Further results on parameters identification for the KA model

Table 3 collects the remaining material parameters of the KA model. The thermal conductivity k does not appear in the isothermal approximation of the KA model and therefore it was not included in the table. The value assumed for the specific heat c is typical for NiTi and it was taken from the literature (Chang, Shaw e Iadicola 2006). The value of the heat conduction constant ζ was taken from (Chang, Shaw e Iadicola 2006). The heat convection coefficient ξ was set equal to zero, corresponding to insulated boundary conditions.

The nucleation stress-levels were estimated from the uniaxial tensile tests performed at 25 °C and 50 °C and at the slowest strain rate. The corresponding points are plotted in Figure 57 together with the transformation temperatures given by the DSC test. The curves plotted in Figure 57 were obtained by using a fitting procedure based on a least-square type technique applied to the relations (1.49) and (1.50). According to the KA model, the points of intersections of these lines with the the axis $\sigma = 0$ are A_s and M_s. The corresponding values, together with the value calculated for λ_T, are listed in table 3. We note that while the values of A_s obtained from this procedure are very close to the values obtained from the DSC test, the values calculated for M_s differ significantly. However, it is known that transformation temperatures obtained from DSC tests may not agree with those obtained by other test methods due to the effects of strain and load on the transformation. Note also that DSC

data indicate that $M_s > A_s$, which is in contrast with the assumptions of the KA model. The temperature θ_T was calculated as the average of A_s and M_s (S. Kim 1995).

In the isothermal approximation of the KA model, the value of the product $\mu_N := N\mu$, where N is the number of interfaces and μ is the mobility, was chosen so as to obtain a set of hysteretic loops as close as possible to the ones exhibited by the experimental data. collects the values of μ_N calculated for all temperatures and all strain rates. Because μ is constant, the values in Table 4 indicate that N increases with increasing strain rate (cfr. (S. Kim 1995), Table 8.1]). Table 5 collects the values of the number of interfaces chosen in the simulations employing the non-isothermal KA model. In these simulations, a value of $\mu = 6.0\ \mathrm{N^{-1}\ m^3\ s^{-1}}$ was assumed, as indicated in Table 4.

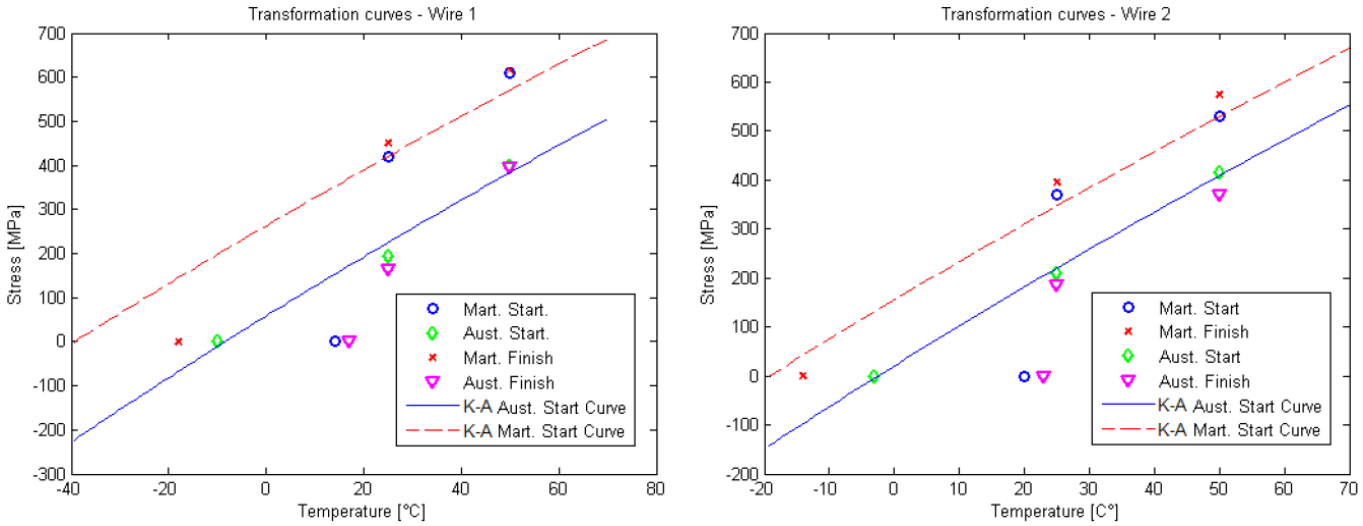

Figure 57 Comparison between the nucleation curves of the KA model and the transformation thresholds obtained from experimental tests. The data at 25°C and 50°C were obtained from uniaxial tensile tests, while data at σ = 0 were inferred from a DSC test.

isothermal KA Model								
	Wire 1				Wire 2			
	25 °C		50 °C		25 °C		50 °C	
Strain rate	$\mu_N * 10^{-11}$		$\mu_N * 10^{-11}$		$\mu_N * 10^{-11}$		$\mu_N * 10^{-11}$	
[mm min^{-1}]	[N^{-1} m^3 s^{-1}]		[N^{-1} m^3 s^{-1}]		[N^{-1} m^3 s^{-1}]		[N^{-1} m^3 s^{-1}]	
	Loading	Unloading	Loading	Unloading	Loading	Unloading	Loading	Unloading
1	2.2	2.6	2.2	3.8	3.0	8.0	2.8	5.8
10	18.0	18.6	18.0	25.0	27.0	47.0	22.0	55.0
20	40.0	44.0	40.0	52.0	50.0	82.0	46.0	102.0
50	120.0	120.0	95.0	120.0	125.0	140.0	92.0	160.0
100	220.0	320.0	220.0	320.0	240.0	265.0	190.0	310.0

Table 4 Values of μN calculated for the isothermal KA model.

KA Model								
	Wire 1				Wire 2			
	25 °C		50 °C		25 °C		50 °C	
Strain rate [mm min^{-1}]	N		N		N		N	
	Loading	Unloading	Loading	Unloading	Loading	Unloading	Loading	Unloading
1	1	1	1	2	1	3	1	3
10	8	8	9	18	9	24	9	35
20	16	16	25	48	18	96	16	106
50	32	32	42	42	38	48	38	48
100	64	64	84	84	84	88	84	88

Table 5 Interfaces number N chosen in simulations for the full KA model.

2.5.4 Further results on parameters identification for the AFD model

The values of the stresses which determine the start and the end of both direct and inverse transformations, denoted as σ_{AMs} , σ_{AMf} , σ_{MAs} , σ_{MAf} and collected in Table 3, were estimated from the uniaxial tests performed at 25 °C and at the slowest strain rate, using the procedure sketched in Figure 6.

The points representing the start and the end of the direct and inverse transformations for the two temperatures 25 °C and 50 °C were fitted with straight lines using a least-square type procedure. Following (Auricchio, Fugazza e DesRoches, Rate-dependent thermo-mechanical modelling of susuperelastic 2008), the product of the slope of these lines and ϵ_L was taken to be an estimate of the constant $\Delta\eta$.

The value of the constant Δu, representing the difference of internal energy between austenite and martensite, was taken from (Auricchio, Fugazza e DesRoches, Rate-dependent thermo-mechanical modelling of susuperelastic 2008).

Finally, we assumed $\theta_\star = \theta_R = 298.15$ K, $\gamma = \zeta\rho$, and $C = c\rho$ with ζ and c as in the KA model.

2.6 Comparison between models

Figure 58 to Figure 61 illustrate the stress-strain curves predicted by the three models at the test temperatures of 25 °C and 50 °C and compared against the experimental data. As can be seen from the figures, for small and moderately large strain rates all the models show a good agreement with experimentally measured curves. At large strain rates, the isothermal approximation of the KA model and the AFD model exhibit smaller stresses near the end of the transformation. As discussed in (S. Kim 1995), this effect is often observed in experiments and it can be attributed to temperature non-uniformities occurring in the wire during non-quasistatic loading. The results obtained for the non-isothermal KA model show that this model can capture the stress increasing with loading rate.

Note also that all experimental stress-strain curves obtained at 50 °C exhibit an initial elastic modulus larger than the value for E_a identified at 25 °C. This is thought to be due to the presence of brass rods connecting the wires to the cross heads in the Criotest - Mazzali system.

As a quantitative index to measure the energy dissipation capacity of the NiTi wires, we selected the equivalent viscous damping ratio, ς_{eq}, defined as the energy dissipated in one cycle divided by the product of 4π and the maximum strain energy. The values of the equivalent viscous damping ratio at the test temperatures and strain rates are collected in tables 6 and 7 together with the values predicted by the two numerical models. The experimental damping ranges from 2.8 % to a maximum of 5.5 %. These results agree with previous studies on the properties of wire subjected to cyclical loading, which found that the maximum equivalent viscous damping was in the range of $4 - 8\%$ (Dolce e Cardone 2001). The values of ς_{eq} predicted by the models show a maximum relative difference of about 15 % at the strain rates 1, 10, 20 mm/min, but the difference rises up to about 44 % at the strain rates 50, 100 mm/min. The damping values predicted by the isothermal models (isothermal KA and AFD) show favorable agreement with the experimental damping at small strain rate, but they over-estimate the damping at large strain rates. The damping values predicted by the non-isothermal KA model shows a good agreement at the higher strain rates.

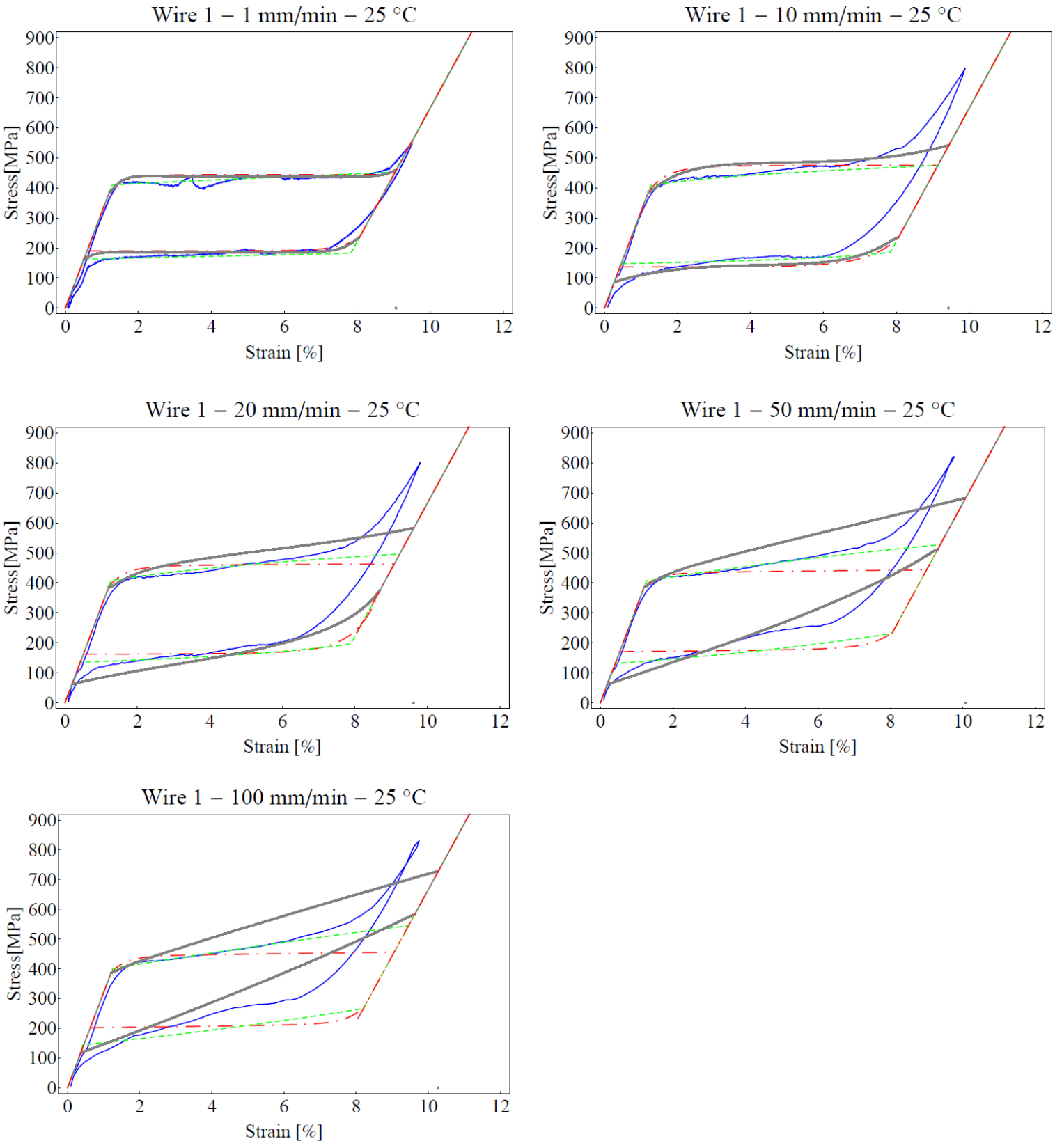

Figure 58 Experimental data obtained for wire 1 at the temperature of 25 . and comparison of simulations based on the full KA model (continuous line), on the isothermal approximation of the KA model (dash-dotted line) and on the AFD model (dashed line).

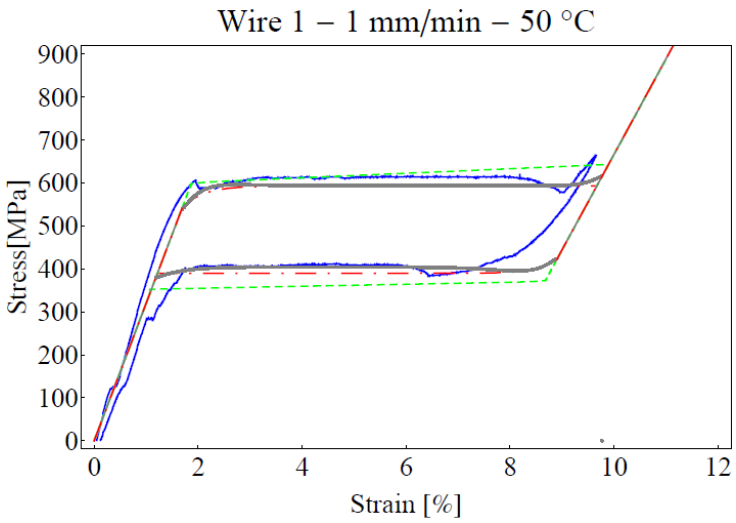

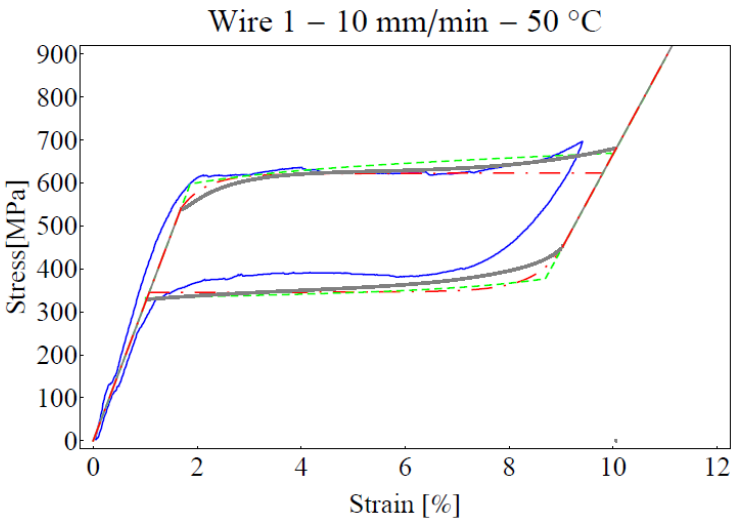

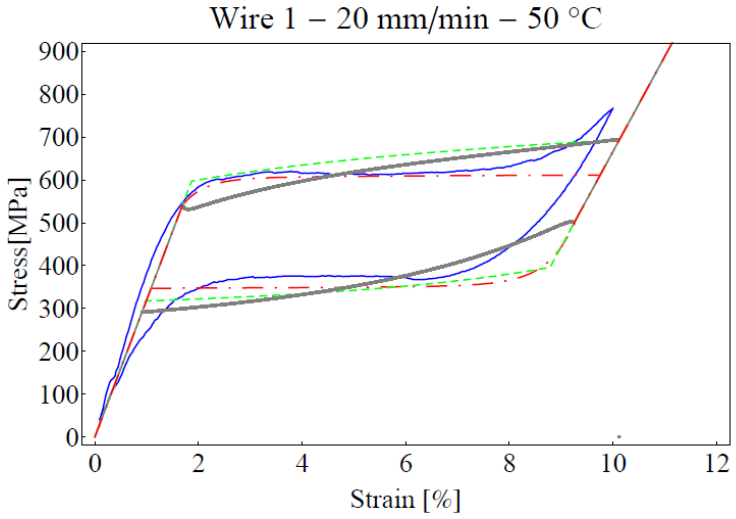

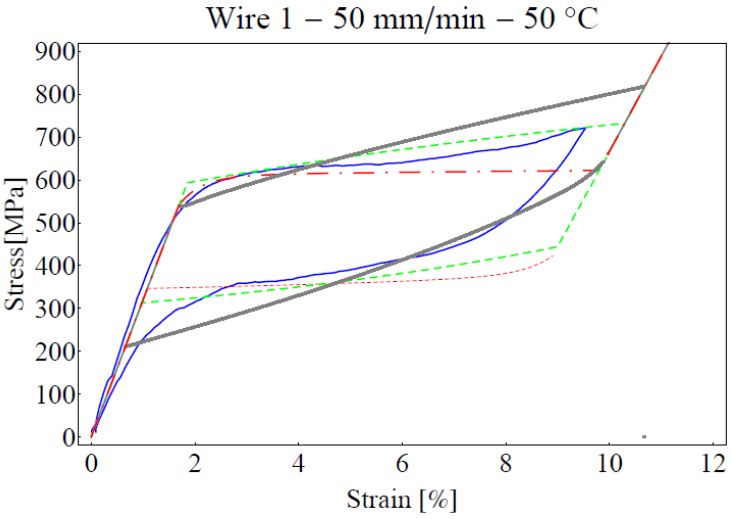

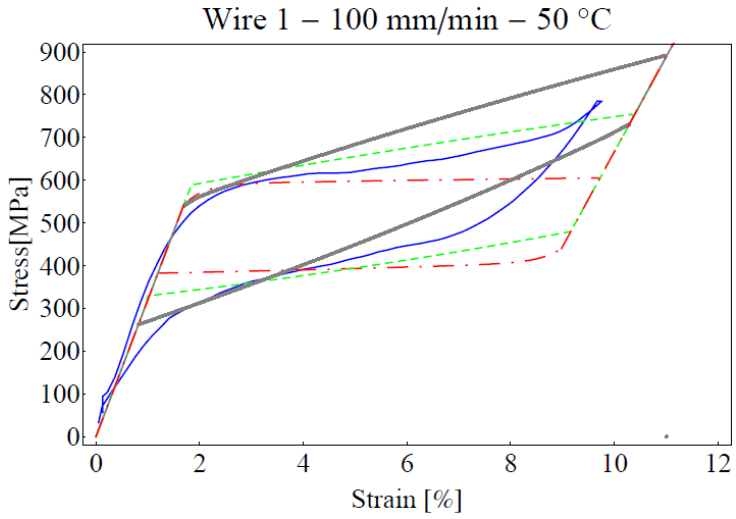

Figure 59 Experimental data obtained for wire 1 at the temperature of 50 . and comparison of simulations based on the full KA model (continuous line), on the isothermal approximation of the KA model (dash-dotted line) and on the AFD model (dashed line).

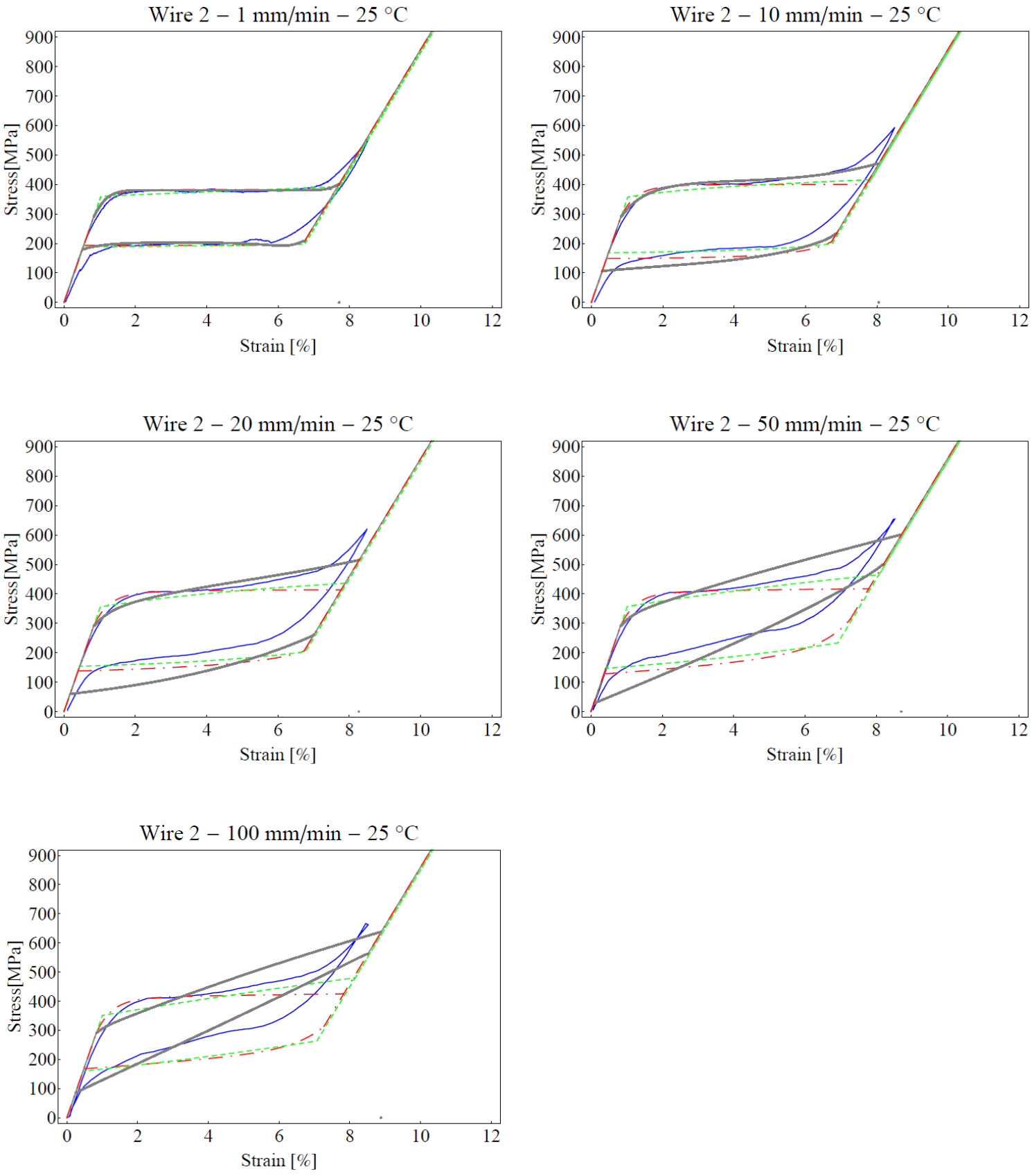

Figure 60 Experimental data obtained for wire 2 at the temperature of 25 . and comparison of simulations based on the full KA model (continuous line), on the isothermal approximation of the KA model (dash-dotted line) and on the AFD model (dashed line).

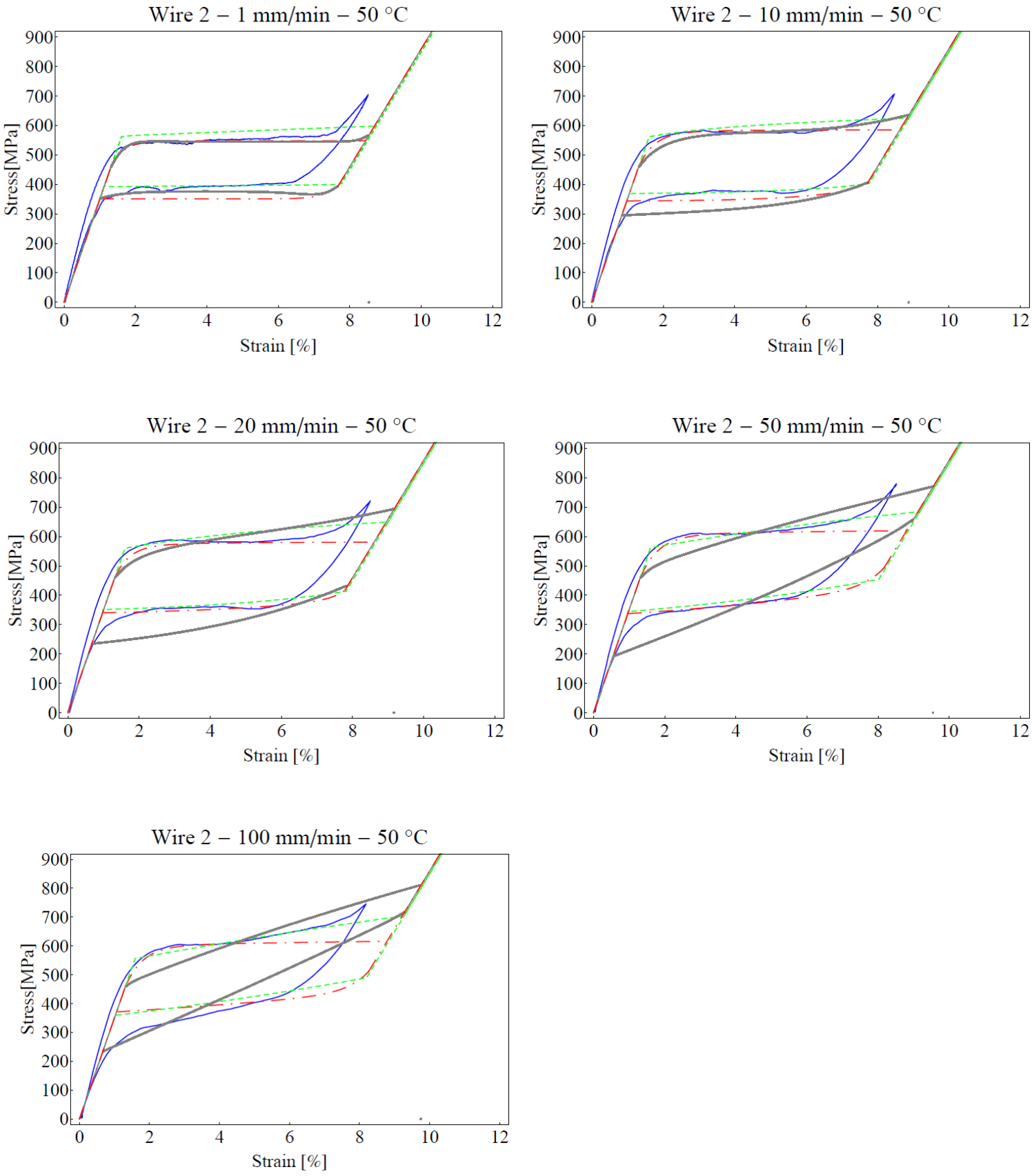

Figure 61 Experimental data obtained for wire 2 at the temperature of 50 . and comparison of simulations based on the full KA model (continuous line), on the isothermal approximation of the KA model (dash-dotted line) and on the AFD model (dashed line).

Strain Rate	ς_{eq}				ς_{eq}			
	25 °C				50 °C			
	Exp.	isothermal KA	KA	AFD	Exp.	isothermal KA	KA	AFD
[mm min^{-1}]	[%]	[%]	[%]	[%]	[%]	[%]	[%]	[%]
1	5.5	7.3	7.1	7.6	4.0	4.3	3.9	5.0
10	4.4	8.8	7.8	8.0	4.3	5.4	4.7	5.4
20	4.1	8.1	7.2	7.9	3.9	5.2	4.3	5.5
50	3.6	7.6	5.2	7.3	4.2	5.0	4.3	4.9
100	3.4	6.8	3.8	6.4	3.5	4.2	3.2	4.3

Table 6 Equivalent viscous damping for wire 1. The experimental values (exp.) are compared against the corresponding values calculated using the full KA model, the isothermal approximation of the KA model and the AFD model.

Strain Rate	ς_{eq}				ς_{eq}			
	25 °C				50 °C			
	Exp.	isothermal KA	KA	AFD	Exp.	isothermal KA	KA	AFD
[mm min^{-1}]	[%]	[%]	[%]	[%]	[%]	[%]	[%]	[%]
1	4.0	6.4	5.8	6.3	2.8	4.4	3.8	3.8
10	4.6	7.7	7.0	6.7	3.6	4.7	4.7	4.3
20	4.4	7.6	7.0	6.7	3.9	4.6	4.4	5.0
50	3.3	7.3	4.7	6.2	3.7	4.6	3.6	4.1
100	2.8	6.3	3.0	5.4	3.9	3.9	2.6	3.6

Table 7 Equivalent viscous damping for wire 2. The experimental values (exp.) are compared against the corresponding values calculated using the full KA model, the isothermal approximation of the KA model and the AFD model.

2.7 Concluding remarks

This chapter reviewed two one-dimensional constitutive models for SMAs and compared them against the experimental behavior of superelastic NiTi wires under uniaxial loading. Representative constitutive models were the model by Kim and Aberayatne (KA model) and the model by Auricchio, Fugazza and DesRoches (AFD model). For the first, we introduced an extension in order to take into account different elastic moduli for the austenite and the martensite phases and an isothermal approximation based on a remark by Kim and Aberayatne (Kim e Abeyaratne 1995).

Uniaxial tensile tests were conducted on superelastic NiTi wires at two different temperatures and various strain rates. The experimental data inferred from quasistatic tests at 25 °C and at the lowest strain rate were used to identify the material parameters of the two models. Numerical simulations based on the constitutive models were compared with the remaining experimental data. The simulations were found to be in good overall agreement with test measurements for small and moderate strain rates.

However, it was observed that discrepancies with experimental data, increasing with increasing strain rates, exist for the AFD model and for the isothermal approximation of the KA model. These are believed to be due to the effect of non-uniformities of temperature occurring inside the NiTi wires at higher strain rates.

Experimental observations showing the presence of exothermic fronts during loading on NiTi strips support this conclusion (Chang, Shaw e Iadicola 2006).

The simulations for the non-isothermal KA model show a shift of the hysteresis loop in the direction of increasing stress as the strain rate increases. However, the results could be probably improved by taking into account other aspects of the experimental response like, for example, annihilation of interfaces or more general kinetic laws. Finally, we note that our experimental results for the largest strain rate are about twenty times faster than the largest strain rate considered in (Kim e Abeyaratne 1995).

3 FIRST EXPERIMENTAL RESULTS ON AN INNOVATIVE SOLUTION: A SMA-BASED SEISMIC PROTECTION DEVICE IN SERIES WITH FRP REINFORCEMENT

3.1 Basic ideas and motivation

In the framework of the MAMAS Project ("Advanced Multi-task Materials for Structural Applications in Construction"), a scientific team (CETMA, ENEA, University of Ferrara) designed a prototypal retrofitting device for buildings made of CFRP (Carbon Fiber Reinforced Polymers) strips in series with Shape Memory Alloy NiTi wires, devoted to strengthening masonry structures when quick prompt ringing is needed to prevent face wall overturning in the post-earthquake emergency.

The MAMAS Project has been managed by the Italian Consortia TRE of Naples and CETMA of Brindisi (2007-2011) with funds of the Italian Ministry of Education, University and Research (MAMAS, 2007). MAMAS focused on the investigation of innovative material properties (resistance, ductility, dissipation capacity, durability, temperature and impact integrity) capable of withstanding extreme natural and anthropogenic actions (earthquakes, accidents and terrorism) to increase the safety of construction/infrastructure. In specific, a scientific team (CETMA Brindisi, ENEA Bologna, University of Ferrara) carried out targeted activities, among the various tasks foreseen by the project itself, to conceive, develop and test a prototypal device made by CFRP (Carbon Fiber Reinforced Polymer) strips in series with SMA (Shape Memory Alloy) wires, devoted to face wall overturning in masonry buildings, in case of repeated aftershocks due to seismic events. In fact, CFRP materials are ideally suited for strengthening of concrete/masonry structure when quick prompt ringing is needed in the post-earthquake emergency. With regard to masonry, CFRP interventions can be widely applied against the most dangerous occurrences as the wall collapse due to out-of-plane actions, but the fiber delamination (i.e. decrease of stiffness and load bearing ability) should be avoided, because repair effectiveness cannot be guaranteed if the earthquake leads to CFRP permanent damage and subsequent structural failure. Thanks to the intrinsic property of super-elasticity, a SMA device, done by thin NiTi wires and added in series with the CFRP strip itself, can provide an undamaged CFRP behaviour during all the seismic sequence, with the additional advantage of recentring the wall subjected to overturning, without almost any residual displacement. The expertise on CFRP (University of Ferrara, see for example (Cecchi et al. 2004), (Cecchi et al. 2005), (Benvenuti, Vitarelli e Tralli 2012), (Milani, Milani e Tralli, Approximate limit analysis of full scale FRP-reinforced masonry building through a 3D

homogenized FE package 2010), (Milani, Milani e Tralli 2009), (Milani, Rotunno, et al. 2006)) and SMA (ENEA, see (Indirli & Castellano, 2008)), gathered in previous research activities, was a fundamental background. The study began with a state-of the-art analysis, focusing on SMA constitutive models and experimental techniques for physical/thermo-mechanical characterization of SMA NiTi wires. Then, the research continued with: laboratory tests on selected NiTinol (Nickel-Titanium Naval Ordinance Laboratory) wires, evaluating their chemical composition, identifying alloy phase transformation temperatures, and performing cycled tensile tests at different temperatures, in order to select/verify the most suitable alloy for the SMA device; conceptual design and engineering of the CFRP+SMA system (from theoretical aspects to field of application, dimensioning, overturning verification, choice of materials, and finally constructive details and drawings); SMA multi-plateau device experimental characterization. The CFRP+SMA system effectiveness has been verified thanks to a laboratory experiments performed on two 1:3 scaled masonry mock-ups, taking into account the following conFiguretions: horizontal actions on the unreinforced mock-up, with progressive CFRP repair/strengthening, until collapse; horizontal actions on the mock-up with CFRP+SMA ringing and local CFRP repairs against the cracks, until failure.

3.2 Possible applications

The effective, but unlinked, use of CFRP strips and SMA devices for repair/strengthening of seismically damaged masonry structures (including heritage) is demonstrated by several applications in the last years, taking place mainly in the framework of post-reconstruction programs and rarely for preventive improvement. On the contrary, the beneficial combination of the two techniques, not foreseen yet, represents the core idea presented in this chapter, highlighting advantages and avoiding drawbacks. The proposed CFRP+SMA system is also conceived to cover the critical time interval immediately after the disaster, when safe, quick, easy and cheap prompt interventions should be provided by emergency teams on a wide scale.

As anticipated in Chapter 1, the development of innovative SMA-based techniques, devoted to seismic protection of masonry structures, began in Italy within the EU funded ISTECH Project, coordinated by FIP Industriale and ENEA as a partner (ISTECH, 1996), (Indirli and Castellano 2008). In particular a multi-plateau device (based on the superelastic properties of groups of NiTiNOL with different length connected in parallel) has the capacity to work at increasing force levels, being also less sensitive to the masonry tensile strength. ISTECH led to significant

exploitations, in particular the reinforcement measures for the Upper Basilica of St. Francis in Assisi already mentioned in Chapter 1, hit by the 1996 Marche-Umbria (Italy) earthquake. At the end of the project, FIP Industriale patented the SMA device (EU Patent, 2000).

Carbon Fibre Reinforced Polymers (CFRPs), for restoring/reinforcing masonry structures, have been widely studied, tested (Figure 62) and applied in several cases of technical relevance after recent seismic events, as shown by a wide amount of papers which may be found in the literature (just to mention some of them: Triantafillou & Fardis, 1997; Abrams, 2000; Tumialan et al., 2001; Borri et al., 2002; Casareto et al., 2003; Faella et al., 2004; Santa-Maria et al., 2004; Turek et al., 2004; Briccoli Bati et al., 2007; Valluzzi, 2007; Corradi et al., 2008; Hancilar et al., 2008).

Figure 62 Examples of different CFRP reinforcement during tests on masonry specimens: (a) panel strengthened with CFRP strips (Borri et al., 2001); (b) creep simulation on sample strengthened with thin CFRP strips (Valluzzi, 2007); (c) CFRP fabric debonded after failure (Santa Maria et al., 2004).

Many earthquakes demonstrated that the most dangerous damage, until collapse, is due to out-of-plane overturning (Figure 63), when the lack of effective connections between orthogonal walls is evident. The recent seismic event occurred in L'Aquila (Italy, April 6, 2009) provides clear examples of failure patterns due to this kind of actions (Indirli et al., 2012), which can be identified in global and local mechanisms, thanks to the MEDEA classification and quick investigation tool (Papa & Zuccaro, 2004; MEDEA, 2005). Prompt interventions in the city of L'Aquila can be roughly divided into two categories:

a) the works performed by the Firemen in the days immediately after the earthquake, often timber structures (Figure 64a-e), rarely strips of various materials (Figure 64f-g);

b) the put-in-safety scaffoldings, mainly inside the "red zone" of L'Aquila historic center, with the widespread and expensive use of tubular steel elements (Figure 65a), as done after previous seismic

events (Figure 65b-d). In our opoinion, the CFRP+SMA device, developed within the MAMAS project, can represent an effective, safe and cheaper alternative to the currently used methodologies for post-earthquake prompt interventions.

Figure 63 Global and local collapse mechanisms associated to out-of-plane-actions detected in L'Aquila (Italy) after the April 6th 2006 earthquake (Indirli et al., 2012).

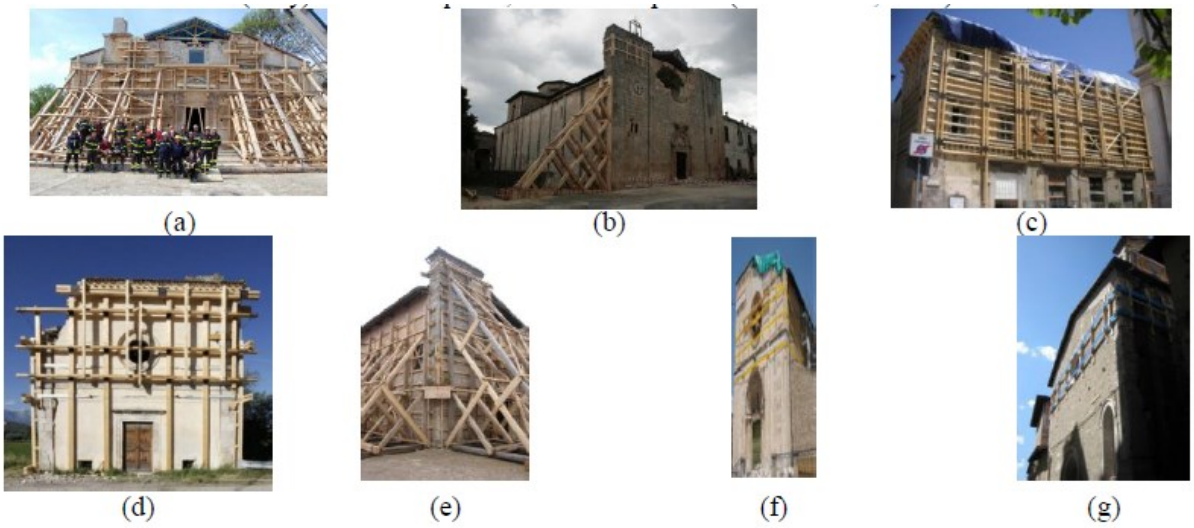

Figure 64 Examples of various prompt interventions performed by the Firemen in the days immediately after the earthquake in l'Aquila, Italy: (a-e) timber materials; (f-g) strips of various materials.

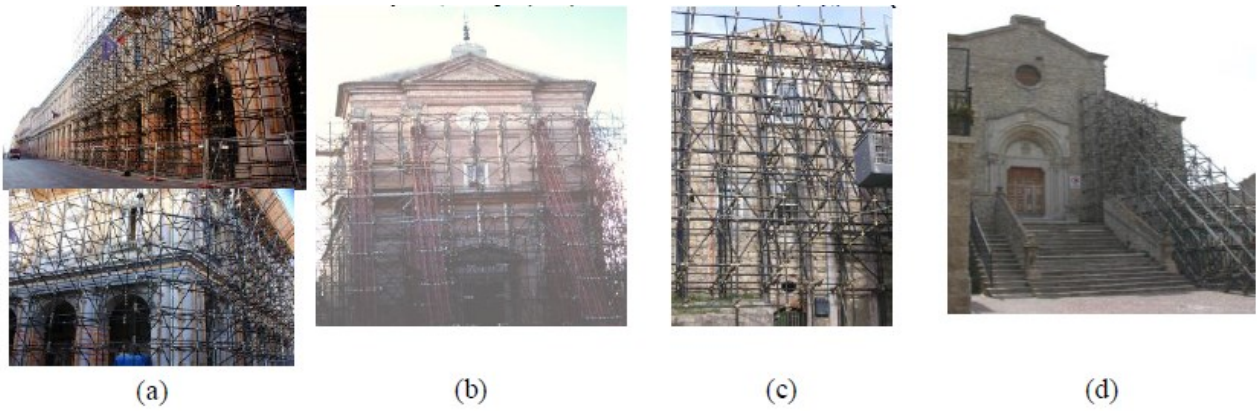

Figure 65 Put-in-safety scaffoldings using tubular steel elements: L'Aquila (a); Camerino, 1997-98 Marche Umbria earthquake (b); San Giuliano di Puglia, 2002 Molise-Puglia earthquake (c-d);

3.3 Description of the new proposed SMA multiplateau device and of the CFRP+SMA retrofitting system

In this paragraph the new SMA seismic protection device of the multiplateau-kind, mentioned in the previous paragraphs is being presented. As previously anticipated, this device is meant to be used within masonry historical buildings in order to integrate classical retrofitting systems based on the use FRP composites or steel chains and to improve the prevention of the overturning phenomena of masonry walls (Figure 66). The device works in uniaxial traction only.

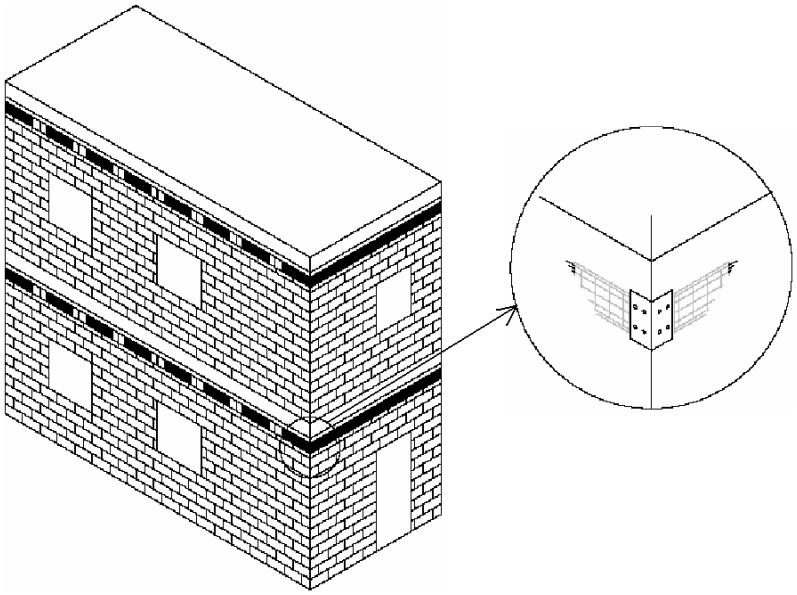

Figure 66 FRP wrapping of a masonry building and detail of the metallic plate to which the device will be connected.

It's thus possible to introduce the device in series with a FRP reinforcement. The advantages in the using of this type of device on the traditional retrofitting systems are mainly related to the simplicity

of the retrofitting on one hand and to the capability of allow for controlled displacements of the wall which is about to overturn at a prescribed limited force on the other hand. Indeed, in this way would be overcome the classic problem which affects traditionally retrofitted buildings: the fragile local crisis of the anchorages of chains (local failure of chain anchorages embedded into the masonry) or FRP strips (delamination) due to the impulsive effects of seismic action. Besides, this device allows for energy dissipation through the development of multiple hysteryses cycles and it may be reused after the seismic event thanks to its recentering capabilities.

The schematics of the device is shown in Figure 67 and Figure 68.

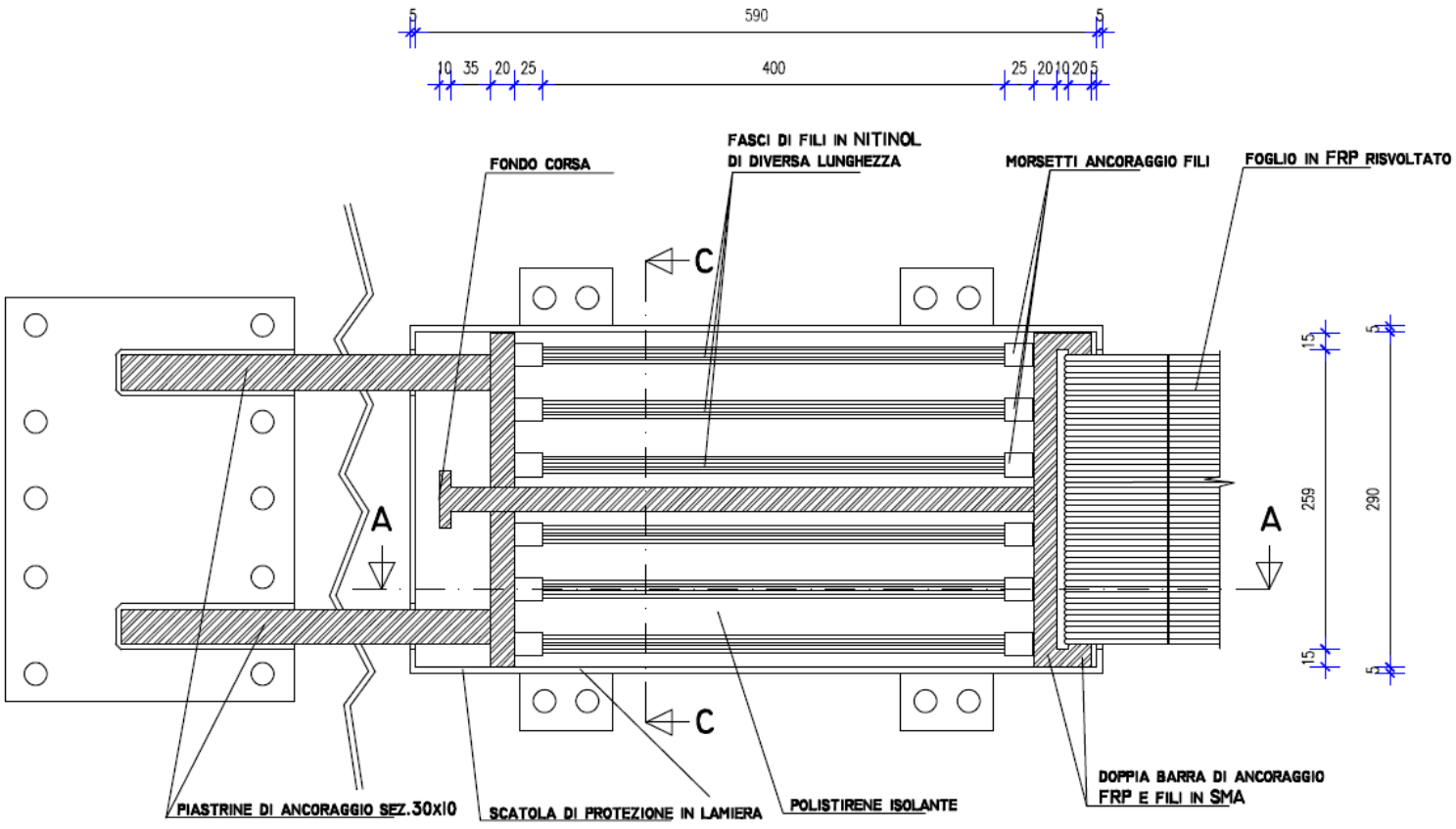

Figure 67 New seismic protection device – Internal view.

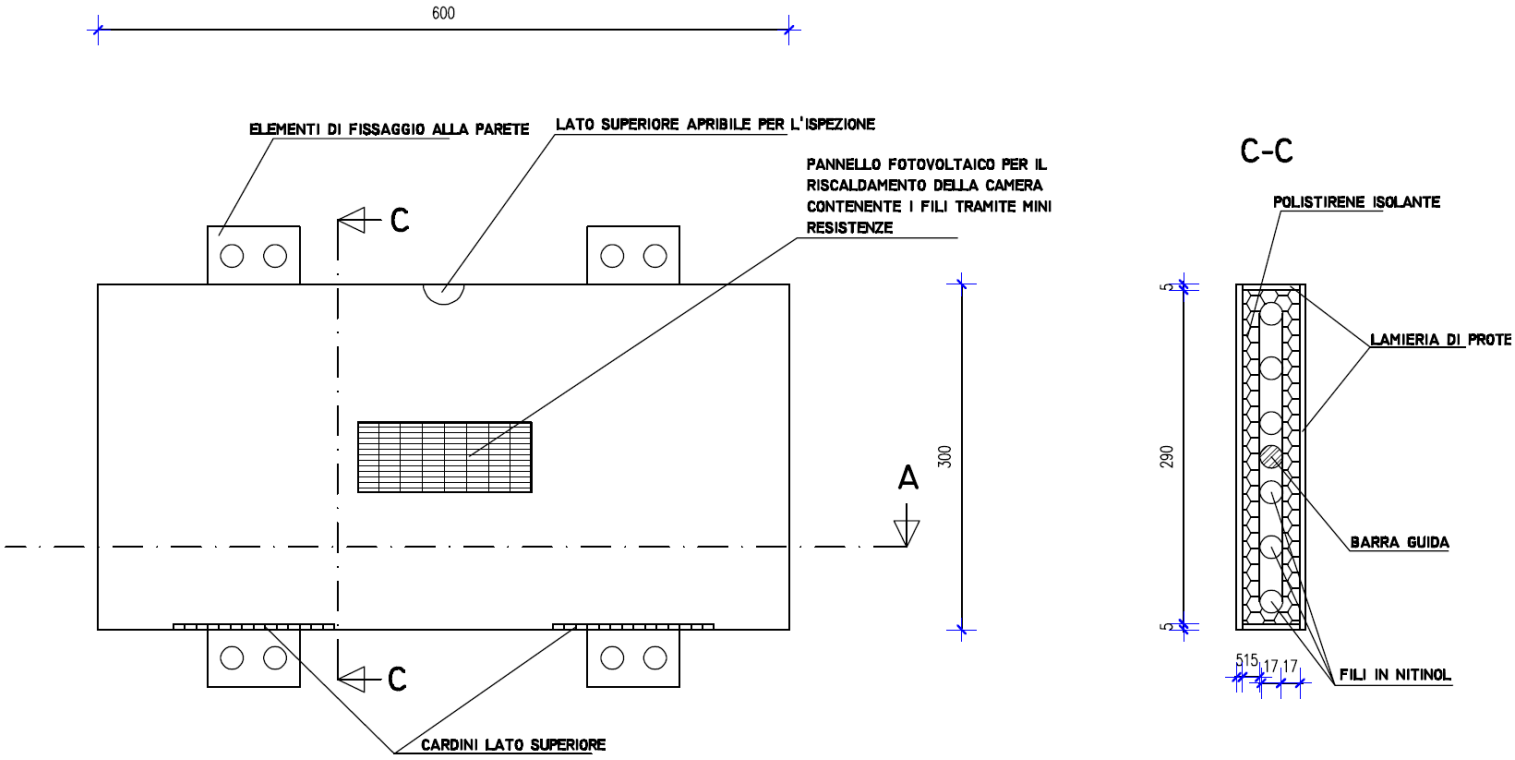

Figure 68 New seismic protection device – External view.

Let's consider a system made of a masonry wall at risk of overturning supported by two orthogonal masonry walls. In order to retrofit this system, two devices will be used one at each end of the wall about to overturn. The devices will be connected through FRP strips to the orthogonal walls. As shown in Figure 67 the main body of the device is made of a steel box whose walls are 5mm thick. The box has a rectangular shape with external dimensions of 600 x 300 x 60 mm and it has to be screwed to the orthogonal wall by mean of four suitable steel elements. The box will be closed on the upper side by a removable cover which allows the inspection. As shown in Figure 68, the internal space is filled with insulating material in order to keep temperature as constant as possible. The interior houses six groups of NiTiNOL wires, symmetrical to the longitudinal axes of the device and of different length in order to allow for a force-displacement multiplateau response of the kind shown in Figure 69. The weight of the device is around 100 N. Usually it's considered safe to allow a maximum excursion of 30-50 mm (cfr. NTC 2008 and Applicative Circular par. C8A.2.2). The force range is between 10 and 50KN, depending on the number of wires, the area of their section and their stiffness.

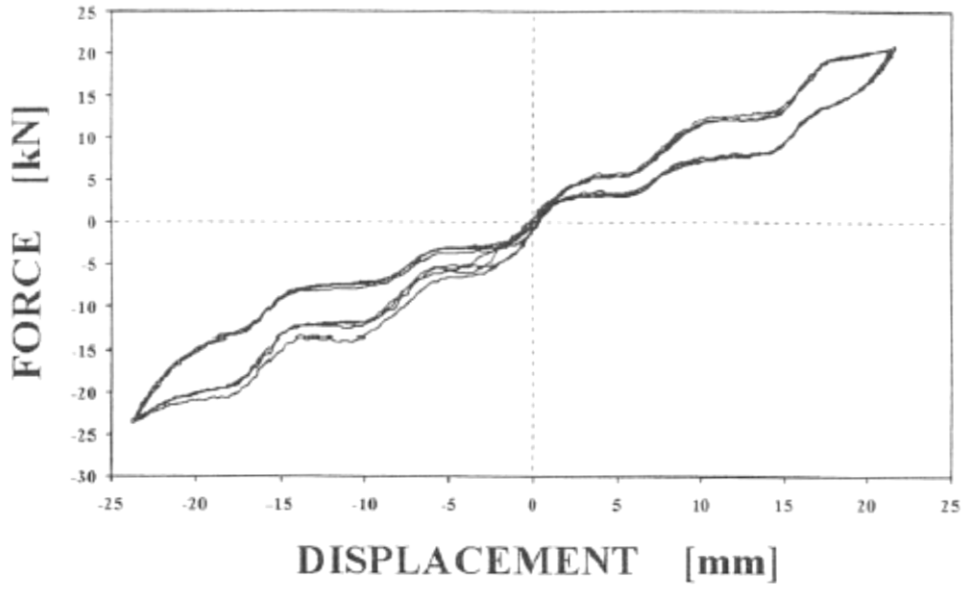

Figure 69 Typical multiplateau superelastic force-displacement response.

The NiTiNOL wires used in the construction of the device were the same described and tested (through one-dimensional tensile tests) in the previous chapter and we remand to that chapter for the details on their mechanical properties and on the tests the wires undergone.

The tests carried on single NiTinol wires allowed to define the dimensional/mechanical features of the SMA device, in which the three parallel groups were made of 8 wires each (with a length of 400 mm), anchored at the ends within the metallic box; $\Delta L/L$ is the maximum completely recoverable strain at the end of the cycle and Nd,nom the total design loading. The length of each wire group can be manually regulated in pretension (or not), in order to calibrate a different three-plateau (multi-plateau) loading/unloading hysteretic behavior, depending on the user's need. Three different conFiguretions (TF1, TF2, TF3, depending on wire pretension) have been used both for SMA device characterization and during tests on a masonry scale model provided by CFRP+SMA devices.

The SMA device in each of the three conFiguretion was subjected to one-dimensional traction tests in the Laboratory of Material Engineering at the University of Ferrara with the same testing equipment used to test the single wires in order to assess its mechanical response in terms of force-displacement. Tests were conducted at room temperature through an INSTRON 4467 testing machine with a 30kN load cell. Data were collected with the software Labview, which takes record of both measured force and displacements. The experimental setup is shown in Figure 70.

Figure 70 Experimental setup for the testing of the new proposed SMA device. University of Ferrara.

To the aim of determining the force-displacement response of the single wire group, during the first test (i.e. conFiguretion TF1) two out of three wire groups were placed out of the anchorages, in order to allow for free displacement, whilst to the remaining group (the central one) an initial length of 400mm was assigned. In Figure 71, ten loading-unloading cycles obtained through a loading rate of 12mm/min and a maximum displacement of 24mm are shown.

In order to obtain a double superelastic plateau, the central wire group has been released (displacement free) whilst to the remaining groups has been assigned an initial length of 400mm and, to one of them, a negative elongation of 15mm. In Figure 72, ten loading-unloading cycles obtained through a loading rate of 12mm/min and a maximum displacement of 32mm are shown.

Finally, in order to obtain a triple superelastic plateau, an initial length of 400mm has been assigned to the first group, a negative elongation of 10mm has been assigned to the second group and a negative elongation of 21mm has been assigned to the last group. In Figure 73 ten loading-unloading cycles obtained through a loading rate of 12mm/min and a maximum displacement of 32mm are shown.

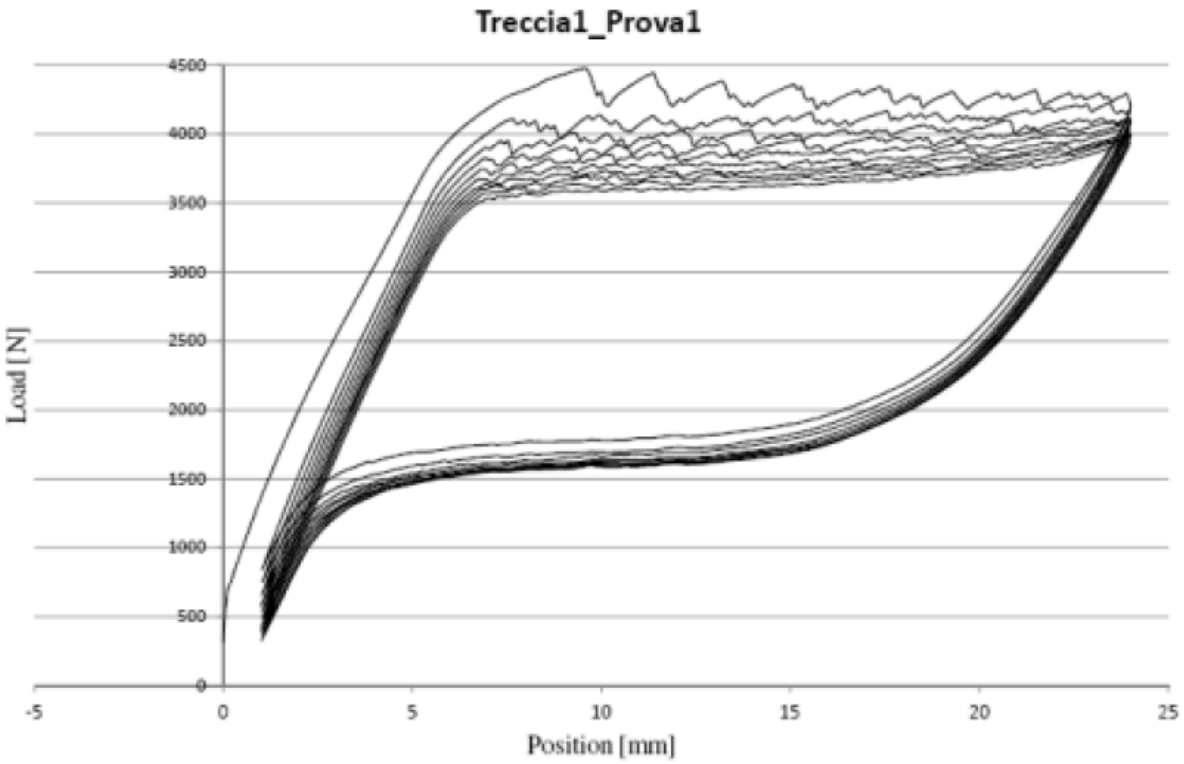

Figure 71 Ten loading-unloading cycles for conFiguretion TF1

Figure 72 Ten loading-unloading cycles for conFiguretion TF2

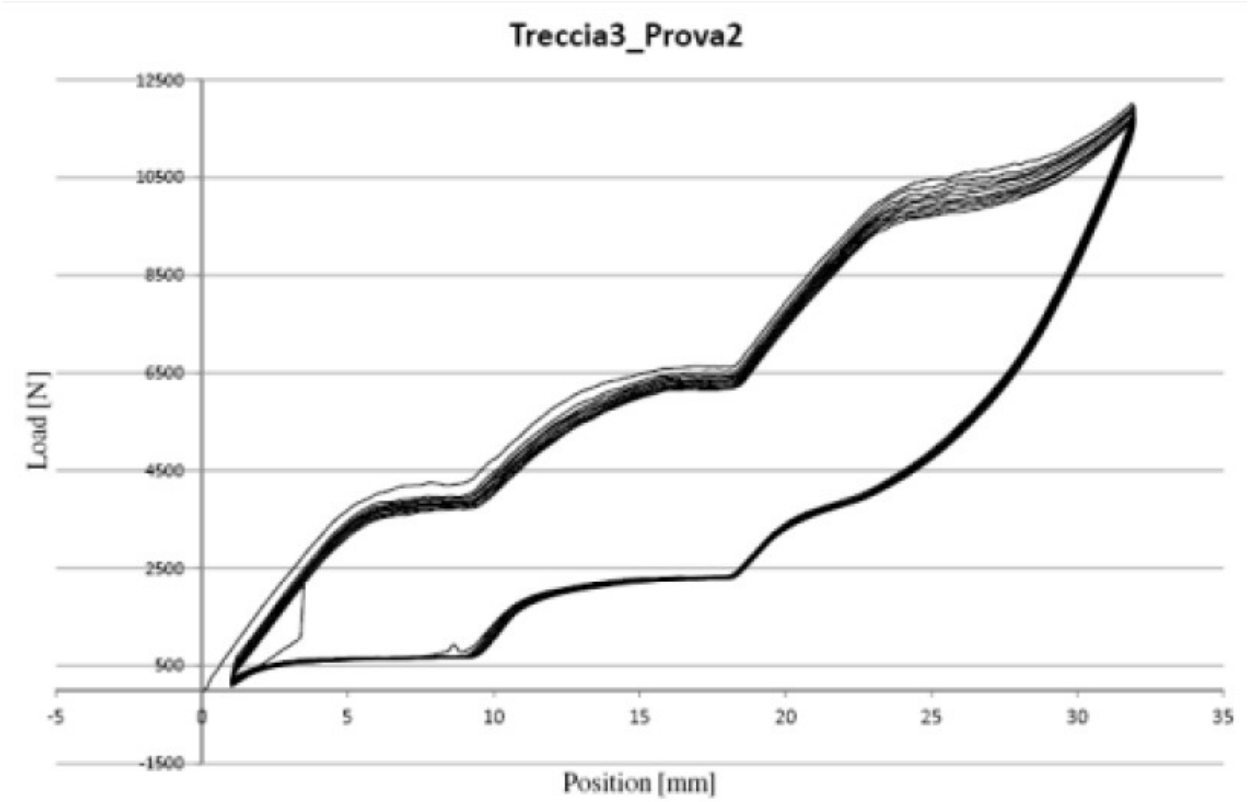

Figure 73 Ten loading-unloading cycles for conFiguretion TF3

From the results shown in the figures above it can be observed that conFiguretion TF1 gives a superelastic monoplateau, conFiguretion TF2 gives a double superelastic plateau whilst conFiguretion TF3 gives a triple superelastic plateau. Actual design parameters and values for the SMA device are summarized in Table 8 Design parameters for the multiplateau SMA device.

single wire dimensional/mechanical data					single plait data		
∅ [mm]	A [mm^2]	N_{max} [kN]	σ_{max} [kN/mm^2]	ΔL/L [%]	n° wires	A [mm^2]	$N_{d,nom}$ [kN]
1.000	0.785	0.510	0.650	8	8	6.28	4.08
∅	wire diameter		σ_{max}	maximum stress value	N_{max}	loading maximum value per wire	
A	wire area/plait area		ΔL/L	maximum strain value	$N_{d,nom}$	design loading value per plait	

Table 8 Design parameters for the multiplateau SMA device.

The traction tests performed on the SMA device confirm the perfect functionality of the device. Incidentally we observe that upon a displacement of 30-32mm (i.e. a strain of 8% on the most loaded wires) the superelastic hardening of the most strained wires is clearly recognizable along the second and third superelastic plateau.

3.4 Experimental tests and application to a simple scale building masonry model

In the Laboratory for Material and Structural Tests of the Department of Structural Mechanics of the University of Florence, under the supervision of Prof. S. Briccoli Bati, an experimental campaign on scale 1:3 models of simple masonry buildings retrofitted with the new device proposed has been carried on. First results are presented in (Indirli, Corvaglia, et al. 2012). The model was a simple masonry box made of four walls and an opening on one of the wall, with dimensions 150x150x100 cm. The model is represented in Figure 74.

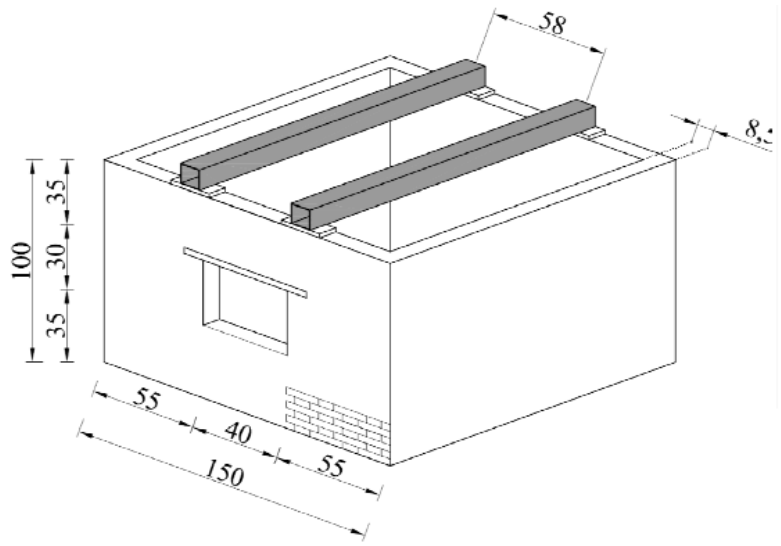

Figure 74 Geometry of the model

The structure was loaded with a vertical load of 60kN applied through two horizontal steel beams and a system of pre-stressed rods, and a horizontal load applied through a system of four hydraulic rams as shown in Figure 75.

3.4.1 Tests without the SMA device

The masonry box is monitored through the devices shown in Figure 75. Each test consists in a controlled increment of the horizontal load until failure shows up. At first, tests were conducted without any retrofitting system. An horizontal preload of 1kN was initially assigned to the back wall. Then, the horizontal load was increased to a maximum of 50 bar pressure into the hydraulic rams, corresponding to a maximum horizontal load of 10kN. Rupture occurred when a local failure

(a long horizontal fracture) of the loaded back wall showed up as shown in Figure 77. Unloading at the same loading rate was finally performed. Results are summarized in terms of Load-Displacement measured by each LVDT transducer in Figure 76.

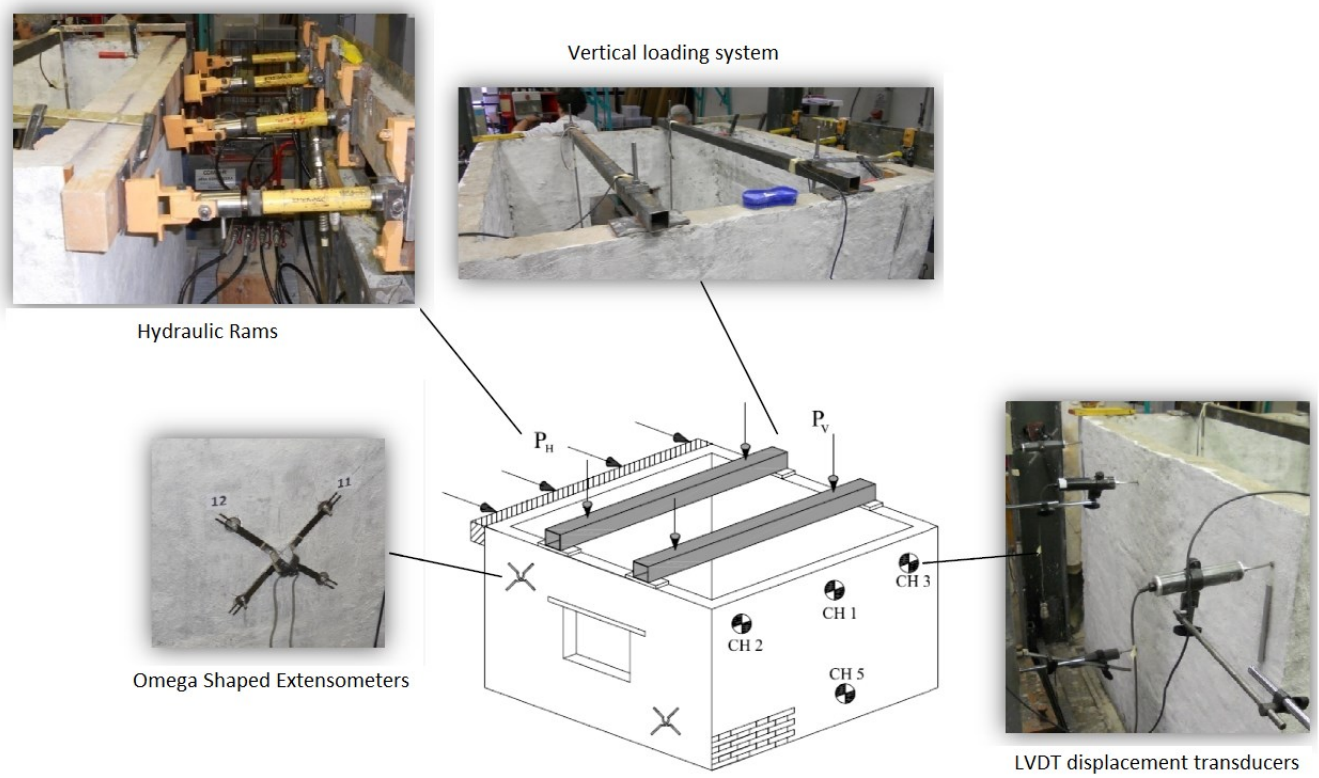

Figure 75 Schematics of the experimental setup

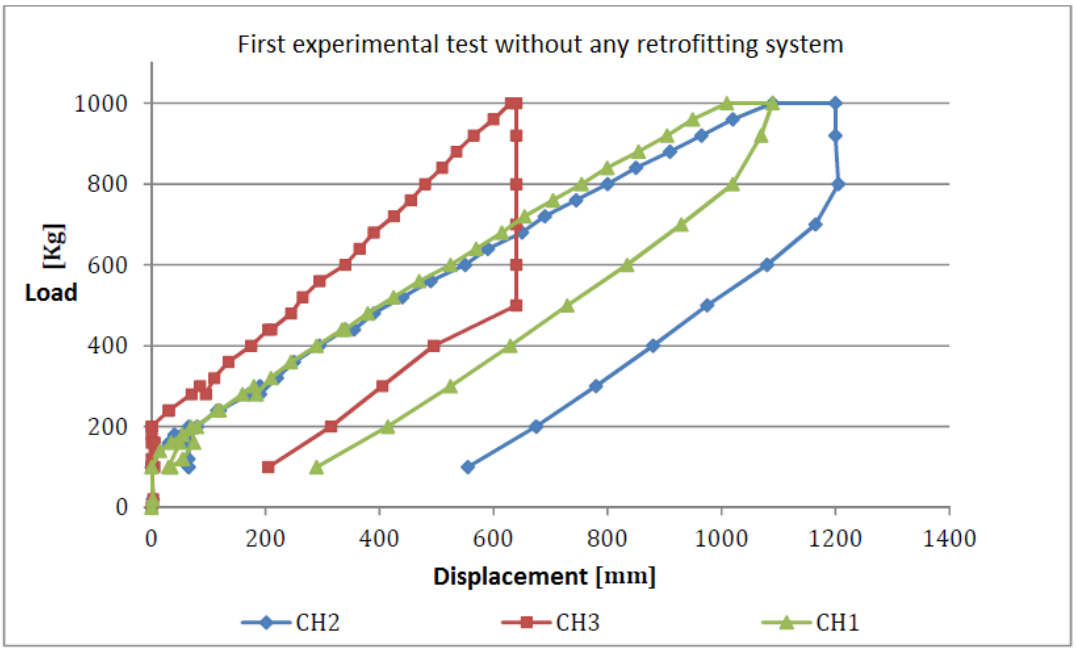

Figure 76 First experimental test results without any retrofitting system

The load displacement diagrams show an almost perfect linear elastic response of the structure up to the maximum load. Upon unloading, after a short vertical path a new linear elastic path is followed, parallel to the loading path.

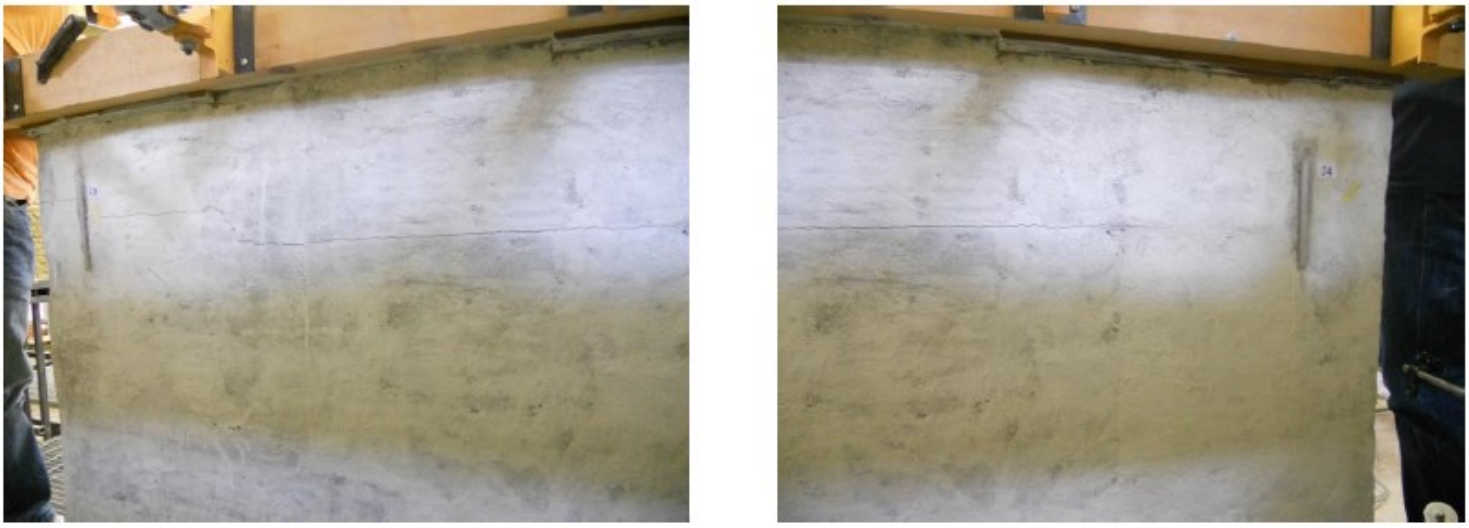

Figure 77 Horizontal crack in the back wall after the first test.

For the second test an horizontal wooden frame and a FRP retrofit made of 5 strips in the back wall was added to the model in order to prevent the formation of the local mechanism observed during the first test, as shown in Figure 78. An horizontal preload of 1kN was initially assigned to the back wall. Then, the horizontal load was increased to a maximum of 125 bar pressure into the hydraulic rams, corresponding to a maximum horizontal load of 25kN. In this second test local failure occurred upon formation of a longitudinal fracture in the front wall (i.e. overturning mechanism of the front wall) as shown in Figure 79. Unloading at the same loading rate was finally performed. Results are summarized in terms of Load-Displacement measured by each LVDT transducer in Figure 80.

Even in this case, load-displacement diagrams show an almost perfect linear elastic path up to the maximum applied load. Upon unloading, after a short vertical path a new linear elastic path is followed, parallel to the loading path. The steepness of the elastic path is comparable to the one obtained during the first test. Indeed, the masonry box is intact up to the formation of the collapse mechanism which involve the front wall. Maximum displacement of 6-7mm are measured during the formation of the mechanism while big residual displacements after unloading (4mm) are measured.

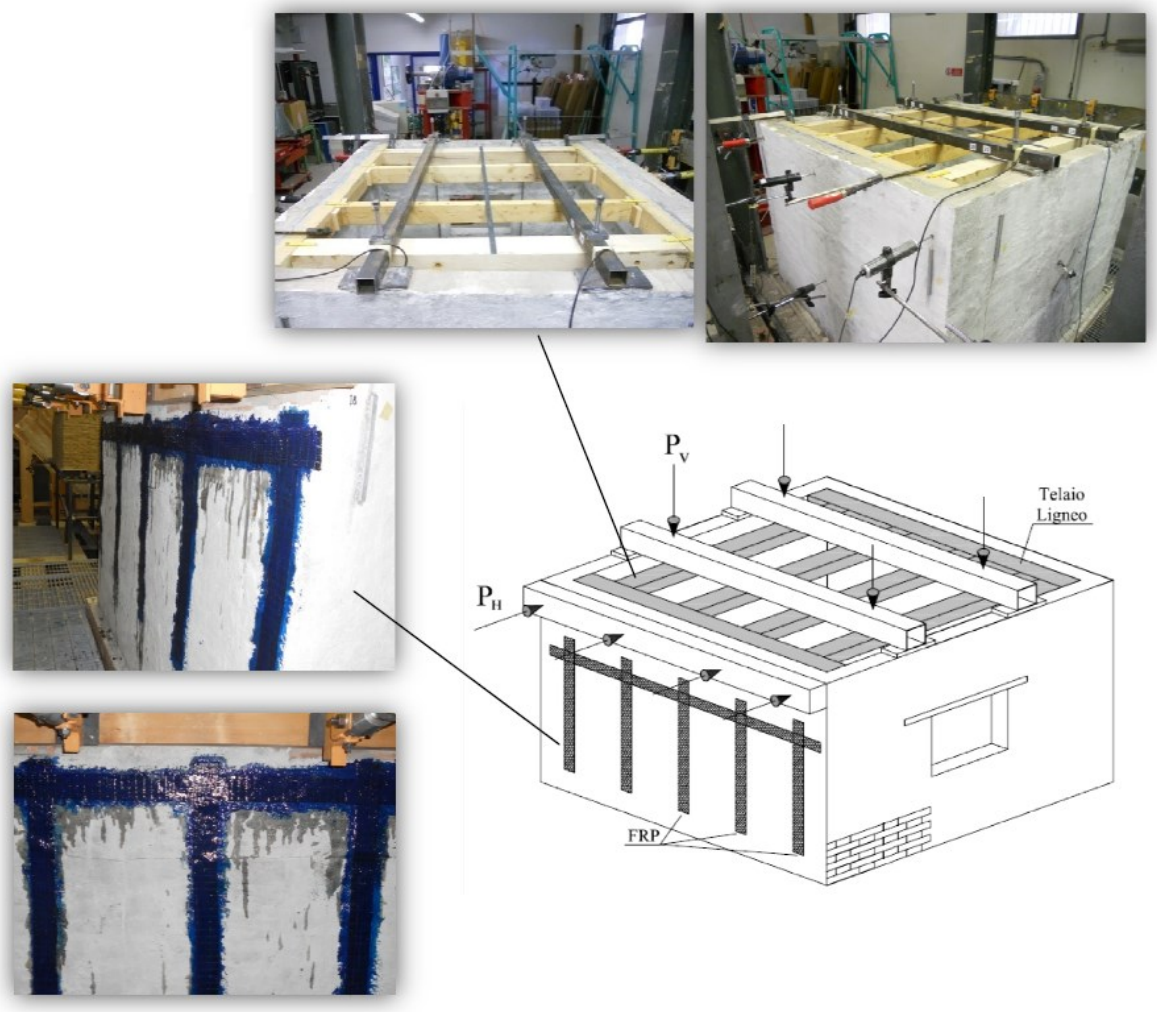

Figure 78 Second test experimental setup

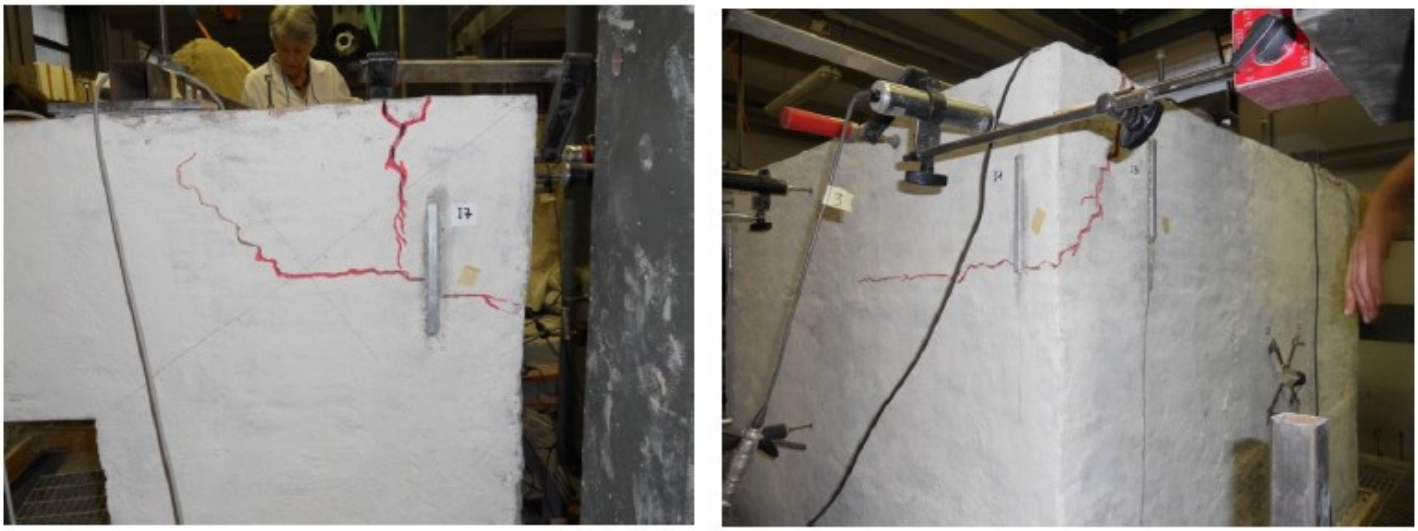

Figure 79 Detail of the cracks in the front wall at the end of the second test.

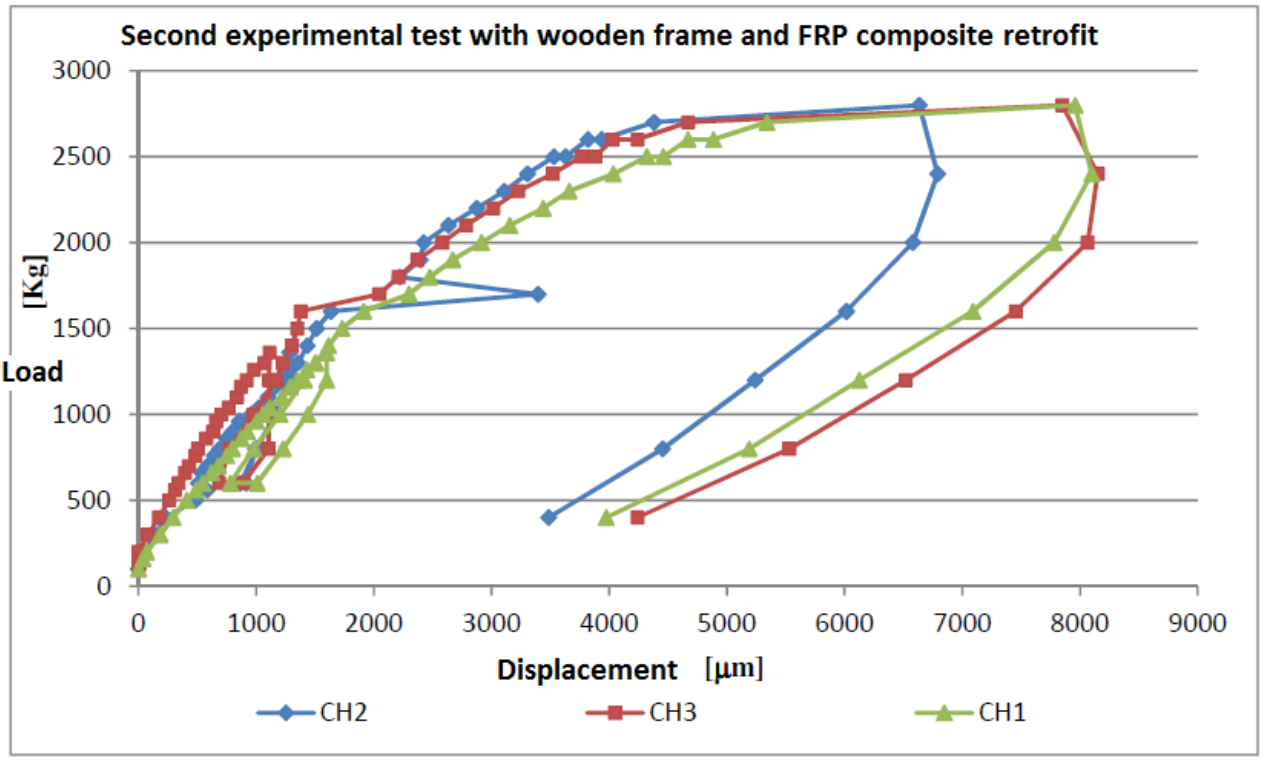

Figure 80 Second experimental test results with back wall retrofitted with FRP.

In the third test five strips of FRP composite where added to the front wall in order to repair the fracture on the front wall created during the previous test and to prevent its opening during the test as shown in Figure 81. An horizontal preload of 4kN was initially assigned to the back wall. Then, the horizontal load was increased to a maximum of 165 bar pressure into the hydraulic rams, corresponding to a maximum horizontal load of 35kN.

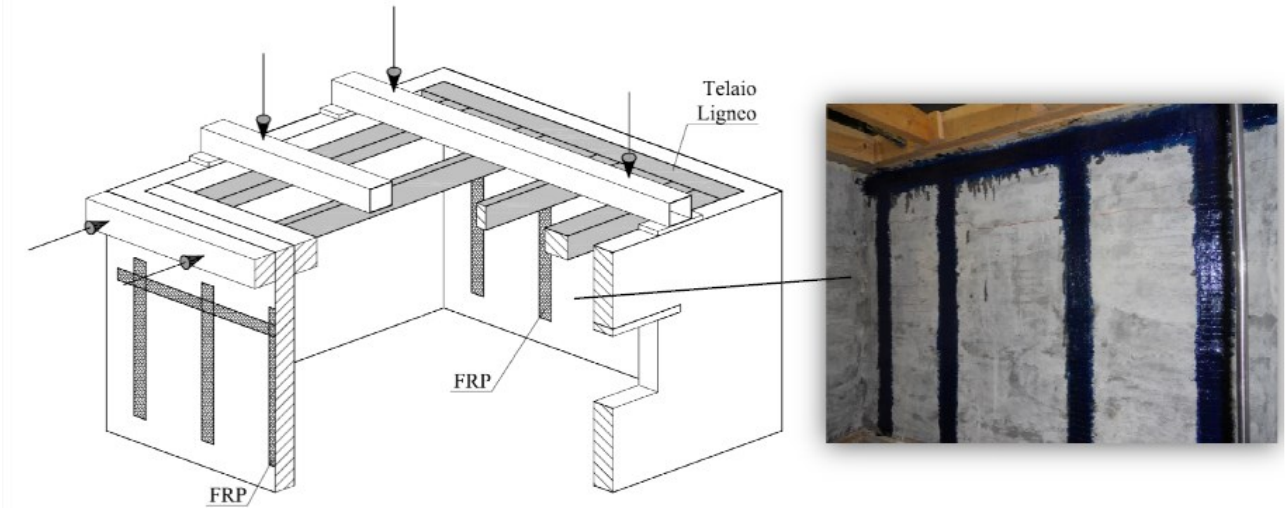

Figure 81 Third test experimental conFiguretion

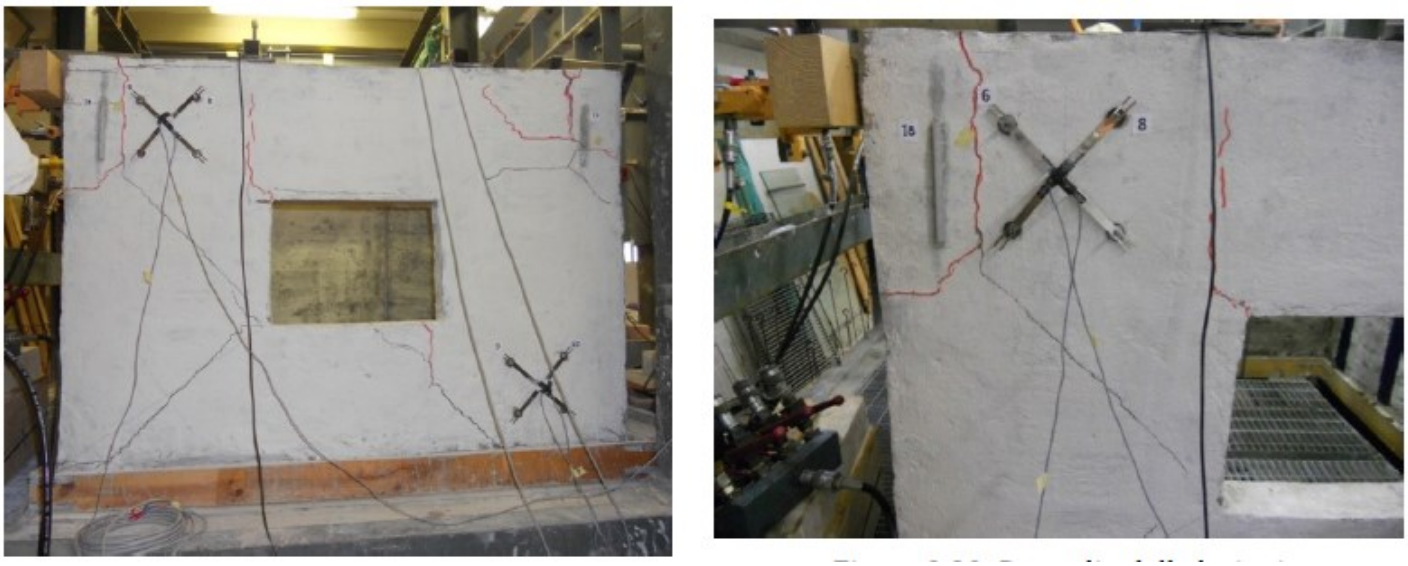

Figure 82 Detail of the cracking pattern at the end of the third test.

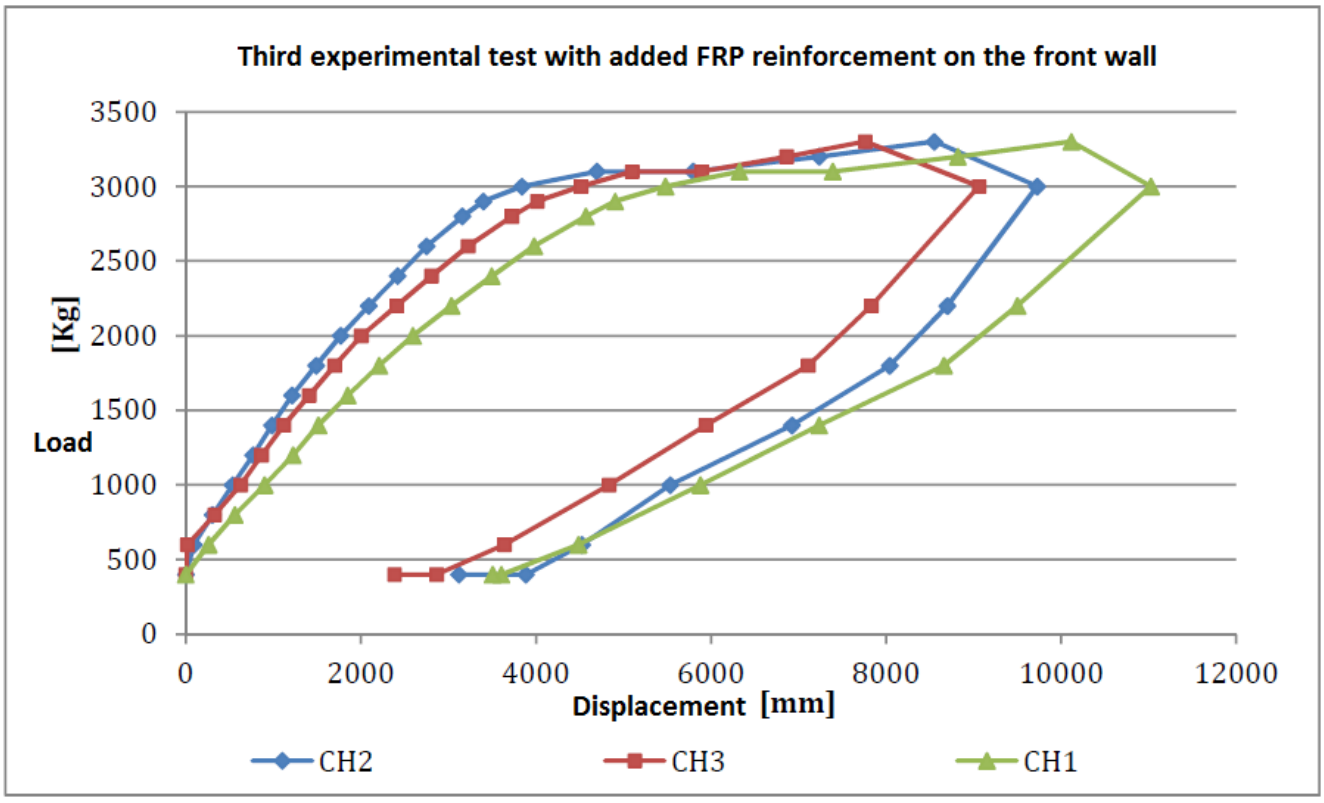

Figure 83 Third experimental test results with front wall added FRP retrofit.

In this third test local failure occurred upon formation of a diagonal fractures in the hollow wall as shown in Figure 81. Moreover, vertical cracks between the front wall and orthogonal walls appeared, showing the beginning of the overturning mechanism of the front wall. Results are summarized in terms of Load-Displacement measured by each LVDT transducer in Figure 83.

Diagrams in Figure 83, at 110-130 bar pressure, show a slight reduction of the global stiffness, due to the formation of diagonal cracks in the hollow wall. At a pressure of 150 bar (30kN) an abrupt diminution of global stiffness due to the formation of the overturning mechanism of the front wall is shown. Maximum displacement are significant upon the formation of the mechanism (8-10 mm) while residual displacements upon unloading are relatively big, 4mm.

For the fourth test, a double all-length FRP strip retrofit was applied to the upper and lower sides of the masonry box, as shown in Figure 84, in order to avoid the occurrence of the mechanisms observed during the third test. In particular, the upper ringing was incomplete since it didn't involve the back wall.

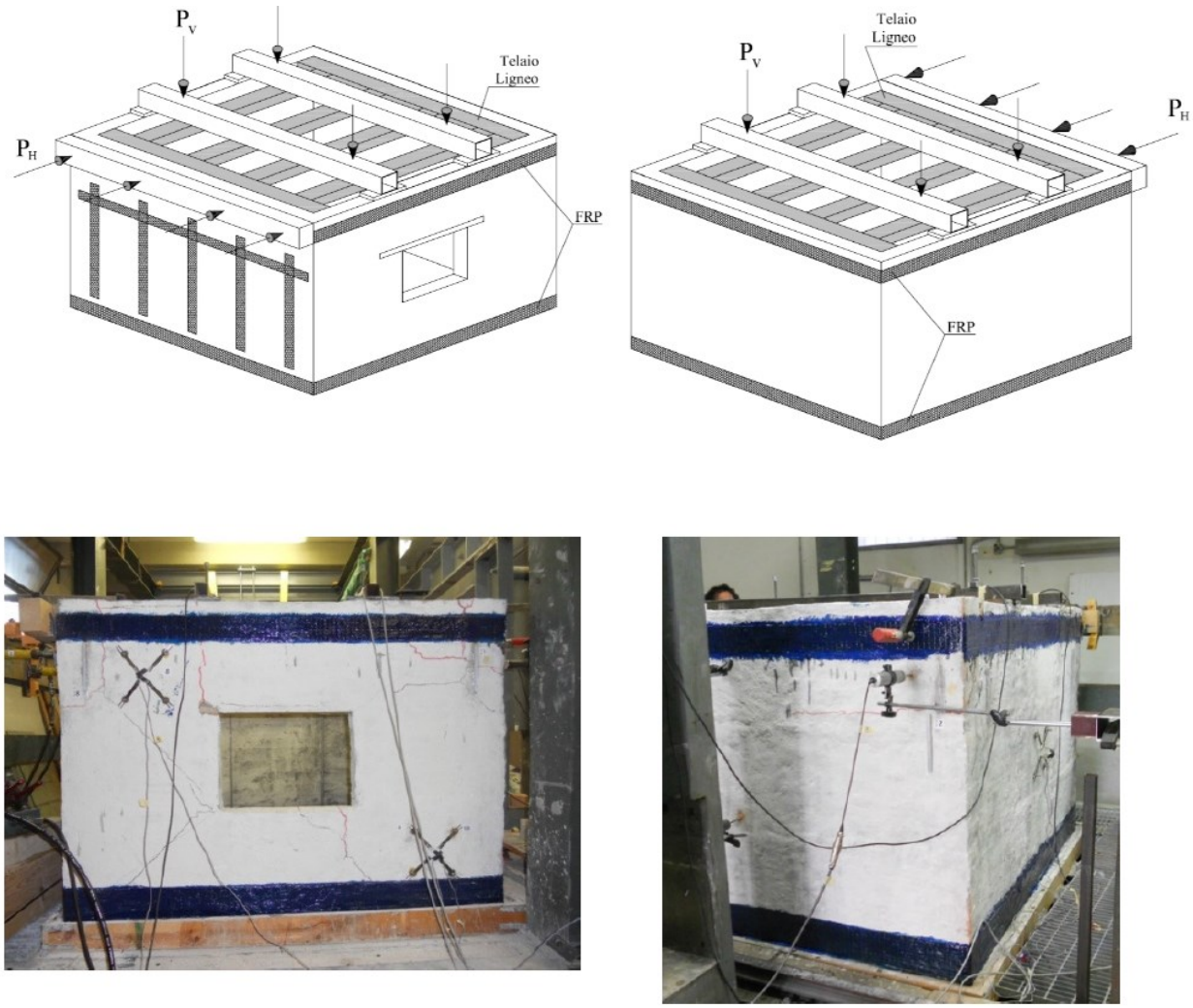

Figure 84 Fourth test experimental setup.

An horizontal preload of 4kN was initially assigned to the back wall. Then, the horizontal load was increased to a maximum of 200 bar pressure into the hydraulic rams, corresponding to a maximum horizontal load of 40kN. Cracks already on the walls from the previous tests opened more and more as shown in Figure 85. Delamination of the FRP strip occurred on the wall part above the opening, as shown in Figure 85 and Figure 86, after the formation of a wide diagonal crack. An analogous occurrence happened on the central part of the front wall, where a vertical crack caused the FRP delamination as shown in Figure 87.

Figure 85 Cracks on the hollow wall and FRP delamination above the opening at the end of the fourth test.

Figure 86 Details of the FRP delamination above the opening at the end of fourth test.

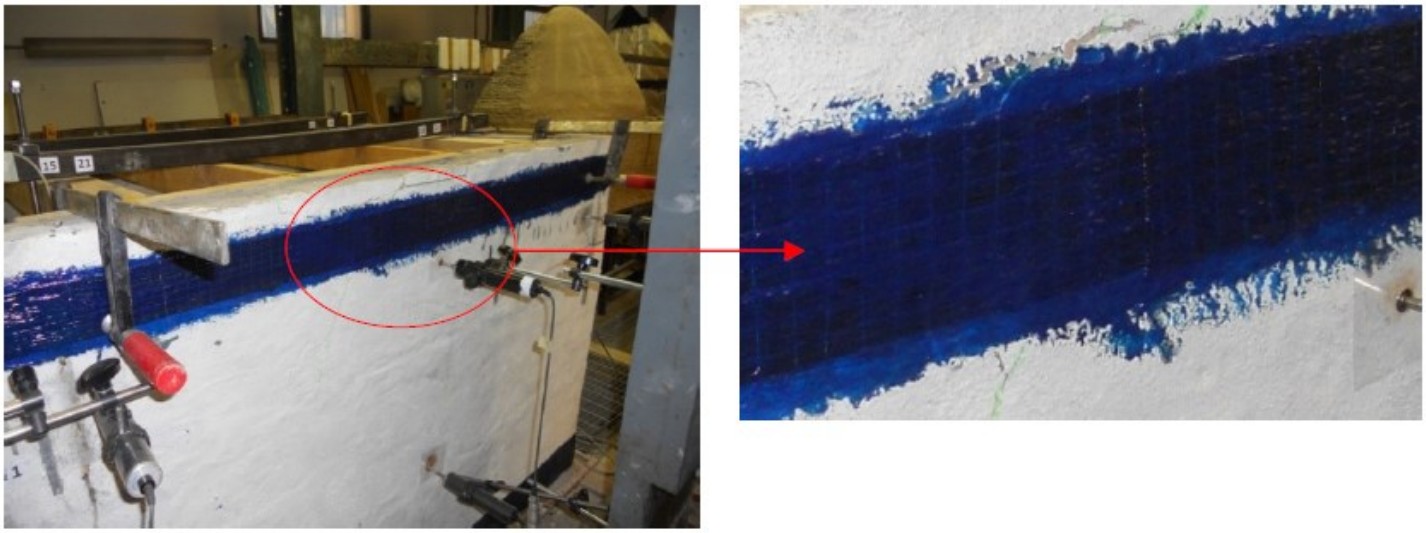

Figure 87 FRP delamination in the central part of the upper front wall.

Results are summarized in terms of Load-Displacement measured by each LVDT transducer in Figure 88.

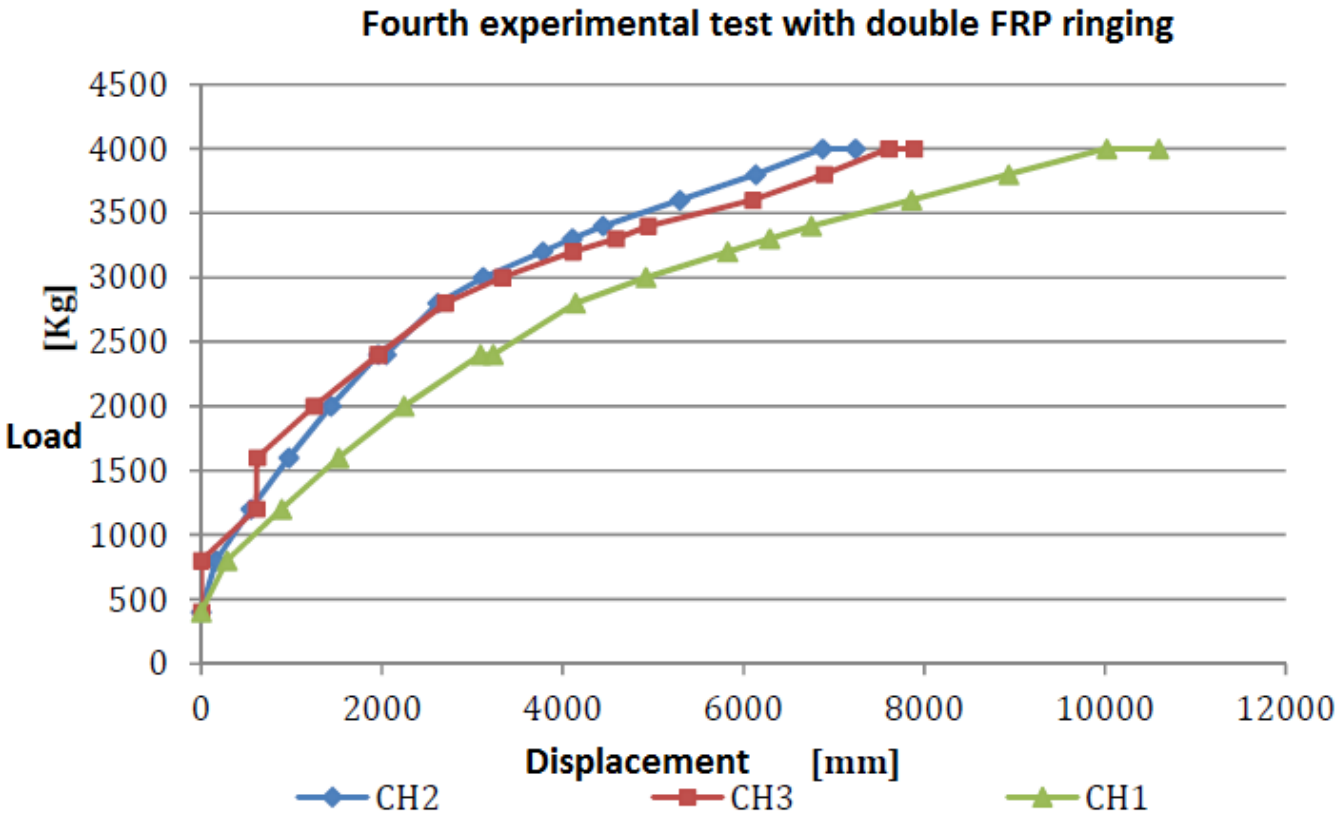

Figure 88 Fourth experimental test results with double FRP ringing.

Diagrams in Figure 88, at 150 bar pressure, show an analogous behavior of the third test. This fact explains why FRP reinforcements do not modify the damage status but inhibit possible collapse mechanisms. At a pressure of 200 stiffness changes but remains linear up to the appearance of delamination phenomena. Maximum displacement are significant upon the formation of the mechanism (8-10 mm).

3.4.2 Tests with the SMA device

The tests without the SMA device have shown that the collapse of the masonry box happens upon a total horizontal load of about 20-30kN, which stands perfectly in the working range of the SMA device. Displacements upon collapse are of the order of magnitude of 10^-2 m and the SMA device is capable of allowing elongations up to 4cm.

The model was modified by leaving a gap between the front wall and the two orthogonal walls, in order to facilitate the overturning mechanism of the wall. Besides, the new SMA device was introduced, in series with the FRP retrofit wrapping, as shown in Figure 89. A series of three tests was conducted, modifying the total length of the different wire groups within the device, in order to get three different conFiguretion for the device:

1) ConFiguretion TF1: An initial positive traction distortion of 0.5% was applied to the central group of wires, whilst the other groups were leaved unclamped (allowing for free displacements). In this way only the central group exploits the superelastic behavior and the device exhibits a monoplateau kind force displacement response.

2) ConFiguretion TF2: An initial positive distortion of 0.5% was applied to the central group of wires whilst a second group of wired gets 0 distortion and the third is left displacement free. In this case the device exhibits a double plateau superelastic response.

3) ConFiguretion TF3: : A initial positive distortion of 0.5% was applied to the central group of wires whilst a positive distortion of 0.8% was applied to the second group and a positive distortion of 0.2% was applied to the third group of wires. In this way the device works with three superelastic plateaus.

Test Number 1: SMA device in the TF1 conFiguretion

Figure 89 The masonry box model before test n. 1 with SMA device

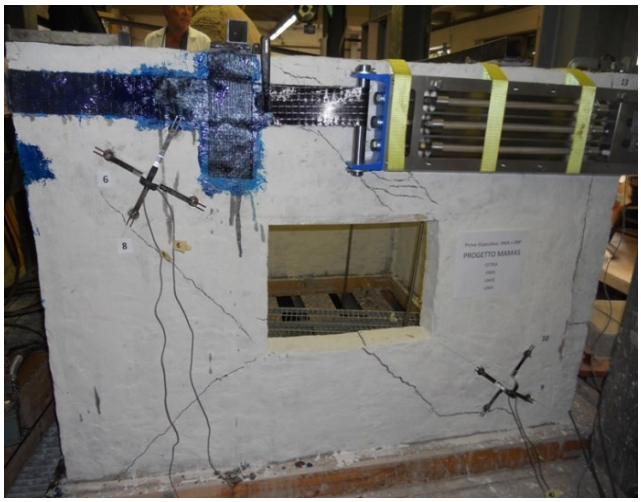

Figure 90 First damage to the hollow wall: total load 16KN

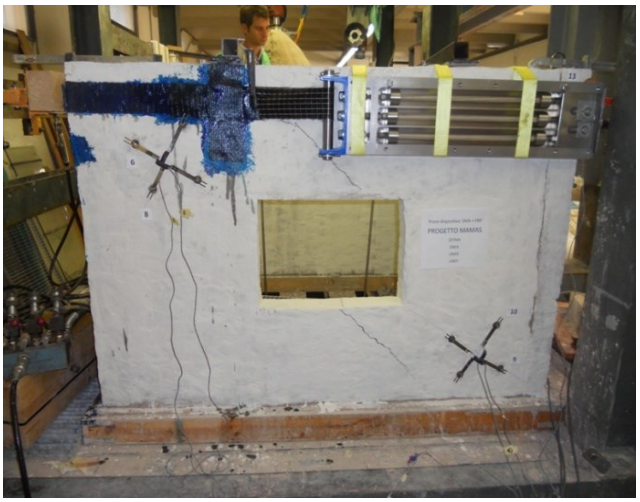

Figure 91 Final damage to the hollow wall: total load 20KN

In Figure 90 is depicted the masonry box before the execution of the test, while in Figure 92 is depicted the masonry box after the execution of the test. In Figure 92 the results of the first test are shown in terms of a force-displacement diagram.

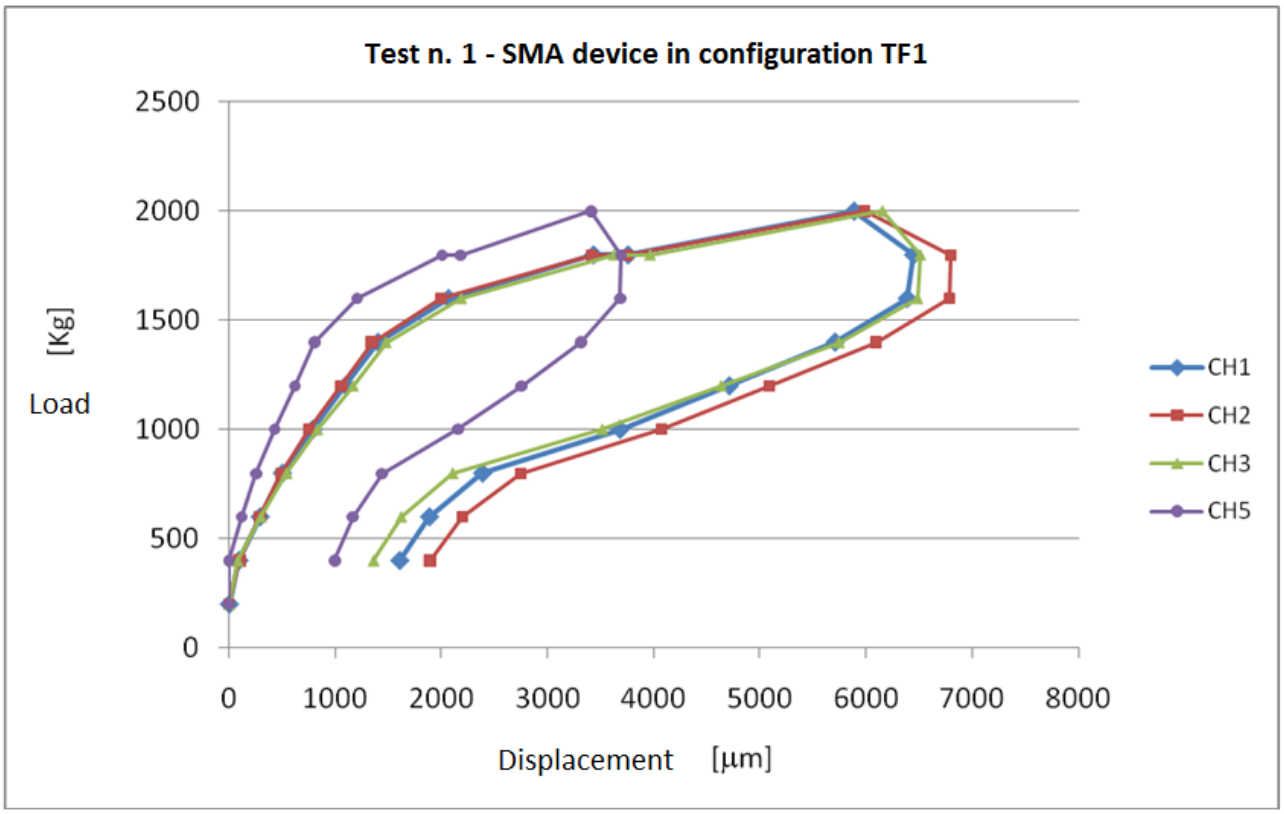

Figure 92 Force-displacement diagram for test n. 1 with SMA device

Description of the test:

In order to avoid local collapse mechanisms like the ones observed during the first series of tests five vertical FRP strips were applied to the wall directly loaded by the hydraulic rams and a complete FRP ringing system was applied to the upper part of the structure (except the wall at risk of overturning). To this system the SMA devices were applied in order to prevent the front wall from overturning. The devices where connected to the orthogonal walls through the FRP strips and to the front wall through a steel plate. The SMA device was in conFiguretion TF1.

The test was conducted at first by applying an initial pressure of 10bar to the hydraulic rams (equivalent to a total effective load of 2kN) and resetting the measuring devices. During the test, the load is progressively increased.

At a pressure of 80bar (16kN total load) shear fractures on the hollow wall appeared and looking at the diagram in Figure 89 it's possible to observe a corresponding reduction in the global stiffness at a displacement of 2.5mm.

At a pressure of 100bar (20kN) diagonal cracks become evident even on the front wall.

Even during unloading, Figure 89, a change in stiffness is observed at 40bar (8 kN). Residual displacements where well below 2mm.

Interpretation of results:

Diagrams in Figure 89 shows that:

- Superelastic plateau is activated at a displacement of around 2.5mm, which was expected.
- Superelastic behaviour allows for the closure of cracks upon unloading.
- The amplitute of the hysterises cycle proves the dissipation capabilities of the device.

Test Number 2: SMA device in the TF2 configuration

In Figure 93 is depicted the masonry box before the execution of the test, in particular a detail of the crack pattern on the hollow wall is shown. In Figure 94 the results of the first test are shown in terms of a force-displacement diagram.

Figure 93 Crack pattern after the execution of the test n. 2 in the hollow wall.

Description of the test:

FRP reinforcement were the same of test n. 1. Again the SMA devices were applied along orthogonal walls. SMA devices are now in conFiguretion TF2 (i.e. double plateau superelastic behavior).

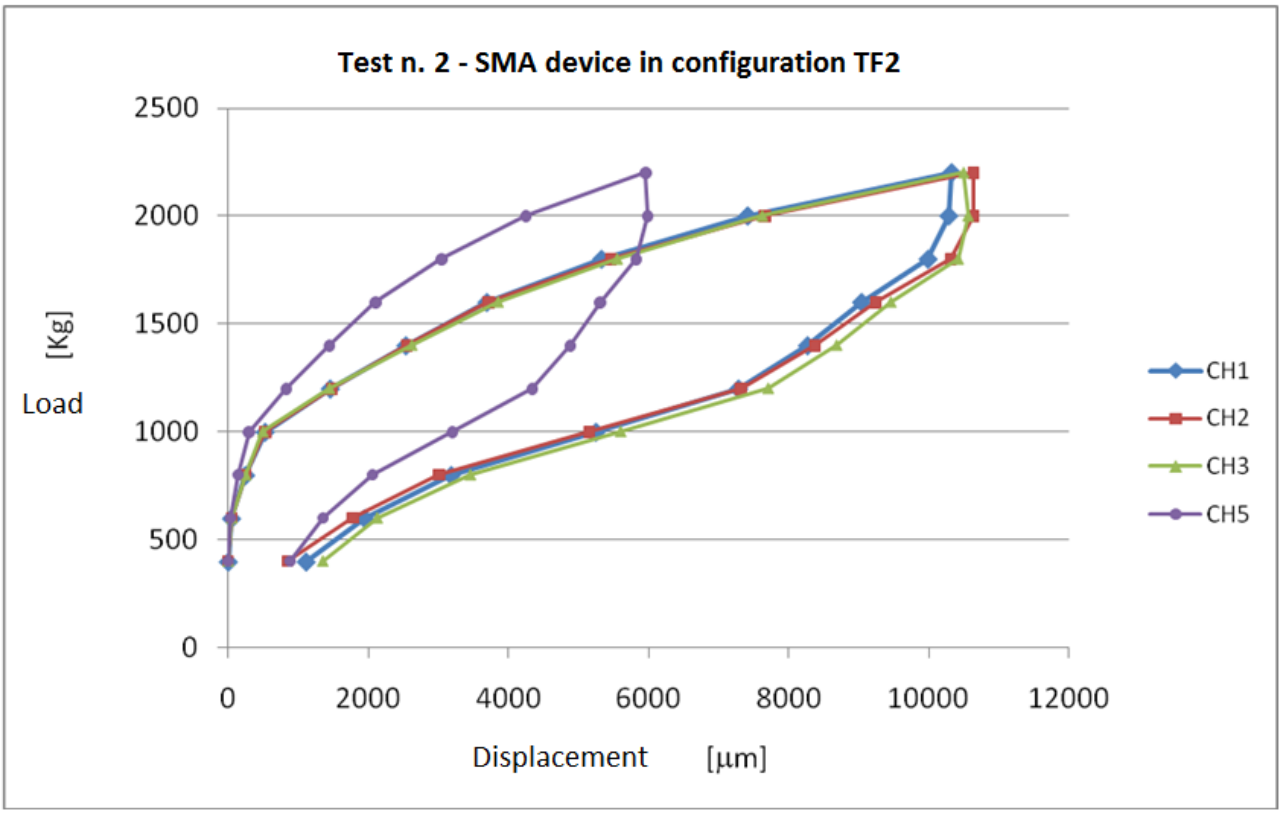

Figure 94 Force-displacement diagram for test n. 2 with SMA device

The test was conducted at first by applying an initial pressure of 20bar to the hydraulic rams (equivalent to a total effective load of 4kN) and resetting the measuring devices. The load was then progressively increased.

At a pressure of 50bar (10kN total load) , looking at the diagram in Figure 94, it's possible to observe a reduction in the global stiffness while the damage level increases.

At a pressure of 110bar (22kN) diagonal cracks become evident even on the front wall, which is now completely detached. The collapse is straight ahead and so unloading was decided.

Interpretation of results:

Diagrams in Figure 89 shows that:

- At a displacement of 4mm, a first superelastic plateau is developed.
- Due to the superelastic behavior the closure of cracks upon unloading is observed.
- The amplitute of the hysterises cycle proves the dissipation capabilities of the device.

- It doesn't appear clearly the second superelastic superplateau even if with a displacement of 8mm an increment in stiffness is observed due to the activation of the second group of wires.

Test Number 3: SMA device in the TF3 configuration

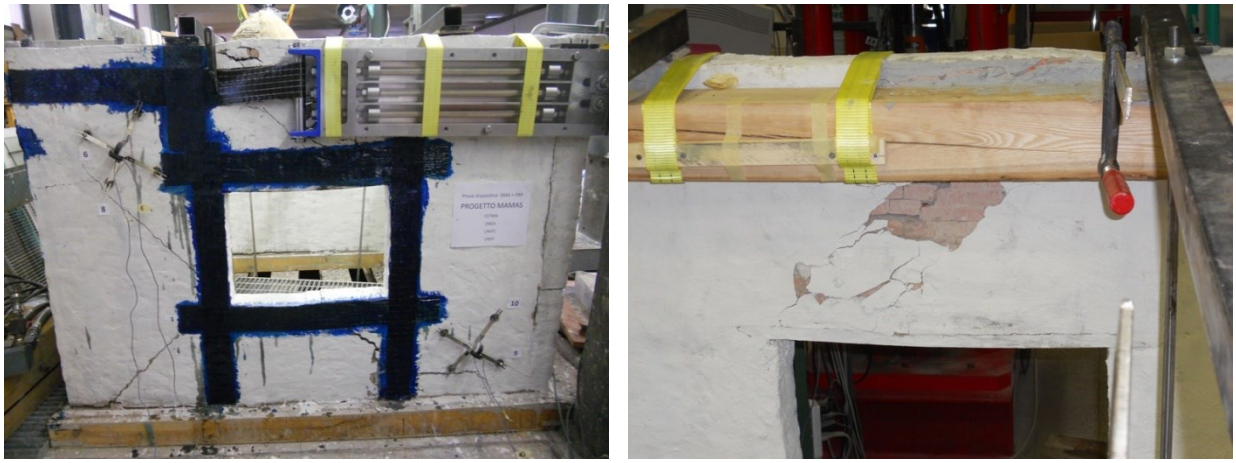

Figure 95 Crack pattern after the execution of the test n. 3 in the hollow wall.

Figure 96 Details of FRP delamination around the hole and detachment of the wall directly loaded by hydraulic rams

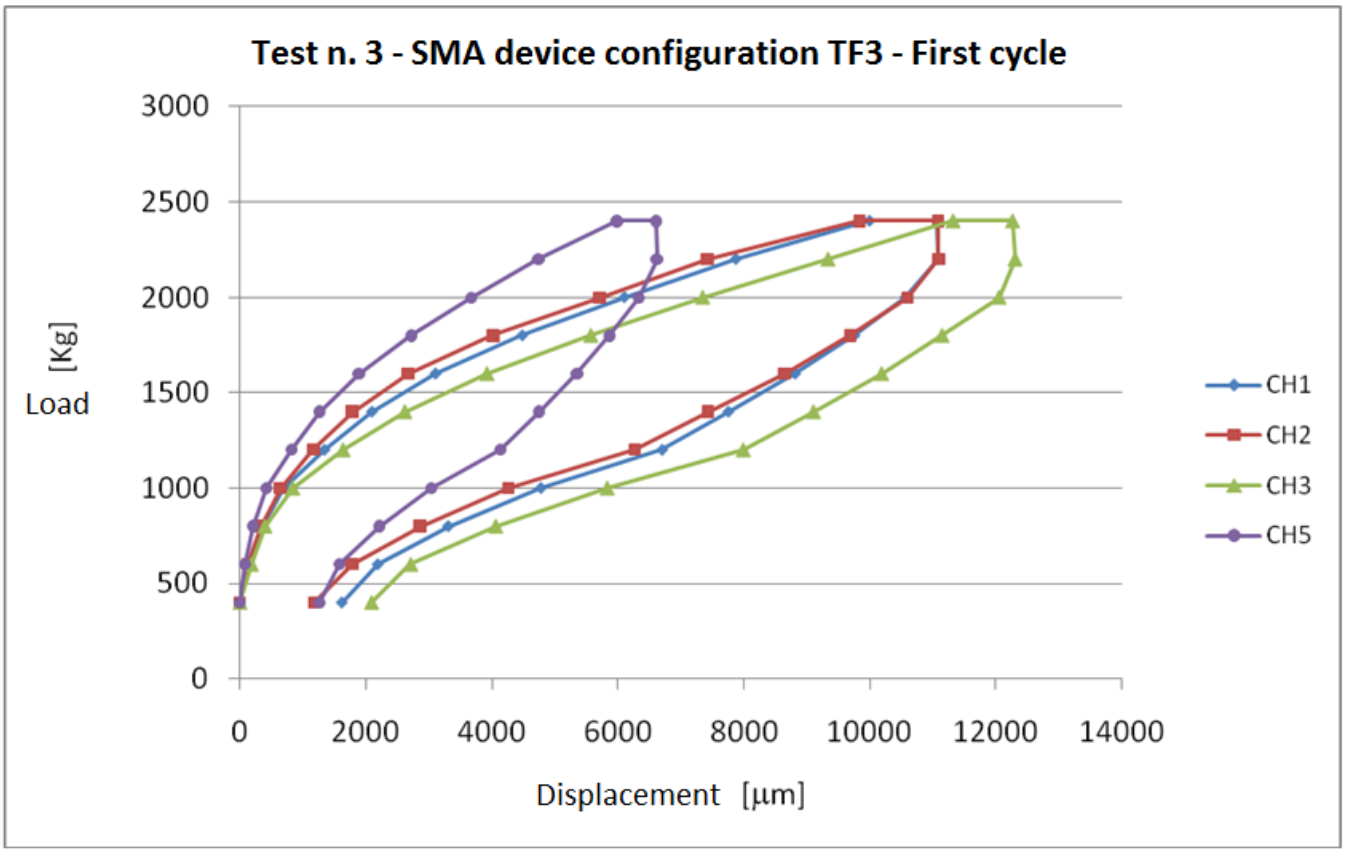

Figure 97 Test n. 3 – First loading-unloading cycle

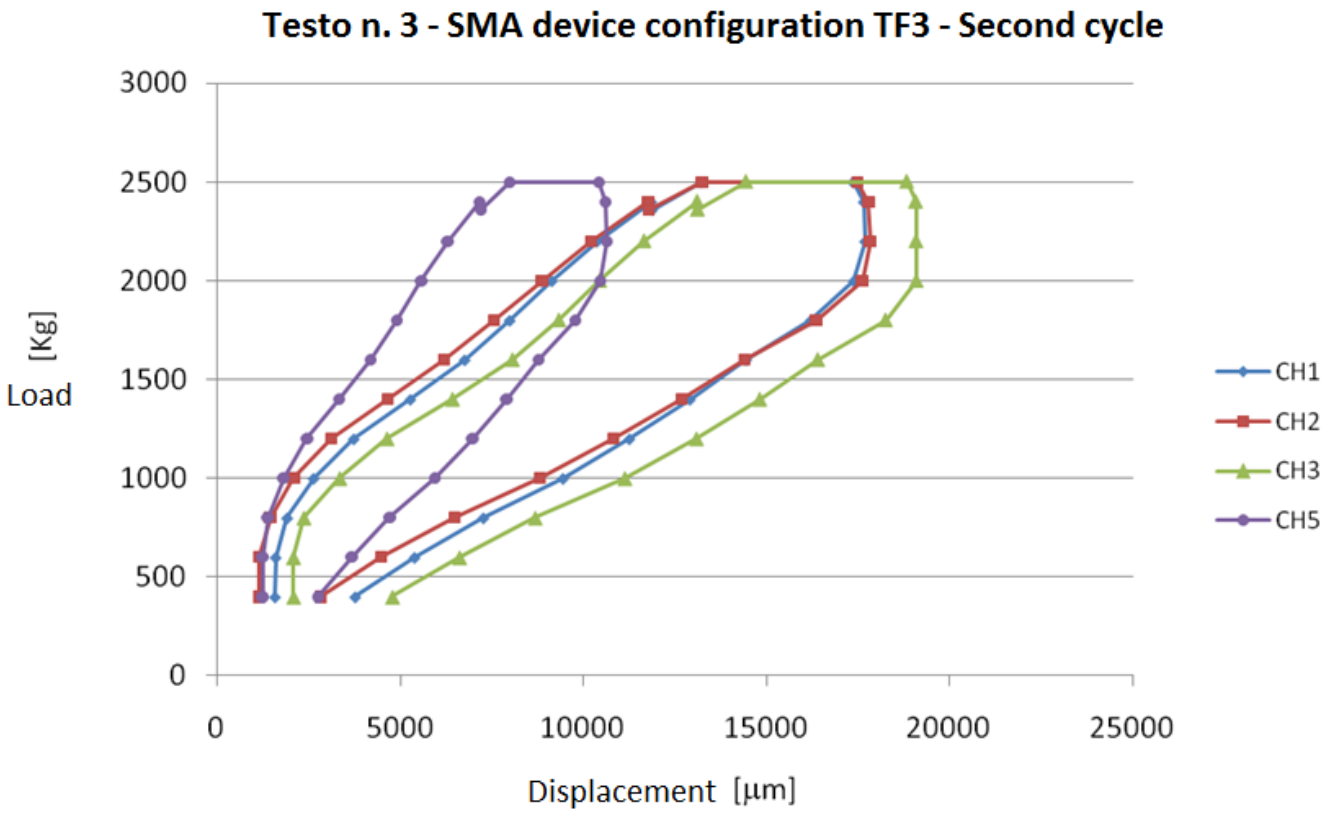

Figure 98 Test n. 3 – Second loading-unloading cycle

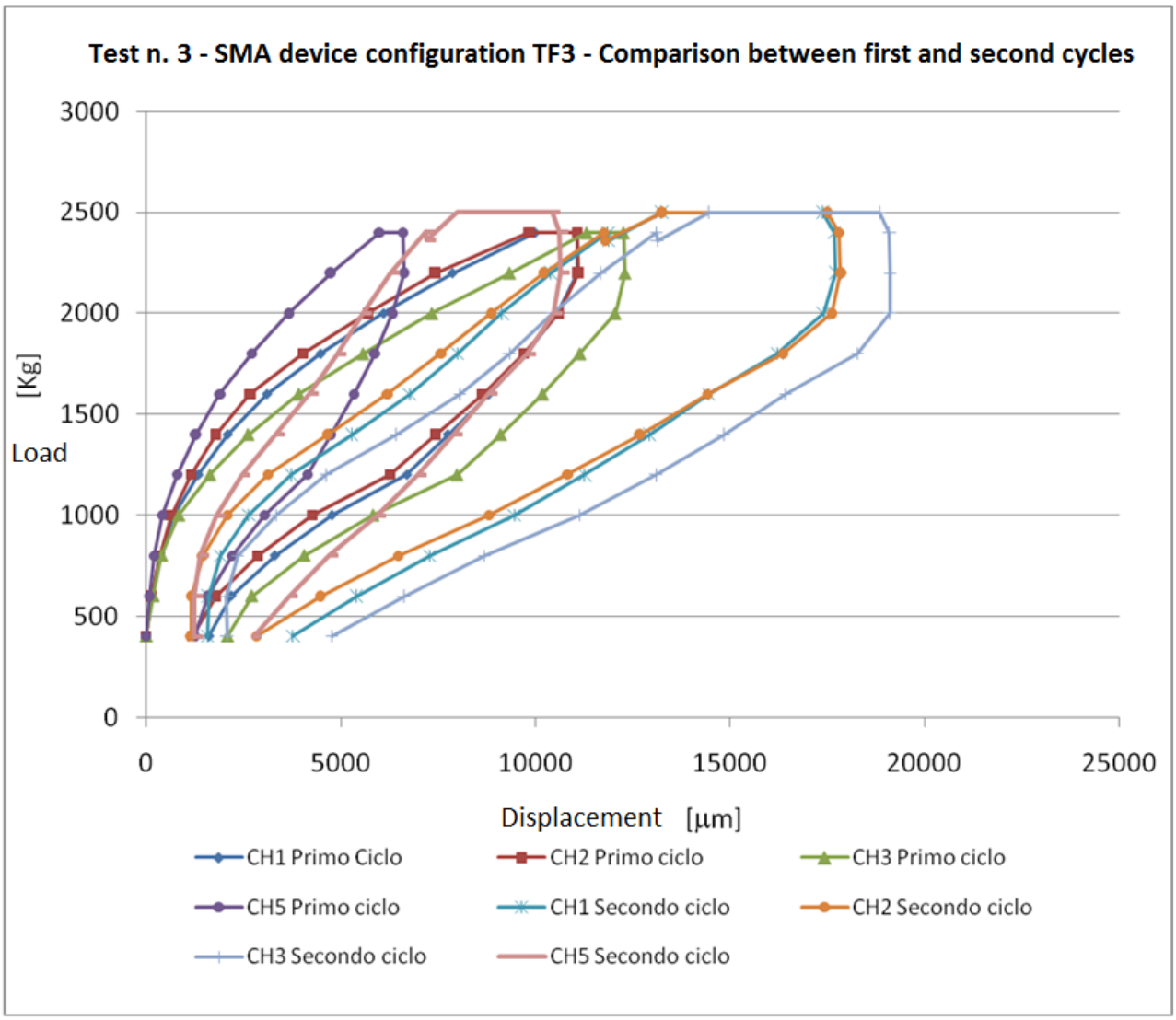

Figure 99 Test n. 3 – Loading-unloading cycles - comparison

Description of the test:

FRP reinforcement present in the previous tests are still present. In addition, a further FRP reinforcement is added around the hole in order to prevent the collapse mechanism observed during test 2. Again the SMA devices were applied along orthogonal walls. SMA devices are now in conFiguretion TF3 (i.e. triple plateau superelastic behavior).

The test was conducted at first by applying an initial pressure of 20bar to the hydraulic rams (equivalent to a total effective load of 4kN) and resetting the measuring devices. The load was then progressively increased.

Looking at the diagram in Figure 97, it's possible to observe a reduction in the global stiffness while the damage level increses, at displacements of 1.5-2 mm (when the first group of wires reaches the superelastic plateau), 5 mm (the second group of wires reaches the superelastic plateau) and 10mm.

At a pressure of 120bar (24kN) the collapse is straight ahead and so unloading was decided.

During unloading new stiffness variations are observed at pressures 100bar (20kN), 60bar (12kN) and 30 bar (6kN). Residual displacement upon complete unloading appear well under the value 2mm.

After some time, with the same modalities a new loading-unloading cycle is performed. The results are shown in Figure 98 and compared to the ones obtained during first cycle in Figure 99. Even during this second cycle, it's possible to observe a reduction in the global stiffness while the damage level increses, at displacements of 2.5-3 mm and a pressure of 50bar (when the first group of wires reaches the superelastic plateau), 5 mm and a pressure of 70bat (the second group of wires reaches the superelastic plateau) and 10-11 and a pressure of 120bar.

At a pressure of 125bar (25kN) the collapse is straight ahead and so unloading was decided.

Again, during unloading new stiffness variations are observed at pressures 100bar (20kN), 60bar (12kN) and 30 bar (6kN). Residual displacement upon complete unloading appear well under the value 4mm.

At the maximum load value (125bar), the detachment of the fiber which was preventing the activation of the diagonal crack near the hole was observed. Fractures on the front wall propagated and brought the structure to collapse.

Interpretation of results:

Diagrams in Figure 99 shows that:

- At each variation in stiffness a superelastic plateau was reached and thus the device in conFiguretion TF3 was working in the full multiplateau range.
- Due to the superelastic behavior the closure of cracks upon unloading is observed.
- The amplitute of the hysterises cycle proves the dissipation capabilities of the device.

3.5 Some numerical simulation

A finite-element numerical simulation of the first test with the SMA device in conFiguretion TF1 was carried on using the finite element software DIANA (Simoni 2012). The masonry walls orthogonal to the directly loaded wall were modelled with Curved Shell Flat Multilayer CQ40L elements. In particular two layers with thickness 4.25cm where assigned: for each layer five integration points were defined. The walls parallel to the direction of the horizontal wall are subject mainly to a plain stress state and are modelled with Plane Stress Elements Q12ME.

Between the hydraulic rims and masonry a wooden beam is placed, in order to grant adequate force distribution. This beam was modelled with a standard beam element.

The front wall is detached from orthogonal walls. Thus, a connecting element which grants a monolateral restraint was introduced. This restraint was modelled with Truss L2TRU Regular elements.

The front wall is connected to the masonry box through the SMA device which acts as a restraint against overturning of the wall. The SMA device is modelled through non linear elastic Truss Element, to which is associated a superelastic constitutive law (which is purely elastic, since no unloading is needed to be modelled), with replicates the response of the real SMA device.

FRP strips are modelled with plate elements which homogenizes both resin and fiber. In Figure 100 is shown the complete FEM model. The results of the numerical simulation are reported in Figure 101, Figure 102, Figure 103 in terms of force-displacement response and are compared to experimental data from test n.1.

The comparison between the load-displacement experimental curves and the ones obtained from numerical simulation shows a good agreement in the first elastic path and in the subsequent inelastic range of displacements.

The deformed shape and the color map shown in , shows the hollow wall is subject to a shear deformation way greater than the wall without openings. This behavior induces a differential displacement on the front wall, which doesn't overturn thanks to the reaction offered by the SMA device. On the wall with opening diagonal inelastic traction deformations are observed, which depart from the corners of the window while involving the whole wall as the load increases.

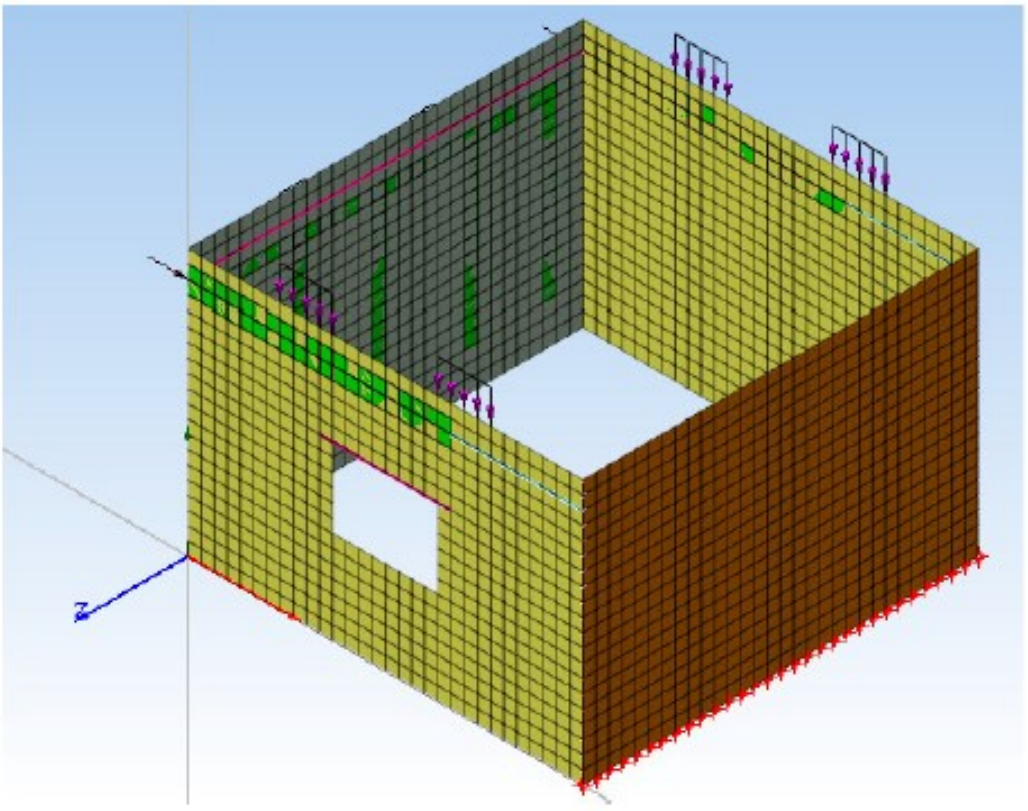

Figure 100 FEM model of the masonry box.

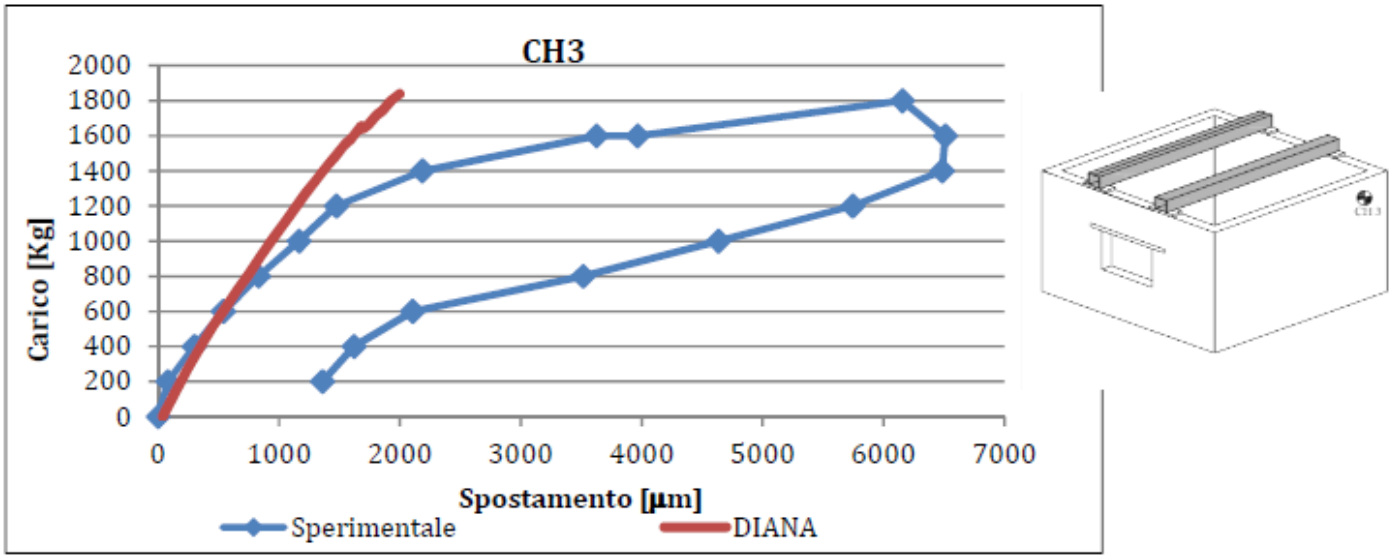

Figure 101 Comparison between experimental data and numerical simulation for test n.1 and CH3

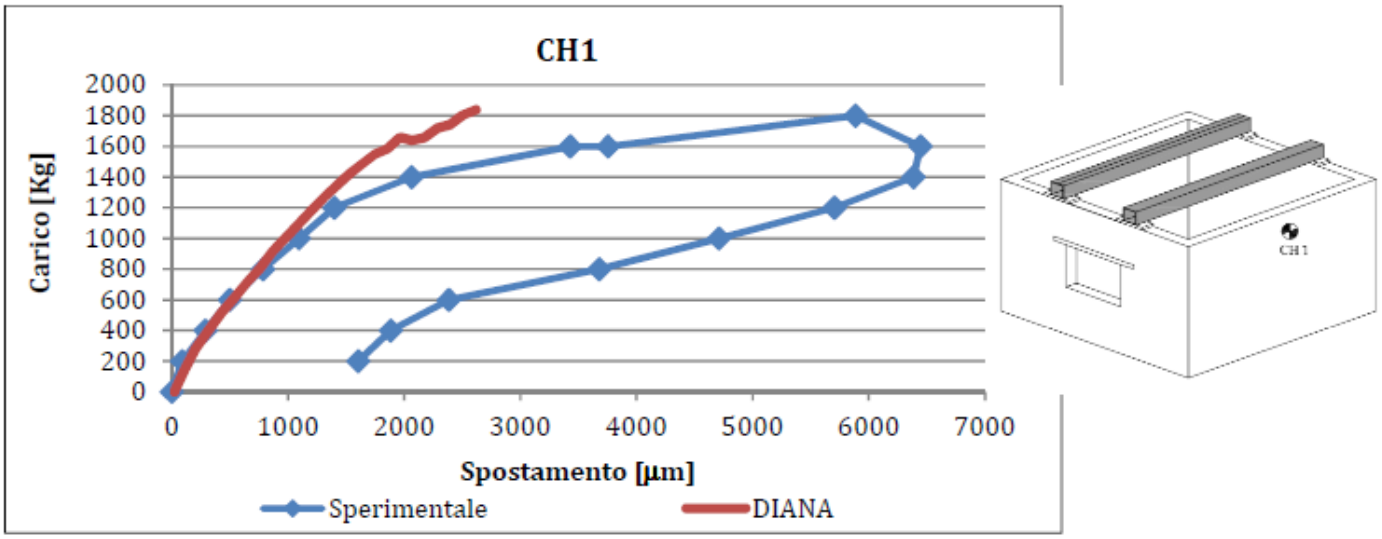

Figure 102 Comparison between experimental data and numerical simulation for test n.1 and CH1

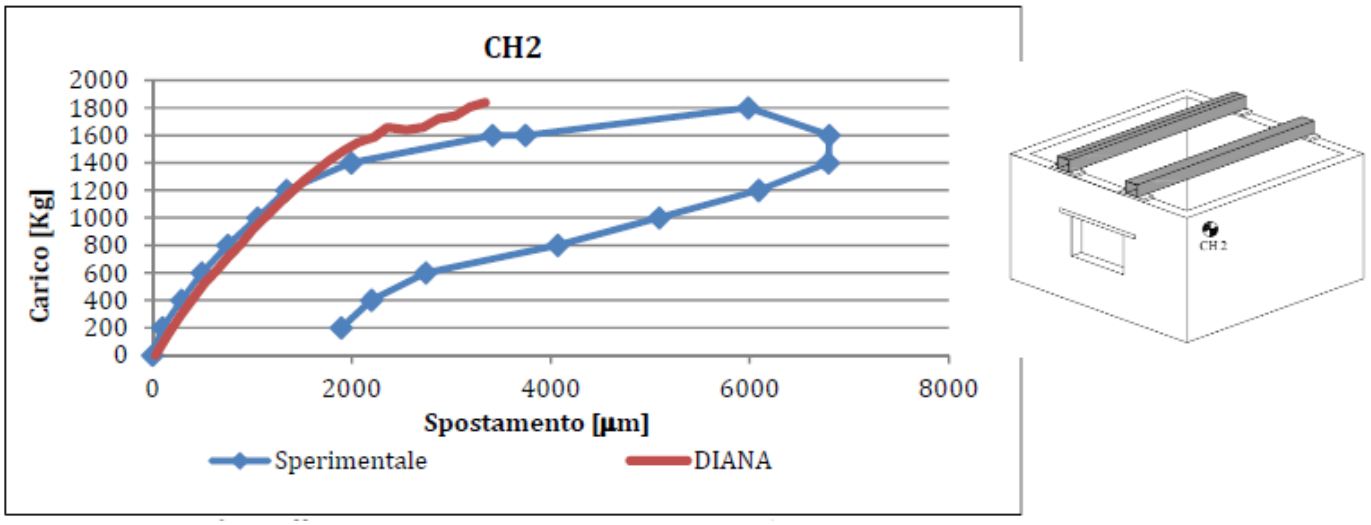

Figure 103 Comparison between experimental data and numerical simulation for test n.1 and CH2

Experimental observation shown in the previous paragraph has analogies with the crack pattern of Figure 104, describing a global behavior of the masonry box with diffuse cracks on the wall with an opening and almost none on the other walls. The loss of stiffness of the whole masonry box observed experimentally for a displacement of 2.5mm finds correspondence on the load-displacement curves obtained through finite element analysis.

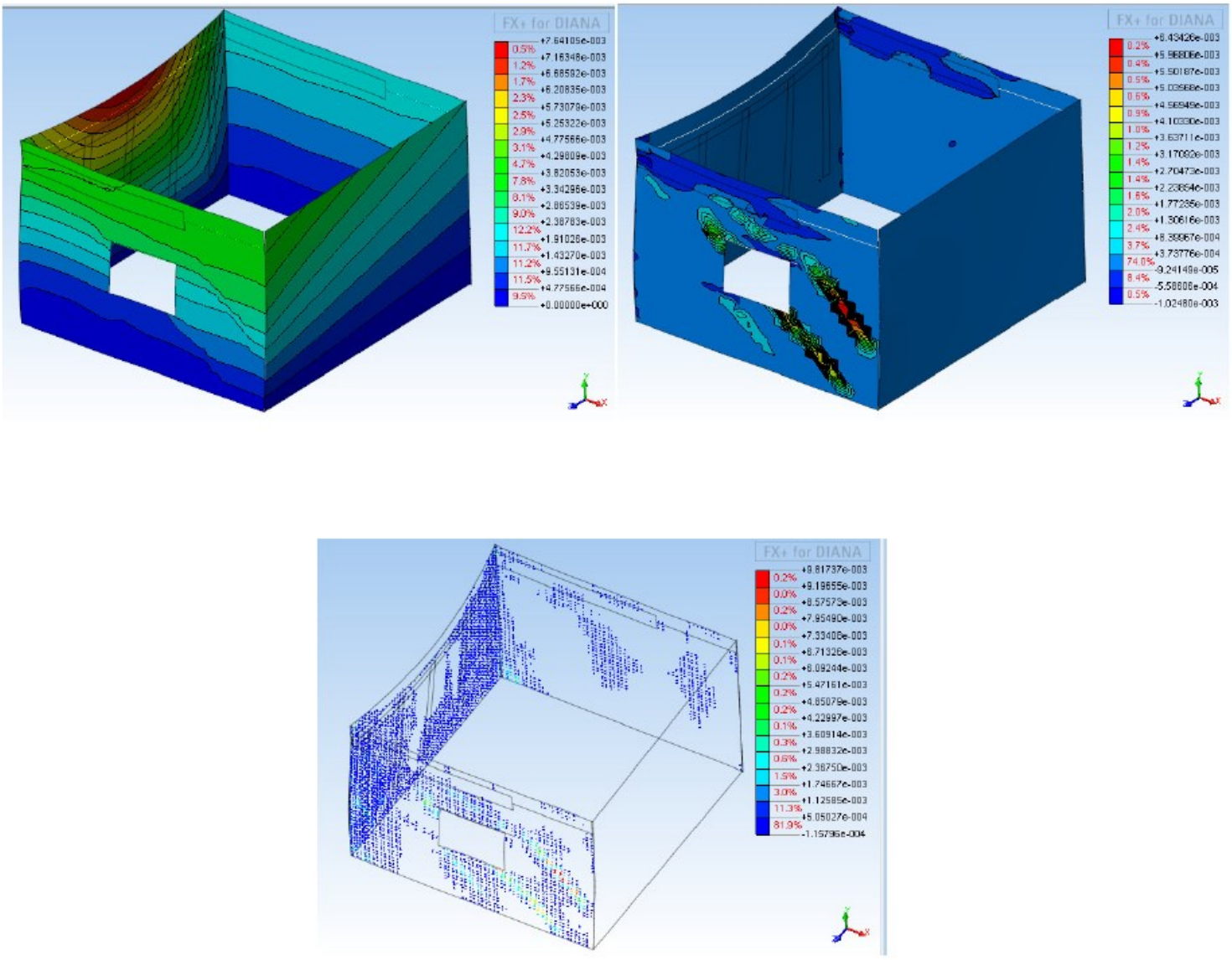

Figure 104 Deformed shape and color map relative to the displacement in the x-direction; inelastic deformations in correspondence of the limit load; crack pattern.

4 EXPERIMENTAL INVESTIGATION OF SHAPE MEMORY POLYMER STRIPS: THE CASE OF DESMOPAN DP 2795A.

4.1 Introduction

Shape memory polymers (SMPs), as already discussed, are polymers that return to their original shape even after undergoing significant deformation, on the application of a suitable trigger. Shape memory polymers can be used as an alternative to shape memory alloys in many applications and more importantly they can be used in applications where shape memory alloys cannot be used. Shape memory polymers are cheaper to produce than shape memory alloys as they can easily be processed into a variety of different shapes and sizes using standard processing methods such as extrusion, molding or forming. Most common shape memory polymers use an increase in temperature to trigger the transition from one shape to another. Their transition temperature can be altered and set to be any temperature within a large window by simply adjusting their chemical structure and composition.

The mechanisms responsible for the memory of the polymer are: the entanglement of polymer molecules, cross-linking and the fact that the polymer has a crystalline state as well as a glassy state. Depending on the specific polymer, one of these four mechanisms is responsible for fixing the transient shape. If glass transition is responsible for the transient shape, then the glass transition temperature T_g is the recovery temperature T_r. If it is due to crystallization the transition temperature T_m is the recovery temperature. If the transient shape is determined due to crystallization, then such shape memory polymers are called crystallizable shape memory polymers and if the transient shape is fixed due to glass transition, such shape memory polymers are called amorphous shape memory polymers. In this chapter an experimental investigation on a particular thermoplastic shape memory polyurethane, named DESMOPAN DP 2795A and produced by Bayer Material Sciences, is presented. The tests were carried out in the laboratories of the Institute für Angewandte Mechanik, RWTH Aachen University. The specimens used in the experimental campaign are bone-shaped strips subjected to axial tensile tests performed at different loading rates and at different temperatures. In order to reproduce the shape memory effect, thermo-mechanical cycles are performed as well. As will be clearer later on, from the results of the thermo-mechanical tests it is possible to infer that DESMOPAN is a crystallizable shape memory polymer. For this reason it is

useful to give a short presentation of the thermomechanical behavior of crystallizable shape memory polymers (an extensive treatment of the subject may be found i.e. in (Landlein e Kelch 2002)).

Crystallizable shape memory polymers can be either thermosets or thermoplastics. Thermoplastic crystallizable shape memory polymers are block copolymers consisting of alternating chains of two different polymers (A and B) linked end to end. The polymers A and B are chosen so that the copolymer exhibits shape memory behavior. One of the constituent polymers, say A, is chosen to have a high transition or glass transition temperature, which we denote by T_h while the other polymer, represented by B, has a lower transition temperature denoted by T_r (for recovery temperature). When the polymer is cooled from a melt-like state the polymer with the higher glass transition temperature, here polymer A, solidifies first forming segregated hard domains. These hard domains are linked together by polymer B, which crystallizes at a lower temperature (T_r). Between these two temperatures ($T_r < T < T_h$) the material behavior is rubber-like, with the hard domains acting as cross-links due to which the polymer returns to its original shape even after

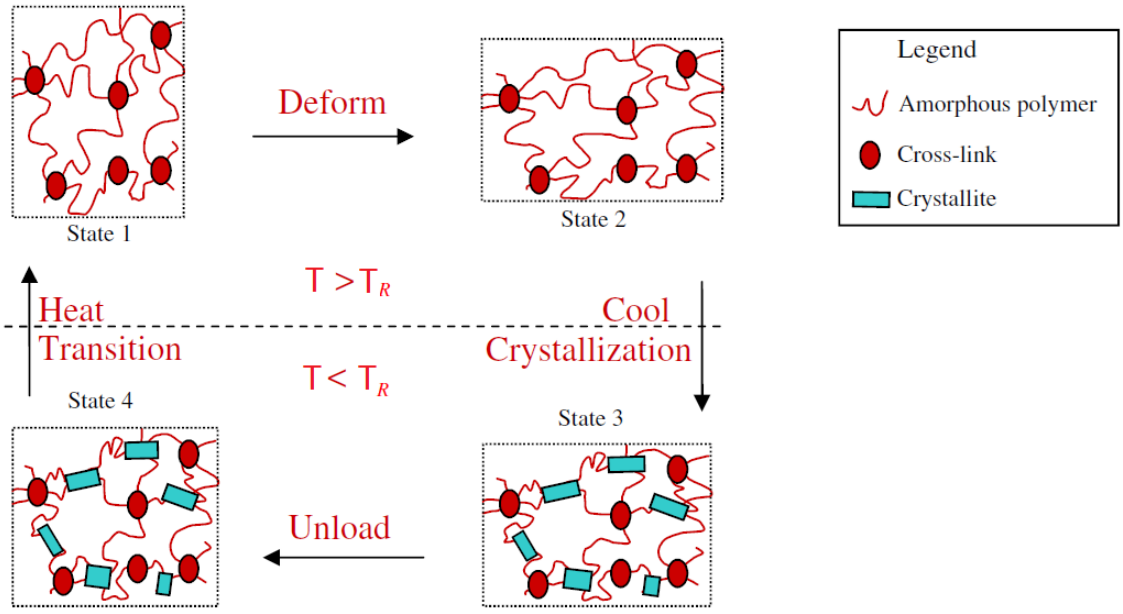

Figure 105 Schematic illustration of the shape memory effect in polymers.

undergoing large deformations. If the polymer is cooled below T_r, polymer B partially crystallizes and the material stiffens, losing its rubber-like behavior. If the material is cooled while it is in a deformed conFiguretion, polymer B crystallizes in this deformed conFiguretion, and these newly formed crystallites act as temporary cross-links which prevent the shape memory polymer from

returning to its original shape. On unloading the specimen at temperatures below T_r a small amount of recovery is observed as the polymer has its original cross-links still in place. On subsequent heating above T_r the crystalline phase associated with polymer B melts and the shape memory polymer returns to its original shape. On further heating above T_h the hard domains also melt and the material returns to the melt-like state.

The orientation of the crystals formed below Tr depends on the deformation undergone by the polymer just prior to cooling. These crystals will have a preferred direction depending on the deformation that will cause the material properties to be anisotropic.

Thermoset shape memory polymers also show similar behavior, except the permanent shape is a result of chemical cross-linking in a crystallizable polymer and not due to the presence of hard domains. Above the transition temperature of the polymer, which we again denote by Tr, the shape memory polymer has a rubber-like behavior due to the presence of chemical cross-links, however upon cooling below Tr, polymer crystallization takes place. These newly formed crystals act to stiffen the shape memory polymer with the crystallites acting as cross-links. If the polymer is deformed prior to cooling, the crystallites, which act as temporary cross-links are formed and as a result the polymer retains its transient shape. The original shape is recovered on heating above the transition temperature.

The behavior of these two types of SMPs, i.e., thermosets and thermoplastic SMPs is hence somewhat similar. The whole process described above is summarized in Figure 105. A typical uniaxial stress–strain curve is shown in Figure 106.

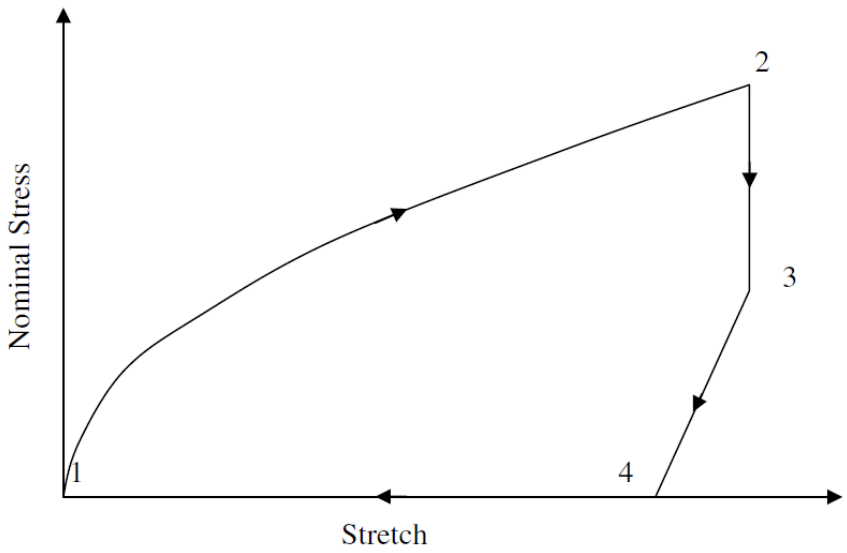

Figure 106 Typical stress-strain curve for a crystallizable shape memory polymer.

In Figure 105, the filled circles represent the cross-links (they could be the hard domains or chemical cross-links), the wavy line connecting the cross-links represents the crystallizable polymer in its amorphous state while the rectangular blocks represent the crystallizable polymer in a crystalline state. State 1 in both figures denotes the undeformed conFiguretion. Above the recovery temperature Tr the polymer's behavior is rubber-like. On deforming at a temperature above Tr, the polymer molecules between the cross-links stretch (state 2). If the polymer is now cooled to a temperature below Tr, crystallization takes place and the crystals are formed in this deformed conFiguretion. The onset of crystallization is accompanied by a sharp drop in the stress (from state 2 to state 3). After unloading (state 3 to state 4) the polymer remains in a deformed conFiguretion with a small amount of recovery. This recovery is due to the presence of two components (amorphous and crystalline) each with their own stress free states. The amorphous part has a tendency to retract to its original conFiguretion while the crystalline part prefers the deformed conFiguretion. As the crystalline part is a lot stiffer, the recovery strain is small (see Fig. 2). The mechanical response of the polymer in this state is similar to that of a semi-crystalline polymer with oriented crystallites, i.e., it is relatively stiff and the mechanical behavior is anisotropic. Usually when this semi-crystalline polymer is subject to small deformations it exhibits elastic behavior, energetic in origin. If however, the polymer is subject to large deformations, inelastic behavior is caused by reorientation of the crystallites and secondary crystallization takes place. During these inelastic processes degradation of the original cross-links can occur reducing the ability of the polymer to return to its original shape on heating. When the polymer is heated to above Tr (from state 4 to state 1) the crystallites melt returning to their original amorphous state, if the cross-links originally present in the polymer remain, the polymer retracts to its original shape. If the polymer is prevented from returning to its stress free state, a retractive force develops that depends on the extent to which the polymer was deformed prior to cooling and is an important parameter when shape memory polymers are used in actuators.

The deformation force may also be applied to a non-heated SMP (below Tr) and at least part of deformation may remain after loading removal (i.e. pseudo-plastic deformation). The deformation introduced in this way can still be recovered at an elevated temperature under a stress free condition. This non-conventional shape memory cycle is different from the ones discussed above, nonetheless it is observable in our tests.

The goal of this experimental work is addressed towards a better understanding of the mechanical behavior of a new polymeric material, in order to assess the basis for future constitutive modeling.

4.2 The material under investigation: DESMOPAN DP 2795A

DESMOPAN DP 2795A is a shape memory polymer derived from thermoplastic polyurethane and produced by Bayer Material Science, Leverkusen, Germany, following a patented process. DESMOPAN has a switching temperature of approximately 40°C. In Figure 107 and Figure 108, provided by Bayer, both the basic mechanical properties and the dependence of the (complex) elastic modulus on temperature are reported. As shown in Figure 108, the elastic stiffness changes quite abruptly at around 40°C when transformation from crystallized state to rubber-like state takes place.

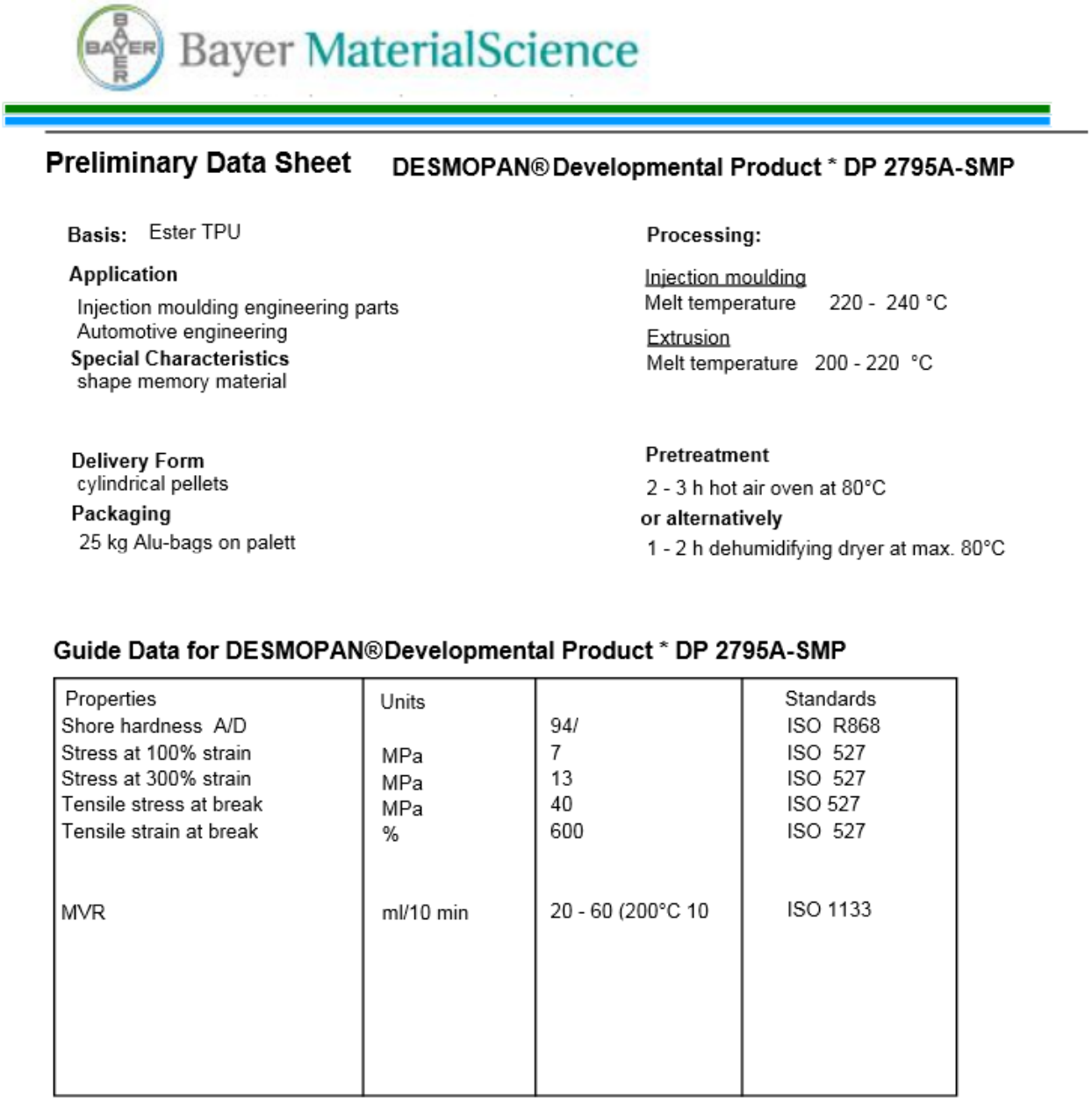

Bayer MaterialScience

Preliminary Data Sheet **DESMOPAN® Developmental Product * DP 2795A-SMP**

Basis: Ester TPU

Application
Injection moulding engineering parts
Automotive engineering

Special Characteristics
shape memory material

Delivery Form
cylindrical pellets

Packaging
25 kg Alu-bags on palett

Processing:

Injection moulding
Melt temperature 220 - 240 °C

Extrusion
Melt temperature 200 - 220 °C

Pretreatment
2 - 3 h hot air oven at 80°C
or alternatively
1 - 2 h dehumidifying dryer at max. 80°C

Guide Data for DESMOPAN® Developmental Product * DP 2795A-SMP

Properties	Units		Standards
Shore hardness A/D		94/	ISO R868
Stress at 100% strain	MPa	7	ISO 527
Stress at 300% strain	MPa	13	ISO 527
Tensile stress at break	MPa	40	ISO 527
Tensile strain at break	%	600	ISO 527
MVR	ml/10 min	20 - 60 (200°C 10	ISO 1133

Figure 107 Beyer DESMOPAN 2795A Data Sheet

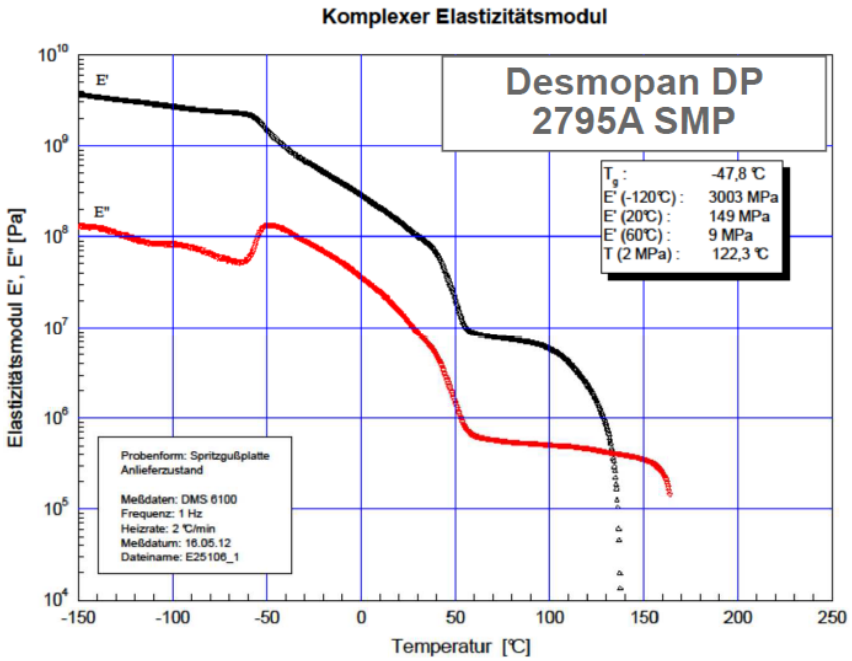

Figure 108 dependence of the (complex) elastic modulus on temperature for DESMOPAN DP 2795A

The shape-memory effect has two prerequisites: a polymer with a molecular network structure that contains at least two phases and a phase shift accompanied by a significant change of mechanical properties. DESMOPAN DP 2795A SMP – a phase-segregated block copolymer – meets these criteria.

The hard segment of DESMOPAN DP 2795A SMP is made up of polyurethane groups, among other molecules. The transition temperature of the hard segment is very high, exceeded only when the material is completely melted for injection molding or extrusion. This gives the material its permanent form. The soft phase of the material, which consists of long-chain polyesters, has a much lower transition temperature. When heat is applied, it can be fixed in a temporary form and stabilized by crystallizing the soft segments in a lattice structure.

Later, the crystallites of the soft segments can be heated, triggering the shape-memory effect: the material snaps back to its permanent form. Unlike traditional TPUs, DESMOPAN DP 2795A SMP has two phases. These can be engineered in clever ways for applications using shape-memory polymers.

DESMOPAN DP 2795A SMP is very suited for application thanks to its unique features besides shape memory effect: it has high resistance to wear (it exhibits high levels of tear strength, tear resistance and scuff resistance. Under certain conditions – wear in water, for instance – it has a

longer life than that of high-grade steel), it is weatherproof (its properties remain stable when exposed to UV light, moisture, and other elements), it is chemically resistant (it is resistant to corrosion from a wide range of substances, including oils, greases, and many solvents), it is environmentally friendly (it doesn't contain no plasticizers and is free of hydrolytic stabilizers) and recyclable.

DESMOPAN DP 2795A has already found application in the automotive field (it's used in the manufacture of wearing resistant surfaces in the interior of vehicles, cable sheathings and seals), in sport and leisure fields (hard wearing-reduced abrasion sport gearing), in coating and films field (durable skins for inflatable boats, solar modules with DESMOPAN embedding film, watertight and breathable films for rain jackets), in hoses, cables, belts and profiles field (pneumatic and hydraulic hoses with high compressive strength, toothed belts with outstanding wear resistance) and in agriculture, industry and mechanical engineering fields (abrasion-resistant elements, easy-to-grip soft-touch surfaces).

4.3 The experimental setup

In the experimental campaign a great number of tensile tests on DESMOPAN were performed, at different temperatures and different loading rates. Two different sets of specimens were available. The first set of specimens was composed by cold hand-machined bone shaped specimens, obtained from 3 mm thick DESMOPAN strips. The second set of specimens was made up of factory-molded bone shaped specimens, obtained directly from Bayer. In Figure 109 the two kind of specimens are depicted.

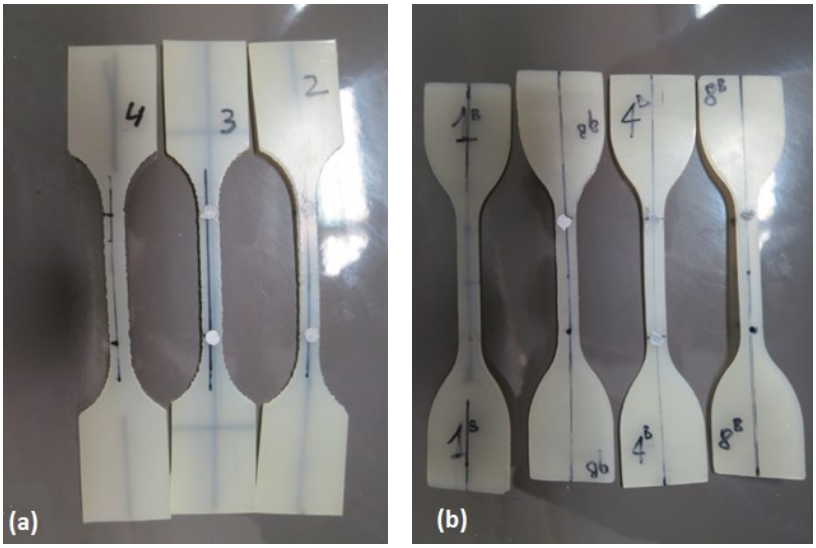

Figure 109 DESMOPAN bone shaped specimens, (a) hand-machined, (b) factory-molded.

The tensile tests were performed in the laboratories of the RWTH Aachen University through a Zwick-Roell universal testing machine with a 5kN load cell, heating chamber and liquid nitrogen cooling device. The experimental setup is shown in Figure 110.

Figure 110 Zwick-Roell universal testing machine at the RWTH Aachen University

The testing machine was used in conjunction with testXpert II software e was controlled though a windows based personal computer.

The machine is capable of allowing for extremely low loading speeds while granting excellent speed-constancy. The drive also delivers high crosshead travel resolution; this is important in tests on components requiring a high degree of travel-precision. The high test speed range can be used without restriction. In addition, test loads up to 110% of the machine nominal load are permissible

to compensate for heavy combinations of test fixtures, accessories etc. The faster return speeds reduce cycle times and increase test throughput, with AC drive technology ensuring that the motor is maintenance free.

Moving cross heads is guided very accurately via two steel columns, enabling precise force application to the specimen. This is advantageous for flexure, tests, compression tests and precision tests on components.

The testing machine is equipped with Xforce load cells developed and manufactured by the Zxick Roell Group. The effect of parasitic influences (such as temperature and transverse forces) on test results is significantly less than with other, comparable load cells. In addition, Xforce loads cells are very stable and less sensitive to transverse forces in compression and flexure tests, for example.

The machine is equipped with testControll II digital measurement electronics, mounted vertically on the load frame, which provides 6 flexible time-synchronized slots, enabling several sensors to be used at the same time. High data transmission rate (2000Hz) allows fast measurement combined with maximum reproducibility. This is highgly advantageous for rapid tests, short brittle fracture events and for tear growth. The high drive control frequency of 1000Hz enables fast, precise force and strain control. Benefits include enabling components to be loaded very quickly and accurately with the specified force.

Displacement are measured through a sophisticated optomechanical system.

The machine is equipped with an electric heating chamber, shown in Figure 111.

The heating chamber is used to perform tensile tests at high temperature. A picture of a specimen during an high temperature tensile test is shown in Figure 112.

In order to perform tensile tests at low temperature the heating chamber has been converted into a cooling chamber thanks to the upgrade of the system with an automated liquid nitrogen barrel which inject liquid nitrogen into the chamber in order to keep temperature at the value desired. A picture of the system is shown in Figure 113. The system was added to the testing machine in a second time, and in order to manage the risks linked to the usage of liquid nitrogen, the whole lab environment has been suited to the task, introducing a new aeration system and an O2-level environmental sensor, connected to an alarm system.

Figure 111 Zwick-Roell heating chamber

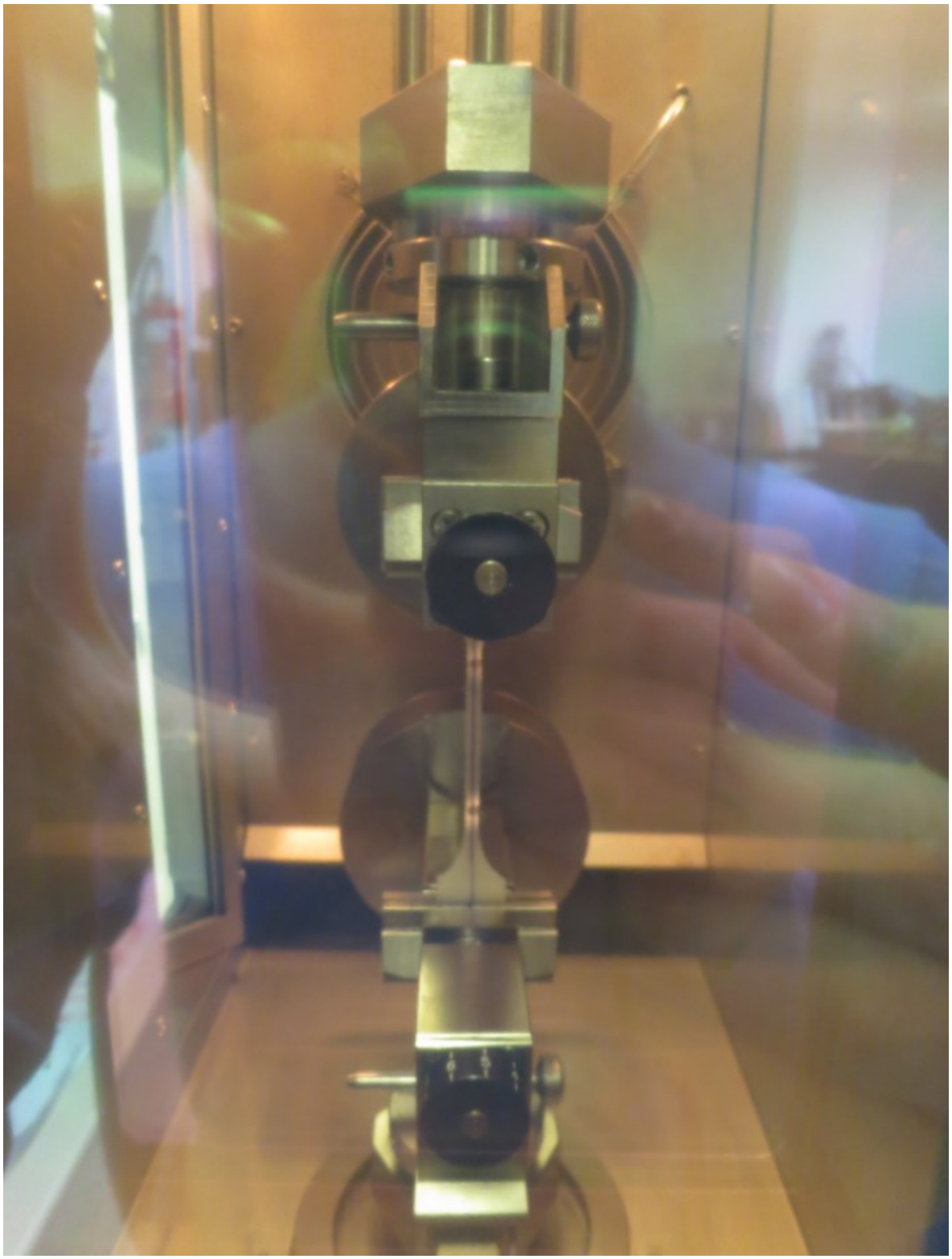

Figure 112 Tensile test in the heating chamber.

Figure 113 Liquid nitrogen cooling system.

Test results and test programming was conducted through the PC suite testXpert II which allows basically to define every single step of a test in terms of applied displacement and applied

temperature and to follow real-time data flowing in a force displacement chart like the one shown in Figure 114.

Figure 114 Test result data flowing into the testXpert II software.

4.4 The Tests

Two different sets of tests were performed: simple tensile tests and more complex thermo-mechanical cycles. The simple tension tests were performed at two different fixed loading rates (10 mm/min and 200 mm/min, the "slow" and "fast" test respectively) and under different temperatures of the heating chamber (20 °C, 40°C and 60°C for the cold hand-machined specimens and 0°C, 20°C, 40°, 60° and 80°C for the factory molded specimens). During the traction tests a maximum strain of 300% was reached and five inner cycles were performed by unloading the specimen to

zero stress when reaching a strain level respectively of 20%, 50%, 100%, 200% and 300%. Before starting the tests, each specimen was thoroughly heated to the prescribed temperature.

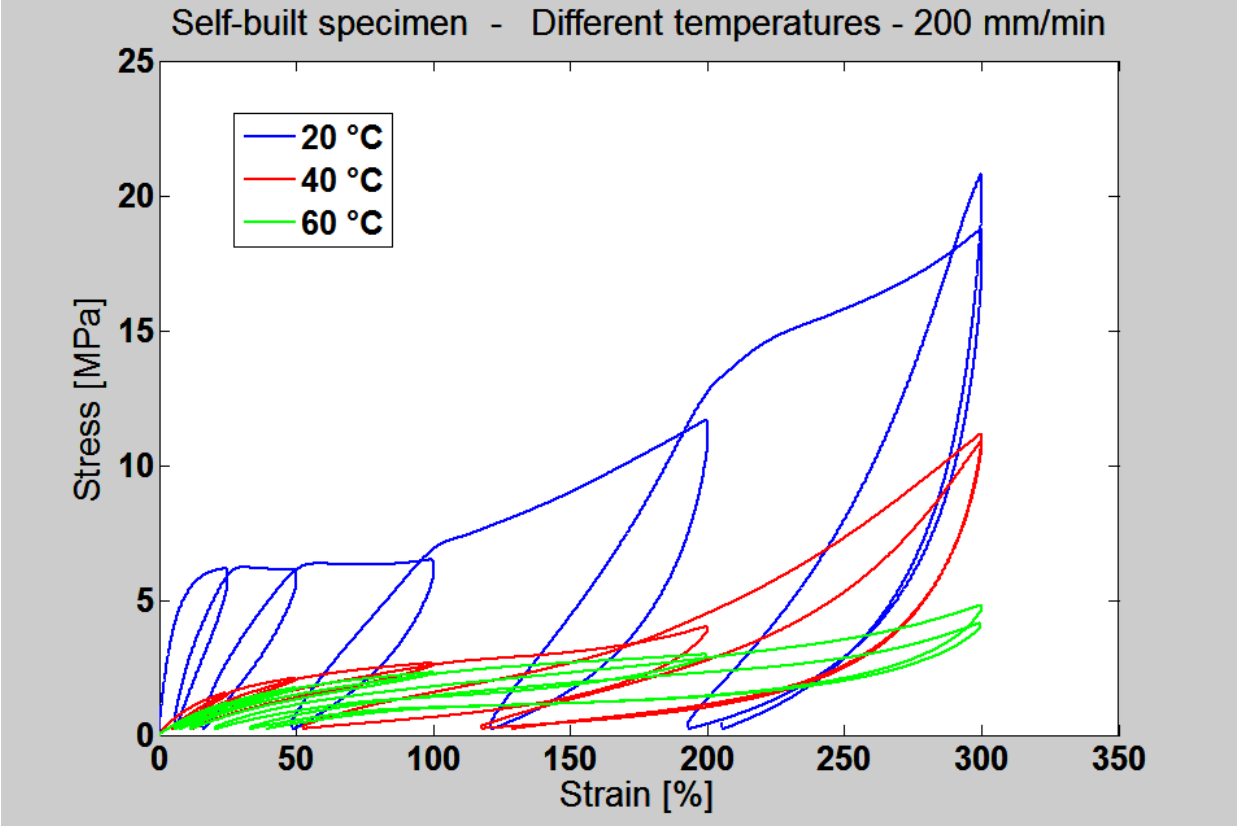

Figure 115 Comparison between tensile tests on hand-machined specimens at different temperature and 200mm/min loading rate.

In Figure 115 a comparison of the 200mm/min tests for the self-machined respectively at different temperatures of 20°C, 40°C and 60°C is shown. The general behavior consists in an initial linear elastic path, followed by a pseudo-plastic hardening up to the maximum strain reached by the test. Internal cycles shows some hysteresis. As temperature goes up the specimen experiments a steep drop of the tangent stiffness which reduces from around 70MPa for the 20°C specimen to around 7 MPa for specimens above 40°C, that is one order of magnitude reduction. This fact is due to the transition from the crystallized state (lower temperature) to a rubber-like state (higher temperature). The transition temperature for DESMOPAN is indeed 40°C, according to Bayer's specifications. Moreover, a sort of Mullin's effect may be noticed observing the inner cycles in each single test, that is a reduction of the tangent stiffness with the increasing of the strain level: the steepness of the inner cycles gradually decreases as strain increase. Finally, comparing different temperature tests and looking at the inner cycles, one can notice that as the temperature increases an higher and

higher fraction of the total strain is recovered upon unloading, with an abrupt change in terms of recovered strain after overpassing 40°C that is transition temperature. Hysteresis is negligible in the internal cycles of specimens at high temperature. This is another consequence of the transition to the rubber-like state. Incidentally it should be noticed that even the remarkable residual deformation observed at lower temperatures may be recovered by heating the specimen above the transition temperature in a stress free state: for this reason the residual strain is also known as pseudo-plastic deformation.

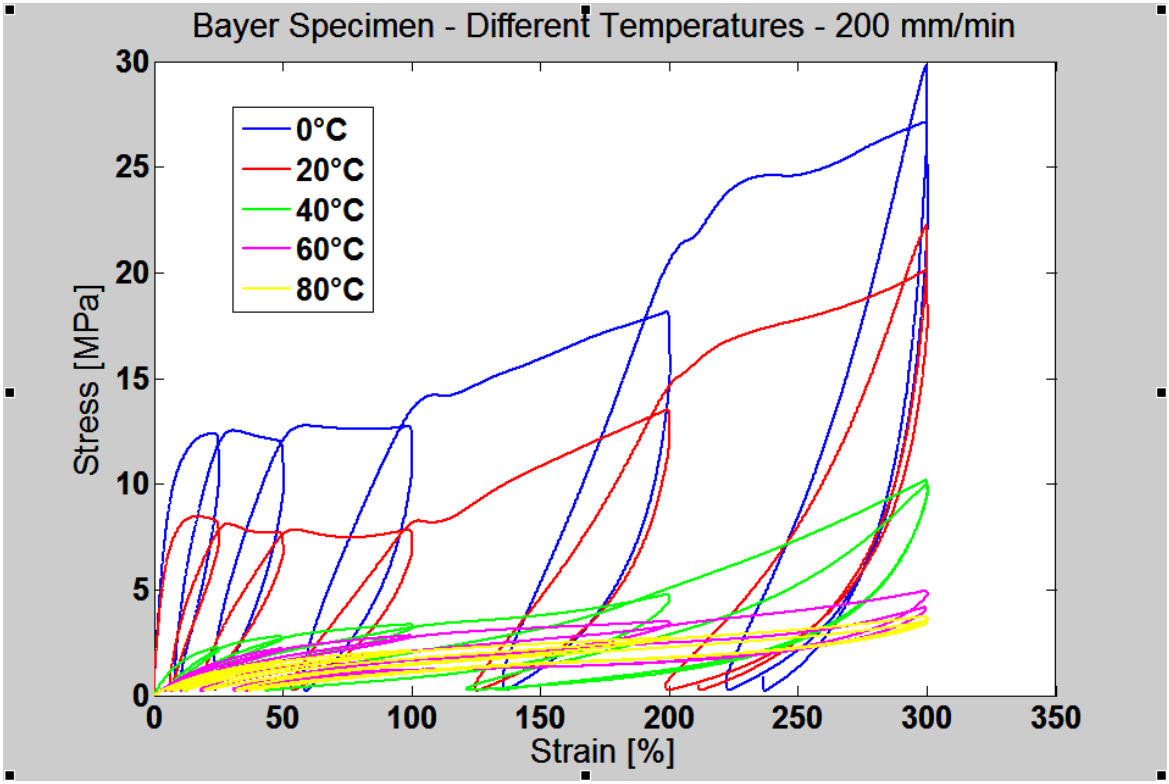

Figure 116 Comparison between tensile tests on hand-machined specimens at different temperature and 200mm/min loading rate.

In Figure 116 a comparison of the fast 200mm/min tests for the Bayer molded specimens at different temperatures of 0°C, 20°C, 40°C, 60°C and 80°C is shown. Even in this case, as temperature goes up the specimen experiments a steep drop of the tangent stiffness which reduces from around 135 MPa for the specimens under 40°C to around 13 MPa for specimens above 40°C, that is again one order of magnitude reduction. This fact is again due to the transition from the crystallized state (lower temperature) to a rubber-like state (higher temperature). A sort of Mullin's effect may be noticed observing the inner cycles in each single test, that is a reduction of the tangent stiffness with the increasing of the strain level: the steepness of the inner cycles gradually decreases as strain

increase. Finally, comparing different temperature tests and looking at the inner cycles, one can again notice that as the temperature increases an higher and higher fraction of the total strain is recovered upon unloading, with an abrupt change in terms of recovered strain after overpassing 40°C that is transition temperature. Hysteresis is negligible in the internal cycles of specimens at high temperature. Again, this residual strain may be recovered by heating the specimen. It's worth of notice the fact that Bayer specimens appear significantly stiffer than the hand machined ones. In general let's observe that the mechanical behavior of specimens does not change smoothly with temperature but quiet abruptly while going across transition temperature.

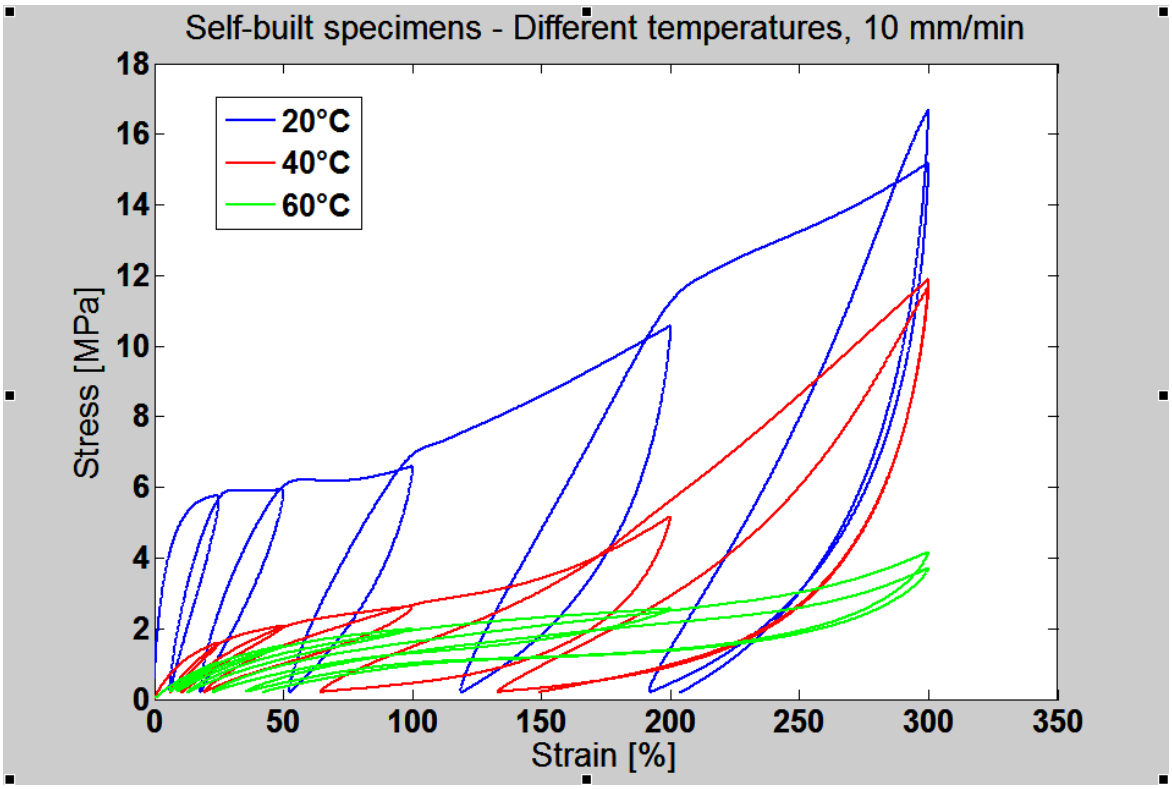

Figure 117 Comparison between tensile tests on hand-machined specimens at different temperature and 10mm/min loading rate.

In Figure 117 a comparison of the slow 10mm/min tests for the self-machined specimens at different temperatures of 20°C, 40°C and 60°C. The test required about 45 minutes each. Even in this case, as temperature goes up the specimen experiments a steep drop of the tangent stiffness which reduces from around 70 MPa for the specimens under 40°C to around 7 MPa for specimens above 40°C, that is again one order of magnitude reduction. This fact is again due to the transition from the crystallized state (lower temperature) to a rubber-like state (higher temperature). Mullin's effect may be noticed observing the inner cycles in each single test, that is a reduction of the tangent

stiffness with the increasing of the strain level: the steepness of the inner cycles gradually decreases as strain increase. Finally, comparing different temperature tests and looking at the inner cycles, one can again notice that as the temperature increases an higher and higher fraction of the total strain is recovered upon unloading, with an abrupt change in terms of recovered strain after overpassing 40°C that is transition temperature. Hysteresis is negligible in the internal cycles of specimens at high temperature. Again, this residual strain may be recovered by heating the specimen.

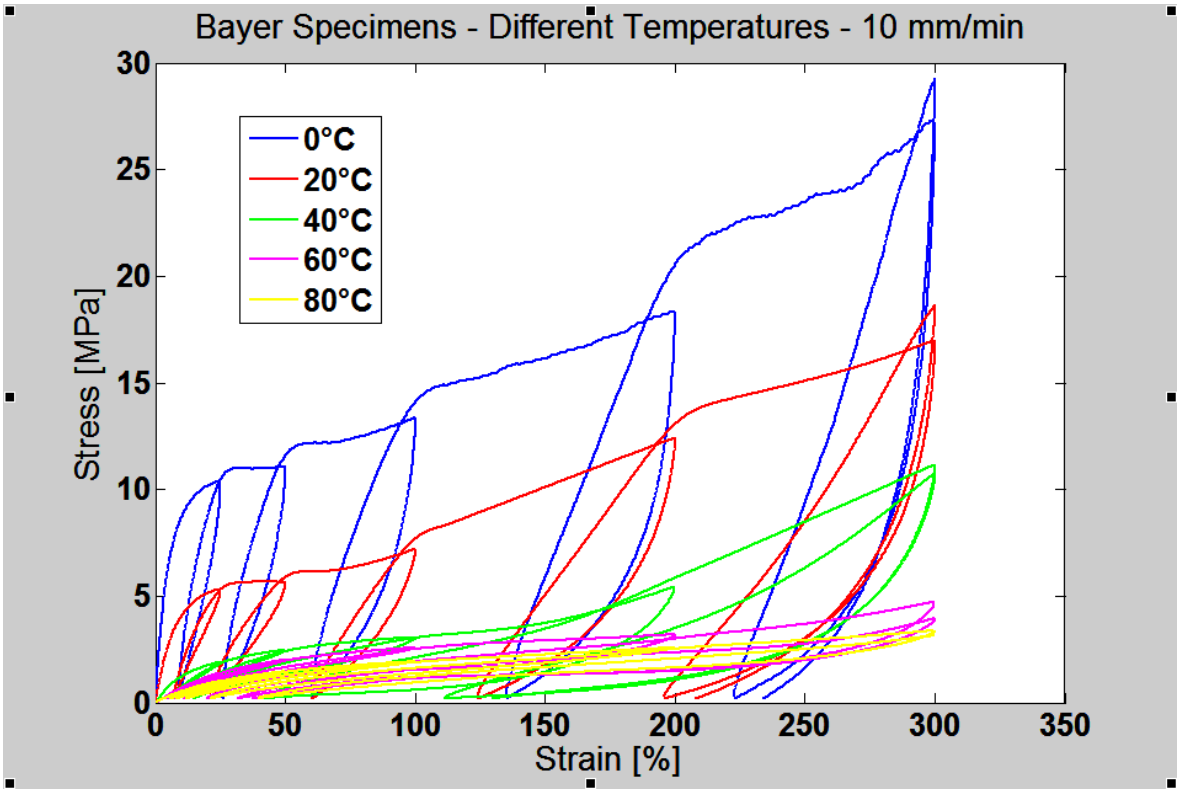

Figure 118 Comparison between tensile tests on hand-machined specimens at different temperature and 10mm/min loading rate.

In Figure 118 a comparison of the slow 10mm/min tests for the Bayer molded specimens at different temperatures of 0°C, 20°C, 40°C, 60°C and 80°C. The test required about 45 minutes each. Even in this case, as temperature increases the specimen undergoes a steep drop of the tangent stiffness which reduces from around 130 MPa for the specimens under 40°C to around 13 MPa for specimens above 40°C, that is again one order of magnitude reduction, due to the transition from the crystallized state (lower temperature) to a rubber-like state (higher temperature). Mullin's effect may be noticed observing the inner cycles in each single test, that is a reduction of the tangent stiffness with the increasing of the strain level: the steepness of the inner cycles gradually decreases as strain increase. Finally, comparing different temperature tests and looking at the inner cycles, one

can again notice that as the temperature increases an higher and higher fraction of the total strain is recovered upon unloading, with an abrupt change in terms of recovered strain after overpassing 40°C that is transition temperature. Hysteresis is negligible in the internal cycles of specimens at high temperature. Again, this residual strain may be recovered by heating the specimen. It's worth of notice again the fact that Bayer specimens appear significantly stiffer than the hand machined ones. In general let's observe that the mechanical behavior of specimens does not change smoothly with temperature but quiet abruptly while going across transition temperature

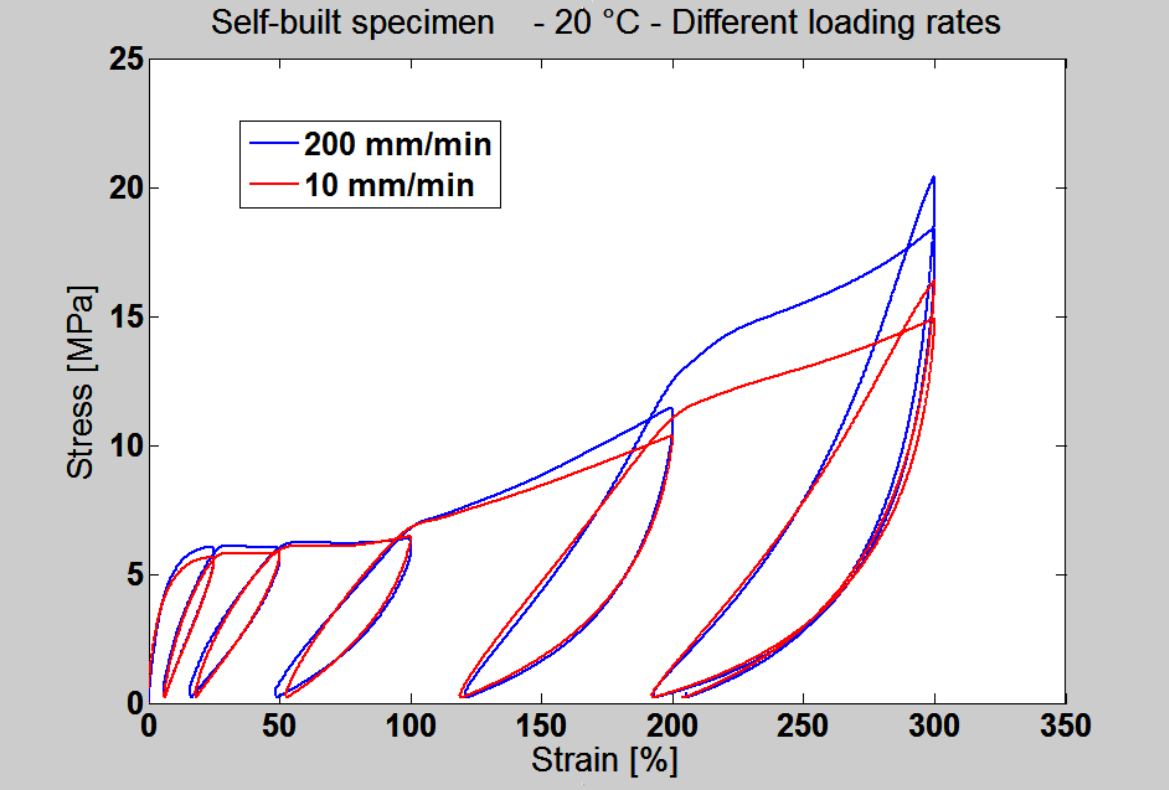

Figure 119 Comparison between 10mm/min and 200mm/min tests at 20°C for hand machined specimens.

In Figure 119 a comparison between slow and fast tests at 20°C on the self-machined specimens is shown. At 20°C the specimen is in its crystallized state. A weak dependence on the loading rate is found, stronger at higher strain values. The same fact is even more striking when considering the 60°C tensile test, with the specimen in its rubber-like state, as shown in Figure 120.

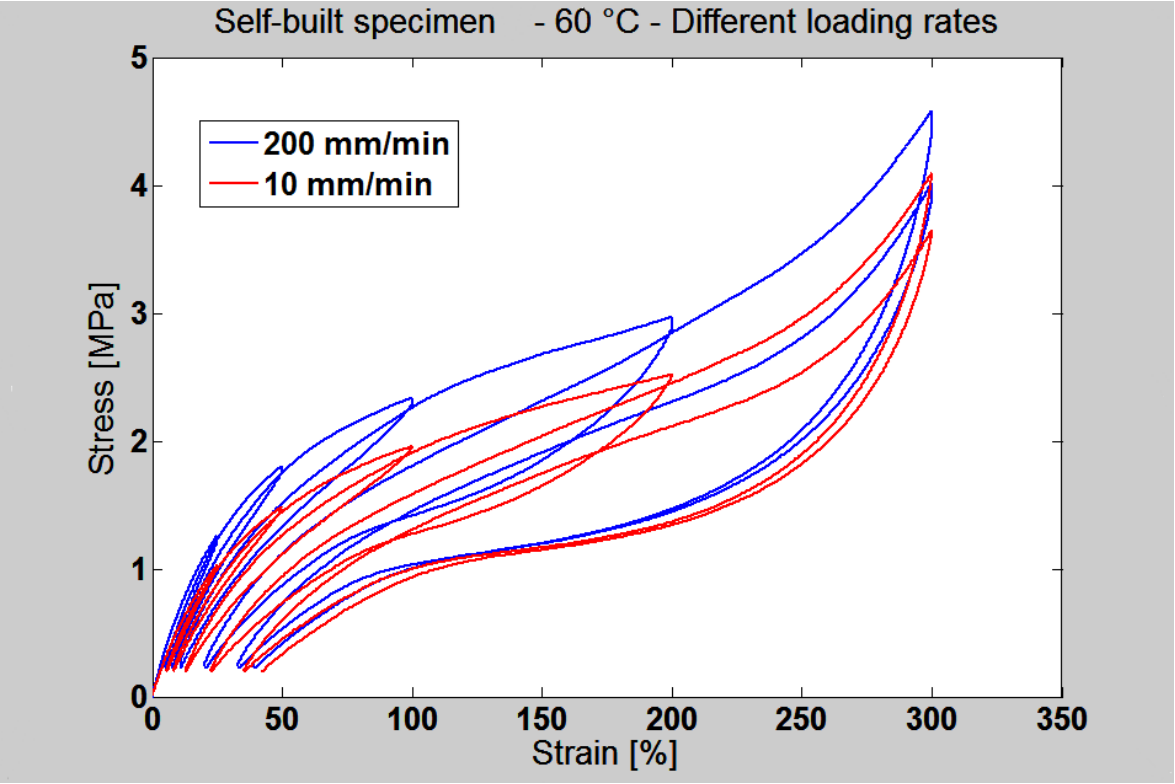

Figure 120 Comparison between 10mm/min and 200mm/min tests at 60°C

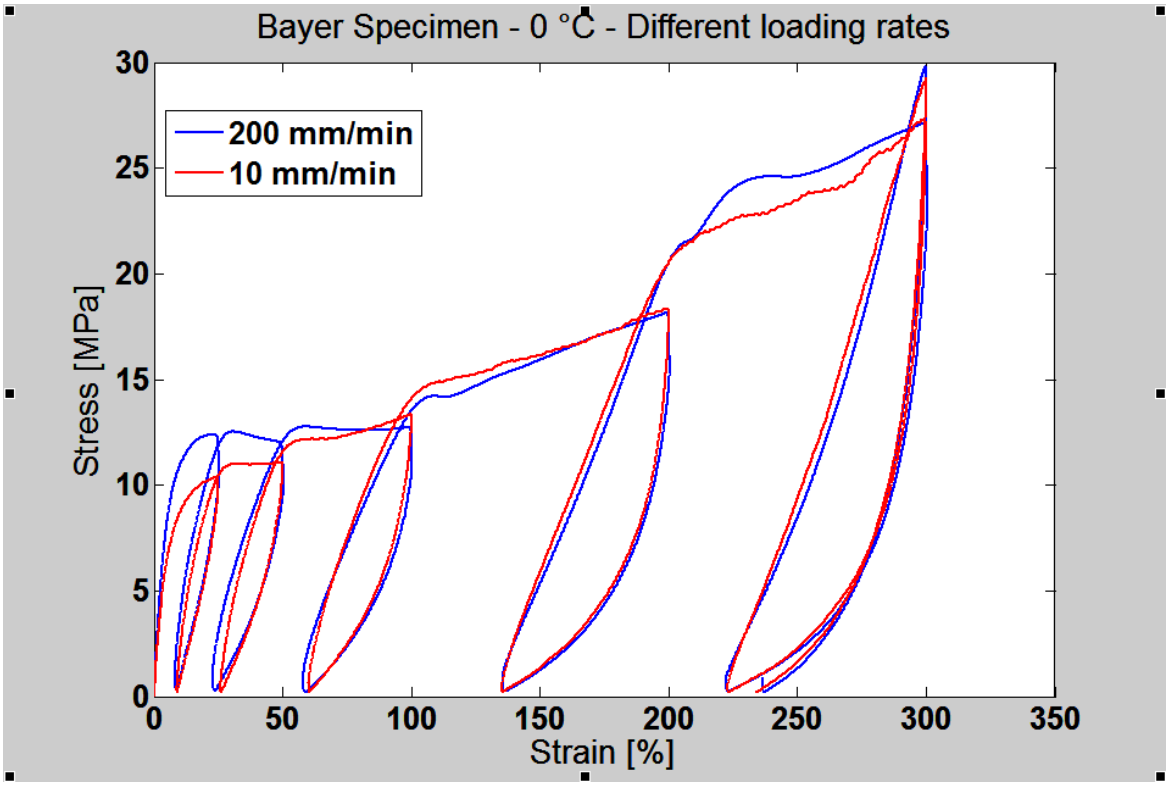

Figure 121 Comparison between 10mm/min and 200mm/min tests at 0°C for factory molded specimens.

Here the dependence on loading rate is clear since the beginning of the test and goes throughout all the test. The observations made for the hand-machined specimens are still valid when considering factory molded specimens.

In Figure 121 a comparison between fast and slow test at 0°C for factory molded specimens is shown. The dependence of the response from the loading rate is there but it's interpretation remains troublesome since a localized deviation of the two responses is shown only at yielding and at the end of the test while in between the difference between the two response may be considered negligible.

In Figure 121 a comparison between fast and slow test at 0°C for factory molded specimens is shown. The dependence of the response from the loading rate is there but it's interpretation remains troublesome since a localized deviation of the two responses is shown only at yielding and at the end of the test while in between the difference between the two response may be considered negligible. Internal cycles are substantially unaffected by the different loading rate and so are residual strains upon unloading, hysteresis areas and Mullin's effect.

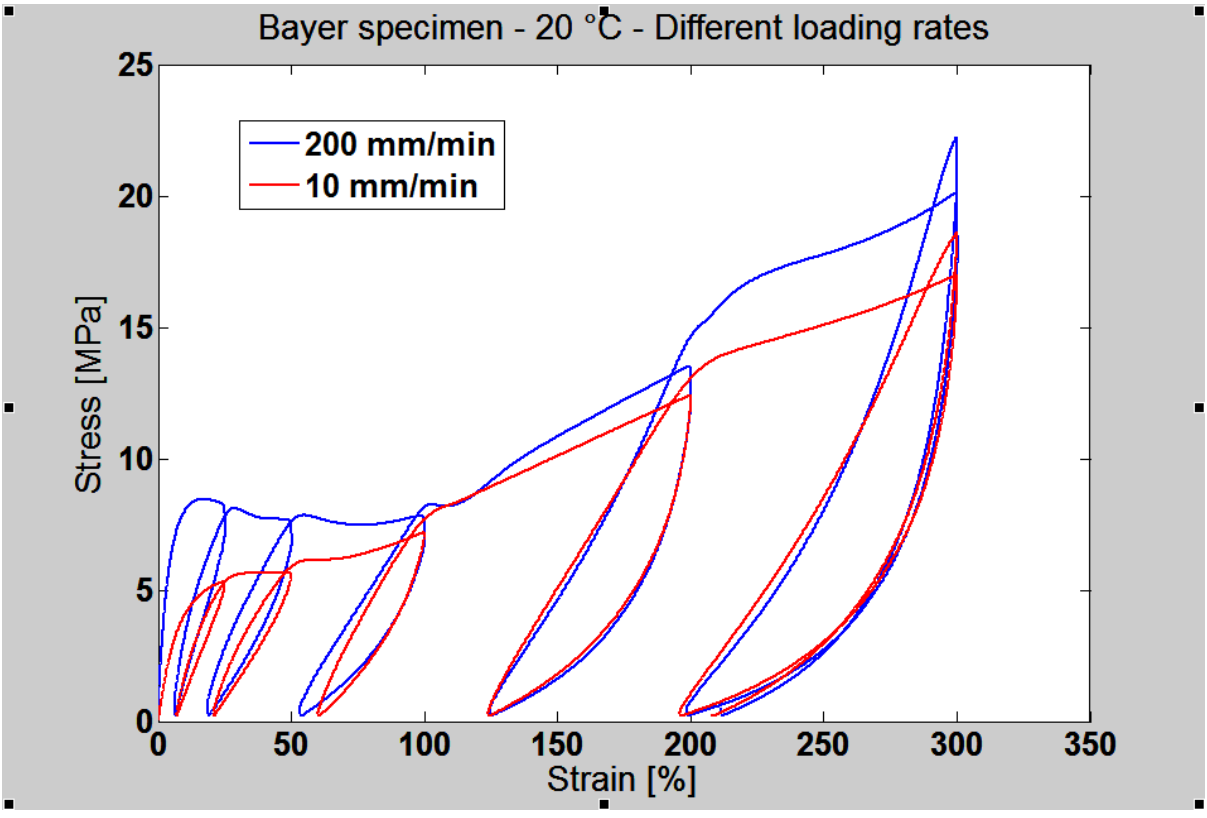

Figure 122 Comparison between 10mm/min and 200mm/min tests at 20°C for factory molded specimens.

In Figure 122 a comparison between fast and slow test at 20°C for factory molded specimens is shown. The dependence of the response from the loading rate is there but it's interpretation remains troublesome since while a difference in the response between the two tests may be observed throughout all the test it doesn't show a clear rate-dependence law. Moreover it's not clear if the difference in the response should be attributed only to the different loading rate or even to the different loading histories for the different specimens used for the two tests. Again internal cycles are substantially unaffected by the different loading rate and so are residual strains upon unloading, hysteresis areas and Mullin's effect.

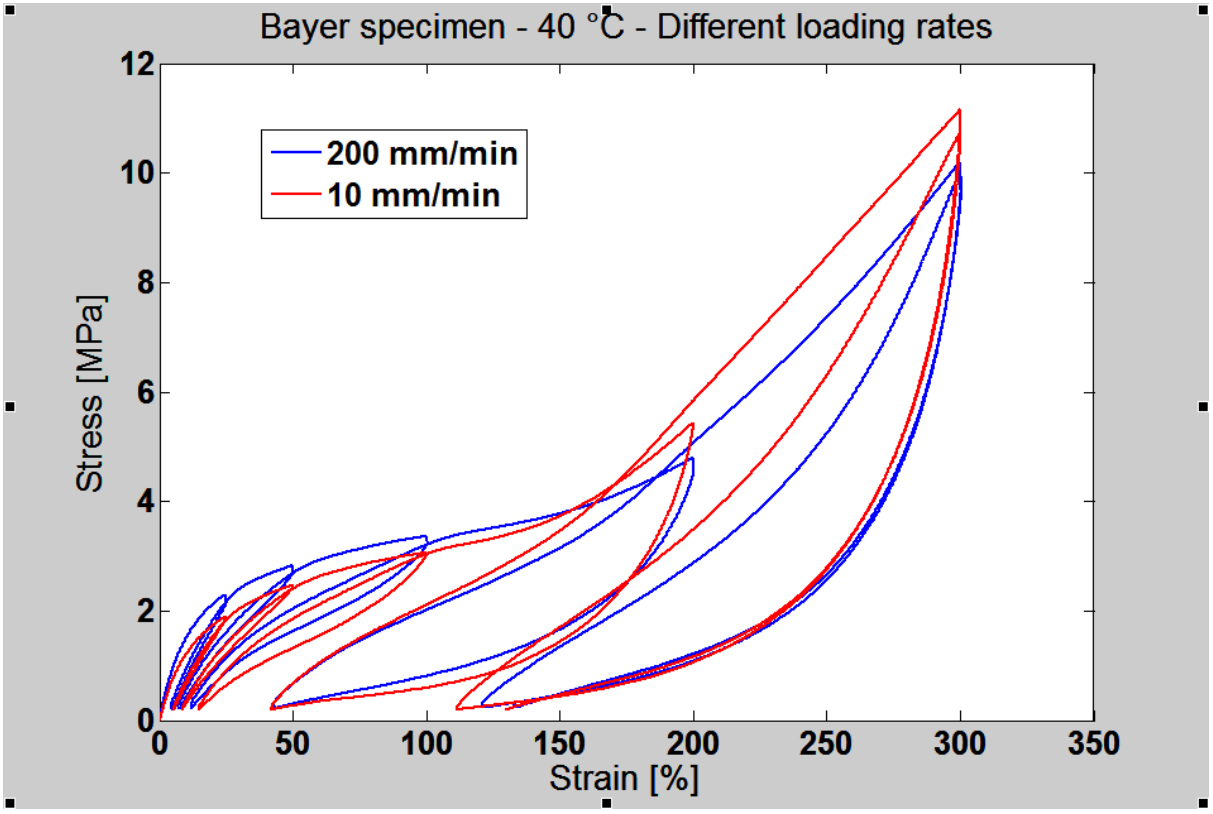

Figure 123 Comparison between 10mm/min and 200mm/min tests at 40°C for factory molded specimens.

In Figure 123 a comparison between fast and slow test at 40°C for factory molded specimens is shown. The dependence of the response from the loading rate is there but again it's interpretation remains troublesome since while a little difference in the response between the two tests may be observed throughout all the test it doesn't show a clear rate-dependence law. Moreover it's not clear if the difference in the response should be attributed only to the different loading rate or even to the different loading histories for the different specimens used for the two tests. Again internal cycles

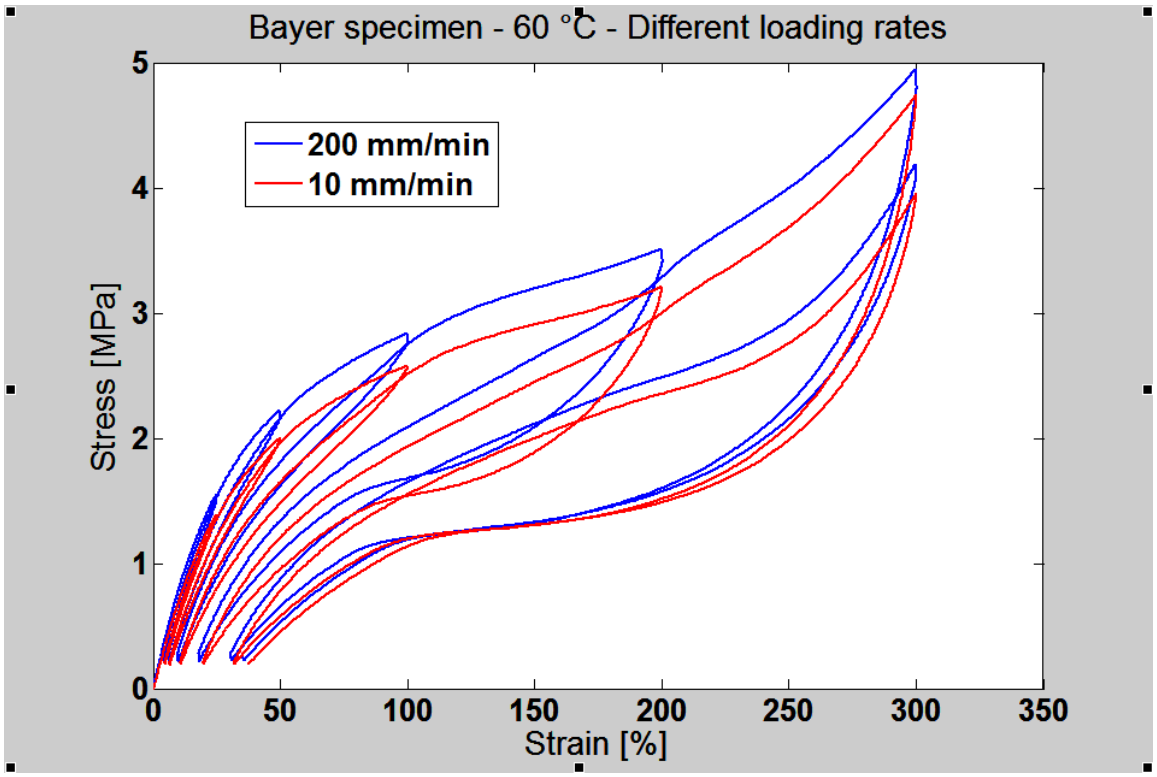

Figure 124 Comparison between 10mm/min and 200mm/min tests at 60°C for factory molded specimens.

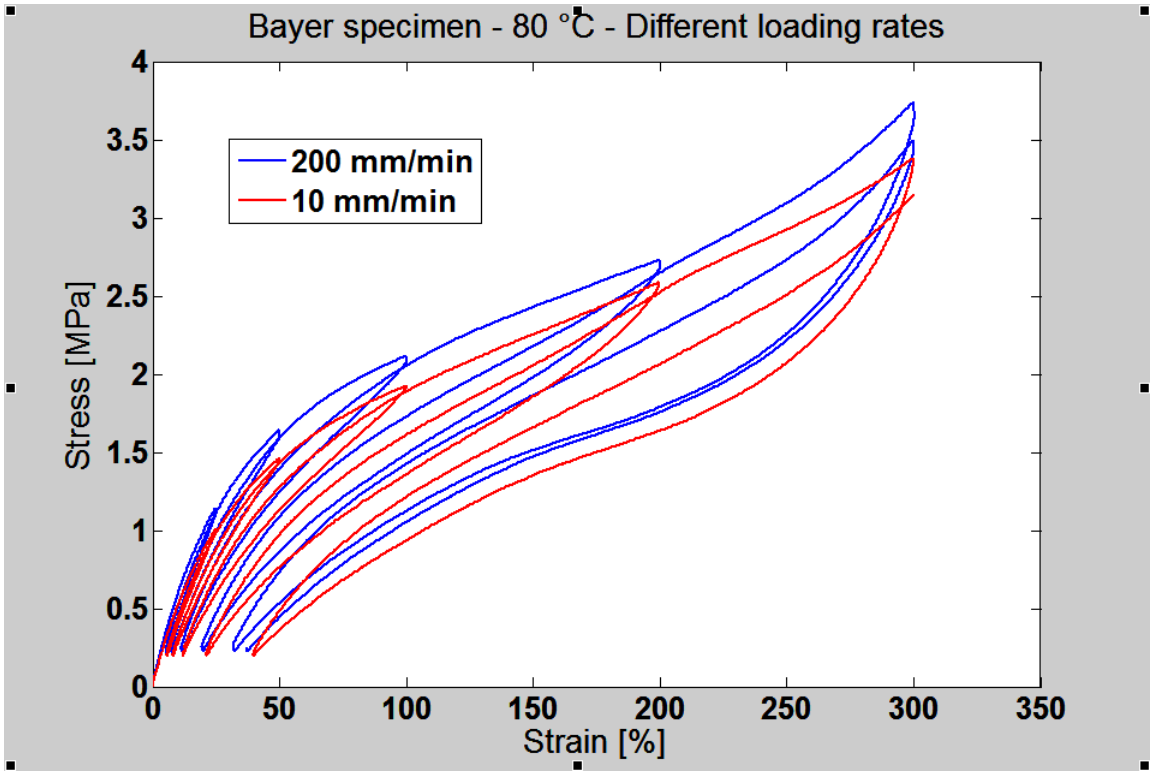

Figure 125 Comparison between 10mm/min and 200mm/min tests at 80°C for factory molded specimens.

are substantially unaffected by the different loading rate and so are residual strains upon unloading, hysteresis areas and Mullin's effect.

In Figure 124 a comparison between fast and slow test at 60°C for factory molded specimens is shown. The dependence of the response from the loading rate is there and this time it's quiet straightforward. Again internal cycles are substantially unaffected by the different loading rate and so are residual strains upon unloading, hysteresis areas and Mullin's effect.

In Figure 125 a comparison between fast and slow test at 80°C for factory molded specimens is shown. The dependence of the response from the loading rate is there and this time it's quiet straightforward. Again internal cycles are substantially unaffected by the different loading rate and so are residual strains upon unloading, hysteresis areas and Mullin's effect. Summarizing, rate-dependence is quiet clear above transition temperature while under transition temperature is quiet difficult to assess.

In the tensile tests at constant temperature previously described no shape memory effect was exploited. For this reason a thermo-mechanical cycle, represented in Figure 126 for the Bayer molded specimen, was performed.

The test was made up of six stages; at first, the specimen was heated up to a temperature of 80°C, in its rubber-like state, while keeping it at zero stress. During the first stage (stage 1) a 200 mm/min load was applied until a 250% strain was reached, while keeping temperature at 80°C. After that (stage 2) the clamps were fixed in their position for 10 minutes at 80°C in order to allow for relaxation of the specimen. During this stage a drop in stress was detected, mainly due to relaxation effects. Next (stage 3) temperature was dropped to 0°C at a rate of 5°C/min while keeping the clamps fixed in the same position as before, in order to obtain a "constrained cooling" loading path. During stage 3, a gradual drop in stress was measured while the specimen turned into its crystallized state. At the end of the cooling clamps were released until zero stress was measured in the specimen, in order to allow for the strain recovery of the free specimen (stage 4). Next (stage 5) clamps were fixed again in their position and temperature was newly raised to 80°C at a rate of 5°C/min. At the end of this stage stress was back to the level before the "constrained cooling" path and the specimen is again in its rubber-like state. Finally, (stage 6) the specimen was unloaded to zero stress while keeping temperature fixed at 80°C. At the end of this stage, only a slight residual strain was detected, for the specimen was in its rubber-like state. During stage 1, the usual nonlinear elastic behavior typical of rubbers and observed in the previous tests was shown. Stage 2 was necessary to allow for relaxation of the specimen.

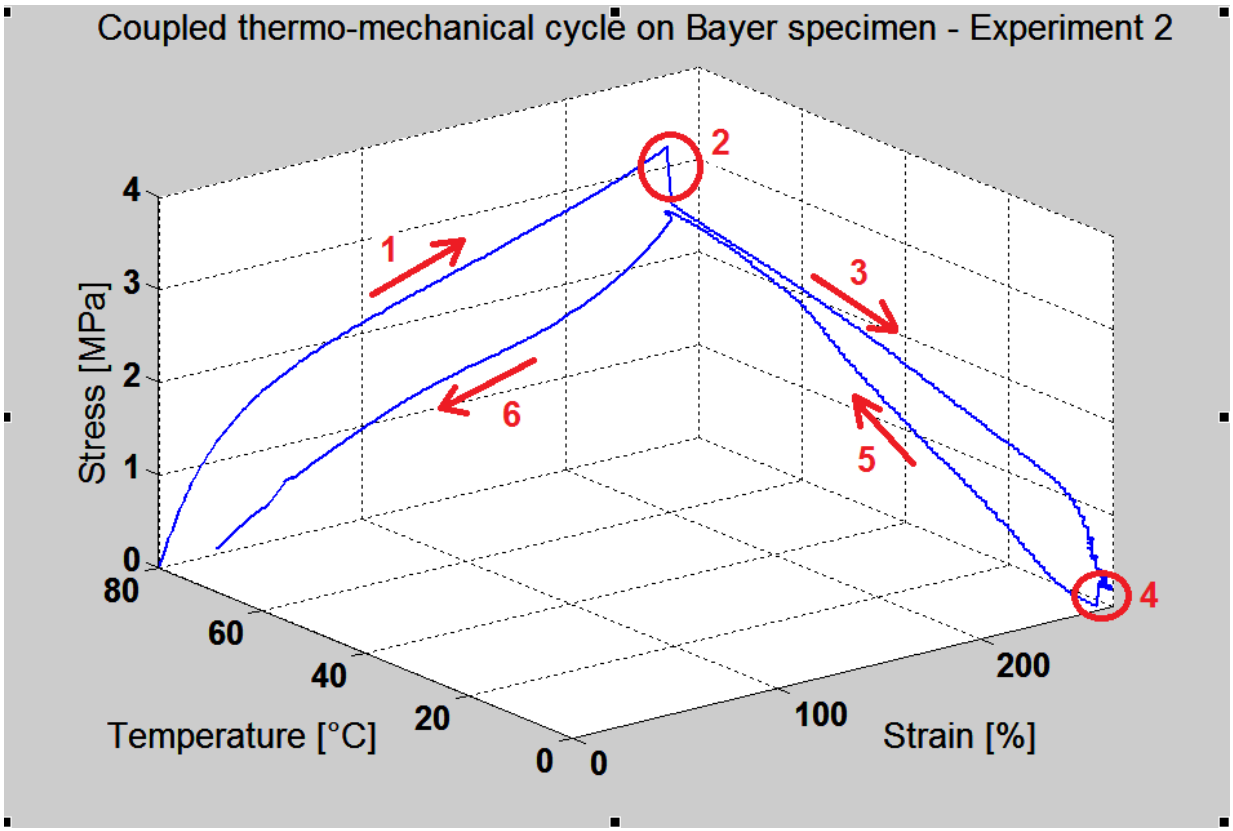

Figure 126 Thermo-mechanical cycle for a Bayer molded specimen.

The decrease in stress during stage 3 is typical of crystallizable shape memory polymers. Amorphous shape memory polymers show instead a sharp rise in stress during constrained cooling. Thus we can infer that DESMOPAN is a crystallizable SMP and not an amorphous SMP. Again, stage 4 allowed for specimen relaxation. During stage 5 strain is fixed and after heating is complete the material recovers almost entirely the initial stress level. Finally, stage 6 which was conducted at high temperature shows an almost complete recovery of strain. The double hysteresis loop (at fixed temperature and at fixed strain) is worth to be noticed.

4.5 Concluding remarks

Simple tensile tests at different loading rates and under different temperatures and thermo-mechanical cycles were performed on bone shaped specimens of DESMOPAN, a new polyurethanic shape memory polymer developed by the Material Science Division of Bayer. The tests performed on DESMOPAN completely revealed the thermo-mechanical behavior of this new crystallizable shape memory polymer. On the basis of these results, in the next future a simple

thermo-mechanical constitutive model is being developed, in order to provide a simple quantitative tool for the calculations required in structural applications.

4.6 Final conclusions

In this PhD thesis the mechanical behavior of two different smart materials have been experimentally investigated. Shape memory alloys wires where tested and the results were used to calibrate and assess two different constitutive models. The same wires where used to develop a new seismic dissipater for masonry buildings meant to be placed in series with FRP retrofitting systems and was tested on scale models of masonry boxes in order to assess its capability of improving structural response under horizontal loads. Finally a totally new shape memory polymer was tested in order to assess its thermo-mechanical behavior to set the basis for future research on shape memory polymers constitutive modeling.

4.7 Acknowledgements

I would like to thank to my PhD advisors, Prof. Antonio Tralli and Dr. Raffaella Rizzoni, for supporting me during these past three years and for having provided insightful discussions about the research. I thank Prof. Stefanie Reese for having me hosted in her Instute für Angewandte Mechanick at the RWTH Aachen University during my five months visiting period abroad and for having given to me the opportunity of conducing experimental tests on new shape memory polymers. I thank Dr. Johannes Schnepp for his help in coordinating experiments and for his scientific advice and knowledge and for the many insightful discussions and suggestions. I'm very grateful to Bernd Kohl for his help in using and adjusting testing machines in the laboratory of the IFAM. I would like to thank Prof. Ferdinando Auricchio, for his help in organizing my experience abroad. I also thank Prof. Silvia Briccoli Bati (University of Florence) for coordinating experimental campaign on scale model of masonry boxes and SMA device. A final thank to my PhD mates whose support during these years has been invaluable.

I dedicate this thesis to my family

Bibliography

Abeyaratne, R., and J. K. Knowles. "On the driving traction acting on a surface of strain discountinuity in a continuum." *Journal of the Mechanics and Physics of Solids*, 1990: 345-360.

Abeyaratne, R., and J.K. Knowles. "A continuum model of a thermoelastic model capable of undergoing phase transitions." *Journal of the Mechanics and Physics of Solids*, 1993: 541-571.

—. *Evolution of phase transitions, a continuum theory.* Cambridge University Press, 2006.

Abeyaratne, R., and J.K. Knowles. "Kinetic relations and the propagation of phase boundaries in solids." *Archive for Rational Mechanics and Analysis*, 1991: 119-154.

Abeyaratne, R., and J.K. Knowles. "On the kinetics of an austenite-martensite phase transformation induced by impact in a Cu-Al-Ni shape-memory alloy." *Acta Materialia*, 1997: 1671-1683.

Abeyaratne, R., and S. Kim. "Cyclic effects in shape-memory alloys: A one-dimensional continuum model." *International Journal of Solids and Structures*, 1997: 3273-3289.

Adachi, H., T. Yokoi, K. Hatori, and K. Morishita. "Temperature Display Devices." *Japan Patent Office*, 1990.

Airoldi, G., G. Riva, and M. Vanelli. "Superelasticity and shape-memory effect in Ni-Ti orthodontic wires." 1995.

Andreasen, G. F., and T. B. Hilleman. "An evaluation of 55 cobalt substituted Nitinol wire for use in orthodontics." *The Journal of the American Dental Association* 82, no. 6 (1971): 1373-1375.

Asch, M. R. "Initial experience in humans with a new retrievable inferior vena cava filter." *Radiology* 225, no. 3 (2002): 835-844.

Auricchio, F. "A robust integration-algorithm for a finite-strain shape memory alloy superelastic model." *International Journal of Plasticity*, 2001: 971-990.

Auricchio, F., and L. Petrini. "A three-dimensional model describing stress-temperature induced solid phase transformations: solution algorithm and boundary value problems." *International Journal for Numerical Methods in Engineering*, 2004a: 807-836.

Auricchio, F., and L. Petrini. "A three-dimensional model describing stress-temperature induced solid phase transformations: thermomechanical coupling and hybrid composite applications." *International Journal for Numerical Methods in Engineering*, 2004b: 716-737.

Auricchio, F., and L. Petrini. "Improvements and algorithmical considerations on a recent three-dimensional model describing stress-induced solid phase transformations." *International Journal for Numerical Methods in Engineering*, 2002: 1255-1284.

Auricchio, F., and R.L. Taylor. "Shape-memory alloys: modelling and numerical simulation of the finite-strain superelastic behavior." *Computer Methods in Applied Mechanics and Engineering*, 1997: 175-194.

Auricchio, F., D. Fugazza, and R. DesRoches. "Rate-dependent thermo-mechanical modelling of susuperelastic." *Journal of Intelligent Material Systems and Structures*, 2008: 47-61.

Auricchio, F., R.L. Taylor, and J. Lubliner. "Shape-memory alloys: macromodelling and numerical simulations of the superelastic behavior." *Computer Methods in Applied Mechanics and Engineering*, 1997: 281-312.

Ball, J. M., and R. D. James. "Fine phase mixtures as minimizers of energy." *Archive for Rational Mechanics and Analysis*, 1987: 13-52.

Battacharya, K., and R. D. James. "The material is the machine." *Science* 57 (2005): 53-54.

Benvenuti, E., O. Vitarelli, and A. Tralli. "Delamination of FRP-Reinforced Concrete by means of an eXtended Finite Element Formulation." *Composites. Part B.*, 2012: 3258-3269.

Bernard, A. L., and M. A. Guedeau-Boudeville. "Permeation through Lipid Bilayers by Adhesion of Giant Vesicles on Decorated Surfaces." *Langmuir* 16 (2000): 6801-6808.

Bhattacharya, K., and S. Conti. "Crystal symmetry and the reversibility of martensitic transformations." *Nature*, no. 428 (2004): 55.

Bondaryev, E., and C.M. Wayman. "Some stress-strain-temperature relationships for shape memory alloys." *Metallurgical Transactions A*, 1988: 2407-2413.

Bouvet, C., S. Calloch, and C. Lexcellent. "A phenomenological model for pseudoelasticity of shape memory alloys under multiaxial proportional and nonproportional loadings." *European Journal of Mechanics - A/Solids*, 2004: 37-61.

Boyd, J.G., and D.C. Lagoudas. "Thermomechanical response of shape memory composites." *Journal of Intelligent Material Systems and Structures*, 1994: 333-346.

Brinson, L.C. "One-dimensional constitutive behavior of shape memory alloys: Thermomechanical derivation with non-constant material functions and redefined martensite internal variable." *Journal of Intelligent Material Systems and Structures*, 1993: 229-242.

Carpenter, P., V. Rimbau, D. Raithel, and P. Peeters. "Endovascular repair of abdominal aortic aneurysms: current status and future directions." *American Journal of Roentgenology* 175, no. 2 (2000): 289-302.

Cattaneo, M. "Caratterizzazione biomeccanica sperimentale di stent-grafts." *Tesi di Laurea, Politecnico di Milano*, 2006.

Chang, B., J. Shaw, and M.A. Iadicola. "Thermodynamics of shape memory alloy wire; modeling, experiments and applications." *Continuum Mechanics and Thermodynamics*, 2006: 83-118.

Chang, B.C., J. Shaw, and M. Iadicola. "Thermodynamics of shape memory alloy wire: modeling, experiments and applications." *Continuum Mechanics and Thermodynamics*, 2006: 65-114.

Charlesby, A. *Atomic Radiation and Polymers.* Oxford: Pergamon Press, 1960.

Chiozzi, A., R. Rizzoni, Merlin M., and Tralli A. "Experimental comparison for two one-dimensional constitutive models for shape memory alloy wires used in anti-seismic applications." *European Congress on Computational Methods in Applied Sciences and Engineering ECCOMAS.* Wien, 2012.

Clark, P., I. Aiken, J. Kelly, and Higashino M. "Experimental and analytical studies of shape memory alloy dampers for structural control." *Proceedings of passive damping.* 1995.

Coats, L., and P. Bonhoeffer. "New percutaneous treatments for valve disease." *Heart* 93, no. 5 (2007): 639-644.

Contro, R., V. Dallolio, G. Franzoso, and D. Gastaldi. "Biomechanical study of a pathologic lumbar functional spinal unit and a possible surgical treatment through the implant of an interspinous device." *Biomechanics Applied to Computer Assisted Surgery*, 2005: 39-52.

Corbi, O. "Shape memory alloys and their application in structural oscillations attenuation." *Simulation Modeling Practice and Theory*, 2003: 387-402.

Croci, G., A. Bonci, and A. Viskovic. "The use of shape memory alloys devices in the basilica of St Francis in Assisi." *Proceedings of the final workshop of ISTECH project.* 2000. 117-140.

Dai, K. R., X. K. Hou, Y. H. Sun, and R. G. Tang. "Treatment of intra-articular fractures with shapememory compression staples." *Injury* 24, no. 10 (1993): 651-655.

DesRoches, R., and M. Delemont. "Seismic retrofit of simply supported bridges using shape memory alloys." *Engineering Structures*, 2002: 325-332.

Dolce, M., and D. Cardone. "Mechanical behaviour of shape memory alloys for seismic application 1. Martensite and Austenite NiTi bars subjected to torsion." *International Journal of Mechanical Sciences*, 2001: 2631-2656.

Dolce, M., and D. Cardone. "Mechanical behaviour of shape memory alloys for seismic applications 2: Austenitic NiTi wires subjected to tension." *International Journal of Mechanical Sciences*, 2001: 2656-2677.

Dolce, M., D. Cardone, and R. Marnetto. "SMA re-centering devices for seismic isolation of civil structures." *Proceedings of SPIE.* 2001. 238-249.

Dos Santos, F. P., and S. Cismasiu. "Comparison Between Two SMA Constitutive Models for Seismic ." *Journal of Vibration and Control*, 2011: 234-245.

Duerig, T. W. *Engineering Aspects of Shape Memory Alloys.* London: Butterworth Heinemann, 1990.

Falk, F. "Model free-energy, mechanics and thermodynamics of shape memory alloys." *Acta Metallurgica*, 1980: 1773-1780.

Falk, F. "One-dimensional model of shape memory alloys." *Archives of Mechanics*, 1983: 63-84.

Falk, F., and P. Konopka. "Three-dimensional landau theory describing the martensitic transformation of shape memory alloys." *Journal de Physics*, 1990: 61-77.

Fischer, F., and K. Tanaka. "A micromechanical model for the kinetics of martensitic transformation." *International Journal of Solids and Structures*, 1992: 1723-1728.

Fried, E., and M. Gurtin. "Dynamic solid-solid transitions with phase characterized by an order parameter." *Physica*, 1994: 287-308.

Fu, C. C., and A. Grimes. "Shrink-Induced Nanowrinkles: Tunable Nanowrinkles on Shape Memory Polymer Sheets." *Advenced Materials* 21, no. 44 (2009): 4413-4510.

Fugazza, D. *Shape-memory alloy device in earthquake engineering: Mechanical properties, constitutive modelling and numerical simulations.* Pavia: Master's thesis, Rose School, 2003.

Funakubo, H. *Shape Memory Alloys.* Gordon and Breach Science Publishers, 1987.

Gall, K., Y. Yakacki, R. Liu, and N. Shandas. "Thermomechanics of the shape memory effect in polymers for biomedical applications." *Journal of Biomedical Materials Research*, 2005: 339.

Gao, X., and L. Brinson. "A simplified multivariant SMA model based on invariant plane nature of martensitic transformation." *Journal of Intelligent Material Systems and Structures*, 2002: 795-810.

Gao, X., M. Huang, and L. Brinson. "A multivariant micromechanical model for SMAs." *International Journal of Plasticity*, 2000: 1345-1369.

Granghi, F., and D. Wolons. "Characterization of the pseudoelastic damping behavior of shape memory alloy wires using complex modulus." *Smart Materials and Structures*, 1999: 49-56.

Grasser, E.J., and F.A. Cozzarelli. "A proposed three-dimensional constitutive model for shape memory alloys." *Journal of Intelligent Material Systems and Structures*, 1994: 78-79.

Gunes, I. S., and S. C. Jana. "Shape Memory Polymers and Their Nanocomposites: A Review." *Journal of Nanoscience and Nanotechnology* 8 (2008): 1616-1637.

Han, Y.L., Q.S. Li, A.Q. Li, and A.Y.T. Leung. "Structural vibration control by shape memory alloy damper." *Earthquake Engineering and Structural Dynamics*, 2003: 483-494.

Hayashi, S. *Technical Report on Preliminary Investigation of Shape Memory Polymers.* Nagoya Research and Development Center, Mitsubishi Industries Inc., 1990.

Helm, D., and P. Haupt. "Shape memory behaviour: modelling within continuum themomechanics." *International Journal of Solids and Structures*, 2003: 827-849.

Hu, Y., and I. Müller. "Nonequilibrium thermodynamics of pseudoelasticity." *Continuum Mechanics and Themrodynamics*, 1993: 163-204.

Huang, M., and L. C. Brinson. "A multivariant model for single crystal shape memory alloy behavior." *Journal of the Mechanics and Physics of Solids*, 1998: 1379-1409.

Huang, M., X. Gao, and L. C. Brinson. "A multivariant micromechanical model for SMAs Part II ." *International Journal of Plasticity*, 2000: 1371-1390.

Huang, W. M., and B. Yang. "Thermo-moisture responsive polyurethane shape-memory polymer and composites: a review." *Journal of Materials Chemistry* 20 (2010): 3367-3381.

Huang, W.M., B. Yang, Y. Zhao, and Z. Ding. "Thermo-moisture responsive polyurethane shape-memory polymer and composites." *Journal of Materials Chemistry*, 2010: 3367-3381.

Humbeeck, J.V. "Damping capacity of thermoelastic martensite in shape memory alloys." *Journal of Alloys and Compounds*, 2003: 58-64.

Huo, Y. "A mathematical model for the hysteresis in shape memory alloys." *Continuum Mechanics and Thernodynamics*, 1989: 283-303.

Iadicola, M.A., and J.A. Shaw. "The effect of uniaxial cyclic deformation on the evolution of phase transformation fronts in pseudoelastic NiTi wire." *Journal of Intelligent Materials and Structures*, 2002: 143-155.

Idelsohn, S., J. Pena, and D. Lacroix. "Continuous mandibular distraction osteogenesis using superelastic shape memory alloy (SMA)." *Journal of Material Science* 15, no. 4 (2004): 541-546.

Indirli, M. "Demo application of shape memory alloy devices: the rehabilitation of S. Georgio Church Bell Tower." *Proceedings of SPIE.* 2001. 262-272.

Indirli, M., and M.G. Castellano. "Shape memory alloy devices for the structural improvement of masonry heritage structures." *International Journal of Architectural Heritage*, 2008: 93-119.

Indirli, M., et al. "Fibre Reinforced Polymers (FRP) strips in series with Shape Memory Alloy (SMA) wires: theory, application and experimental results of a prototypal anti-seismic device in the framework of the MAMAS project." *15 WCEE.* Lisbona, 2012.

Ivshin, Y., and T. Pence. "A constitutive model for hysteretic phase transition behavior." *International Journal for Engineering Sciences*, 1994: 681-704.

Ivshin, Y., and T. Pence. "A constitutive model for hysteretic phase transition behavior." *International Journal of Engineering Sciences*, 1994: 681-704.

Kahn, M.M., and D. Lagoudas. "Modeling of shape memory alloy pseudoelastic spring elements using Preisach model for passive vibration isolation." *Proceedings of SPIE.* 2002. 336-347.

Karaca, H. E., and et al. "Magnetic Field-Induced Phase Transformation in NiMnCoIn Magnetic Shape-Memory Alloys - A New Actuation Mechanism with Large Work Output." *Advanced Functional Materials* 19, no. 7 (2009): 983-998.

Kim, S. J., and R. Abeyaratne. "On the effect of the heat generated during a stress-induced thermoelastic phase transformation." *Continuum Mechanics and Thermodynamics*, 1995: 311-332.

Kim, S.J. "A Continuum Model for Phase Transitions in Thermoelastic Solids and Its Applications to Shape Memory Alloys." *PhD Thesis, MIT Cambridge*, 1995.

Lagoudas, D.C. *Shape Memory Alloys: Modeling and Engineering Applications.* Springer, 2008.

Landlein, A., A.M. Schmidt, and R. Langer. "AB-Polymer networks based on oligio(e-caprolactone) segments showing shape memory properties." *Proceedings of Natural Academy of Sciences USA.* 2001. 842-847.

Landlein, A., and R. Langer. "Biodegradable, elastic shape-memory polymers for potential biomedical applications." *Science* , 2002: 1673.

Landlein, A., and S. Kelch. "Shape-Memory Polymers." *Angwandte Chemie*, 2002: 2034-2057.

Laster, Z., and A. D., Ayliffe P. R. MAcBean. "Fixation of a frontozygomatic fracture with a shape-memory staple." *British Journal of Oral and Maxillofacial Surgery* 39, no. 4 (2001): 324-325.

Leclercq, S., and C. Lexcellent. "A general macroscopic description of the thermomechanical behavior of shape memory alloys." *Journal of the Mechanics and Physics of Solids*, 1996: 953-957.

Lendlein, A., and H. Jiang. "Light-induced shape-memory polymers." *Nature* 434 (2005): 879-882.

Lendlein, A., and R. Langer. "Biodegradable, Elastic Shape-Memory Polymers for Potential Biomedical Applications." *Science* 296, no. 5573 (2002): 1673-1676.

Leng, J., and L. Haibao. "Shape-Memory Polymers - A Class of Novel Smart Materials." *MRS Bulletin* 34, no. 11 (2009): 848-855.

Leon, R.T., R. DesRoches, J. Ocel, and G. Hess. "Innovative beam column using shape memory alloys." *Proceedings of SPIE.* 2001. 227-237.

Lexcellent, C., A. Vivet, C. Bouvet, S. Calloch, and P. Blanc. "Experimental and numerical determinations of the initial surface of phase transformation under biaxial loading in some polycrystalline shape-memory alloys." *Journal of the Mechanics and Physics of Solids*, 2002: 2717-2735.

Lexcellent, C., B.C. Goo, Q.P. Sun, and J. Bernardini. "Characterization, thermomechanical behavior and micromechanical-based constitutive model of shape-memory Cu-Zn-Al single crystals." *Acta Materialia*, 1996: 3773-3780.

Li, F.K., Y. Chen, W. Zhu, and X. Zhang. "Shape memory effect of polyethylene/nylon6 graft copolymers." *Polymer*, 1998: 6929-6934.

Li, H., M. Liu, and J.P. Ou. "Vibration mitigation of a stay cable with one shape memory alloy damper." *Structural Control and Health Monitoring*, 2004: 1-36.

Liang, C., and C.A. Rogers. "One-dimensional thermomechanical constitutive relations for shape memory materials." *Journal of Intelligent Material Systems and Structures*, 1990: 207-234.

Liew, K.M., S. Kitipornchai, T. Ng, and G.P. Zou. "Multi-dimensional superelastic behavior of shape memory alloys via nonlinear finite element method." *Engineering Structures*, 2002: 51-57.

Likhacev, A. A., and Y. N. Koval. "On the differential equation describing the hystreretic behavior of shape-memory alloys." *Scripta Metallurgica*, 1992: 223-227.

Lin, P., H. Tobushi, K. Tanaka, T. Hattori, and M. Makita. "Pseudoelastic behaviour of tini shape memory alloy subjected to strain variations." *Mechanics of Materials*, 1994: 694-701.

Lin, R.C., H. Tobushi, K. Tanaka, T. Hattori, and M. Makita. "Pseudoelastic behaviour of tini shape memory alloy subjected to strain variations." *Mechanics of Materials*, 1994: 694-701.

Lipscomb, I. P., and L. D. Nokes. *The Application of Shape Memory Alloys in Medicine.* Norfolk, Va, USA: Paston Press Ltd, 1996.

—. *The Applications of Shape Memory Alloysin Medicine.* Wiley, 1996.

Liu, C., H. Qin, and P. T. Mather. "Review of Progree in Shape-Memory Polymers." *Journal of Materials Chemistry* 17 (2007): 1543-1559.

Liu, Y.,, Z. Xie, and Humbeeck J.V. "Cyclic deformation of NiTi shape memory alloys." *Materials Science and Engineering*, 1999: 273-275.

Lubliner, J. "A maximum-dissipation principle in generalized plasticity." *Acta Mechanica*, 1984: 225-237.

Lubliner, J., and F. Auricchio. "Generalized plasticity and shape memory alloys." *International Journal of Solids and Structures*, 1996: 991-1003.

Machado, L.G., and M.A. Savi. "Medical applications of shape memory alloys." *Brazilian Journal of Medical and Biological Research* 36, no. 6 (2003): 683-691.

Machi, S. "New trends of radiation processing applications." *Radiation Physics and Chemistry*, 1996: 333-336.

Marketz, F., and F. D. Fischer. "Modelling the mechanical behavior of shape memory alloys under variant coalescence." *Computational Materials Science*, 1996: 210-226.

Masud, A., M. Panahandeh, and F. Auricchio. "A finite-strain finite element model for the pseudoelastic behavior of shape memory alloys." *Computer Methods in Applied Mechanics and Engineering*, 1997: 23-37.

Mather, P. T., X. Luo, and I. A. Rousseau. "Shape Memory Polymer Research." *Annual Review of Materials Resaerch* 39 (2009): 445-471.

Mather, P.T., C. Liu, and C. Burstone. "Shape Memory Polymer Orthodontic Appliances, and Methods of Making and Using the Same." *World Patent Applications* , 2005.

Maugin, G.A. *The thermomechanics of plasticity and fracture.* Cambridge University Press, 1992.

Mayers, J.J., D. Lagoudas, and B.K. Henderson. "An experimental investigation of shape memory alloy pseudoelastic springs for passive vibration isolation." *AIAA space 2001 conference and exposition.* 2001.

Milani, G., E. Milani, and A. Tralli. "Approximate limit analysis of full scale FRP-reinforced masonry building through a 3D homogenized FE package." *Composite Structures*, 2010: 918-935.

Milani, G., E. Milani, and A. Tralli. "Upper Bound limit analysis model for FRP-reinforced masonry curved structures. Part I : unreinforced masonry failure surfaces." *Computer and Structures*, 2009: 1516-1533.

Milani, G., T. Rotunno, E. Sacco, and A. Tralli. "Failure load of FRP strengthened masonry walls: experimental results and numerical models." *Structural Integrity and Durability*, 2006: 29-50.

Moumni, Z., W. Zaki, and Q.S. Nguyen. "Theoretical and numerical modeling of solid-solid phase change: application to the description of the thermomechanical behavior of shape memory alloys." *International Journal of Plasticity*, 2008: 614-645.

Müller, C., and O. Bruhns. "A thermodynamic finite-strain model for pseudoelastic shape memory alloys." *International Journal of Plasticity*, 2006: 1658-1682.

Müller, I, and H. Xu. "On the pseudo-elastic hysteresis." *Acta Metallurgica et Materialia*, 1991: 263-271.

Müller, I. "On the size of the hysteresis in pseudoelasticity." *Contiuum Mechanics and Thermodynamics*, 1989: 125-142.

Müller, I. "Pseudoelasticity in shape memory alloys - an extreme case of thermoelasticity." *Acad. Naz. Lincei. Proc. of the Meeting on Finite Thermoelasticity*, 1986: 123-150.

Müller, I., and K. Wilamanski. "A model for phase transformation in pseudoelastic bodies." *Nuovo Cimento*, 1980: 238-318.

Ookubo, Y. "Polyurethane Recording Media Utilizing Shape Memory." *Japan Patent Office*, 1995.

Ortin, J. "Preisach modeling of hysteresis for a pseudoelastic cu-zn-al single crystal." *Journal of Applied Physics* , 1992: 1454-1461.

Otsuka, K., and C. M. Wayman. *Materials Science Forum.* Cambridge University Press, 1998.

Otsuka, K., and C.M. Wayman. *Shape Memory Materials.* Cambridge University Press, 1998.

Otsuka, K., and X. Ren. "Physical metallurgy of Ti–Ni-based shape memory alloys." *Progress in Materials Science* 50, no. 5 (2005): 511-678.

Panico, M., and L. Brinson. "A three-dimensional phenomenological model for martensite reorientation in shape memory alloys." *Journal of the Mechanics and Physics of Solids*, 2007: 2491-2511.

Patankar, N. A. "Mimicking the Lotus Effect: Influence of Double Roughness Structures and Slender Pillars." *Langmuir* 20 (2004): 8209-8213.

Patoor, E., A. Eberhard, and M. Berveiller. "Micromechanical modelling of superelasticity in shape memory alloys." *Journal of Physics IV*, 1996: 277-292.

Patoor, E., A. Eberhardt, and M. Berveiller. "Micromechanical modelling of the shape memory behavior." *Mechanics of Phase Transformation and Shape Memory Alloys*, 1994: 23-27.

Pelton, A. *SMST-97: Proceedings of the Second International Conference on Shape Memory and Superelastic Technologies.* California, 1997.

Pelton, A.R., N. Kusnezov, and G.P. Carman. "Smart materials applications for pediatric cardiovascular devices." *Pediatric Research* 1, no. 2 (2008): 552-558.

Perkins, J. *Shape Memory Effect in Alloys.* New York: Plenum Press, 1975.

Piedboeuf, M.C., and R. Gauvin. "Damping behaviour of shape memory alloys: strain amplitude, frequency and temperature effects." *Journal of Sound and Vibration*, 1998: 885-901.

Poncin, P., and C. Millet. "Comparing and optimizing Co-Cr tubing for stent applications." *Proceedings of the Materials and Processes for Medical Devices Conference*, 2004: 279-283.

Popov, P., and D.C. Lagoudas. "A 3-D constitutive model for shape memory alloys incorporating pseudoelasticity and detwinning of self-accommodated martensite." *International Journal of Plasticity*, 2007: 1679-1720.

Qidwai, M.A., and D.C. Lagoudas. "On thermomechanics and transformation surfaces of polycrystalline niti shape memory alloy material." *International Journal of Plasticity*, 2000: 1309-1343.

Raniecki, B., and C. Lexcellent. "Rl-models of pseudoelasticity and their specifications for some shape memory alloys." *European Journal of Mechanics - A/Solids*, 1994: 21-50.

Raniecki, B., and C. Lexcellent. "Thermodynamics of isotropic pseudoelasticity in shape memory alloys." *Arch. Mech.*, 1992: 261-284.

Raniecki, B., and C. Lexcellent. "Thermodynamics of isotropic pseudoelasticity in shape memory alloys." *European Journal of Mechanics - A/Solids*, 1998: 185-205.

Raniecki, B., C. Lescellent, and K. Tanaka. "Thermodynamic model of pseudoelastic behaviour of shape memory alloys." *Arch. Mech.*, 1992: 261-284.

Reese, S., and D. Christ. "Finite deformation pseudo-elasticity of shape memory alloys - constitutive modelling and finite element implementation." *International Journal of Plasticity*, 2008: 455-482.

Ren, X., and K. Otsuka. "Origin of rubber-like behaviour in metal alloys." *Nature* 389 (1997): 579-581.

Rizzoni, R., A. Chiozzi, M. Merlin, and A. Tralli. "Comparative assessment of two constitutive models for superelastic shape-memory wires against experimental measurement." *Mechanics of Advanced Materials and Structures*, 2013: accepted.

Saadat, S., M. Noori, H. Davoodi, and Z. Hou. "An overview of vibration and seismic application of NiTi shape memory alloy." *Smart Materials and Structures*, 2002: 218-229.

Sattapan, B., J. E. Palamara, and H. H. Messer. "Torque during canal instrumentation using rotary nickel-titanium files." *Journal of Endodontics* 24, no. 10 (1993): 651-655.

Schmerling, M. A., M. A. Wilkor, and A. E. Sanders. "A proposed medical application of the shape memory effect: an Ni-Ti Harrington rod for treatment of scoliosis." *Journal of Biomedical Materials Research* 10 (1976): 879-902.

Seward, S., and P. Krulevitch. "Shape Memory Alloy/Shape Memory Polymer Tools." *US Patents*, 2002.

Sharp, A., H.V. Panchawagh, A. Ortega, and R. Artale. " Towards a Self-Deploying Shape Memory Polymer Neuronal Electrode." *Journal of Neural Engineering*, 2006: 23-30.

Shaw, J.A. "A thermomechanical model for a 1-D shape memory alloy wire with propagating instabilities." *International Journalof Solids and Structures*, 2002: 1275-1305.

Shaw, J.A., and S. Kyriakides. "Thermomechanical aspects of NiTi." *Journal of the Mechanics and Physics of Solids*, 1995: 1243-1281.

Simoni, M. *Simulazioni numeriche di prove sperimentali su edifici in scala in muratura anche in presenza di rinforzi in FRP e dissipatori superelastici.* Ferrara: Tesi di Laurea, 2012.

Sittner, P., P. Takakura, Y. Hara, and M. Tokuda. "On transformation pathways of general stress controlled thermoelastic martensitic transformation in shape memory alloys." *Journal of Physics IV*, 1996: 357-366.

Sittner, P., Y. Hara, and M. Tokuda. "Experimental study on the thermoelastic martensitic transformation in shape memory alloy polycrystal induced by combined external forces." *Metallurgical and Materials Transactions A*, 1995: 2923-2935.

Sittner, P., Y. Hara, and M. Tokuda. "Experimental study on the thermoelastic martensitic transformation in shape memory alloy polycrystal induced by combined external forces." *Metallurgical and Materials Transactions A*, 1995: 2923-2935.

Small, W., and T. Singhal. "Biomedical Applications of Thermally Activated Shape Memory Polymers." *Journal of Material Chemistry* 20 (2010): 3356-3366.

Sokolowski, W. M., and S. Tan. "Advanced Self-Deployable Structures for Space Applications." *Journal of Spacecraft and Rockets* 44 (2007).

Sokolowski, W., and A. Metcalfe. "Medical Applications of Shape-Memory Polymers." *Biomedical Materials*, 2007.

Souza, A.C., E.D. Mamiya, and N. Zouain. "Three-dimensional model for solids undergoing stress-induced phase transformations." *European Journal of Mechanics - A/Solids*, 1998: 789-806.

Sun, L., and W. M. Huang. "The temperature memory effect and the influence of thermo-mechanical cycling in shape memory alloys." *Smart Materials and Structures* 19, no. 5 (2010): 055005.

Sun, Q. P., and K. C. Hwang. "Micromechanics modelling for the constitutive behavior of polycrystalline shape memory alloys." *Journal of the Mechanics and Physics of Solids*, 1993: 1-17.

Takuda, M., M. Takakura, and P. Sittner. "Thermomechanical behavior of shape memory alloy under complex loading conditions." *International Journal of Plasticity*, 1999: 223-239.

Tamai, H., Y. Kitagawa, K. Miura, and T. Fukuta. "Application of SMA rod to exposed-type column base in smart structural system." *Proceedings of SPIE.* 2003. 169-177.

Tanaka, K. "A phenomenological description on thermomechanical behavior of shape memory alloys." *ASME Journal of Pressure Vessel Technology*, 1990: 158-163.

Tanaka, K. "A thermomechanical sketch of shape memory effect: one-dimensional tensile behavior." *Res Mechanica*, 1986: 251-263.

Tanaka, K., and R. Iwasaki. "A phenomenological theory of transformation superplasticity." *Engineering Fracture Mechanics*, 1985: 709-720.

Tanaka, K., and S. Nagaki. "A thermomechanical description of materials with internal variables in the process of phase transitions." *Archive of Applied Mechanics*, 1982: 287-299.

Tanaka, K., F. Nishimura, T. Hayashi, and H. Tobushi. "Phenomenological analysis on sbloops and cyclic behavior in shape memory alloys under mechanical and/or thermal loads." *Mechanics of Materials*, 1995: 281-292.

Tanaka, K., F. Nishimura, T. Hayashi, and H. Tobushi. "Phenomenological analysis on subloops and cyclic behavior in shape memory alloys under mechanical." *Mechanics of Materials*, 1995: 281-292.

Tanaka, K., S. Kobayashi, and Y. Sato. "Thermomechanics of transformation pseudoelasticity and shape memory effect in alloys." *International Journal of Plasticity*, 1986: 59-72.

Tanaka, Y. "Ferrous Polycrystalline Shape-Memory Alloy Showing Huge Superelasticity." *Science* 327 (2010): 1488-1490.

Terriault, P., F. Viens, and V. Brailovski. "Non-isothermal finite element modeling of a shape memory alloy actuator using ansys." *Computational Materials Science*, 2006: 397-410.

Thamburaja, P. "Constitutive equations for martensitic reorientation and detwinning in shape-memory alloys." *Journal of the Mechanics and Physics of Solids*, 2005: 825-856.

Thamburaja, P., and L. Anand. "Superelastic behavior in tension-torsion of an initially textured NiTi shape memory alloy." *International Journal of Plasticity*, 2002: 1607-1617.

Thanopoulos, B.D., C.V. Laskari, G.S. Tsaousis, and I. Tavori. "Closure of atrial septal defects with the amplatzer occlusion device: preliminary results." *Journal of the American College of Cardiology* 31, no. 5 (1998): 1110-1116.

Thiebaud, F., C. Lexcellent, M. Collet, and E. Foltete. "Implementation of a model taking into account the asymmetry between tension and compression, the temperature effects in a finite element code for shape-memory alloys structures calculations." *Computational Materials Science*, 2007: 208-221.

Thomsen, D.L., P. Keller, J. Naciri, and R. Pink. "Liquid crystal elastomers with mechanical properties of a muscle." *Macromolecules*, 2001: 5868-5875.

Torrisi, L. "The NiTi superelastic alloy application to the dentistry field." *Bio-Medical Materials and Engineering* 9, no. 1 (1999): 39-47.

Tragy, S., S. Singh, S. Mukhopadhyay, and U.A. Kaul. "Self- and balloon-expandable stent implantation for severe native coarctation of aorta in adults." *American Heart Journal* 146, no. 5 (2003): 920-928.

Trochu, F., and Qianm Y.Y. "Nonlinear finite element simulation of superelastic shape memory alloy parts." *Computers and Structures*, 1997: 799-810.

Urayama, K. "Selected issues in liquid crystal elastomers and gels." *Macromolecules*, 2007: 2277-2288.

Vedantam, S. "Constitutive equations for rate-dependent pseuodelastic behaviour of shape memory alloys." *Smart Matrials and Structures*, 2006: 1172-1188.

Wang, W. "On the selection of shape memory alloys for actuators." *Materials & Design* 23, no. 1 (2002): 11-19.

Wang, Y., and A.G. Khachaturyan. "Three-dimensional field model and computer modeling of martensitic transformations." *Acta Materialia*, 1997: 759-773.

White, T.J., K.M. Lee, H. Koerner, and R.A. Vaia. "Light-activated shape memory of glassy, azobenzene liquid crystalline polymer networks." *Soft Matter*, 2011: 4318-4324.

Wilde, K., P. Gardoni, and Y. Fujino. "Base isolation system with shape memory alloy device for elevated highway bridges." *Engineering Structures*, 2000: 222-229.

Wu, M. J., and Y. Q. Huang. "Reversible surface morphology in shape-memory alloy thin films." *Journal of Applied Physics* 105 (2009): 3075773.

Xie, T. "Tunable polymer multi-shape memory effect." *Nature* 464 (2010): 267-270.

Xie, T., and I. A. Rousseau. "Facile tailoring of thermal transition temperatures of epoxy shape memory polymers." *Polymers* 50, no. 8 (2009): 1852–1856.

Xie, T., and I.A: Rousseau. "Facile tailoring of thermal transition temperatures of epoxy shape memory polymers." *Polymer*, 2009: 1852-1856.

Yakacki, C. M. "Strong, Tailored, Biocompatible Shape-Memory Polymer Networks." *Advanced Functional Materials* 18, no. 16 (2008): 2428-2435.

Yang, B., and W. M. Huang. "Effects of moisture on the thermomechanical properties of a polyurethane shape memory polymer." *Polymer* 47, no. 4 (2006): 1348-1356.

Yoshino, T., M. Kondo, J. Mamiya, and M. Kinoshita. "Threedimensional photomobility of crosslinked azobenzene liquid-crystalline polymer fibers." *Advanced Materials*, 2010: 1361-1363.

Zaki, W., and Z. Moumni. "A three-dimensional model of the thermomechanical behavior of shape memory alloys." *Journal of the Mechanics and Physics of Solids*, 2007: 2455-2490.

Zhuo, H.T., J.L. Hu, and S.J. Chen. "Study of the thermal properties of shape memory polyurethane nanofibrous nonwoven." *Journal of Materials Science*, 2011: 3464-3469.